

**AN INVESTIGATION INTO THE
AERODYNAMIC BEHAVIOUR OF A
COMPRESSOR CASCADE IN A DROPLET
LADEN FLOW**

Thesis

Submitted in partial fulfilment of the requirements for the degree of

DOCTOR OF PHILOSOPHY

by

DEEPAK NARAYANAN



**DEPARTMENT OF MECHANICAL ENGINEERING
NATIONAL INSTITUTE OF TECHNOLOGY KARNATAKA,
SURATHKAL, MANGALORE – 575025**

FEBRUARY, 2023

DECLARATION

I hereby declare that the research thesis entitled “**An investigation into the aerodynamic behavior of a compressor cascade in a droplet laden flow**” which is being submitted to the **National Institute of Technology Karnataka, Surathkal** in partial fulfilment of the requirements for the award of the degree of Doctor of Philosophy in Mechanical Engineering is a bonafide report of research work carried out by me. The material in this research thesis has not been submitted to any other universities or institutes for the award of any degree.

Register number: **155033ME15F03**

Name of the research scholar: **Deepak Narayanan**

Signature of the research scholar:



1-03-2023

Department of Mechanical Engineering

Place: NITK-Surathkal

Date: 1-03-2023

CERTIFICATE

This is to certify that the Research Thesis entitled “**An investigation into the aerodynamic behavior of a compressor cascade in a droplet laden flow**” submitted by **Mr. Deepak Narayanan (Register Number: 155033ME15F03)** as the record of the research work carried out by him, *is accepted as the Research Thesis submission* in partial fulfilment of the requirements for the award of the Degree of **Doctor of Philosophy**.



Dr. Anish S.

Research guide

Date: 1/3/2023



Chairman- DRPC



This thesis is
dedicated to
My beloved

Family and Friends

ACKNOWLEDGEMENTS

Foremost I would like to express my sincere gratitude to my supervisor **Dr. Anish S** for considering me worthy of working under his esteemed guidance. I am indebted for his continuous support for my Ph.D. study, and his patience, immense knowledge, and motivation. Besides my supervisor, I would like to thank the rest of my thesis committee members, **Dr. Ajay Kumar Yadav** and **Dr. Pruthviraj U** for their encouragement, insightful comments, and hard queries. I would like to express my sincere gratitude to **Prof. Ravikiran Kadoli**, Chairman of the DRPC and Head of the Department of Mechanical Engineering, for providing the necessary permissions to access various research laboratories and facilities available. I take this opportunity to express my deepest regards to **Dr. Mrityunjay Doddamani** for his fruitful suggestions and active cooperation during the entire period of my research. I would also express my gratitude to **Prof. Gangadharan**, **Dr. Arun M**, and **Dr. Renjith M** for providing the necessary support. I acknowledge the continuous support of **Sri. Shiva Shankar**, **Sri. C A Verghese**, **Sri. Pradeep**, **Sri. Mahesh Anchan**, **Sri. Shashidhar** and **Sri Avinash Devadiga** staff members of Carpentry, Machine shop, and Heat Transfer Laboratory for rendering their help in fabricating the experimental setup.

I express sincere thanks to my colleagues Sushanlal babu, Sachin Sateesh, Vashista G A, Rakesh L, Anil B C, Dr. Sreejith B K, Anand S, Avinash G S, Prashantha B, Kiran K N, Sangappa Dasar, Nithul K, Deepak Kumar, Mithun Kanjan for furnishing necessary aids and for their co-operation throughout the period of my research work. Getting through my dissertation required more than academic support, and I have many people to thank for listening to and, at times, having to tolerate me over the past few years. I cannot begin to express my gratitude and appreciation for their friendship. **Yadukrishnan**, **Arya K**, **Sreebash S K**, **Sachin S**, **Fredy James**, **Niyas S**, **Anoop B N**, **Libin P Oommen**, **Sudhish R**, **Sreenish A**, **Nikhil**, **Jithin V V**, **Nighesh P K**,

Anoop K, Arun Pannery have been unwavering in their personal and professional support during the time I spent at the Institute.

I would like to take this opportunity to express my indebted gratitude and respect to my parents, **Sri. V V Narayanan** and Smt. **Bhargavi K**, for the immense blessings they showered all through my entire life and I express my lovely gratitude to my dear sisters, **Dr. Hena Narayanan, Amrutha Anand, Amitha Vijayan**, Elder brother - **Ravi PK**, Elder sister - **Thankamani** and Brother in Laws- **Murali Krsihanan**, and **Aneesh A**. It is their willingness of shielding me from any social and financial responsibilities to facilitate my continuation with my higher studies. I express my sincere thanks to the dearest one **Kavya Venugoplan** who was there with me in all my good and bad moments and supported me. I would like to thank my parents-in-law, **Sri. Vijayan P V** and **Smt. Prasanna Vijayan** for their support in all its form. I honestly acknowledge the unconditional support of my dear wife, **Anjali Vijayan**. Last but not least, I thank God for showering blessings on me and for giving me such a wonderful family and friends.

(DEEPAK NARAYANAN)

ABSTRACT

The injection of water droplets during the compression process is a well-accepted technique for augmenting the power output from a gas turbine engine. Several researches have been carrying out in this area of ‘wet compression (overspray)’ in order to understand its impact on the aerodynamic performance of the compressor since it is a newly introduced concept in this field. Other hand boundary layer suction cavity on the blades is already a well-established technique in the field of turbo machines. The suction cavity helps to minimize boundary layer growth and helps to delay the flow separation. Hence the overall aerodynamic performance of the system would be increased. However the concept of incorporation of boundary layer suction with wet compression technology would be a new method.

The first part of this study analyzes the effect of water injection on the aerodynamic performance of a linear compressor cascade. Studies have been conducted to investigate the impact of incidence angles, water droplet size, and injection ratios (IR) on the stalling characteristics of the compressor blade. Comparative analyses have been made with the dry case. Primarily, the studies have been carried out numerically using RANS simulations. The experimental analysis has also been carried out using flow visualization techniques. The study reveals notable flow modifications in the separated flow region under wet compression. For positive incidence angles, the total loss coefficient considerably decreases at the compressor’s downstream side whereas, wet compression increases the overall pressure losses inside the blade pathway at negative incidence angles. Studies with droplet size and injection ratio reveal the possibility of an optimum value for these parameters for wet compression. The flow visualization studies help to understand the water film formation and its propagation over the blades at negative and positive incidence angles.

In the second part of the study, an active flow control mechanism (suction slots) is used to stabilize the boundary layer flow. Suction slots are provided to control the corner separation of the axial compressor cascade. Studies are carried out in a droplet laden flow, and comparisons are made with dry air conditions. Numerical simulations have been carried out to investigate the effect of different suction slot configurations on the

loss coefficient of the cascade. Four different slot configurations are tested near endwall slot (NES), near midspan slot (NMS), full span slot (FSS), and combined full span-endwall slot (FEWS). It was observed that the suction slot placed on the suction surface of the blade could successfully reduce the flow separation. However, the flow field at other portions of the span deteriorated as a result of this. Full-span suction (FSS) scheme on the suction surface removed boundary layer separation in the middle of the blade while greatly enhancing flow uniformity close to the end wall. Despite the improvement in flow uniformity using the full span suction scheme, a three-dimensional corner separation still existed due to the strong cross-passage pressure gradient. The combined FEWS configuration could further reduce the separation, and the total pressure loss coefficient was reduced significantly by 26 %.

CONTENTS

ABSTRACT	i
CONTENTS	iii
LIST OF FIGURES	vii
LIST OF TABLES	vii
NOMENCLATURE	xix
1 INTRODUCTION	1
1.1 Power Augmentation in Gas Turbine Engine	1
1.2 The Overspray or Wet Compression Process.....	2
1.3 The Need for a Flow Control Method.....	3
1.3.1 Passive control methods.....	3
1.3.2 Active control methods	7
1.4 Motivation for The Present Investigation.....	8
1.5 Structure of the Thesis.....	9
2 LITERATURE SURVEY	11
2.1 Introduction	11
2.2 The Overspray or the Wet compression in a Gas Turbine Engine.....	11
2.3 Effect of Wet Compression on Gas Turbine Engine Performance	11
2.4 Importance of Droplet Size	17
2.5 Impact of Pressure ratio and Evaporation Rate.....	21
2.6 Effect of Ambient Temperature and Heat Rate.....	22
2.7 Various Design Considerations to Improve The Efficiency	23
2.8 Studies on Boundary Layer Suction Control Mechanism.....	26
2.9 Summary of the Literature Review	30
2.10 Problem Definition.....	36
2.11 Objectives.....	36

3	NUMERICAL METHODOLOGY	37
3.1	Blade Profile.....	37
3.2	Types of Configurations.....	38
3.3	The Computational Domain	39
3.4	Mesh Generation	40
3.5	Details of the Solver.....	42
3.6	The Flow Physics	43
3.7	Grid Sensitivity Study	48
3.8	Validation.....	48
4	FLOW ANALYSIS IN COMPRESSOR CASCADE WITH WATER INJECTION	51
4.1	Effect of Incidence Angle on the Loss Coefficient.....	51
4.2	Detailed Flow Behavior at 0° Incidence	53
4.2.1	Comparison of vectors near end wall (at 4 % of the span)	53
4.2.2	Comparison of vectors near midspan (at 45 % of the span)	56
4.2.3	The hub corner vortex formation and its effect on total pressure loss coefficient	58
4.2.4	Effect of Hub corner vortex on loss coefficient at zero incidence angle	61
4.3	Detailed Flow Behavior at Positive Incidence Angles.....	63
4.3.1	Comparison of vectors near end wall (at 4 % of the span)	63
4.3.2	Variation of Blade Loading at Positive Incidence Angles.....	68
4.4	The behavior of Flow at Negative Incidence Angles.....	69
4.4.1	Variation of Blade Loading at Negative Incidence Angles	75
4.5	Summary	77

5 FLOW ANALYSIS IN COMPRESSOR CASCADE AT VARIOUS DROPLET SIZES AND INJECTION RATIOS.....	79
5.1 Effects of Droplet Size	79
5.1.1 The flow deviation at the leading edge	79
5.1.2 Static pressure on the blade surface	83
5.1.3 Influence of droplet size on the loss coefficient	86
5.1.4 Total pressure losses at the downstream of trailing edge	87
5.1.5 Velocity vectors and secondary flow	91
5.1.6 Trajectories of the wake and the Trailing Edge Vortex (TEV) center... 92	
5.1.7 Velocity and vorticity fields downstream of the blade	94
5.2 Effect of Injection Ratio	96
5.2.1 Flow deviation at the inlet and aerodynamic blockage inside the blade passage	96
5.2.2 Static pressure on the blade and the blade loading	98
5.2.3 Variation in the total pressure losses coefficient	100
5.2.4 Velocity and vorticity fields downstream of the cascade	102
5.3 Summary	105
6 WATER INJECTION IN AN ACTIVE FLOW CONTROL ENVIRONMENT.....	107
6.1 Identifying the Axial Location for the Slot	107
6.2 Effect of Wet Compression and Suction Slot on the Performance	110
6.3 Effect of Water Injection on NES Configuration.....	110
6.4 Effect of Water Injection on NMS Configuration.....	114
6.5 Effect of Water Injection on FSS Configuration.....	119
6.6 Comparison of Blade Loading	122
6.7 Need and Creation of Additional Configuration	123

6.7.1	Total pressure loss in the streamwise direction	123
6.7.2	Static pressure coefficient distribution across the blade span near the suction surface of the trailing edge.....	125
6.8	Combined Suction Scheme	126
6.8.1	The flow field analysis of the combined suction slot scheme	127
6.8.2	Total pressure loss in the streamwise direction	129
6.8.3	Varitions in the Turbulent kinetic energy	131
6.8.4	Distribution of static pressure coefficient along the blade span near the suction surface of the trailing edge.....	132
6.9	Summary	133
7	EXPERIMENTAL ANALYSIS: FLOW VISUALIZATION	135
7.1	Experimental Setup	135
7.2	Water Film Measurement and Image Processing.....	136
7.3	Particle Tracking	139
7.4	Flow Visualization at Different Incidence Angles and Free Stream Velocities.....	139
7.4.1	Water rivulets at different incidences angles	139
7.4.2	The water rivulets formation at different air stream velocities.....	143
7.5	Summary	149
8	CONCLUSIONS AND SUGGESTIONS FOR FUTURE WORK.....	151
8.1	Conclusions	151
8.2	Suggestions For Future Work	153
	REFERENCES.....	155

LIST OF TABLES

Table 3.1 Half thickness of NACA 65-009 airfoil in the coordinates of the blade	38
Table 3.2 Computational configurations used in this study.....	39
Table 4.1 Variation of flow separation at different incidence angles	77
Table 4.2 Variation in the mass flow averaged total pressure loss coefficient.....	77
Table 6.1 Percentage deviation of mass averaged total pressure loss coefficient at the outlet	108

LIST OF FIGURES

Figure 1.1 Various passive flow control methods (a) vortex generators (Lu et al. 2012), (b) leading-edge slat (Lu et al. 2012), (c) flow vane (Pechlivanoglou 2013) and (d) an airfoil blade with modified models via serrations (Fish and Lauder 2006; Ibrahim and New 2015).....	4
Figure 1.2 Aerofoil flow (a) with flow suction device (b) with flow injection/blowing device (Talay 1975)	7
Figure 3.1 Schematic representation of blade profile	37
Figure 3.2 Computational domain	40
Figure 3.3 Structured mesh generated for the computational domain	41
Figure 3.4 The O-grid distribution around blade surface	42
Figure 3.5 The y^+ distribution over the endwall and blade surface.....	42
Figure 3.6 Grid sensitivity study.....	48
Figure 3.7 Comparison of static pressure coefficient (C_{ps}) on the blade surface at midspan of present CFD study with experimental and computational results of Ma et al. 2011.....	49
Figure 3.8 Variation of endwall static pressure coefficient (C_{ps}) (a) experimental study (Ma et al. 2011) (b) CFD study (Ma et al. 2011) (c) Present CFD study	50
Figure 3.9 Comparison of total pressure loss coefficient (C_{po}) on a streamwise plane at 50 % of the axial chord downstream of the trailing edge (a) experimental study (Ma et al. 2011) (b) CFD study (Ma et al. 2011) (c) Present CFD study.....	50
Figure 4.1 Schematic representation of different flow incidence.....	51

Figure 4.2 (a) Schematic diagram representing the measurement locations (b) Variation of mass flow averaged total pressure loss coefficient at different positive incidence angles (DC = Dry case; WC = Wet case)	52
Figure 4.3 Variations of mass flow averaged total pressure loss coefficient at different negative incidence angles	53
Figure 4.4 Variation of velocity vector near end wall (4 % of span) (a) Dry case (b) Wet case.....	54
Figure 4.5 Variation of surface streamlines near end wall (4 % of span) (a) Dry case (b) Wet case	55
Figure 4.6 (a) Schematic diagram representing the measurements locations (b) Variations of wall shear on the suction surface of the blade near end wall (at 4 % of the span).....	55
Figure 4.7 Variations of velocity vector near midspan (at 45 % of span) for the dry case and wet case (a) dry case (b) wet case	56
Figure 4.8 Variation of velocity coefficient contour for 0° incidence angle at 0.50 C_{ax} (a) dry case (b) wet case.....	57
Figure 4.9 Variation of velocity coefficient contour for 0° incidence angle at 0.96 C_{ax} (a) dry case (b) wet case.....	57
Figure 4.10 Variations of water particle track inside blade the blade passage	58
Figure 4.11 Limiting streamlines on the blade suction surface and end wall superimposed with total pressure loss coefficient at 1.1 C_{ax} (a) dry case (b) wet case	59
Figure 4.12 Volume streamlines plotted near end wall (a) dry case (b) wet case	62
Figure 4.13 Variation of total pressure loss coefficient at 0.96 C_{ax} and 2.3 C_{ax} (a) dry case (b) wet case	62

Figure 4.14 Variation of surface streamlines near end wall for different incidence angles (at 4 % of span) (a) +2° (b) +4° (c) +6° (d) 8°	64
Figure 4.15 Variations of wall shear on the suction surface of the blade near end wall for different incidence angles (at 4 % of the span) (a) +2° (b) +4° (c) +6° (d) 8°	65
Figure 4.16 Variation of velocity coefficient contour for different incidence angle at 0.50 C_{ax} (a) +2°(b) +4° (c) +6° (d) 8°	66
Figure 4.17 Variation of velocity coefficient contour for different incidence angle at 0.96 C_{ax} (a) +2° (b) +4° (c) +6° (d) 8°	66
Figure 4.18 Variations of water particle track inside blade the blade passage different incidence angles (a) +2° (b) +4° (c) +6° (d) 8°	67
Figure 4.19 (a) Schematic diagram representing the measurements locations (b) Variation of static pressure coefficient on the blade surface at 4 % of the span	68
Figure 4.20 Variation of static pressure coefficient on the blade at 45 % of the span	69
Figure 4.21 Variation of velocity vector near end wall	70
Figure 4.22 Variations of wall shear on the suction surface of the blade near end wall (at 4 % of the span) (a) at -2° (b) at -4° (c) at -6° (d) at -8°	71
Figure 4.23 Variation of Q-criteria plotted near the leading edge region (a) Dry case (b) Wet case	71
Figure 4.24 Limiting streamlines on the blade suction surface and end wall superimposed with total pressure loss coefficient at 1.1 C_{ax}	73
Figure 4.25 Variation of total pressure loss coefficient at 0.96 C_{ax} and 2.3 C_{ax}	74
Figure 4.26 Variation of static pressure coefficient on the blade at 4 % of the span ..	76
Figure 4.27 Variation of static pressure coefficient on the blade at 45 % of the span	76

Figure 5.1 Variation in flow deviation angle at the inlet section near leading edge for different droplet sizes.....	80
Figure 5.2 Variation of particle track superimposed with surface streamline in the case of different droplet sizes near endwall.....	80
Figure 5.3 Variation of particle track superimposed with surface streamline in the case of different droplet sizes near midspan.....	81
Figure 5.4 Velocity coefficient contour plotted at 1 % of span for different droplet sizes (a) 12 μm (b) 20 μm (c) 32 μm (d) 48 μm (e) 60 μm	82
Figure 5.5 Static pressure distribution contour on the pressure surface of the blade (a) DC (b) 12 μm (c) 20 μm (d) 32 μm (e) 48 μm (f) 60 μm	84
Figure 5.6 Static pressure distribution contour on the suction surface of the blade (a) DC (b) 12 μm (c) 20 μm (d) 32 μm (e) 48 μm (f) 60 μm	85
Figure 5.7 Blade loading on the blade at midspan for dry case and wet case at different droplet size.....	85
Figure 5.8 Static pressure distribution on the blade near end wall for dry case and wet case at different droplet size.....	86
Figure 5.9 Mass flow averaged total pressure loss coefficient(a) 12 μm (b) 20 μm (c) 32 μm (d) 48 μm (e) 60 μm	86
Figure 5.10 Total pressure losses coefficient distributions at downstream section 1 for dry case and all droplet sizes (a) DC (b) 12 μm (c) 20 μm (d) 32 μm (e) 48 μm (f) 60 μm	87
Figure 5.11 Mass flow averaged total pressure loss coefficient at 1.1 C_{ax} for the dry case and the wet case of different droplet diameters.....	88

Figure 5.12 Schematic representation of measurement locations downstream of the trailing edge	88
Figure 5.13 Total pressure losses coefficient distributions at three outlet sections downstream of the cascade, for droplet size of 48 μm	89
Figure 5.14 Pitch averaged total pressure loss coefficient from along spanwise direction at three downstream locations.....	89
Figure 5.15 Mass flow averaged total pressure loss coefficient at three outlet sections for dry case and wet case of different droplet sizes	90
Figure 5.16 Velocity vector plotted at three downstream locations for dry case, wet case of droplet size 42 μm and wet case of droplet size 32 μm	92
Figure 5.17 Trajectories of the blade wake and core of the TEV downstream of the cascade at dry case and wet case having droplet sizes 48 μm , 32 μm	93
Figure 5.18 Normalized mean velocity at two downstream location (section 1 at 1.1 C_{ax} , section 2 at 1.5 C_{ax}) for dry case and wet case having droplet sizes 48 μm and 32 μm	94
Figure 5.19 Axial vorticity at two downstream location (section 1 at 1.1 C_{ax} , section 2 at 1.5 C_{ax} for dry case and wet case having droplet sizes 48 μm and 32 μm	95
Figure 5.20 Variation in flow deviation angle at the inlet section near leading edge for different injection ratios.....	96
Figure 5.21 Velocity coefficient contour plotted at 1 % of span for different droplet sizes (a) IR=0.5 % (b) IR=1 % (c) IR =2 % (d) IR =3 % (e) IR=4 %	97
Figure 5.22 Static pressure coefficient distribution on the suction surface of the blade (a) dry case (b) IR=0.5 % (c) IR=1 % (d) IR=2 % (e) IR= 3 % (f) IR=4 %	98
Figure 5.23 Static pressure coefficient distribution over the blade at 50 % of span....	99

Figure 5.24 Static pressure coefficient distribution over the blade at 5 % of span.....	99
Figure 5.25 Mass flow averaged total pressure loss coefficient along the axial direction	101
Figure 5.26 Mass flow averaged total pressure loss coefficient at $1.1C_{ax}$	101
Figure 5.27 Total pressure loss coefficient of dry case and wet case with different injection ratio at $1.1 C_{ax}$	102
Figure 5.28 Normalized mean velocity at two downstream location (section 1 at 1.1 C_{ax} , section 2 at $1.5 C_{ax}$ for dry case and wet case with injection ratios 4 % and 2 %	103
Figure 5.29 Normalized mean axial vorticity at two downstream location (section 1 at $1.1 C_{ax}$, section 2 at $1.5 C_{ax}$ for dry case and wet case with injection ratios 4 % and 2 %	104
Figure 5.30 Trajectories of the (a) blade wake and (b) core of the TEV downstream of the cascade at dry case (DC) and wet case having injection ratios 4 % and 2 %	104
Figure 6.1 Geometric details of Model.....	108
Figure 6.2 Static pressure coefficient superimposed with limiting streamlines on the blade suction surface for all models.....	109
Figure 6.3 Different slot configurations on the suction surface (a) NES (b) NMS (c) FSS.....	110
Figure 6.4 Static pressure coefficient superimposed with surface streamline on the suction surface of the blade (a) Base case-Dry (b) NES-Dry (c) NES-Wet	111
Figure 6.5 Limiting streamlines on the suction surface and end wall (a) NES-Dry (b) NES-Wet.....	111

Figure 6.6 Static pressure coefficient contour on the slot (a) NES-Dry (b)NES-Wet	112
Figure 6.7 Variations in the wall shear distribution in the axial direction around the slot and the enhanced view near end wall (a) NES-Dry (b) NES-Wet.....	113
Figure 6.8 Velocity curl on the plane normal to the slot (close to the slot, 0.05 mm from the slot) (a) NES-Dry (b) NES-Wet.....	114
Figure 6.9 Static pressure coefficient superimposed with surface streamline on the suction surface of the blade (a) Base-Dry (b) NMS-Dry (c) NMS-Wet.....	115
Figure 6.10 Limiting streamlines on suction surface and end wall (a) NMS-Dry (b) NMS-Wet.....	115
Figure 6.11 Velocity coefficient contour on the plane at 1 % of span (a) NMS-Dry (b) NMS-Wet.....	116
Figure 6.12 Velocity coefficient vector plotted at the initial point of separation of the dry case, $0.0095 C_{ax}$ for (a) NMS-Dry (b) NMS-Wet	116
Figure 6.13 Axial velocity contour plotted on the plane normal to the blade suction surface (0.05 mm distance from the blade surface towards flow direction) (a)NMS-Dry (b) NMS-Wet	117
Figure 6.14 Variations in the wall shear distribution in the axial direction around the slot and the enhanced view near end wall (a) NMS-Dry (b) NMS-Wet.....	118
Figure 6.15 Velocity curl on the plane normal to the slot (close to the slot, 0.05 mm from the slot) (a) NMS-Dry (b) NMS-Wet.....	118
Figure 6.16 Static pressure coefficient superimposed with surface streamline on the suction surface of the blade (a) Base case-Dry (b) FSS-Dry (c) FSS-Wet.....	119

Figure 6.17 Limiting streamlines on the suction surface and end wall (a) FSS-Dry (b) FSS-Wet.....	120
Figure 6.18 Velocity curl on the plane normal to the slot (close to the slot, 0.05 mm from the slot) (a) FSS-Dry (b) FSS-Wet.....	121
Figure 6.19 Static pressure coefficient distribution over the blade at 5 % of the span and midspan.....	123
Figure 6.20 Mass averaged total pressure loss coefficient along the axial direction from leading edge to $1.45 C_{ax}$	124
Figure 6.21 Static pressure coefficient distribution along the blade span near suction surface at trailing edge	125
Figure 6.22 Schematic representation of combined slot scheme (FEWS).....	126
Figure 6.23 Static pressure coefficient superimposed with surface streamline on the suction surface of the blade (a) Base-Dry (b) FEWS-Dry (c) FEWS-Wet.....	127
Figure 6.24 Limiting streamlines on the suction surface and end wall (a) FEWS-Dry (b) FEWS-Wet.....	128
Figure 6.25 Variations in water droplet mass concentration at the corners of the end wall slot (a) at the corner near the trailing edge (b) at the corner near the leading edge	128
Figure 6.26 Static pressure coefficient distribution over the blade at 5 % of the span and midspan.....	129
Figure 6.27 Variations of the velocity contour coefficient along the streamwise direction (a) dry case (b) wet case	130
Figure 6.28 Variation of total pressure along the streamwise direction	130
Figure 6.29 Variation of total pressure along the streamwise direction	131

Figure 6.30 Static pressure coefficient distribution along the blade span near suction surface at trailing edge	132
Figure 7.1 (a) Wind tunnel of low-speed compressor cascade (b) Enhanced view of cascade (c) Nozzle	136
Figure 7.2 Schematic representation of water film measurement set up	137
Figure 7.3 Various stages of processing of wanted image (a) Unprocessed image (b) Image after bandpass filtration (c) Image after gaussian filtration (d) Image after CLAHE (e) Sharpened image (f) Detected image.	138
Figure 7.4 Variation of water rivulets concentration at different incidence angles at different time periods the 20s, 25s, and 30s from the experimental investigation (a) +5° (b) +15° (c) -5° (d) -15°	140
Figure 7.5 Droplets trajectories on the blade at the various angle of incidence (a) +5°, (b) +15°, (c) -5°, (d) -15° and (e) schematic representation of impact angle (θ).....	142
Figure 7.6 The change in the angle of impact with respect to axial location for +15° and +5° incidence angle.	143
Figure 7.7 Variation in concentration of water rivulets on the pressure side of the blade for 0° incidence angle at different air stream velocity (a) 19.19 m/s (b) 21.74 m/s (c) 24.31 (d) 26.82 m/s	144
Figure 7.8 Flow modification near trailing edge for 0° incidence angle at different air stream velocity (a) 19.19 m/s (b) 21.74 m/s (c) 24.31 (d) 26.82 m/s	145
Figure 7.9 Flow modification near trailing edge for +5° incidence angle at different air stream velocity (a) 19.19 m/s (b) 21.74 m/s (c) 24.31 (d) 26.82 m/s	147
Figure 7.10 Flow modification near trailing edge for -5° incidence angle at different air stream velocity (a) 19.19 m/s (b) 21.74 m/s (c) 24.31 (d) 26.82 m/s	147

Figure 7.11 Flow modification near trailing edge for -10° incidence angle at different air stream velocity (a) 19.19 m/s (b) 21.74 m/s (c) 24.31 (d) 26.82 m/s 148

Figure 7.12 Flow modification near trailing edge for $+10^\circ$ incidence angle at different air stream velocity (a) 19.19 m/s (b) 21.74 m/s (c) 24.31 (d) 26.82 m/s 148

NOMENCLATURE

C	Chord length (mm)
C_{ax}	Axial chord (mm)
$C_{f,c}$	Aerodynamic skin co-efficient
C_{po}	Total pressure loss co-efficient
C_{ps}	Static pressure co-efficient
D_d	Droplet diameter (μm)
F	Focal point
H	Total span (mm)
I	Incidence angle (degree)
m_∞	Mass flow rate of mainstream (kg/s)
m_w	Mass flow rate of water droplet (kg/s)
N	Node
P_s	Static pressure (Pa)
P_t	Total pressure (Pa)
$P_{t,\infty}$	Total pressure of mainstream (Pa)
$P_{t,w}$	Total pressure of water droplet (Pa)
S	Saddle point
s	Blade spacing (mm)
u	Axial velocity (m/s)
U_∞	Velocity of mainstream (m/s)
y	Pitch distance (mm)
z	Span distance (mm)

Greek symbol

ρ_∞	Density of mainstream (kg/m^3)
θ	Impact angle (degree)

Superscripts

—	Pitch averaged
---	----------------

= Mass averaged

Abbreviation

AL	Attachment line
CLAHE	Contrast limited adaptive histogram equalization
DoG	Difference of Gaussian
DC	Dry case
FEWS	Combination of FSS scheme with endwall scheme
FSS	Full span slot
HI	High impingement region
IR	Injection ratio
LE	Leading edge
LI	Low impingement region
NES	Near endwall slot
NMS	Near midspan slot
PS	Pressure surface
RANS	Reynold's Averaged Navier Stokes
SL	Suppression line
SS	Suction surface
SST	Shear stress transfer
TE	Trading edge
TEV	Trading edge vortex
WC	Wet case

CHAPTER 1

INTRODUCTION

Energy, which is essential for all facets of existence, is crucial to the economic development of the nations. In order to compete favorably on the global stage and promote sustainable development, nations must use energy effectively. The demand for electricity is rising at its quickest rate in more than a decade. The preference for power plant types that use gas turbines as their primary component has increased due to recent changes in the worldwide environment for power production. The profitability of operating gas-fired power plants is rising as the natural gas prices in countries like the United States show a decline due to new discovery methods such as fracking. In India, coal-based thermal power plants continue to rule the power sector. The environment's deterioration and the occurrence of various natural disasters due to the various pollutants released by coal-based power plants are also quite concerning. Natural gas utilized in the gas-fired power plants is a cleaner fuel than coal and can produce electricity more effectively. Due to their environmental benefits, gas based power plants are becoming more and more prevalent today, also gaining increasing support from the government (Newell et al. 2021).

1.1 Power Augmentation in Gas Turbine Engine

The compressor, combustion chamber, and turbine comprise a gas turbine engine's three primary components. Air is drawn from the atmosphere by the compressor, compressed, and sent to the combustion chamber, where it is combined with fuel and ignited. Inside the combustion chamber, it greatly increases temperature and pressure. On their way out, the hot exhaust gases pass the turbine, where some of their energy is used to turn the turbine. The turbine turns the generator that is linked with it at a speed of over 3000 rpm. Electricity is generated by the generator's coils and then sent to the power grid.

The major part of the power delivered from a gas turbine is used for the compression process. It is approximately 40 – 60 % of the energy generated by the engine of the gas turbine. Any decrease in compression work results in an immediate increase in the output as well as efficiency of gas turbines. Inlet fogging and overspray (also known as wet compression) are the two methods that can be used to reduce the compression work. Each of these techniques used different ways to reduce the compression work. The incoming air is cooled in the inlet fogging technique before it enters the compressor impeller. The incoming air can be cooled using a variety of approaches, which include mechanical chillers with a refrigerant, absorption chillers, and evaporative inlet cooling. However, the inlet fogging relies on the humidity and temperature of the surrounding air. This difficulty can be overcome with the overspray technique.

1.2 The Overspray or Wet Compression Process

The wet compression (WC) technique involves injecting atomized water into the compressor's incoming air stream. The water evaporates as it passes through the compressor's stages. Because constant evaporation occurs during wet compression, the compression is thermodynamically close to being isothermal, significantly reducing the work required by the compressor. The engine's overall efficiency will rise due to this reduction (Härtel and Pfeiffer 2003; Utamura et al. 1997). Although the work performed by the compressor is substantially less due to overspray, the higher gas mass flow through the compressor increases compressor power consumption due to the compression's evaporation-induced low compressor discharge temperature (CDT), and fuel mass flow increases. The increased mass flow through the turbine causes the cycle pressure ratio to rise, increasing the turbine's power.

The benefits of wet compression are not just an increase in the turbine output but an improvement in the heat rate and a possible NO_x reduction. Even though the performance enhancement of the overall gas turbine engine system has been identified, a proper understanding of the effects of overspray on the aerodynamic behavior of the two-phase flow (air-water droplets) is not yet adequately understood. The present investigation is aimed in this direction.

1.3 The Need for a Flow Control Method

Due to boundary layers' weak capacity to overcome adverse pressure gradients, flow separation frequently occurs in the compressor. It has an adverse effect on the performance of compressors with highly loaded blades. Flow separation can result in decreased aerodynamic stability and efficiency as well as an increase in loss. The highly loaded compressor design has been continuously developed by a large number of researchers. It is now possible to control flow separation and improve compressor performance due to passive and active flow control technology (Guo et al. 2013; Hu et al. 2017; Svorcan et al. 2014; Zhang et al. 2019). Passive flow control approaches can function only in a single operating environment and cannot fastly adapt to a changing flow field. Active flow control methods, as opposed to passive control methods, can be turned on and off based on the operating circumstances, which is particularly useful for sophisticated aero compressors.

1.3.1 Passive control methods

The use of surface treatments (Afshari et al. 2016, 2017), devices with porous material systems, form optimization, and morphing technology are examples of passive flow control techniques. Some of the passive control methods used to control the flow around airfoil structures are shown in Figure 1.1. A vortex generator is a small device attached to a wall that may create a streamwise vortex (Figure 1.1 (a)). Local geometrical flaws lead to longitudinal vortices that mix the flow locally, energizing the boundary layer, delaying or preventing separation, or causing secondary flow motion, reorganizing the entire flow field (Lu et al. 2012). The leading-edge slats, first introduced in Great Britain (Handley 1922) and first used for aircraft (Van Dam 2002), were known as passive flow controllers by delaying the flow (Figure 1.1 (b)). The boundary layer obtains kinetic energy and momentum by accelerating the flow using leading-edge slats, which delays the stall phenomenon (Rumsey and Ying 2002). Flow vanes are used in wind turbines as power regulators and stall controllers (Pechlivanoglou 2013). Figure 1.1 (c) illustrates how the flow vanes have significantly shorter chord lengths than the main body, allowing them to be placed over the suction surface of airfoils. The morphology of humpback whales inspired the leading-edge serration passive flow

control technique, as shown in Figure 1.1 (d) (Fish and Lauder 2006; Ibrahim and New 2015). This bio-inspired method has lately been studied experimentally or statistically for various objectives. A customized airfoil blade with sinusoidal wave serrations on the leading edge manages the boundary layer separation (Wang and Zhuang 2017). Other than these methods, flow control is achieved by using roughness material. Roughness results in vortex sheds, intensifying the boundary layer's flow. By dispersing roughness elements at a spacing roughly equivalent to one-half of the spanwise wavelength of the critical mode, three-dimensional static roughness can be a helpful tool in postponing the transition to turbulence on a swept wing (White and Saric 2000)

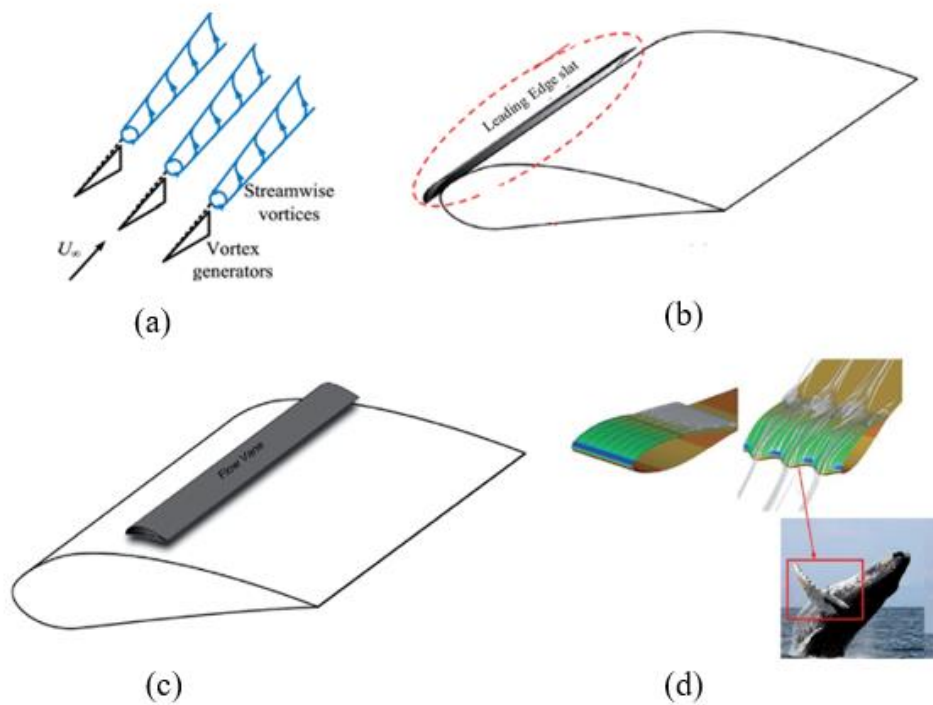


Figure 1.1 Various passive flow control methods (a) vortex generators (Lu et al. 2012), (b) leading-edge slat (Lu et al. 2012), (c) flow vane (Pechlivanoglou 2013) and (d) an airfoil blade with modified models via serrations (Fish and Lauder 2006; Ibrahim and New 2015)

In addition to conventional passive control techniques, new technologies have been emerging day by day. Micro cylinders, Gurney flaps, self-activated deployable flaps, airfoils with cavities, and a novel idea for the pre-stall controller using roughness material, flexibility, and partial flexibility are some of the technologies created in recent years. The new concept pre-stall control technique for controlling laminar separation bubbles increases lift and decreases drag. However, the utilization of matter consumption and energy is significantly less.

The leading-edge microcylinder works on the theory that it can accelerate the velocity over the airfoil's suction surface, reducing the Kelvin-Helmholtz instability of fluid flow. To assure stall delay and reduce the flow separation zone, Luo et al. 2017 developed a microcylinder and placed it in front of the leading edge of the NACA0012 airfoil. By placing a micro cylinder with a sufficient diameter in front of the leading edge, an increase of 27.3 % at blade torque was achieved based on the numerical calculation made by Wang et al. (Wang et al. 2018). Gurney flap is a compact boundary layer passive control technique that is simple to deploy on an airfoil's trailing edge. By raising the lift coefficient, the Gurney flap can impact aerodynamic efficiency. At a Reynolds number of 3.6×10^5 , Shukla and Kaviti 2017 numerically evaluated four symmetric NACA airfoils in conjunction with a dimple, a Gurney flap, and a combination of the two. According to their findings, when the angle of attack was 12° , the NACA0021 airfoil with a combination of Gurney flap and dimple performed more aerodynamically. Aerodynamic experts have concentrated on a method to emulate the biological flows in birds' wings in order to lessen the harmful effects of flow and boost the lift coefficient. In order to regulate flow separation, a self-activated spanwise flap near the trailing edge of the airfoil has been designed. When flow separation takes place on the suction surface of the wing, the self-activated flap begins to pop up due to backflow to deal with crucial flight situations. Thus, perching manoeuvres or gusts can prevent the wing from suddenly increasing the angle of attack. The physical process of the flow field over a NACA0020 airfoil with an elastically attached flap was studied by Rosti et al. 2018 at a Reynolds number of 2×10^4 . These flaps were found to be effective in preventing the rapid lift loss caused by dynamic stall breakdown. Additionally, a more favorable aerodynamic reaction was obtained during the ramp-up motion of the

movable flap, such as an increase in lift amount. Self-activated deployable flaps were also examined by Schluter 2010 and Arivoli and Singh 2016. Despite having limited impact in Reynolds number and heavy stall conditions, their findings showed that deployable flaps played key roles in terms of aerodynamic performance. The concept behind the principle of airfoils with cavity is to create a convenient pressure gradient when two counter-rotating vortices inside the cavity are trapped. Additionally, these trapped vortices over the suction surface ensure an additional low-pressure area while also producing less drag. As a result, this technique has recently attracted the attention of aerodynamic researchers. Lam and Leung 2018 reported a thorough numerical analysis of the aeroacoustics of a cavitied NACA 0018 airfoil at a Reynolds number of 2×10^4 and a Mach number (Ma) of 0.2. The lift-to-drag ratio rose as a result of the cavity. Additionally, the cavitied airfoil design was noiseless at low Reynolds number regimes because it generated less acoustic power.

The flow over wind turbine blades operating at low Reynolds number ranges can be passively controlled by the control approach with the roughness material. Roughness results in vortex sheds, which intensify the flow in the boundary layer. The flow over the surface of the airfoil is ensured by attached energetic flow, which prevents boundary layer flow separation (Genç et al. 2016; Huebsch 2000; Koca et al. 2018). Flexible membrane, a thin membrane-like material with a fixed leading edge and a free, scalloped trailing edge that can be easily adapted to the flow environment, is a biologically inspired wing. Additionally, they have the ability to modify the wing plan form for a particular flight scenario, and their flight can be distinguished by highly chaotic and three-dimensional wing oscillations. A membrane wing makes the vehicle easier to fly and is better able to adapt to atmospheric disturbances (Mueller and DeLaurier 2003; Shyy et al. 1999; Smith 1996; Timpe et al. 2013). In order to examine interactions between fluid and membrane, the fluid-structure interaction (FSI) method was applied to numerical modeling. It has been found that the segmented airfoil's interaction with the flow reduces flow separations at high angles of attack. In comparison to a rigid airfoil near the stall angle, it has been discovered that an airfoil with three distinct flexible zones exhibits the best aerodynamic performance and increases the lift coefficient by 39 %.

1.3.2 Active control methods

Compared to fixed structures with pre-set actuators, adopting active flow control techniques could be significantly more effective in reducing the restrictions on the range of feasible configurations. A mechanism that tries to change the hydrodynamic pressure field in the interest zones, where more remarkable performance in both aeroacoustic and aerodynamic aspects is anticipated, is boundary layer flow manipulation utilizing active flow control methods. The energy required to manipulate a flow field actively is connected to the challenges. An effective active flow control application should be able to suppress noise to predetermined levels while preserving aerodynamic performance and using the least amount of energy (Szoke 2019).

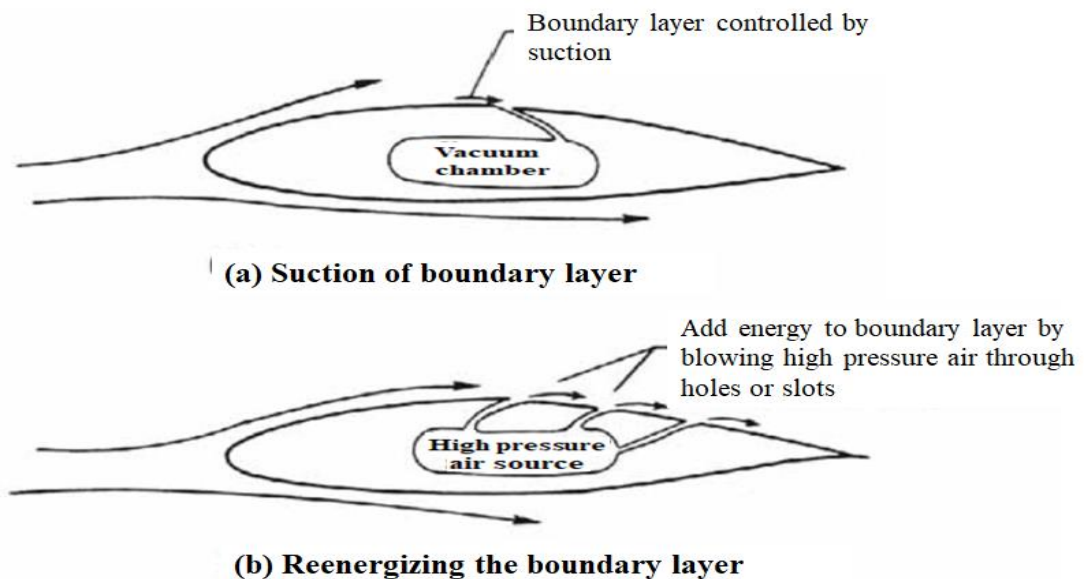


Figure 1.2 Aerofoil flow (a) with flow suction device (b) with flow injection/blowing device (Talay 1975)

The principles of boundary layer flow suction and boundary layer flow blowing, account for the majority of active flow control techniques development from their early stages up to the present. The fundamental concept behind controlling boundary-layer flow through flow suction and flow blowing is seen in Figure 1.2. The low-energy fluid accumulated near the wall is removed partially or totally by replacing this fluid layer with an adjacent fluid layer having relatively high energy or mixing with it. However,

in blowing, instead of removing the low-energy fluid, it is energized with the aid of a more energetic flow component. It is accomplished by blowing high-pressure air or adding kinetic energy (Talay 1975). Both strategies can modify the maneuverability, delay separation, raise stall angle, decrease drag coefficients, increase lift coefficients, and decrease the noise level (Donovan et al. 1998; Talay 1975). Synthetic jet flow control has been intensively explored in recent years (Alstrom 2013; Cater and Soria 2002; De Giorgi et al. 2015; Murugan et al. 2016; Tuck and Soria 2008; Yadav et al. 2020; You and Moin 2008) and is regarded as a useful technique for controlling flow separation over an airfoil. Without increasing the net mass flow rate, the synthetic jet flow management technology can add or remove enough momentum from the boundary layer to keep the flow from separating. Synthetic jets add no net mass to the system since they are zero net mass flux jets. In the case of synthetic jets, two vortices occur for two-dimensional flow, which encourages more momentum mixing than continuous jets for an airfoil (Feng et al. 2019). Recent research on flow control employing a mixed continuous and synthetic jet which reveals that the flow separation point shifts toward the trailing edge as the mean jet velocity increases (Singh et al. 2021).

1.4 Motivation for The Present Investigation

The increasing use of gas turbines in the power generation industry has created an additional incentive for the further improvement of their performances. In this context, improving the net power output from a gas turbine engine using the wet compression (overspray) technique is significant. The possibility of augmenting the power output with a water injection system has already been confirmed. However, the detailed aerodynamic effects on the compressor's blades imposed by the presence of liquid droplets in the compressor flow have not been fully understood. Also, the overspray can alter the stage matching characteristics of the compressor. Hence, exploring the two-phase flow aerodynamics inside the compressor cascade arrangement is very important. Additionally, it is also seen that the stalling of the compressor blade can be controlled using suction slots on the compressor blade. This thesis hypothesizes that combining an active flow control technique with wet compression may yield a promising result in stabilizing the flow around the compressor blade.

1.5 Structure of the Thesis

The remaining chapters of the thesis are organized as below,

Chapter 2: This chapter presents an extensive literature review on wet compression effects and active flow control methods in the axial compressor. The critical parameters that influence the compressor performance are identified. After conducting a critical analysis of the various parameters research problem is identified, and objectives are stated in this chapter.

Chapter 3: The computational methodology adopted for the computational fluid dynamics (CFD) study is detailed in this chapter. The physical model, governing equations, boundary conditions, and the physics of the problem are detailed. The grid sensitivity analysis and validation with experiment are also given in this chapter.

Chapter 4: The effect of incidence angle on the aerodynamic performance of compressor cascade is detailed. The study is carried out for dry cases and wet cases. In the wet case, water droplets are injected into the domain, and their effect on the flow behavior in the blade passage is studied in detail.

Chapter 5: The effect of water droplet size and the injection ratio on the compressor aerodynamic performance is given in this chapter. Optimum droplet size and injection ratio are identified from the tested cases.

Chapter 6: This chapter details the study of an active flow control method. Suction slots are provided on the blade surface. Simulations are carried out on various configurations of the slot for dry and wet cases, and the results are detailed in this chapter.

Chapter 7: Experimental flow visualization studies are carried out for various incidence angles and inlet velocities. The results of this flow visualization study are presented in this chapter. Since it is a flow visualization analysis, most of the results are qualitative.

Chapter 8: This chapter summarizes the significant observations and concludes the research findings. Additionally, this chapter provides a few suggestions for future research.

CHAPTER 2

LITERATURE SURVEY

2.1 Introduction

This chapter analyses the past works on wet compression (Overspray) and the associated effect on compressor aerodynamics. The critical parameters of Overspray are identified and discussed in detail. In the later part of this chapter, methods related to the passive flow control mechanism in the axial compressor are discussed.

2.2 The Overspray or the Wet compression in a Gas Turbine Engine

Overspray is a technique that implements water injection for gas turbines to improve their performance compared to traditional cooling methods proposed in the late 1940s by Kleinschmidt 1947. The improved performance is due to the transfer of air extracted heat to the working fluid as steam. Wet compression enhanced the cycle efficiency and cycle pressure ratio, yielding the highest efficiency when the pressure ratio and inlet turbine temperature remain unchanged. Numerous experimental and analytical studies have been made on overspray since the 1950s.

2.3 Effect of Wet Compression on Gas Turbine Engine Performance

One critical parameter in the wet compression process is the water-air ratio or injection ratio. Davison 1957 experimentally investigated a double entry centrifugal compressor to understand water injection's impact on its performance. The maximum total pressure ratio was increased to 8.1 % by changing the water ratio from 0 to 0.055. However, the peak adiabatic efficiency decreased approximately to 16 % during the change in the water-air ratio. It was found that a 3.6 % increment of maximum equivalent air weight flow and 94 % increment of maximum equivalent total weight flow, respectively, by the injection of water into the compressor. White and Meacock 2004 introduced a new method by integrating the meanline compressor performance and droplet evaporation for examining compressor performance stage by stage with the effect of wet compression. It was noticed that when the injection ratio was increased, a progressive

movement of performance characteristics took place to a higher flow and pressure ratio. White and Meacock 2004 noted an increased mass flow during wet compression because of the injected water and cooling due to evaporation. Hence, special attention was to be given while fixing the injection ratio. With the increase in injection ratio, the aerodynamic efficiency was found to be decreased. Further detailed analysis showed increased flow coefficient occurred during earlier stages compared to design value and decrement in flow coefficient in later stages.

Bhargava et al. 2000 conducted experiments and modeling to understand how compression air humidity affects the pollution and stability limit of flames permitted in the gas turbine. Data was gathered across a wide array of equivalence ratios, air stream moistures, and pilot levels. The influence of these parameters on NO_x and CO emission has been analyzed using trends in the measured data. When moisture was introduced to the air stream, NO_x emissions decrease considerably. The drop in the NO_x was mainly due to a reduction in the equilibrium temperature (T_{eq}). However, an increase in moisture for flames resulted in a reduction in NO_x .

Mathioudakis 2002 used analytic relations to investigate how an industrial gas turbine was affected when injected with water in its combustion chamber. The relations were derived using an order of magnitude approach that accounts for changes in gas properties as a result of water injection and the variations in the correlation of performance parameters of the component. They evaluated the fluctuation of performance characteristics due to water injection into the compressor's outlet to minimize NO_x emissions. Analytical formulas were proposed to determine the variations in fuel-to-air ratio, compressor pressure ratio, power output, and efficiency. The water/fuel ratio was demonstrated to be the major parameter affecting the magnitude of deviation. The formulas illustrated the quantities of performance that derive the dependency of changes in different parameters and provided insight into the physics of the changes caused by water injection.

To examine the water injection effect, a modeling and simulation technique using multiphase code and compressor meanline code (one dimensional) was developed by Hale et al. 2005. The multiphase code primarily took care of the heat transfer involved with the change in the water phase, whereas the compression system flow properties

were modeled by mean line code with the aid of gas properties and heat transfer. By adding water vapor alone, the gas properties changes, resulting in a reduction in blade incidence and leading the fan and high-performance compressor (HPC) to shift off-design in the direction of the choke. Since the vaporization occurs when liquid water is added to the water vapor, the rotors' inlet temperature gets reduced which causes the fan and HPC to stall by raising the angle of incidence. This phenomenon is stronger towards the rear side of the fan having a higher temperature where vaporization is possible at a higher rate. Roumeliotis and Mathioudakis 2006 explored the impact of water injection in between the stages and at the inlet of the compressor on the compressor operation. In addition to an engine output model, a model for wet compression was employed. The compressor performance map was generated using the wet compression model, which comprises a stage stacking model (one-dimensional) and a model for droplet evaporation. The total performance and individual stage activities due to the effects of water injection were investigated. The influence of water injection on the total engine efficiency was studied following the incorporation of the map generation process in an engine performance model. It was shown that the effect may be assessed using a variety of factors, including strength, thermal efficiency, surge margin, and droplet movement through the stages. Water injection produced substantial stage rematching, causing the compressor to stop, and performance improved with the point of injection approaching the compressor inlet.

Through experimental investigation, Roumeliotis and Mathioudakis 2007 investigated the changes in compressor stage output and stability in response to water injection up to 2 %. Aerodynamic measurements were taken to investigate the airflow in the rows of blades. There was no noticeable impact on the pressure-rise coefficient when the water injection was up to 2 % of the airflow. The stall at the operating point does not alter significantly; hence, the water injection had no impact on the compressor's stability. The flow redistribution was not found in the case of water injection. Hence aerodynamic measurements revealed that injection of water had no significant impact on blade operation. The impact of water injection on power consumption was noticed, and it was seen that water quantity entering the stage increases linearly with the quantity supplied. Since a decrease in compression efficiency was calculated, the impact of

water injection on the efficiency is also understood. This reduction was in proportion to the amount of water going into the compressor.

Further research was carried out on the Pesanggaran power plant's two gas turbine units (GT1 and GT2) by Alam et al. 2015. Using GTPro, they assessed the performance of the operation of the wet compression system. Plant Engineering and Cost Estimator (PEACE) was used to calculating the operating and capacity costs, and the time required to pay back the system's investment cost. The performance improvement due to the use of a wet compression method is very important as compared to saturated fogging, according to simulation results. With 2 % overspray, the overall incremental power attributable to wet compression systems is 25.42 % and 23.09 % for GT1 and GT2 respectively. It was found that the wet compression system has an improved thermal efficiency owing to the specific consumption of fuel and heat rate, lowering the ratio of fuel consumption to power produced than traditional fogging. The overall thermal efficiency improvements in GT1 and GT2 using a wet compression system at 2 % overspray were 2.20 % and 1.92 % respectively. It was observed that the incremental capacity cost associated with the investment in a wet compression system is lower when compared with traditional fogging and is proportional to the increase in overspray percentage.

Kofar-Bai et al. 2018 studied the impacts of wet compression on the outputs of a gas turbine engine's turbine, three-stage compressor, and combustor. Injecting water droplets into the inlet of gas turbine engines raised the turbine expansion and compression ratios, which gave the machine more work and decreased fuel consumption by 3.75 %. The outlet temperature of the compressor, turbine, and combustor is lowered by 9.5 %, 7.0 % and 7.3 %, respectively, and the efficiency of the compressor was raised by 5.85 %. In another study, the same group analyzed wet compression technology numerically by choosing a single stage of the transonic compressor (NASA stage 35) (Dayyabu Gambo Kofar-bai et al. 2018). Mass and heat transfer, thermodynamic process, and other factors that affected the droplets of water in the gas turbine compressor's wet compression had also been investigated. The findings revealed that injection of water droplets in larger quantities at the inlet of the compressor, completely evaporated within the rotating blade rows, increases mass flow

rates, and reduces compression work, both of which have a noticeable impact on the efficiency and output of the compressor. Moisture content in the air increases as the water droplets evaporate, causing a drop in the temperature in front of the rotor blade location and allowing vapor to form. Together, these variables alter the fluids' thermodynamic properties, accelerating the mixture's convective heat and mass transfer. The heat convection between the droplets of water and the compressed air is a primary reason for cooling the passage of the compressor, which aids in reducing the loss in the flow due to the water injection, making the compressor perform better with improved efficiency.

Sun et al. 2019 conducted a numerical study of supercritical wet compression on a centrifugal compressor employed in an energy storage system and its impacts on internal flow and output. It was observed that wet compression was a viable option for the supercritical air compression process. The water injection ratio in supercritical air was less due to the maximum evaporation cap. Wet compression increased isentropic efficiency and overall pressure ratio while lowering specific work of compression. At the pressure ratio assigned in the experiment, 0.3 % was the optimum injection ratio of water, which decreased the specific work to 0.65 %. With the effect of wet compression, the impeller loss near the stall point increases because of the higher wake loss due to the delay of numerous droplets by the passage vortex. Wet compression also lowered air velocity, resulting in less diffuser friction loss.

Due to its enhanced efficiency, the wet compression technology was effectively applied in various gas turbine power generating sectors (Bhargava et al. 2007; Jolly et al. 2003; Meher-homji 2000). In the Alstom GT24, with a 1.2 % overspray, a 5.6 % improvement in output power and a 2 % rise in heat rate were achieved (Jolly et al. 2003). Wet compression's benefits and the factors affecting the total variations in the compressor as well as the performance of the gas turbine have been widely discussed (Bhargava and Meher-Homji 2005; Shao and Zheng 2005; Utamura et al. 1997). According to an analysis of overspray fogging and inlet evaporative methods, it was observed that combining fogging with overspray yielded greater output for any particular amount of water flow. The WCR (wet compression and regenerative) gas turbine was a cost-effective solution for efficient gas turbines (Shao and Zheng 2005). With 1 % water

injection, stage stacking research on a GE9E gas turbine indicated a 20 % improvement in performance and a 3 % increase in efficiency.

Utamura et al. 1997 introduced a MAT cycle technology for enhancing thermal efficiency and the specific performance of a gas turbine. To achieve this, the suction side of a linear flow compressor was injected with water and illustrated theoretically and experimentally that the compressor characteristics can be modified with a comparatively lesser quantity of water. A 1 % increase in the water-to-air ratio of external air could enhance the performance by 10 %. The analytical rate of heat for an extra fuel consumption because of an increment in the output originating from a reduction in the required compressor power was thermal efficiency times lesser than the Brayton cycle. With respect to 1 % water spray, the theoretical function drop was 6.8 %. A compressor with a 0.79 adiabatic efficiency was yielded by 4 % water injection. When tested using a 130 MW class simple cycle power station by adding water to the air at an injection ratio of 0.4 %, generator output shifted from 115 MW to 121 MW, and thermal efficiency achieved a relative growth of 1.1 %.

The addition of steam to the combustion chambers boosts the efficiency of gas turbines (GT). The thermal efficiency can be improved if exhaust heat is used for generating steam. The partial steam injected gas turbine (STIG) cycle can be employed to efficiently enhance GT output power and also increase the efficiency of an existing gas turbine according to Fischer et al. 2001. The full STIG cycle has many advantages, including a high output power considering the size of the gas turbine and the efficient use of steam cooling. Other power plants, such as combined-cycle, require additional water treatment and facilities. Technically, steam injection is rather appealing. Nonetheless, the aspects of economics must be considered.

Bagnoli et al. 2004 studied the impact of water injection into the interstage of a gas turbine (GE Frame 7EA) on its performance by aero-thermodynamic modeling. Various water injecting locations, flow speeds, and ambient conditions were used to examine the compressor performance and the parameters affecting the gas turbine (ISO and HOT cases) net performance. A parametric study on the 1st and 17th stages of the compressor reveals stage loading redistribution (in the first stage, unloading was taking place, and in the 17th stage, loading was increased). With an increase in the spraying of

water, the operating point of the 17th stage gradually approaches the surge line, implying that by using the interstage injection approach, the water amount must be carefully selected. When compared to other injection points, water injection upstream of the pump renders maximum power boost, regardless of the ambient conditions. At 40° C and 40 % RH ambient conditions, compared to the ISO condition, 1.2 % injection and 1.4 % of water-to-air ratios upstream of the initial stage could successfully restore the reduction in power output and the loss in the cycle efficiency of the gas turbine, respectively.

From these analyses, it is understood that the total quantity of water that may be sprayed into the compressor is restricted by ambient conditions, the overall permissible output power of gas turbines (due to shaft strength and capacity of the electric generator), and the surge limit of the compressor.

2.4 Importance of Droplet Size

Utamura et al. 1999 investigated Overspray experimentally and analytically in detail by using a 105 MW gas turbine (Hitachi frame 96); a power output gain of 10 % and an increment in efficiency by 3 % was obtained with an overspray of 1 %. The study on the 17-stage compressor by their droplet evaporation model concluded that the droplets larger than 30 μm size led to incomplete evaporation inside the compressor, and the droplets having a size less than 20 μm showed complete evaporation. For measuring the effectiveness of wet compression, a new parameter, 'incremental efficiency' (power increment/ additional consumption of fuel), was put forward. When compared to the dry case, thermal efficiency seemed to be 10 % higher.

A one-dimensional wet compression analysis was carried out at constant polytropic efficiency, blade speed, and gas constant by Horlock 2001. The changes that might have happened for polytropic index and constant pressure-specific heat by the evaporation inside the compressor were assumed to be the first order. He assumed a constant droplet temperature for calculating the evaporation rate inside to avoid the effect of convective heat transfer from droplets. The study revealed a decrement in temperature at the inlet of the compressor by the initial evaporation of water droplets. However, the compressor's delivery temperature fell even more sharply under engine running

conditions. This was most likely due to the residual droplets continuing to evaporate, but it could also be due to compressor stages mismatching.

Härtel and Pfeiffer 2003 conducted a wet compression study on the overall compressor performance by accounting for the droplet size, compression rate, and polytropic efficiency. They implemented two analytical models; the ideal model and the droplet model. During the ideal model's compression, the thermodynamic change did not affect the temperatures, and the droplets were tiny. This was based on the assumption that a thermodynamic equilibrium existed in an air-liquid mixture. The droplet model overcame the limitations faced in the first model. By analyzing the model, they showed the dependency of maximum spray flow rate at the compressor discharge corresponds to complete saturation for a given pressure ratio with polytropic efficiency. For a lower efficiency compressor, the value of the maximum spray rate would be higher. In the case of a 2 % lower spray flow rate, the polytropic efficiency decrement in specific work was insignificant due to the stage mismatching.

The underlying theory of the thermodynamic behavior of droplets and the transfer of heat occurring at the inlet fogging was discussed by Chaker et al. 2004a, in addition to the practical issues concerning the execution and benefits of inlet fogging to gas turbine engines. Large droplets cannot evaporate entirely, resulting in air that is undersaturated at the compressor inlet if larger droplets are used for the inlet fogging process. Larger droplets might cause damage to compressor blades and coatings of the blades by the effect of gravity or the presence of obstacles like trash screens, silencers in the inlet duct, and so on. This resulted in excessive water pooling on the duct floor, necessitating a drainage system of more capacity and increasing the risk of duct surface corrosion. The deformation at the tip of the compressor blade happens in extreme conditions. Numbers of advantages are noticed for smaller droplets having a range of 5 to 15 microns in the inlet air fogging of gas turbines. With the aid of experimental results, it could be proved that this droplet size range does not cause the compressor blade to degrade or any wear of coatings of the blade. Smaller droplets are less likely to fall out since they may get carried along with airflow around the obstacles in the air duct. They also have a larger evaporative surface area. Since the evaporation occurs primarily at the water-air interface, the exposed surface region strongly influences the evaporation

rate. Type of nozzle, operating pressure, and nozzle capacity are three significant factors that influence droplet size distribution. It is suggested that the measurement position and air velocity might explain substantial variance in a droplet's diameter. The reduction in droplet size at more incredible airflow speeds is due to airflow pushing tiny droplets out of the way of bigger droplets, minimizing collision and agglomeration. Wet compression's physical mechanism is more complicated due to the many factors involved in evaporation. The existence of water droplets inside the pathway of the blade is necessitated by the Overspray when compared to that of inlet fogging. These processes are aided by interactions of physical factors such as droplet and droplet, droplets with the air, and droplets with the wall. Droplet size impacts the compressor's specific work and outlet temperature, evaporation rate, and irreversible entropy generation. The contributions of reduced aerodynamic efficiency and thermodynamic losses are much less than the effort reduction caused by evaporative cooling. Droplets with smaller value Sauter mean diameters (SMD) were shown to have a faster evaporation rate (Bhargava et al. 2007). In fact, the droplet size impacted the evaporation, loading, and unloading rate of the later and early compressor stages (Khan and Wang 2009; Wang et al. 2008; Wang and Khan 2008).

Numerous analytical studies (Khan and Wang 2008; Lin et al. 2018, 2019; Payne and White 2008; Williams and Young 2007) revealed more about the interactions between droplet-wall and droplet-air. Smaller droplets of size around 5-10 μm showed 0 % slip before entering the rotor pathway. However, the local pressure gradient influences the slip velocity along the pitch-wise direction inside the blade passage. It should be emphasized that inertia and friction forces impact droplet motion (Williams and Young 2007), and the extent of film development across the blade surface is the criterion for the impact of aerodynamic shear force. Unlikely, the pressure gradient is affected by droplet trajectory. The distribution of pressure over the blade can be influenced by the factor of how the surface of the blade is impacted by the droplet (Payne and White 2008).

Payne and White 2008 developed a numerical method (three-dimensional) to analyze the two-phase flow by considering water droplets' evaporation. The model was employed with a single-stage compressor. When the size of the droplet is 4 μm , the

axial velocity is decreased, which led to a change in the distribution of pressure over the blades. Many researchers conducted experimental studies to analyze how water droplets propagate once they enter the rotor blades' walls during wet compression (Eisfeld and Joos 2009; Joos 2006). The droplets showed two different behaviors while experimenting by keeping Mach number 0.7 as free stream conditions and an approximate Sauter mean diameter (SMD) of 16-36 μm as droplet size (Joos 2006). First, the separation of a droplet with a size less than 10 μm took place in the next one by the third portion of the suction surface. Secondly, the water film formation at the trailing edge led to the formation of water ligaments. Sun et al. 2013 exhibited that in the combustor upstream, the droplets of water having a size lesser than five μm evaporated utterly. Droplets that are bigger achieve full evaporation after entering the compressor. This concludes that to attain complete evaporation, fine mists should be supplied in water injection before the combustor. The floor phenomenon was evaluated by fixing a Mach number of 0.85 as free stream conditions and the injection ratio of water as 2 % on a transonic compressor (Eisfeld and Joos 2009). When falling on the rotor blades' leading-edge, the droplets splits into many tiny droplets using splashing. The rate of evaporation is in turn, affected by splashing. Water film is formed on the blade's surface when injected water droplets fall on it and shift to the back of the upper portion of the blade's surface because of the combined action of aerodynamic shear force and a centrifugal force (Atlantic et al. 2002; Lin et al. 2018).

Zamrodah 2016 studied the size and distribution of droplets at the injection point in the engine's inlet, significantly impacting engine output. Larger droplets have a tendency to move into the compressor's casing and impact negatively on it, which leads to the shrinking of the case and the clearances of the blade to be diminished. Smaller droplets applied close to the hub surface appear to follow the streamlines more precisely and evaporate more quickly. The faster and more total evaporation of the droplets results in an optimal reduction in air temperature, enhancing compressor performance. The description of a three-dimensional aero-thermal analysis code used to measure droplet trajectory and evaporation in the multistage compressor. Two multistage compressors were used in the research.

2.5 Impact of Pressure ratio and Evaporation Rate

The aerodynamic analysis procedure suggested by Hill 1963 could examine the performance characteristics of a water-injected axial compressor. When compared with experimental results obtained from the high and medium pressure ratio compressor of turboshaft engines, they seem to be very close to these analytical results. It was found that the compressor pressure ratio could not affect the amount of work reduction when water injection was done at a specified value of evaporation parameters. However, the evaporation inside the compressor led to variation in the stage work distribution. Apart from the initial droplet size and their distribution, the rotational speed and the geometry of the compressor cause more changes in the process of mixing and evaporation rate. The findings from all the earlier researchers were limited due to the limitations in the technologies that prevailed at that time, like the availability of droplet size measurement techniques, heat transfer measuring devices, etc. Later, several works conducted by improving these technologies to reduce the experiment's constraints led to more wet compression findings. The studies highlighted the size of droplet effect on the process of evaporation within and upstream of the compressor (Dayyabu Gambo Kofar-bai et al. 2018; Kleinschmidt 1947; Kofar-Bai et al. 2018; Roumeliotis and Mathioudakis 2006). Zheng et al. 2003 carried out work similar to Hill 1963 by incorporating a discussion on evaporation time, droplet size, evaporation rate, and the water droplet breakup. The analysis of the dry and wet compression was done using the polytropic index. It was discovered that genuine wet compression has a lower polytropic index than dry compression, which further lowers compressor work, discharge temperature, and compressor efficiency. At constant values of the evaporation rate and pressure ratio, the compressor discharge temperature falls relative to the isentropic compression process. At high compression ratio levels, wet compression was efficient. It was found that droplets with a tiny diameter increased evaporation.

Sexton and Sexton 2003 introduced a diffusion-controlled evaporation model and carried out a parametric study on a 16-stage compressor with a pressure ratio of 19.8 to understand the stage-by-stage performance by the effect of evaporative and Overspray fogging. The water droplet would reach air velocity by the rapid entrainment of each water droplet into the air stream, resulting in negligible convective mass and heat

transfer effects. The study revealed that there would be better performance when combined with Overspray fogging and direct water injection into the compressor.

Mohan et al. 2016 conducted the thermo-fluid dynamic investigation of wet compression. The two-phase model (gas-liquid) was developed in this study as air with scattered water droplets within a simple cylinder-piston system. The effects of various parameters like compression speed and thermodynamic properties such as RH, pressure, and temperature on Overspray were studied. The necessary thermodynamic curves were generated using an analytical model. The differences between developed thermodynamic curves and dry isentropic curves were studied. The analysis revealed that heat is removed from the air around in wet compression due to droplet evaporation, leading to a lowering of temperature and pressure reduction. The heat was removed from the air around due to the evaporation of droplets. The water droplets' evaporation rate was increased by tiny droplets, lesser compression speeds, and a higher percentage of Overspray.

2.6 Effect of Ambient Temperature and Heat Rate

According to Ingistov 2000 research, the gas turbine performance was crucially influenced by the temperature of the surrounding air. The inlet air cooling by introducing fog directly into the compressor suction was effective and secure as long as the Fog curtain (FC) is positioned upstream of the trash screen and downstream of the silencer, which has been subjected to dirt and oily deposits. Overall benefits, including economic aspects of chilling inlet air, which may be used to supplement the gas turbine's power in a cogeneration plant, were studied by Ondryas et al. 1990. The distribution of water, which was chilled, in the inlet air system, was marked out. The enhancement of power in a gas turbine through chilling inlet air could be used under higher ambient temperatures, generally synchronized with on-peak power generation. While chillers are expensive equipment, the advantages of on-peak power generation can overcome the expense if an exhaustive study is carried out. It has to take with utmost caution that the inlet system material between the chilled water coils and the compressor plenum be replaced by stainless steel. Electricity costs vary by region, and energy and capacity rates can differ and be assessed on an individual basis. Willems

and Ritland 2003 exhibited four different recuperated gas turbine cycle layouts. These layouts take into account the evaporative inlet effect as well as after cooling effect. The effect of surrounding temperature, relative humidity on each layout output, and the turbine's inlet temperature was studied using a parametric approach. The efficiency was increased to 3.2 % if the inlet air undergoes evaporative cooling. However, the power and cycle efficiency was enhanced to 110 % and 16 %, respectively, while it undergoes evaporative after cooling.

Studies on droplet size and evaporation time on two alternative regenerative steam-injection gas-turbine (RSTIG) systems were examined by Nishida et al. 2005. It was found that the thermal efficiency increased and the air ratio of the regenerative system decreased as a result of the steam injection in the regenerative system. The exergy of the heat exhausted was recovered in the heat-recovery steam generator (HRSG). The total effectiveness of the electric power generation exceeded 70 % when the heat output was increased. Willems and Ritland 2003 proposed a method for analyzing the inlet fogging system efficiency and also validating the impact of evaporative cooling. Inlet fogging systems is studied quantitatively based on various environmental factors under which the gas turbine is operated. The use of appropriate equipment for the effective detection of dry-bulb temperature was also discussed in this article. The drainage rate for a control system that modulates the fog injection rate based on the compressor inlet temperature (CIT) dry-bulb value is self-corrected. It may be added to any inlet filter house design to preserve the required temperature at the inlet. The studies also showed that fogging may be adjusted to maintain any CIT between dry bulb and wet bulb temperatures, which is a valuable feature for generating stations deployed to a given load over extended periods. The CIT control system functioned effectively in engine load levels between 90 and 100 percent of rated load without any additional logic to compensate for decreased airflow.

2.7 Various Design Considerations to Improve The Efficiency

The fogging system operation of the combined cycle power plant (655 MW), concept, construction, and implementation were discussed by Gajjar et al. 2003. The engineering aspects of the implementation as well as the practical problems were mentioned. Meher-

Homji and Mee III 2000 studied how direct evaporative cooling impacts the practical aspects of fogging of air at the inlet to the compressor of a gas turbine. This research looked at several practical issues such as nozzle placement, quality of water, running conditions, and issues related to maintenance that came up when such systems were implemented. Nozzle located downstream of the air filter location was comparatively more acceptable. However, if nozzles were located downstream, the risk comes from nozzle loosening or grid structure damage caused by flow-induced vibration. Both of these issues were addressed as being solvable by cautious and conservative design. The lock wiring of the nozzles provides a line of protection even though it's not providing any positive restraint in the case of nozzle loosening. The amount of cooling determines the quantity of water needed, the mass flow rate of the turbine, and ambient temperature. Chaker et al. 2004b proposed and presented the practical consideration of droplet size of a fog nozzle, calculation, and the details needed for the gas turbine applications with the aid of experimental and theoretical findings. The different techniques for measuring the droplet size were discussed. The techniques like laser light dispersion and imaging were widely adopted for the study of inlet fogging applications in gas turbines. The two light scattering methods, spatial and flux techniques, were thoroughly discussed. The various mean and representative diameters definitions and their detailed formulas were mentioned. Arithmetic Mean Diameter (AMD) D_{10} , Surface Area Mean Diameter (SAMD) D_{20} , Volume Mean Diameter (VMD) D_{30} , Sauter Mean Diameter (SMD) D_{32} , Absorption Diameter (AD) D_{21} and Evaporative Diameter (ED) D_{31} are the different mean diameters. D_{01} , D_{05} and D_{09} are representative diameters. Among these, the importance of SMD and D_{09} were demonstrated and associated with the surface area of the water-air interface, which is a primary function of inlet air fogging. It was described that the surface area is optimized to improve the transfer of heat between the droplet's surface and air by disintegrating water into smaller droplets through atomization in the inlet air fogging of gas turbines. Hence, the commonly used nozzles (pin type and swirl type) in this area are studied and given a detailed explanation and application of these nozzles. Because of the wide variety of duct configurations and structures, many problems become critical in developing and installing fogging systems.

Brun et al. 2006 presented a simple approach for evaluating the main parameters that influence the aerodynamic stability of linear cascade in a gas turbine with a single shaft. This method was used to study the water injection. This method studied the phenomenon of water injection on a gas turbine (frame-type). With inlet and inter-stage water injection, it was observed that rotating stall and many other issues related to aerodynamic stability of the compressor like a flutter in the gas turbine would occur. It was suggested that the consumers and technicians adopt this technique for classifying the applications of greater risk, limiting the operating range of gas turbines to reduce the risk of blade failure and minimizing the aerodynamic instability as well as an eventual catastrophic failure.

Ingistov 2001 described the new cleaning methods for massive multistage axial compressors used in Gas Turbine Units (GTU). The Inter-stage Injection System (IIS), which is currently being tested in GTU No. 2, has shown evidence of favorable results in compressor cleanness and ambient air compression efficiency. IIS needs a low-to-moderate water supply pressure (1050-2450 kPa). The water injection holes in the nozzle assembly were not as tiny as those found in fogging nozzles or as wide as those found in on-line cleaning water nozzles. It is suggested that maintaining a good balance between the water jet and the water spray needs an optimal ratio. The borescope analysis showed a small amount of corrosion-resistant coating loss near the rotating blades' leading edge, which was anticipated. Erosion-resistant coatings would be used to shield the blade material from possible water particles impingement, reducing the risk of water erosion. Chrome carbide-type coatings are sprayed or brush-applied in the form of slurry and were applied at low temperatures.

Jolly 2002 discussed the thermodynamic advantages of wet compression as well as the risk of using wet compression systems on a combustion turbine. The verification of design and performance testing on the wet compression system of a combustion turbine (GE Frame 6B) and revealed a nine percent increase in production and a 1 % increase in heat rate. It is pointed out that water distribution, deterioration of compressor inlet duct materials and compressor fouling, compressor casing distortion, combustion dynamic pressure, and control system integration were the primary components of such risk.

Savic et al. 2005 evaluated the complexity of the system, the viability of integrating the system for the control of gas turbines, the operating principle of the plant, performance of the gas turbine, operation and maintenance costs, three separate commercially viable spray technologies—pressure-swirl (PSW), hot water injection (HWI) and air-driven atomization in terms of risk and both the technical and economic advantages based on droplet sizing results. The PSW system was found to be the most acceptable high fogging system after evaluating the complexities of PSW and HWI with the actual power benefits. The HWI system's major disadvantages were the necessity of an auxiliary heat exchanger and the effect of air preheating caused by adiabatic mixing with hot water injection. Due to the inevitable high-pressure loss at the inlet caused by the large number of nozzles needed, the air-assisted injection (AAI) system was virtually unsuitable for high fogging use. Resulting in higher overall prices, the air AAI system cannot compete with the pressure swirl (PSW) system commercially. On the other hand, this option looks to be more favorable for basic fogging applications.

2.8 Studies on Boundary Layer Suction Control Mechanism

Compressor performance may be improved by reducing the accumulation of low-energy fluid and eliminating the high-entropy fluid from the flow channel (Kerrebrock et al. 1997). The boundary layers formed near the blade and the endwall (areas with unfavorable pressure gradients) in an axial compressor could be controlled by the implementation of boundary layer suction (BLS). As a result, the pressure ratio was greatly improved. By creating and evaluating a special aspirated compressor stage that achieves a total pressure ratio of 3.5 at a tip speed of 1500 feet per second, the idea of BLS is verified and substantiated by Merchant et al. 2000. Viscous flow control using aspiration made it possible to design compression systems that were more practical, compact, and effective than would otherwise be attainable. The compressor stage of the aspirated fan, which gave a pressure ratio of 3.4:1 at 1500 f/s, was experimentally investigated by Merchant et al. 2005. It was observed that even though there was a reduction in adiabatic efficiency by 0.5 %, an aspiration of 1 % of the inlet mass flow rate was more than enough to improve the stall margin.

Boundary layer suction control was numerically investigated on two compressor cascades by Shuang et al. 2010. The distribution of static pressure on the blade surface was altered by suction from the boundary layer, which enhanced flow behavior. It was observed that the slot provided only a part of the blade height reduced the flow separation and flow field improvement at that location. However, the flow field in the remaining region was not improved and generated additional losses. The compound scheme having a slot on both the suction surface and endwall showed the most significant increase in performance.

According to Chen et al. 2014, the three-dimensional corner separation development section should be situated at the optimal chordwise position downstream of the three-dimensional corner separation. The suction surface of the vanes should be close by for the ideal pitch-wise location. The total pressure loss coefficient was found to be reduced by 15.2 % and 9.7 % in CFD calculations and experimental investigation, respectively, with an aspiration of 1 % of the inlet mass flow rate at design operating conditions. A similar experimental study was carried out by Guo et al. 2010 on a compressor cascade with blades of significant camber angle to examine the changes in the aerodynamic performance of the cascade by the introduction of BLS. The parameters which affect the efficiency of the boundary layer suction, like the location of aspiration where the slot had to implement and the rate of suction, were studied with the help of this investigation. The flow fields through the cascade were visualized using the ink-trace flow visualization method. Aspiration provided on the suction surface, aspiration provided on the end wall, and aspiration provided on both the suction surface and endwall were the three suction configurations selected for the study and were compared with each other. According to experimental findings, a proper suction design decreased losses more effectively with a larger suction flow rate than one with a smaller suction flow rate, although the rate of reduction in loss slows if the rate of aspiration increases. It was shown that the boundary layer near the midspan becomes capable of withstanding the adverse pressure gradient in the flow passage by implementing aspiration on the suction surface.

An experimental study was conducted by Guo et al. 2013 on a heavily loaded compressor cascade to examine the impact of aspiration provided on the inlet on the

vortex's formation and the loss's generation. The flow filed on the suction surface of the blade as well as the endwall was studied by the ink-tracks flow visualization technique. In a rectangular wind tunnel, ten traverse planes were measured from the cascade, upstream to downstream. Tested planes demonstrated the formation, growth, and decrease of several large vortices associated with the extra losses. With an aspiration of 2.5 % of the inlet mass flow rate, the overall loss in the cascade without suction is reduced by 25 %.

Zhang et al. 2013 implemented slots on the end wall of a high-turning compressor cascade to investigate the efficiency of the boundary suction control method. Both experimental investigation and numerical analysis were carried out at low Mach numbers. These aspiration holes were flexible in distribution, adjustable in size, simple to manufacture, and highly strong. The outcome of the analysis suggested that the optimum location for BLS was just before the corner separation point or near the suction surface of the blade. Hence the study emphasized that the aerodynamic performance may be considerably improved by compound suction in which boundary layer suction is provided on both the suction surface as well as endwall. The quantitative analysis of this work highlights that the total loss coefficient was reduced by 27.24 % aspiration of 1.28 percent of the intake mass flow rate.

The efficiency of BLS depends on several parameters like the optimum location of the slot, rate of aspiration, the shape of suction geometry, and other aerodynamic parameters. Fu et al. 2006 studied these parameters' impact through detailed numerical analysis and compared them with the cascade's aerodynamic performance. The results showed that boundary layer suction increases flow turning ability and decrease fluid accumulation near suction surface corners with low energy. The study discussed that the appropriate changes in the flow behavior are based on the aspiration rate and location. Similar studies were carried out by Guo et al. 2016. They found that the energy of the fluid close to the corner formed by the suction surface and end wall was low due to the strong boundary layer effect. This accumulation of low-energy fluid gets removed more by the action of BLS, which improves the flow turning.

Besides suction from the blade surface, few researchers studied the advantages of casing aspiration. Mao et al. 2018 carried out numerical simulations on a linear

compressor cascade to investigate the efficiency of casing aspiration on the overall aerodynamic performance. It was observed that the aspiration scheme couldn't control TLV formation and its propagation. The structure of TLV was split into two halves if aspiration was provided behind the starting point of TLV. The frontal component of TLV has an increasing strength which causes a higher mixing loss; hence the total control effect is created by the combined effects of these two halves. According to this study, the blade loading redistribution along the chord towards the tip of the blade was recognized as an aspiration on the casing. Cao et al. 2021 studied the breakdown of the tip leakage in the aspirated compressor. The vortex was found to be different in the aspirated compressor blades and normal compressor blades; this difference is accomplished by the unfavorable pressure gradient formed by BLS. The study exhibited that the tip leakage loss was decreased when the tip clearance size was increased for all aspirated cascades tested, contrary to conventional compressor cascades.

A novel aspiration concept was designed and referred to as natural aspiration. In this method, a through-hole slot was provided on the blade to transmit pressure-side fluid to the suction side to energize the boundary layer near the suction surface of the blade (Jain et al. 2015). The pressure gradients exist between the pressure surface and suction surface to guide the flow from the pressure side to the suction side without the aid of energy. A suction slit was provided partially along the span of the rotor blade (NASA rotor 37) in a transonic linear compressor for employing natural aspiration to increase the stall margin of a transonic.

The flow control method 'BLS' was found to be very effective in an ultra-highly loaded (UHL) supersonic compressor cascade by Cao et al. 2020. Suction at a 30 % axial chord may eliminate trailing edge separation and lower the loss coefficient by up to 53 %. The outcome of the analysis says that the combined slot scheme can eliminate the separation of flow which happens near the endwall-suction surface corner and near the trailing edge, thus reducing the loss coefficient by 55 %. It was noticed that the end wall suction scheme could decrease the loss coefficient by up to 38 %.

The aspiration was studied in a multistage compressor by Siemann et al. 2016. In the first stator for the reference arrangement, hub corner separation was significantly reduced by using aspiration. The hub corner separation in the second stator increased.

The unloading of the first and third stators and the increment in loading of the second stator, primarily the fourth stators, were noticed. The fourth stator's stage efficiency increased by 1.3 percent, and its output pressure increased by 4.59 percent as a result.

2.9 Summary of the Literature Review

Sl No	Author	Anal ysis Mode	Parameter studied	Inference
1	Davison 1957	E	Impact of water injection ratio	<ul style="list-style-type: none"> • The total pressure ratio is increased to 8.1 % while changing IR from 0 to 0.055. • Peak adiabatic efficiency is decreased 16 % approximately.
2	White and Meacock 2004	N	Impact of injection ratio	<ul style="list-style-type: none"> • A higher-pressure ratio is achieved. • Aerodynamic efficiency was found to be decreased while increasing the injection ratio.
3	Bhargava et al.200	E	Effect of air humidity on pollution	<ul style="list-style-type: none"> • Nox emission decreases considerably when moisture was introduced to the air stream.
4	Mathioudakis 2002	N	Developing analytical formula	<ul style="list-style-type: none"> • Could determine the variation in Fuel-to-air ratio, compressor ratio, power output, and efficiency.
5	Hale et.al 2005	N	Developing multiphase code and Mean line Code	<ul style="list-style-type: none"> • Multiphase code can take care of the heat transfer involved. • Mean line code can take care of compressor system flow properties.
6	Roumeliotis and Mathioudakis 2006	N	Impact of water injection in between the stages and at the inlet of compressor	<ul style="list-style-type: none"> • Aerodynamic performance improved with point-of-injection approaches in the compressor inlet.
7	Roumeliotis and Mathioudakis 2007	E	Effect of injection ratio up to 20 % on the compressor stage output and stability	<ul style="list-style-type: none"> • No noticeable impact on the pressure coefficient when the water injection ratio was up to 2 % of the flow. • Stall at the operating point does not alter significantly.

				<ul style="list-style-type: none"> • Water injection had no impact on the compressor's stability.
8	Alam et al 2015	E	Injection ratio analysis on GT1, GT2 gas turbine	<ul style="list-style-type: none"> • With 2 % overall incremental power attribute to WC for GT1 and GT2 is 23.09 %, 25.42 %. • Thermal efficiency is improved 2.20 % and 1.92 % respectively for GT1 and GT2 turbine addition of 2 % IR.
9	Kofar Bai et al 2018	E	Water injection	<ul style="list-style-type: none"> • Decreased fuel consumption by 3.75 %. • The outlet temperature of the compressor, turbine and combustor is lowered 4.5 %, 7.0 % and 7.3 %. • Efficiency raised by 5.85 %.
10	Kofar Bai et al 2018	E	Mass and heat transfer, thermodynamic process and other factors affected the droplets of water is analysed	<ul style="list-style-type: none"> • Injection of water droplets in large quantities at the inlet of the compressor completely evaporated within rotating blade. • Mass flow rate increases, specific compressor work is reduced.
11	Sun et al 2019	N	Super critical wet compression impacts on internal flows and output	<ul style="list-style-type: none"> • Wet compression was viable option for super critical air compression process. • Isentropic efficiency and overall pressure ratio is increased. • Specific work is reduced to 0.65 % at 0.3 % of injection.
12	Jolly et al 2003	E	Varying injection ratio	<ul style="list-style-type: none"> • A 5.6 % improvement in output power with 1.2 % over spray. • 2 % rise in heat ratio were achieved.
13	Zheng et al 2005	E	Varying injection ratio	<ul style="list-style-type: none"> • A 20 % improvement in performance and 3 % increase in efficiency is obtained with 1 % water injection ratio.
14	Bugnoli et al 2004	N	Various water injection locations, flow speeds and	<ul style="list-style-type: none"> • If inter stage injection is used water amount must be carefully selected.

			ambient conditions on multistage compressor	<ul style="list-style-type: none"> • Water injection upstream of the pump renders maximum power boost regardless of the ambient conditions.
15	Utamura et al 1999	E	Droplet size	<ul style="list-style-type: none"> • The droplets larger than 30 μm size led to incomplete evaporations inside the compressor. • The droplets having a size less than 20 μm showed complete evaporations.
16	Chaker et al 2004	E	Droplet size	<ul style="list-style-type: none"> • Large droplet cannot evaporate entirely resulting in air that is under saturated at the compressor inlet. • Larger droplets cause damage to compressor blades and coating of the blades. • Smaller droplets gives advantages in wet compression.
17	Khan and Wing 2008, Lin et al 2018, Payne and White 2008, Williams and Young 2007	N and E	Droplet size	<ul style="list-style-type: none"> • Smaller droplet size 5-10 μm showed 0 % slip before entering the rotor passage. • Inertia and friction forces impact droplet motions. • The distribution of pressure over the blade can be influenced by the impact of droplet in the blade.
18	Payne and White 2008	N	Droplet size	<ul style="list-style-type: none"> • Axial velocity decreased when the size of the droplet is 4 μm.
19	Eisfeld and Joos 2009	N	Droplet size	<ul style="list-style-type: none"> • Droplets having size less than 10μm is separated from the third portion of the suction surface. • Water film formation at the trailing edge led to the formation of water ligaments.
20	Atlantic et al 2002, Lin et al 2018	N and E	Water film	<ul style="list-style-type: none"> • Water film formed on the blade is shifted to the back of the upper portion of the blade's surface because of combined action of

				aerodynamic shear force and centrifugal force.
21	Zamrodah et al 2016	N	Droplet size	<ul style="list-style-type: none"> • Large droplets are a tendency to move into the compressor casing, which leads to shrinking of the case and clearance of the blade to be diminished. • Smaller droplet close to the hub surface appear to follow streamlines more precisely and evaporate more quickly.
22	Mohan et al 2016	N	Compression speed, Thermodynamic properties, relative humidity, pressure and temperature	<ul style="list-style-type: none"> • Heat is removed from the air around wet compression is due to droplet evaporation. • The water droplet's evaporation was increased by tiny droplets, lesser compressor speed and higher percentage of overspray.
23	Kerrebrock et al 1997	E	Boundary layer suction	<ul style="list-style-type: none"> • Boundary layers formed near blade and endwalls in the compressor can be controlled. • Pressure ratio is greatly improved.
24	Merchant et al 2000	E	Boundary layer suction	<ul style="list-style-type: none"> • Pressure ratio 3.5 is obtained at 1500 f/s.
25	Merchant et al 2005	E	Boundary layer suction	<ul style="list-style-type: none"> • Pressure ratio of 3:4:1 is obtained at 1500 f/s. • 1 % of aspiration of the inlet mass flow is more than improve stall margin even though adiabatic efficiency is reduced by 0.5 %.
26	Shuang et al 2010	N	Boundary layer suction	<ul style="list-style-type: none"> • Static pressure distribution on the blade surface is altered by the suction enhanced the flow behaviour. • Slot provided only a part of the blade height is reduced the flow separation and flow field improvement at that location only. • Compound scheme slot (slot on both blade and end wall) shows the most significant

				increase in aerodynamic performance.
27	Chen et al 2014	N	Boundary layer suction	<ul style="list-style-type: none"> • Total pressure loss coefficient is reduced by 15.2 % in CFD, 9.7 % in experiment with 1 % suction mass flow rate.
28	Guo et al 2010	E	Locations of aspiration, rate of aspiration	<ul style="list-style-type: none"> • A proper suction design decreased losses more effectively with a larger suction rate. • Bond layer near midspan becomes capable of withstanding the adverse pressure gradient in the flow passage by the implementation of aspiration on the suction surface.
29	Guo et al 2013	E	Boundary layer suction	<ul style="list-style-type: none"> • With an aspiration ratio of 2.5 % inlet mass flow rate, overall loss in the cascade without suction is reduced by 25 %.
30	Fu et al 2006	N	Locations of aspiration, rate of aspiration, shape of suction geometry	<ul style="list-style-type: none"> • Boundary layer suction increases flow turning ability and decrease fluid accumulation near suction surface corner with low energy.
31	Mao et al 2018	N	Tip leakage vortex (TLV)	<ul style="list-style-type: none"> • Aspiration scheme couldn't control TLV formation and propagation. • Structure of TLV is split into two halves if aspiration is provided behind the starting point of TLV.
32	Cao et al 2021	N	Tip leakage vortex (TLV)	<ul style="list-style-type: none"> • Tip leakage loss is decreased when tip clearance is increased.
33	Cao et al 2020	N	Boundary layer suction	<ul style="list-style-type: none"> • Suction at 30 % axial chord can eliminate trailing edge separation and lower the loss coefficient by upto 53 %.
34	Siemann 2016	N	Corner separation and overall performance	<ul style="list-style-type: none"> • Hub corner separation is significantly reduced by aspiration. • Hub corner separation in the second stator is increased.

				<ul style="list-style-type: none"> • Fourth stator's stage efficiency is increased 1.3 % and its output pressure is increased by 4.5 %.
E :- Experimental N:- Numerical				

2.10 Problem Definition

Many experts have confirmed the feasibility of increasing power production after looking into the effects of the operation of gas turbines fitted with a water injection system. The evolution of the theory, however, and the explanation of the Overspray-related phenomena are not always accurate and consistent. We still don't fully understand the precise aerodynamic impacts that liquid droplets in the compressor flow have on the blades. The effect of wet compression combined with an active flow control method is not studied. This combined approach may bring more stability to the flow in the compressor passage

2.11 Objectives

The specific objectives for the study are listed below.

1. To numerically study the effect of incidence angles on the aerodynamic performance of compressor cascade with upstream water injection. Analyze the stalling characteristics of the blade, loss coefficient, and exit flow behavior compared with the dry case.
2. To numerically study the effect of droplet diameter and injection ratios on the flow separation, and total pressure loss coefficient across the blade passage.
3. To numerically investigate the combined effect of an active flow control method (suction slot) in a water injection environment on the aerodynamic performance of the compressor blades. The analysis includes study on flow separation, development of secondary flow and total pressure loss coefficient across the blade passage.
4. To experimentally investigate the water rivulet formation and its propagation on the compressor blades through the flow visualization technique

CHAPTER 3

NUMERICAL METHODOLOGY

An overview of the computational approach used, and a general description of the compressor blade geometry are provided in this chapter. The grid independence study and validation carried out are also included in this chapter.

3.1 Blade Profile

The airfoil profile employed in this study is NACA 65-009 (Figure 3.1). As per the NACA airfoil naming standard, the first digit "6" stands for the series name. The second digit "5" indicates that the minimum pressure region of the airfoil is located 50 % of the chord from the leading edge. The third digit "0" stands for the lift coefficient. The final two numbers "09" indicate that the maximum airfoil thickness is 9 percent of the chord and occurs at a chord thickness of 40 %.

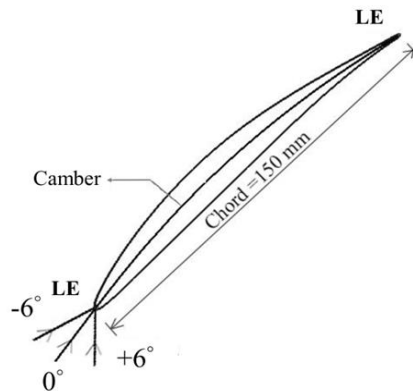


Figure 3.1 Schematic representation of blade profile

Table 3.1 shows the half thickness of the NACA 65-009 blade, where the x and y coordinates of the blade profile are expressed as percentages of the chord. The profile has a circular camber line with a camber angle of 23.22° and a stagger angle of 42.7° . The entrance angle of flow is 54.31° based on the relationship between the angles. The axial chord (C_{ax}) is 110 mm long and the chord length (C) is 150 mm. The blade has an aspect ratio of 2.47. This gives the blade a total span (h) of 370 mm.

Table 3.1 Half thickness of NACA 65-009 airfoil in the coordinates of the blade

x (% c)	y (% c)	x (% c)	y (% c)
0	0	40	4.4964
0.5	0.6948	45	4.4667
0.75	0.8388	50	4.3308
1.25	1.0521	55	4.077
2.5	1.4166	60	3.7314
5	1.9593	65	3.3138
7.5	2.3823	70	2.8404
10	2.736	75	2.3256
15	3.2994	80	1.7883
20	3.7287	85	1.2465
25	4.0527	90	0.729
30	4.284	95	0.2754
35	4.4316	100	0

3.2 Types of Configurations

In the first phase of the study effect of incidence angles, droplet size, and injection ratio on the loss coefficient and the improvement of the flow field is analyzed. In the second phase, the effect of an active flow control method (aspiration) using a suction slot is studied in a droplet-laden flow. To study the effect of incidence angle, the angle of impact is varied from negative incidence -8° to positive incidence angle 8° by an increment of interval $+2^\circ$ ($-8^\circ, -6^\circ, -4^\circ, -2^\circ, 0^\circ, 2^\circ, 4^\circ, 6^\circ, \text{ and } 8^\circ$). The widely accepted convention is that if the flow is leaning towards the pressure surface it is regarded as a positive incidence (Figure 3.1). The droplet size is varied from $12 \mu\text{m}$ to $60 \mu\text{m}$ to study the effect of droplet diameter. This range of diameter is taken based on the fact that the water injection ratio varies from 0.5 % to 4 % for practical applications.

In the second part of this study, a slot is provided on the blade surface. Four different configurations are analyzed depending on the axial position and shape of the slot. In the first configuration, the slot is kept on the lower end of the blade and covered 25 %

of the blade height on the suction side. This configuration is named as near-end wall slot (NES). In the second configuration, the slot is positioned at the center of the blade and occupied 50 % of the blade span. This configuration is named as “near midspan slot” (NMS). The third configuration is the “full span slot” (FSS), where the slot runs through the entire span and the fourth configuration is FEWS, this is a combination of the FSS scheme with a slot provided at the end wall which is positioned from 1 % to 98 % axial chord and 2 mm away from the suction surface with a width of 1 mm. More detailed information about each of these configurations is given in Chapter 6. A summary of all the configurations and parameters used in this study are provided in Table 3.2

Table 3.2 Computational configurations used in this study

SI No	Objectives	Fixed parameters	Parameters/configurations investigated
1	Effect of incidence angle	IR = 1 % D _d = 20 μm	-8°, -6°, -4°, -2°, 0°, 2°, 4°, 6°, 8°
2	Effect of droplet size	i = +6° IR = 1 %	12 μm, 20 μm, 32 μm, 48 μm, 60 μm
3	Effect of injection ratio	i = +6° D _d = 20 μm	0.5 %, 1 %, 2 %, 3 %, 4%
4	Effect of different slot configuration	Slot location = 60 % C _{ax} Suction rate = 1 % IR = 1 % D _d = 20 μm	Slot positioning on the blade

3.3 The Computational Domain

In Figure 3.2, the computational domain is shown. The exit plane is positioned 1.5 times the axial chord from the trailing edge. The inlet of the fluid domain is kept two times the axial chord from the leading edge. The blade is modeled only up to mid-span by giving symmetric boundary conditions in order to decrease computational time and

effort. Translational periodicity is given as one pitch, accordingly, periodic interfaces are defined.

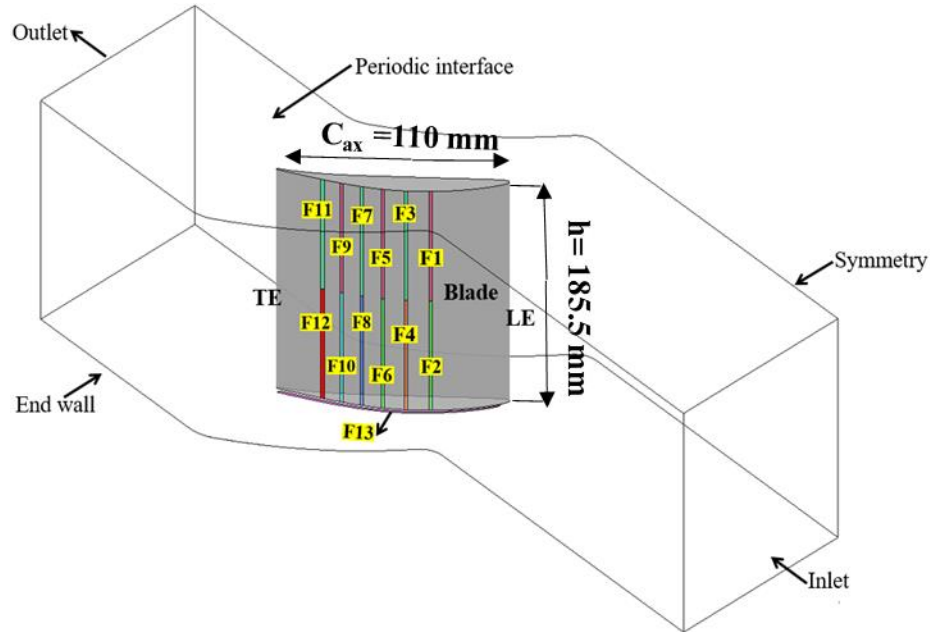


Figure 3.2 Computational domain

For the second part of the study, slots are provided for the aspiration of fluid on the blade suction surface. Several studies are carried out to determine an ideal location for the slot. Twelve spots are selected for the slot and these are named as F1, F2, etc. up to F12. The F1 and F2 are located at 20 % C_{ax} , F3 and F4 are located at 30 % C_{ax} , F5 and F6 are located at 40 % C_{ax} , F7 and F8 are located at 50 % C_{ax} , F9 and F10 are located at 60 % C_{ax} and F11 and F12 are located at 70 % C_{ax} respectively. Apart from this one slot (F13) is provided at the endwall. When simulating the base case (no slot condition), all these slots are treated as wall boundaries. While simulating the configuration with slots, these slots are assigned different boundary conditions. For example, during the simulation of FSS configuration, the faces F1 and F2 are treated as outlets, and the rest of the faces are assigned wall boundary conditions.

3.4 Mesh Generation

A commercial software ICEM CFD is used to generate the grid and perform computational modeling. For grid generation, fully structured hexahedral elements are used (Figure 3.3). Mesh refinement is offered around the blade surface and endwalls in

order to capture the boundary layer regions. The O grid and H grid are used in conjunction to achieve this. There are 30 node points in the O-grid around the blade and endwall, and its exponential growth rate is 1.2. (Figure 3.4). The y^+ value is kept below 1 for all computational domains, with the exception of a small area over the leading edge and suction surface, where it is observed to be 4.8. (Figure 3.5). A near-wall grid distance of 0.02 mm has been kept throughout the domain to achieve the necessary y^+ value.

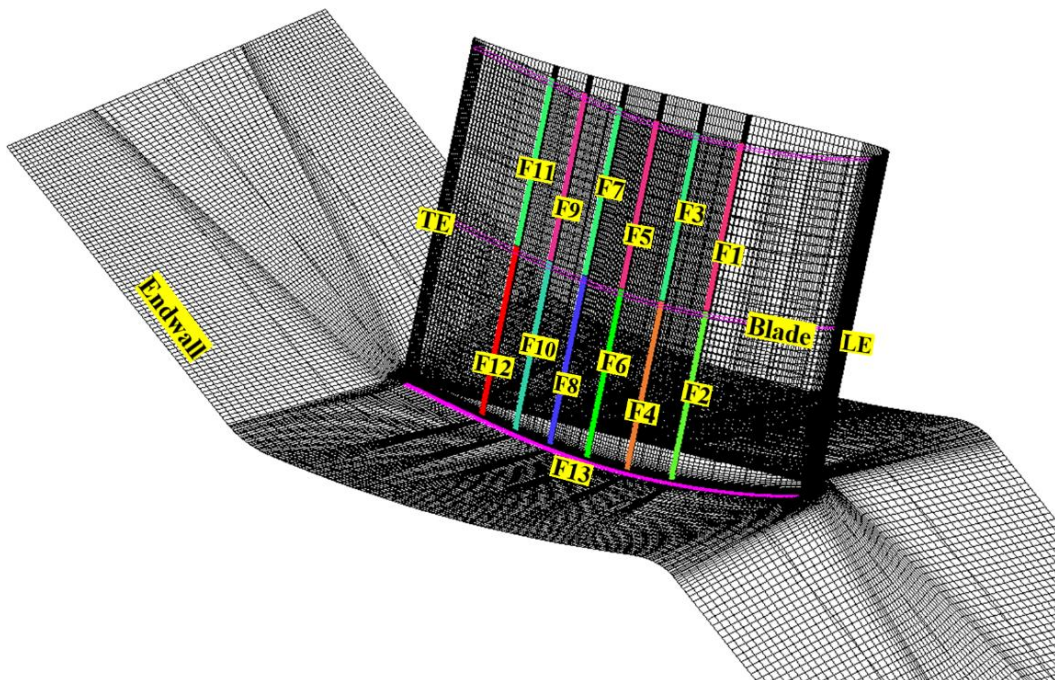


Figure 3.3 Structured mesh generated for the computational domain

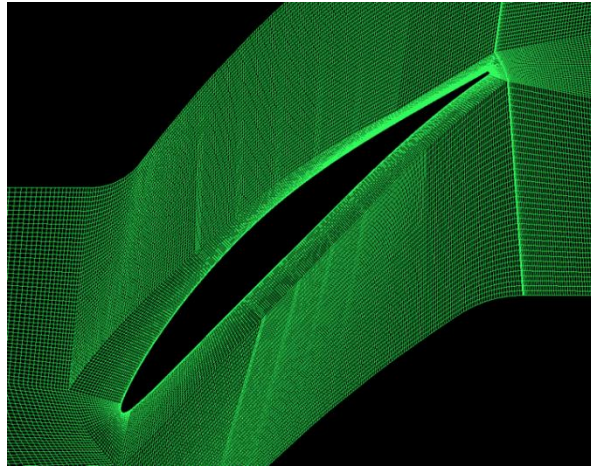


Figure 3.4 The O-grid distribution around blade surface

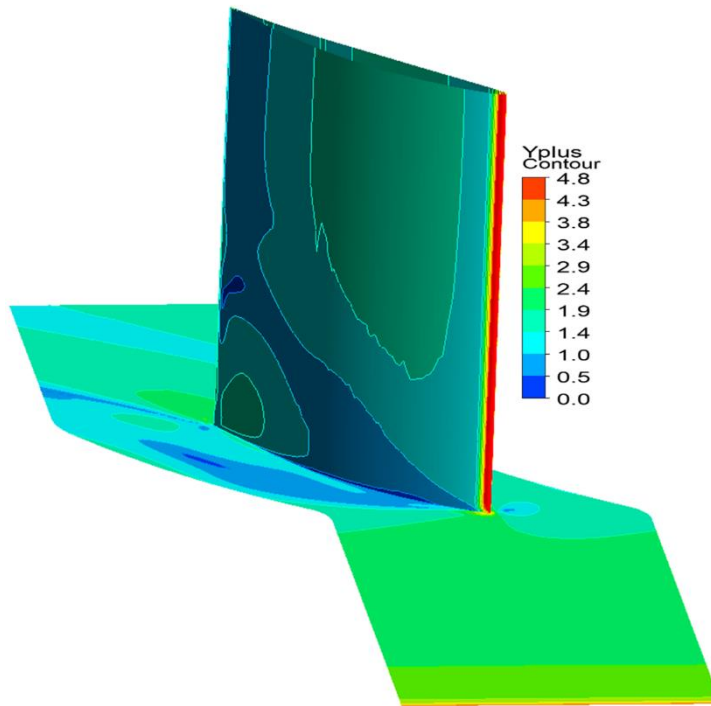


Figure 3.5 The y^+ distribution over the endwall and blade surface

3.5 Details of the Solver

All the simulations are carried out using the commercially available finite volume solver ANSYS CFX. This solver is widely applied in different applications, particularly in the turbomachinery area, because of its exceptional accuracy, reliability, efficiency, and affordability. Three-dimensional Navier stokes equations (for velocity and

pressure) are solved as an implicitly connected single system using a coupled solver. The coupled solver for each iteration solves the three momentum equations and pressure-based continuity equation at the same time. During discretization, CFX uses the vertex-centered approach. The values of the unknown variables solved are stored in the vertex, and the region surrounding the vertex is the control volume.

3.6 The Flow Physics

In the current study, the air is considered as continuous phase and water droplet as discrete phase. The Reynold's Averaged Navier Stokes (RANS) equations mentioned in Equations 3.1 and 3.2 are used to model the continuous phase.

$$\frac{\partial \bar{p}}{\partial t} + \frac{\partial \bar{\rho u}_i}{\partial x_i} = 0 \quad (3.1)$$

$$\frac{\partial \bar{\rho u}_i}{\partial t} + \frac{\partial \bar{\rho u}_i u_j}{\partial x_j} = \frac{\partial (\bar{\tau}_{ij} - \overline{\rho u'_i u'_j})}{\partial x_j} - \frac{\partial \bar{p}}{\partial x_i} \quad (3.2)$$

where τ is the stress tensor (including both normal and shear components of the stress).

Reynolds stresses $\overline{\rho u'_i u'_j}$ are produced by an oscillating velocity field. In order to solve this nonlinear term, a second model known as the turbulence model is required. The SST k - ω model, which simulates shear stress transmission, is used to model the turbulence. The SST model accounts for the transfer of turbulent shear stress and offers incredibly precise predictions of the start and size of flow separation when modeling flows with unfavorable pressure gradients. The model effectively combines the free-stream independence of the k - ω model in the far field with its precise and reliable formulation in the near-wall region. The k - ε model has been converted into a k - ω formulation in order to achieve this. The following modifications have been made to the standard k - ω model to make the SST k - ω model. The altered k - ε model is multiplied by the original k - ω model using a blending function, and both models are then combined. The standard k - ω model is supposed to be activated by the blending function of one close to the wall and the converted k - ε model by zero far from the

surface. The equation for the SST model contains a damped cross-diffusion derivative part.

The transport equations of the SST k - ω model are,

$$\frac{\partial \overline{\rho k}}{\partial t} + \frac{\partial \overline{\rho k u_i}}{\partial x_i} = \frac{\partial}{\partial x_j} \left(\Gamma_k \frac{\partial \overline{k}}{\partial x_j} \right) + \tilde{G}_k - Y_k + S_k \quad (3.3)$$

$$\frac{\partial \overline{\rho \omega}}{\partial t} + \frac{\partial \overline{\rho \omega u_i}}{\partial x_i} = \frac{\partial}{\partial x_j} \left(\Gamma_\omega \frac{\partial \overline{\omega}}{\partial x_j} \right) + \tilde{G}_\omega - Y_\omega + D_\omega + S_\omega \quad (3.4)$$

Where,

\tilde{G} : - k or ω generation due to the mean velocity gradients

Γ : - effective diffusivity of k or ω

Y : - dissipation of k or ω due to turbulence

D_ω : - cross diffusion term

S : - source terms of k or ω

One atm is chosen as the reference pressure for the entire domain. At the inlet, the static pressure of zero (relative to reference pressure) is provided, and at the outlet, an average velocity of 40 m/s is applied. The velocity at three cartesian coordinates is presented in accordance with the necessary incidence angles to examine the impact of those angles. An adiabatic, non-slip wall makes up the bottom wall. Since only half of the span is taken into account for simulations, the top face of the domain is given a symmetric boundary condition. A linear periodic interface boundary condition with a conservative interface flux is applied to the remaining two faces. The blade wall is regarded as an adiabatic, non-slipping wall as well. In the entire domain, the ambient temperature is set to 300 K. For the solver, an upwind advection technique is chosen. While the simulation is running, many variables are observed at the inlet, blade passage, and outflow to confirm that the solution has come to a convergence. The simulation is seemed to have converged when the residuals drop to a minimum imbalance of 10^{-7} .

When simulating the injection of water, water droplets are treated as fully linked, distributed particles inside the continuous fluid (air). The water droplets are thought to have zero slip velocity in a continuous medium, like airflow. Applying the Lagrangian approach, it is possible to track the water droplets in the flow from input to output. The equation of motion of the particle is,

$$\frac{d\vec{u}_p}{dt} = F_D(\vec{u} - \vec{u}_p) + \frac{g(\rho_p - \rho)}{\rho_p} + \vec{F} \quad (3.5)$$

Where,

\vec{F} : - An additional acceleration (force/unit particle mass) term

$F_D(\vec{u} - \vec{u}_p)$: - Drag force per unit particle mass

\vec{u} : - Fluid phase velocity

\vec{u}_p : - Particle velocity

Using Equation 3.5, the trajectory of the water droplet is computed. To predict particle dispersion due to fluid phase turbulence, one can use the stochastic tracking model or the particle cloud model. The stochastic tracking (random walk) model incorporates the impact of transient turbulent velocity fluctuations on particle trajectories using stochastic techniques. The statistical evolution of a cloud of particles is plotted using the particle cloud model over a predetermined path. The particle concentration inside the cloud is represented by a Gaussian probability density function centered on the mean trajectory. An easier way of tracking packages is used rather than tracking each and every particle put into the domain. A group of particles is represented statistically by parcels. Calculating particle collisions using parcels is far more effective. The computation makes use of the O'Rourke algorithm. In O'Rourke's method, parcel trajectories are not checked for intersection using geometry, but rather with a stochastic estimate of collisions. Furthermore, O'Rourke makes the assumption that two parcels can only collide if they are located in the same continuous-phase cell. These two suppositions are true only when the continuous-phase cell size is small in proportion to the spray size. O'Rourke's method is second-order accurate at estimating the likelihood of crashes in these circumstances. Combining the theory of parcels with O'Rourke's

approach enables collision computation in real-world spray applications. The particles disintegrate into smaller particles as a result of viscous forces in the flow. For modeling secondary particle breakage, Schmehl model is utilized; the new secondary particle break-up models currently available in CFX, considering three different breakup regimes. In the Schmehl, the droplet deformation and break up are based on experimental findings. A mass flow rate is allocated to the water droplets when they are injected at the domain's inlet depending on the inlet's total mass flow rate. The mass flow rate of air divided by the mass flow rate of a water is known as the injection ratio or IR.

At the input, water droplets are assumed to be uniformly distributed, and particle diameter distribution follows the Rosin-Rammler equation with a Rosin-Rammler power of 1.5. (Eqn 3.6).

$$R = \exp \left[-\left(\frac{d}{d_e}\right)^\gamma \right] \quad (3.6)$$

Where,

γ : - Rosin Rammler power or the parameter describing the spread

d : - Particle size

d_e : - Measure of fineness or the diameter at which $R = 1/e$

Water droplet interactions with the top wall are examined in terms of the perpendicular and parallel coefficients of restitution. The stated values, 0 and 1, are based on the notion that after some time, the particles that are bouncing because of the top wall's impingement will have been deposited there. The particles that adhere to the wall, therefore, have a perpendicular coefficient value that is close to zero. The simulations are run with multiple injection ratios (ranging from 0.05 to 4 percent of the input mass flow rate), varied incidence angles (including negative and positive angles), different droplet dimensions (from 12 μm to 60 μm), and different suction slot layouts.

The rate of temperature change for the particle can be obtained from the following equation.

$$m_p C_w \frac{dT_p}{dt} = \pi d_p \lambda Nu (T - T_p) + \frac{dm_p}{dt} h_{fg} \quad (3.7)$$

Where C_w is the specific heat of water, T_p is the temperature of droplet, λ is the thermal conductivity of the continuous phase, Nu is the Nusselt number, $\frac{dm_p}{dt}$ is the rate of change of mass transfer and h_{fg} is the latent heat of vaporization. The two terms of the right hand of the equation 3.7 are convective heat transfer and latent heat transfer associated with mass transfer respectively.

The evaporation model uses two mass transfer correlations depending on whether the droplet is above or below the boiling point. This is determined through the Antoine Equation given below (Eqn 3.8),

$$\log_{10} P_{sat} = A - \frac{B}{T + C - 273.15} \quad (3.8)$$

Where A, B and C are constant coefficients,

When the particle is above the boiling point, the rate of mass transfer is determined by the convective heat transfer (Eqn 3.9)

$$\frac{dm_p}{dt} = \frac{\pi d_p \lambda Nu (T - T_p)}{h_{fg}} \quad (3.9)$$

When the particle is below the boiling point, the rate of mass transfer is given by the formula below (Eqn 4.0)

$$\frac{dm_p}{dt} = \pi d_p \rho_v d D_v Sh \frac{M_v}{M} \log\left(\frac{1 - f_p}{1 - f}\right) \quad (4.0)$$

Where ρ_v , D_v are the density and diffusivity of vapor, Sh is the Sherwood number, M_v and M are respectively the molecular weights of the vapor and the mixture in the continuous phase, and f_p and f are the molar fractions in the droplet and in the gas phase.

No water film formation, No particle collisions and steady flow, these are the assumptions in this study.

3.7 Grid Sensitivity Study

To determine the ideal amount of grid components, a grid sensitivity analysis has been conducted. The examination of grid sensitivity is shown in Figure 3.6. For the grid independent study, various mesh sizes were chosen, including 1.5 million, 2.5 million, 3.5 million, 4.5 million, and 5.5 million. The graph below shows the mass averaged total pressure loss coefficient and averaged static pressure coefficient on the blade against the various grid element counts at an axial point of $1.1 C_{ax}$. Figure 3.6 (a) and Figure 3.6 (b) shows that after 1.5 million elements, further grid refinement does not result in a noticeably different outcome. Hence, for further simulations, a model with 3.5 million elements is chosen.

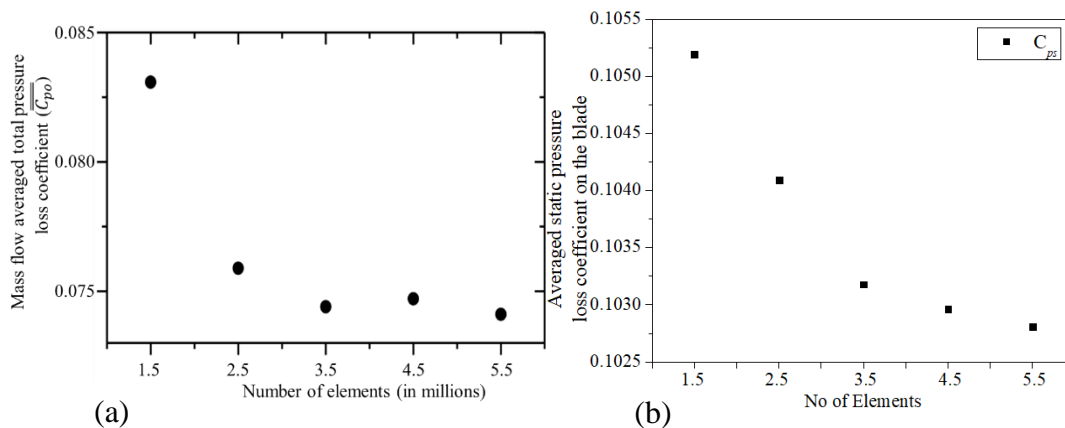


Figure 3.6 Grid sensitivity study (a) Variations in total pressure loss coefficient at outlet (b) Variations in the static pressure loss coefficient on the blade

3.8 Validation

The outcomes of the experimental and numerical study by Ma et al. 2011 are used to validate the current numerical simulations (Ma et al. 2011). A constant velocity of 40 m/s is the inflow boundary condition. The walls are smooth, immobile, and adiabatic. Static pressure of 1 atm, or atmospheric pressure, is the boundary condition at the outflow. Figure 3.7 compares the blade loading at the mid-span of the current CFD simulation with the experimental and computational results of Ma et al. 2011, shown

against the normalized axial chord. Comparisons of the end wall static pressure coefficient and the total pressure loss coefficient (C_{po}) are shown in Figure 3.8 and Figure 3.9 respectively, on a streamwise plane 50 percent of the axial chord length downstream of the trailing edge. To get the C_{ps} (Eq. (3.7)) and C_{po} (Eq. (3.8)), the static pressure and total pressure loss values are normalized with respect to the inlet dynamic pressure as follows.

$$C_{ps} = \frac{P_s}{0.5\rho_\infty U_\infty^2} \quad (3.7)$$

$$C_{po} = \frac{\overline{P_{t,\infty}} - P_t}{0.5\rho_\infty U_\infty^2} \quad (3.8)$$

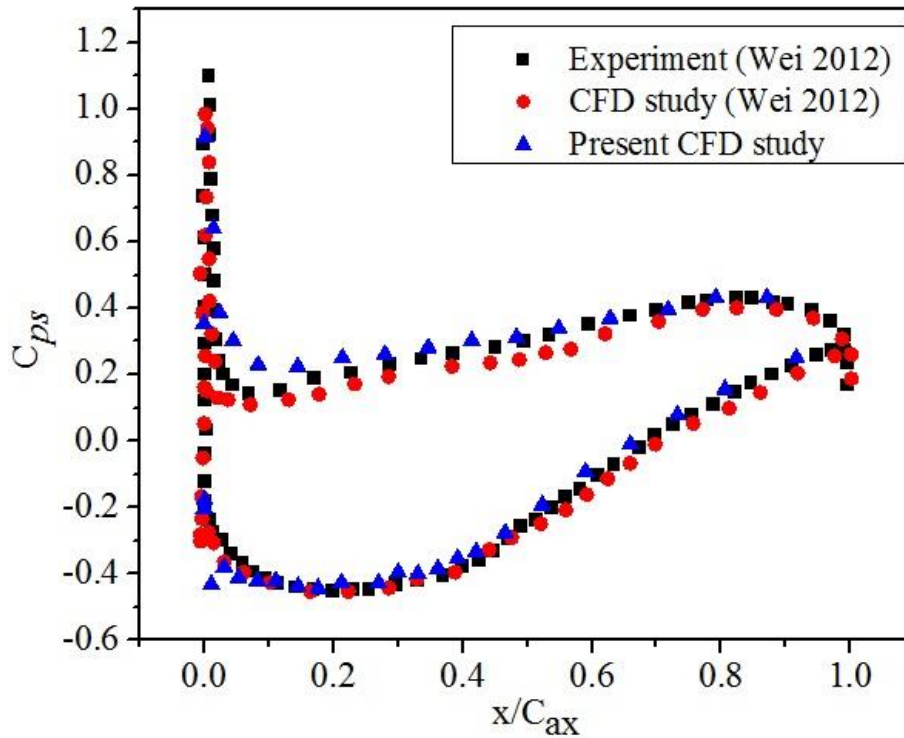


Figure 3.7 Comparison of static pressure coefficient (C_{ps}) on the blade surface at midspan of present CFD study with experimental and computational results of Ma et al. 2011.

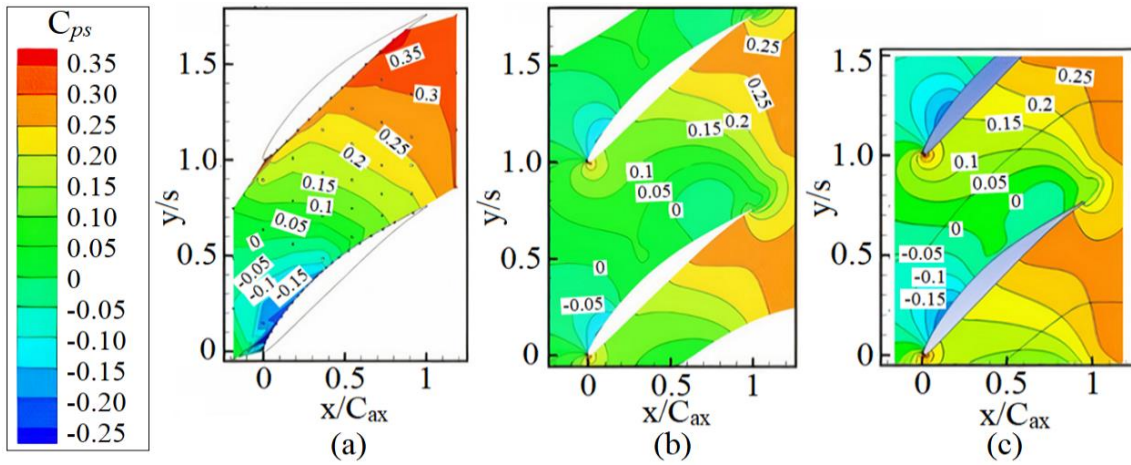


Figure 3.8 Variation of endwall static pressure coefficient (C_{ps}) (a) experimental study (Ma et al. 2011) (b) CFD study (Ma et al. 2011) (c) Present CFD study

The results obtained from the present CFD simulation are matching well with the results of Ma et al. 2011 qualitatively and quantitatively. However, there is a slight variation in the total pressure loss coefficient (Figure 3.9) which is due to the difference in the modeling of turbulence. The computational result of Ma et al. 2011 utilized the Spalart-Allmaras model for turbulence modeling while the present study utilized the SST $k - \omega$ model. The Spalart-Allmaras is a single equation turbulence model while the SST $k - \omega$ model uses two equations to close the RANS equation.

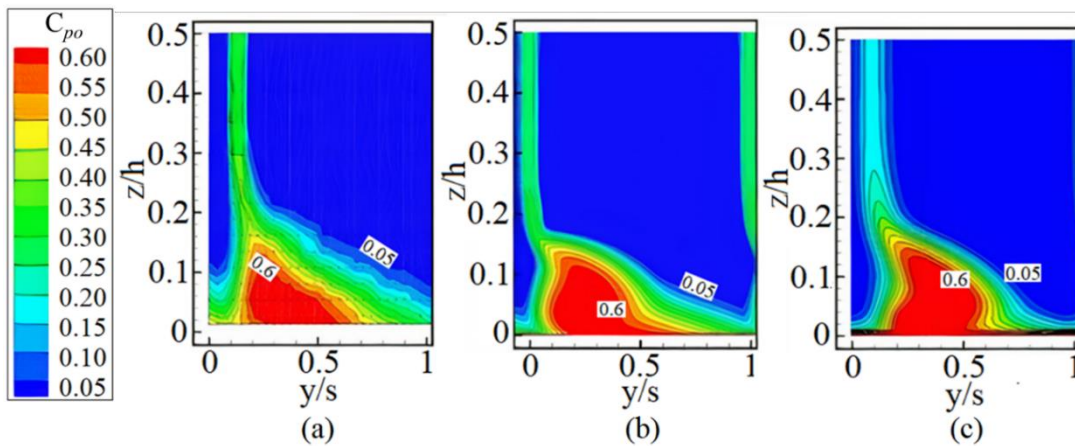


Figure 3.9 Comparison of total pressure loss coefficient (C_{po}) on a streamwise plane at 50 % of the axial chord downstream of the trailing edge (a) experimental study (Ma et al. 2011) (b) CFD study (Ma et al. 2011) (c) Present CFD study

CHAPTER 4

FLOW ANALYSIS IN COMPRESSOR CASCADE WITH WATER INJECTION

The impact of water injection on the compressor cascade performance is covered in this chapter. The primary measure used to evaluate aerodynamic performance is thought to be the total pressure loss coefficient. Nine incidence angles vary between -8° and $+8^\circ$ in steps of 2° are used in the simulations. A thorough flow field investigation is also conducted to understand the variations caused by water droplets on the continuous medium. The schematic diagram showing the different flow incidence is exhibited in Figure 4.1.

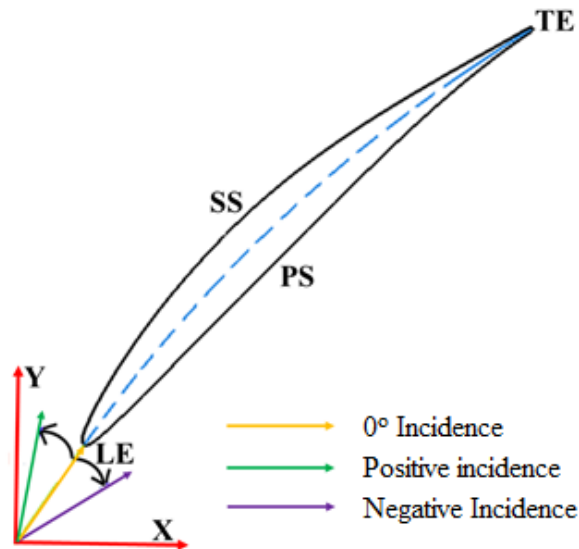


Figure 4.1 Schematic representation of different flow incidence

4.1 Effect of Incidence Angle on the Loss Coefficient

Figure 4.2 and Figure 4.3, depict the fluctuation of the total pressure loss coefficient for positive and negative incidence angles, respectively. Figure 4.2 (a) gives the idea about the axial locations along which the measurements is taken for the plots Figure 4.2 and Figure 4.3. Wet and dry instances are contrasted with one another. Total pressure loss coefficient mass averaged values are computed at different streamwise planes from input to exit and are plotted along normalized axial location (x/C_{ax}). The leading edge

of the blade is represented by $x/C_{ax} = 0$, and the trailing edge is represented by $x/C_{ax} = 1$. The mass flow averaged total pressure loss coefficient is expressed as shown below, Eq (4.1) (Horlock 2001). A mass averaged quantity is obtained by integrating the scalar time mass flow divided by total mass flow over the region. The variables are defined in nomenclature, hence not detailed here. accounting in the scenario of water injection.

$$\bar{C}_{po} = \frac{\frac{m_{\infty}}{m_{\infty+m_w}} \bar{P}_{t,\infty} + \frac{m_w}{m_{\infty+m_w}} \bar{P}_{t,w} - \bar{P}_t}{0.5\rho_{\infty} U_{\infty}^2} \quad (4.1)$$

Introducing water droplets to the dry case exhibits promising results as far as loss coefficient is concerned. For the zero-incidence angle, the loss coefficient at the exit is reduced by 32.7 % with the introduction of water droplets. Based on the variation of slope four regions are identified. Region I refers to the inlet of the computational domain to the leading edge of the blade. As the incidence angle increases the losses in the blade passage also increase. The variation of loss coefficient in this region is almost similar for all the tested cases. The sudden change in the slope of the curve after $x/C_{ax}=0$ (region II) indicates this fact. The slope of the curve further rises after the trailing edge ($x/C_{ax}=1$) up to an x/C_{ax} of 1.5 (region III). This sudden rise is due to the mixing of pressure side and suction side flows from the blade passage.

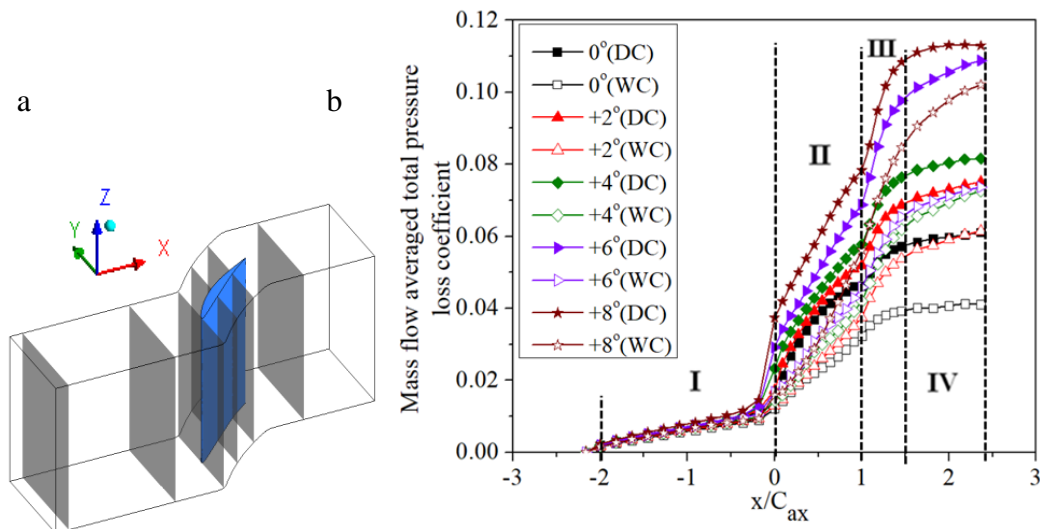


Figure 4.2 (a) Schematic diagram representing the measurement locations (b) Variation of mass flow averaged total pressure loss coefficient at different positive incidence angles (DC = Dry case; WC = Wet case)

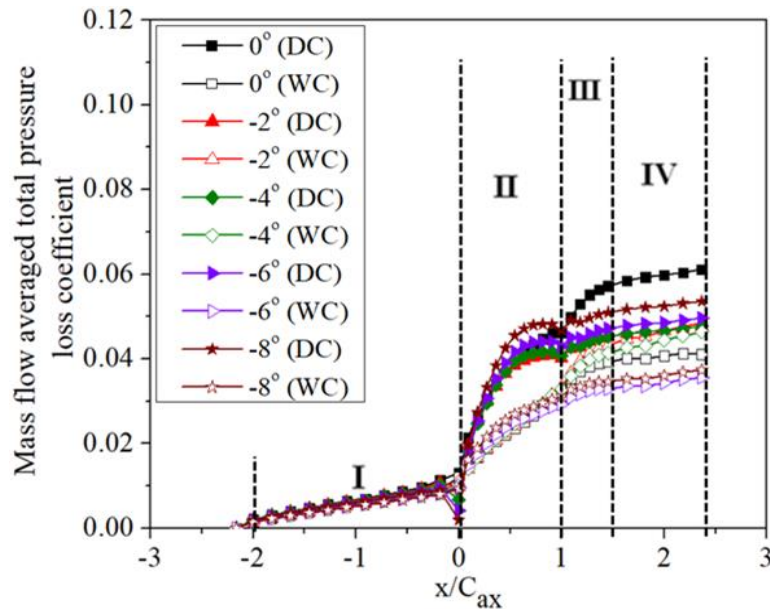


Figure 4.3 Variations of mass flow averaged total pressure loss coefficient at different negative incidence angles

Before the leading edge (LE) the loss coefficient is almost similar for wet and dry cases. After the LE the differences in the mass averaged loss coefficient start widening between the wet and dry cases. In region IV there is no further significant loss generation, particularly for the dry cases. The curve is almost flat for dry cases in this region. However, there are some exceptions at $+8^\circ$ and $+6^\circ$ incidence angles. There is a significant amount of loss generation in region IV during the wet case. The behaviors of the flow in these regions are explained in the upcoming section.

4.2 Detailed Flow Behavior at 0° Incidence

Zero incidence angle refers to the case where the flow enters the leading edge along the camber line. In this section, the flow behavior is compared for wet and dry cases at this incidence angle.

4.2.1 Comparison of vectors near end wall (at 4 % of the span)

There are two visible recirculation zones (Figure 4.4) near the end wall for dry as well as the wet case. A strong recirculation zone is visible on the suction side. Almost blocks the entire passage. Compared to the dry case, the aerodynamic blockage is more in the

wet case near the end wall region. Another recirculation is visible at the trailing edge region.

The effect of water droplets is seen in both these recirculations. The flow separation initiates at $0.45C_{ax}$ for both cases. However, for the wet case, the flow gets attached immediately after the initial point of separation near the suction surface of the blade as shown in the closeup view of the vector (red spot region). The reverse flow starts at the initial separation point and gets separated. This separated flow moves in the streamwise direction by the influence of stronger onward flow compared to the dry case due to the reduction of viscous effect by the addition of water droplet particles. Hence a small recirculation zone develops due to this attachment of flow followed by the initial separation. This attachment of flow occurs primarily from the momentum exchange of the injected droplets and the continuous media. The surface streamline plots also exhibit this phenomenon clearly (Figure 4.5). Figure 4.6 (a) shows the polyline along which the wall shear stress values are calculated and Figure 4.6 (b) shows the wall shear stress plotted on the suction surface of the blade near the end wall (at 4 % span of the blade). The wall shear stress plot helps to identify the separation point for both cases and it is seen that the separation occurs almost at the same location ($0.45 C_{ax}$).

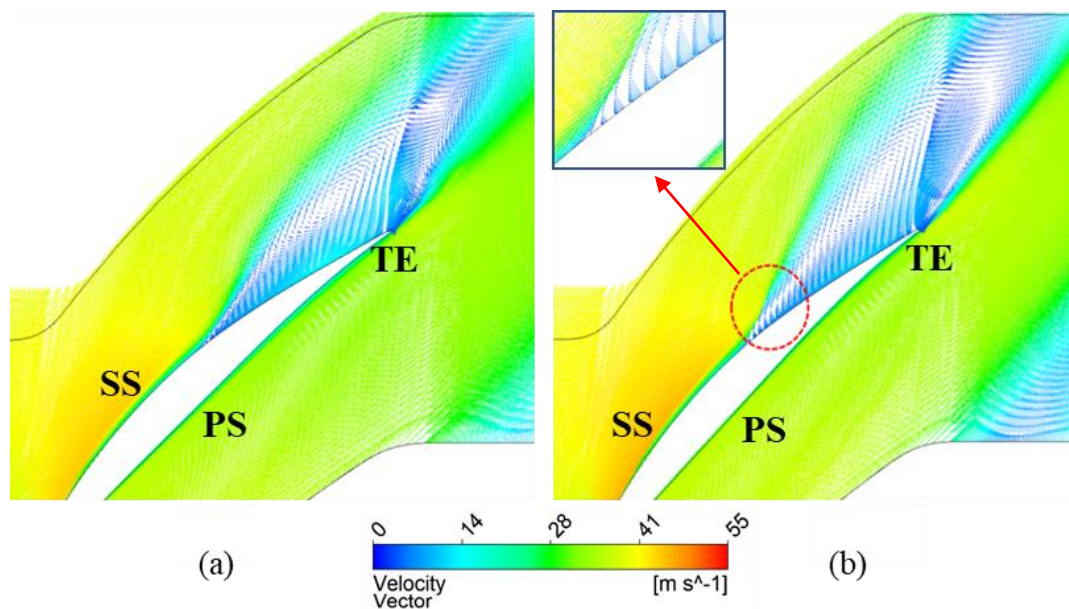


Figure 4.4 Variation of velocity vector near end wall (4 % of span) (a) Dry case (b) Wet case

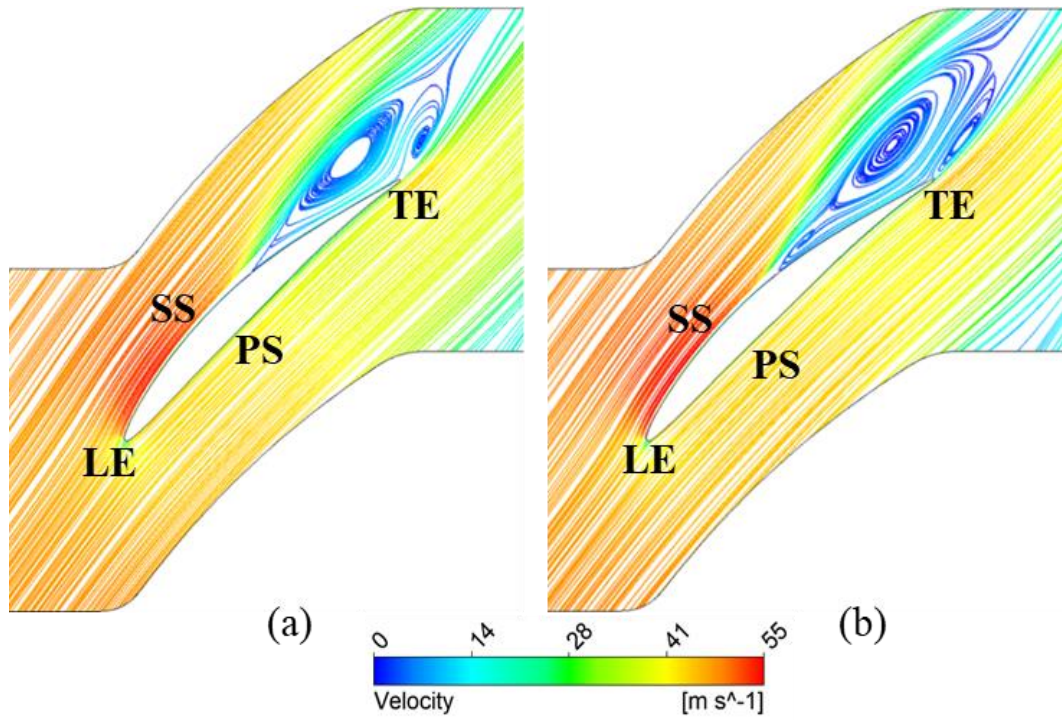


Figure 4.5 Variation of surface streamlines near end wall (4 % of span) (a) Dry case (b) Wet case

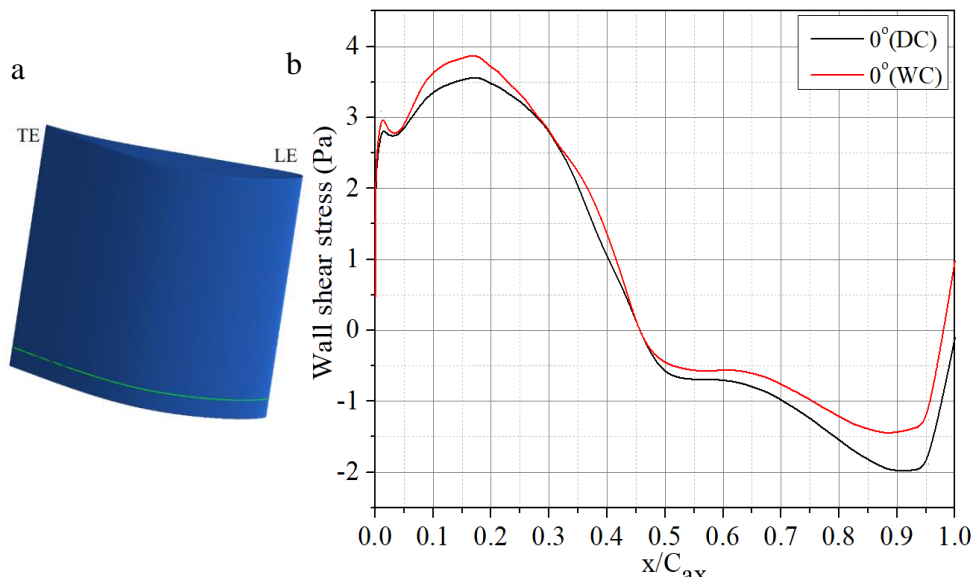


Figure 4.6 (a) Schematic diagram representing the measurements locations (b) Variations of wall shear on the suction surface of the blade near end wall (at 4 % of the span)

4.2.2 Comparison of vectors near midspan (at 45 % of the span)

As we move towards the midspan the recirculation zones are limited only to the trailing edge region. Near the trailing edge, a higher flow recirculation is observed for the dry case (Figure 4.7). The velocity coefficient (u/U_∞) inside the blade passage ($x/C_{ax}=0.50$) and near the trailing edge ($x/C_{ax}=0.96$) is shown in Figure 4.8 and Figure 4.9. The difference in the contour is quite evident for the wet cases.

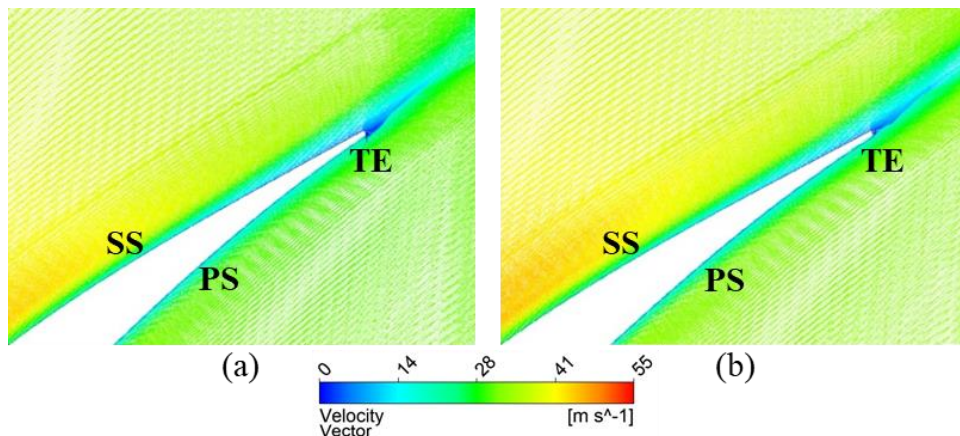


Figure 4.7 Variations of velocity vector near midspan (at 45 % of span) for the dry case and wet case (a) dry case (b) wet case

In the mid passage (midspan) region the variation of the velocity contour in the transverse direction is gradual and smooth, whereas for the wet case there are two distinct boundaries for the contours. The contours in the mean flow region are disturbed by the particle tracks. However, this has not been observed inside the separated flow region. Inside the separated flow regime, the presence of particle tracks is minimal. Few representative particle tracks are shown (Figure 4.10).

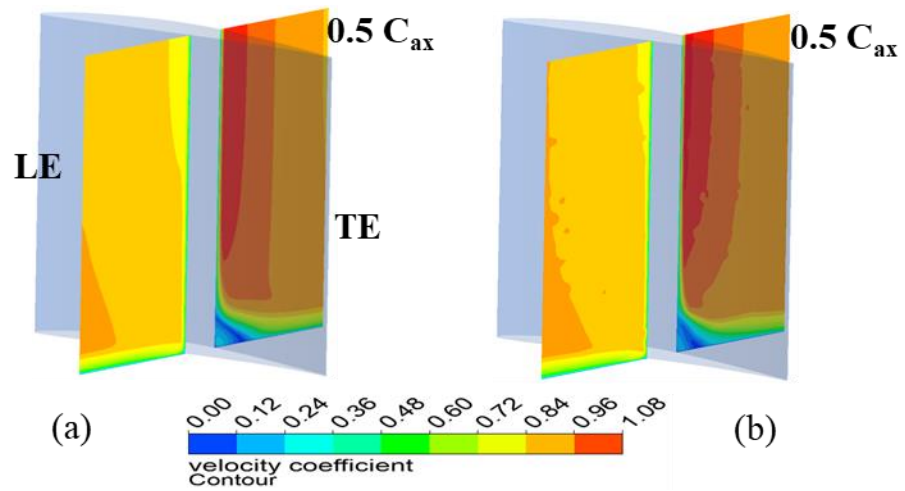


Figure 4.8 Variation of velocity coefficient contour for 0° incidence angle at $0.50 C_{ax}$ (a) dry case (b) wet case

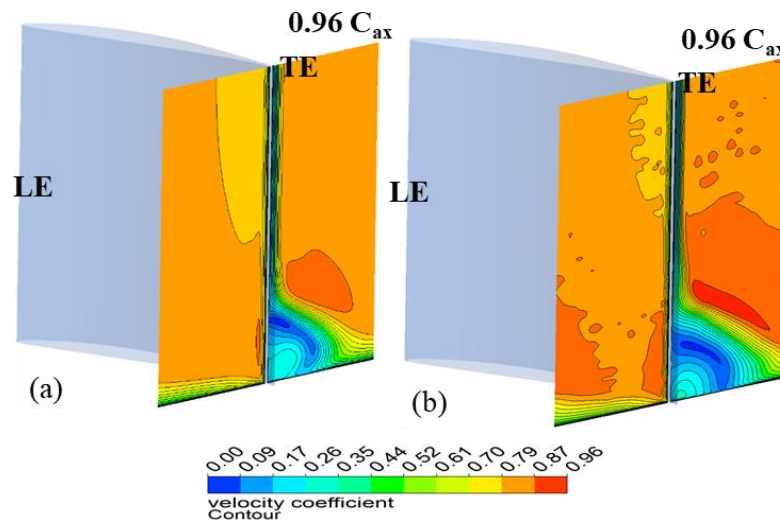


Figure 4.9 Variation of velocity coefficient contour for 0° incidence angle at $0.96 C_{ax}$ (a) dry case (b) wet case

The color of the track represents the velocity coefficient. An upward shift of the particle tracks from the end wall is observed. This upward movement of the tracks is visible from the point of separation (Nearly $0.45 C_{ax}$). The separated flow regime covers almost 20 % span near the trailing edge region and water particle present in this region is found to be minimum; it is almost completely devoid of any particles very close to the end wall.

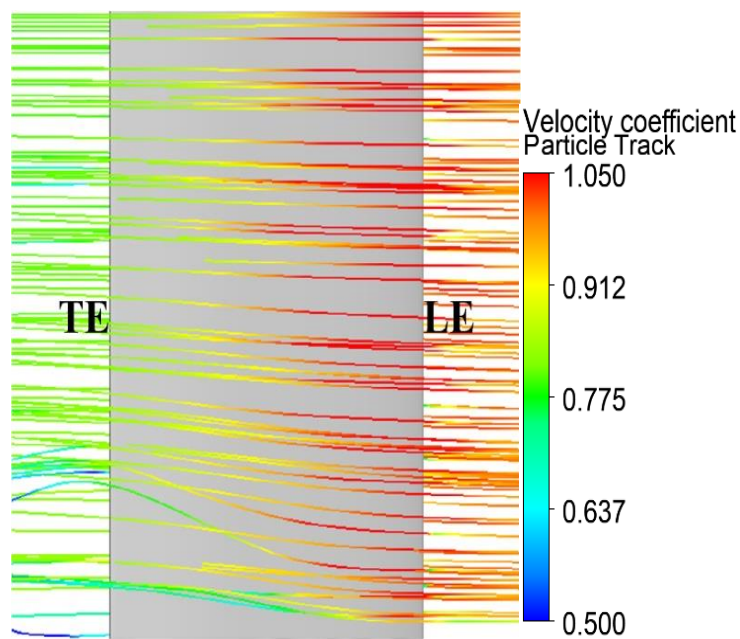


Figure 4.10 Variations of water particle track inside blade the blade passage

4.2.3 The hub corner vortex formation and its effect on total pressure loss coefficient

Figure 4.11 shows the limiting streamlines on the blade suction surface and end wall superimposed with the total pressure loss coefficient at $1.1 C_{ax}$. In this Figure, the node-saddle point pair N1-S1 represents the horseshoe vortex system in the leading edge region. A node is a point shared by an infinite number of skin friction lines or limiting streamlines. All of the skin friction lines are pointed outward from a nodal point of separation and pointed inward toward the node at a nodal point of attachment. In the realm of limiting streamlines or the skin friction lines, a saddle point is a location where two specific (critical) lines converge, acting as barriers that prevent one set of streamlines from reaching the adjacent set.

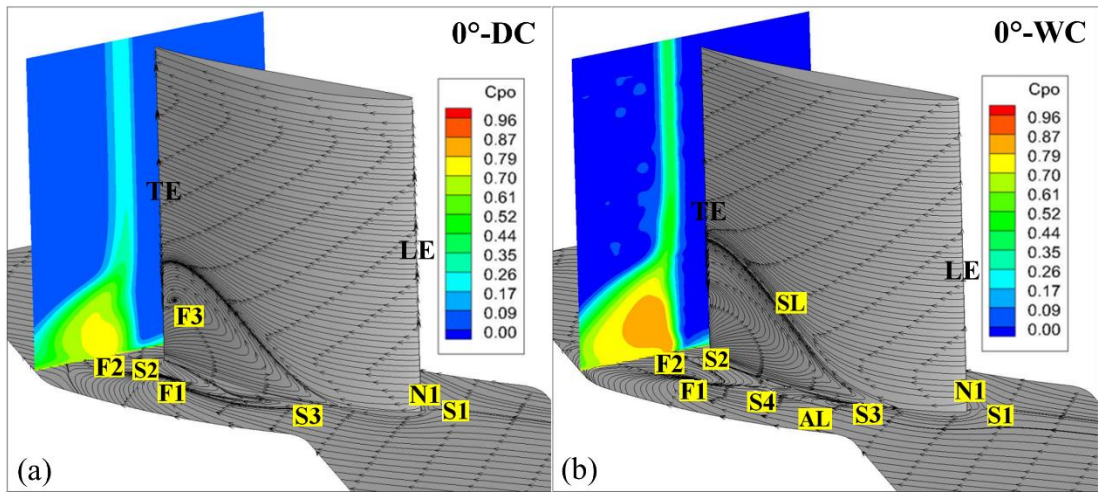


Figure 4.11 Limiting streamlines on the blade suction surface and end wall superimposed with total pressure loss coefficient at $1.1 C_{ax}$ (a) dry case (b) wet case

The dividing streamline is bifurcated into two, one is moved toward the suction surface, other one moves towards the pressure surface named as suction surface leg and pressure surface leg respectively. A focus point F1 is formed by the spiral of the suction surface leg of the dividing streamline on the endwall. The pressure surface leg of the dividing streamline flows towards the trailing edge of the nearby blade before forming a vortex of focal point F2, indicating a significant effect from the crossflow. With saddle point, S1 as their origin, focus F1, and point of terminations F2, these dividing streamlines may be referred to be endwall dividing streamlines of global separation in accordance with Lighthill's closed separation criterion (Lighthill 1963). In the wet scenario, it is observed that the focal point's F2 strength is somewhat less strong. Consequently, in the wet condition, a very tiny recirculation zone that is not associated with a significant flow reversal forms near the trailing edge. The skin friction lines from node N1 in the leading edge region intersect the corner between the blade and the hub wall at saddle point S3. This S3 is seen as a semi-saddle point on the hub wall and on the blade suction surface too. Local lines of separation are formed when these lines converge at a position other than the saddle point, where their origin lies (Tobak and Peake 1981). On the hub wall, the skin friction lines from the saddle point S3 form two separate local dividing streamlines. The first one form a spiral and terminates into the focal point F1 and the other one spirals and terminates into the focal point F3 on the suction surface in the dry case.

In the wet case, the dividing lines spiral over the suction surface but are not terminated into focal point F3. The hub wall's focal point F1 serves as the corner vortex's base, and the vortex filament (or core) that springs from it symbolizes the vortex's spanwise motion. On the hub wall and suction surface, respectively, the local lines of separation for the dry case are denoted as N1 to S3 to F1 and N1 to S3 to F3. In the wet case, N1 to S3 to F1, SL is the local line of separation on the hub wall and suction surface respectively.

The semi saddle point S3 at $0.23 C_{ax}$, is the starting point of hub corner vortex formation for the dry case. This point is moved towards the leading edge for the wet case (the saddle point is at $0.18 C_{ax}$). It implies that the formation of the hub corner vortex is slightly earlier by the addition of water injection at a 0° incidence angle. Due to the wall's viscous effects, the endwall boundary layer moves at a slower velocity, but it has nearly the same cross-stream pressure gradient as the free stream. The corner areas between the blade and the endwall on the endwalls are susceptible to having a viscous effect that is dominating. Strong flow separations and dense boundary layers may develop at the corners. Since the streamline radius of curvature is lower at the hub wall than it is in the free stream, this causes cross-passage motion and the build up of low stagnation pressure fluid close to the endwall-suction surface corner. When there is a rise in pressure in the blade passage due to higher blade loading circumstances, the low stagnation pressure fluid cannot handle it, and the endwall corner stalls. The blade loading is hence high. The corner vortex attaches to the flow path and widens the aerodynamic blockage, which reduces the blade's capacity to raise pressure. Additionally, the subsequent blending of the flow in the separated section with the flow in the main passage may result in a major total pressure loss and, as a result, a decline in the compressor's aerodynamic efficiency.

Even if the hub corner vortex can be seen in both dry and wet cases, some differences are observed in these cases. The focal point of vortex F1 on the hub wall is moved away from the hub-suction surface corner for the wet case. But in the dry case, the focal point F1 is comparatively closer to the hub-suction surface corner. This is because the addition of water particles enhances the reattachment of flow immediately after the initial point of separation. Thus the flow is diverted to the corner of the hub-suction

surface corner. The streamwise flow and the dividing streamline from the saddle points S3 form a line of attachment named "AL". The streamline originates from this new saddle point S4, then interacts with cross passage flow, and pushes the hub corner vortex of focus point F1 away from the corner. This is the reason for the shifting of focal point F1 away from the hub-suction surface corner in the wet case.

4.2.4 Effect of Hub corner vortex on loss coefficient at zero incidence angle

The hub corner vortex grows bigger and interacts with the trailing edge and other vortices to form a major loss core region as shown by the streamlines in Figure 4.12. The major loss coefficient region is seen near the endwall and it is contributed by the vortex formed near the endwall trailing edge corner. This vortex formation is present in both dry and wet configurations. However, its intensity is high for the dry case. Secondary flow streamlines are visible near the endwall. These are cross-flow streamlines inside the boundary layer that moves across the mainstream flow under influence of the crossflow pressure gradient that exists between the pressure surface of one blade and the suction surface of the neighboring blade. At the blade end wall corner, these streamline rolls up. Even though this happens for both dry and wet cases, the pressure gradient is quite high for the dry case and so the cross-flow of boundary layer fluid is stronger in the dry case. This ends up in a larger corner vortex for the dry case at the trailing edge.

The total pressure loss coefficient at the downstream location near the trailing edge region ($0.96 C_{ax}$) and the downstream location far away from the trailing edge ($2.3C_{ax}$) is plotted in Figure 4.13 respectively. The mass averaged loss coefficient at the trailing edge is 0.047 for the wet case and that for the dry case is 0.069. It shows that there is a 30 % reduction in losses with wet compression near TE. On the other hand, as we move towards the exit this percentage is coming down. At $2.3 C_{ax}$ the percentage difference is 25 %. After the trailing edge the difference in the loss coefficient for the dry case and the wet case is getting reduced. Looking at the contour plot in Figure 4.13, it can be understood that the width of the loss region is almost similar for both cases, but the difference lies in their peak values. The peak value for the loss coefficient is higher for

the dry case and it reflects in the mass average calculations also. At the downstream location, due to the circumferential mixing of the flow, the loss coefficient attains a uniform value near the endwall.

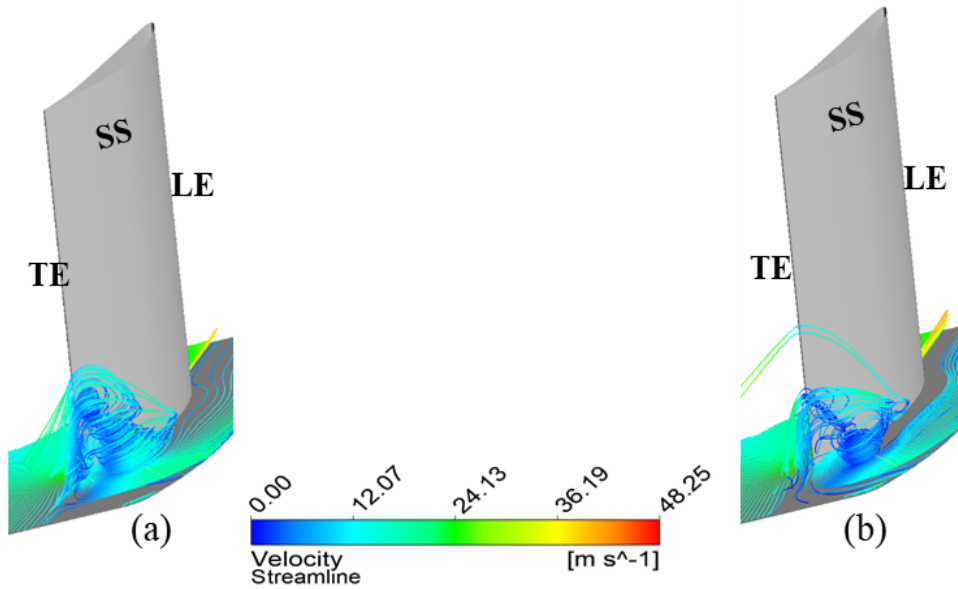


Figure 4.12 Volume streamlines plotted near end wall (a) dry case (b) wet case

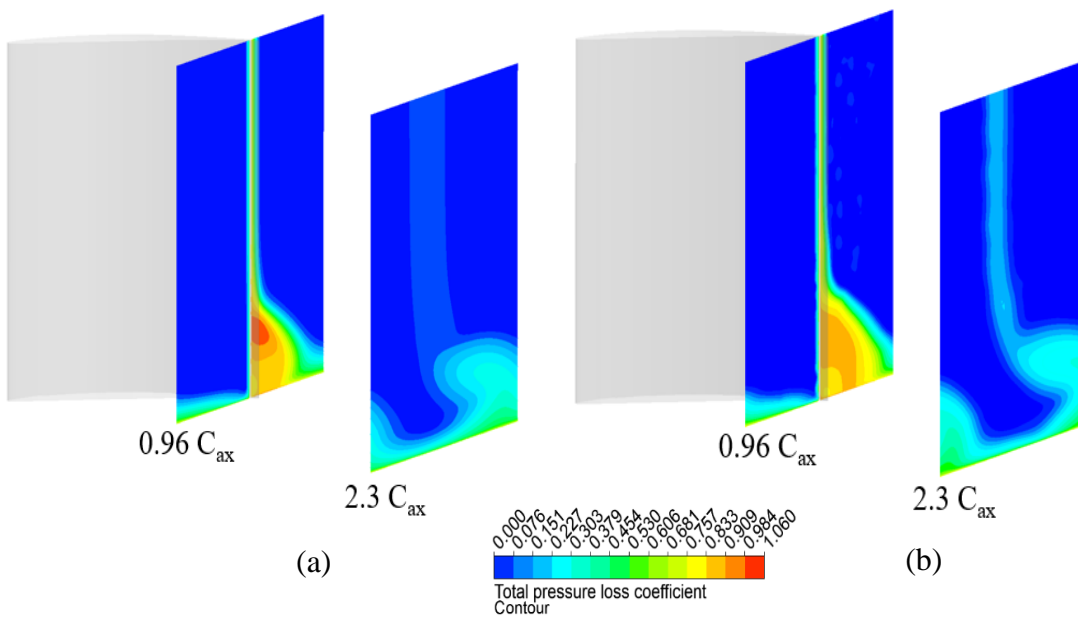


Figure 4.13 Variation of total pressure loss coefficient at $0.96 C_{ax}$ and $2.3 C_{ax}$ (a) dry case (b) wet case

4.3 Detailed Flow Behavior at Positive Incidence Angles

The impact of water injection at positive incidence angles is examined at four distinct incidence angles (2° , 4° , 6° , and 8°). For the purpose of comparing the flow behaviors, differences in surface streamlines are displayed and explained below.

4.3.1 Comparison of vectors near end wall (at 4 % of the span)

In general, the positive incidence angle causes a separation of flow from the suction side of the aerofoil-shaped blade. In the present study also similar observation is made, but the significant question is, “How the flow separation behaves in the presence of water droplets?” Figure 4.14 shows the surface streamlines near the endwall (4 % of span) at different positive incidence angles.

The presence of water droplets enhances the flow separation near the endwall and causes an increase in the loss coefficient near the endwall region. This is contradictory to the observations we made in Figure 4.2 where the mass averaged loss coefficient values are coming down with the presence of water droplets. This ensures that the increased disturbance due to water droplets is limited to the endwall region only. Similar to the zero incidence case two prominent recirculation zones are present at positive incidence as well. The recirculation near the trailing edge is more prominent with the dry case.

Figure 4.15 shows the variation of wall shear stress on the suction surface of the blade near endwall (at 4 % of the span). The wall shear stress shows the extent of the recirculation region near the endwall. The negative values indicate the separated flow regime. The point of separation moves towards the leading edge with an increase in the incidence angle, in other words, the flow separation occurs early. Towards the trailing edge, the shear stress values become positive, indicating the blade is coming out of stalling. This reattachment is due to the trailing edge vortices and it is clearly visible at lower positive incidence angles ($+2^\circ$ and $+4^\circ$). Even more interesting is, that this reattachment near the trailing edge is slightly earlier and stronger for the wet case than the dry one. At higher positive incidence angles, the reattachment near the trailing edge is slightly delayed due to the presence of a stronger streamwise vortex.

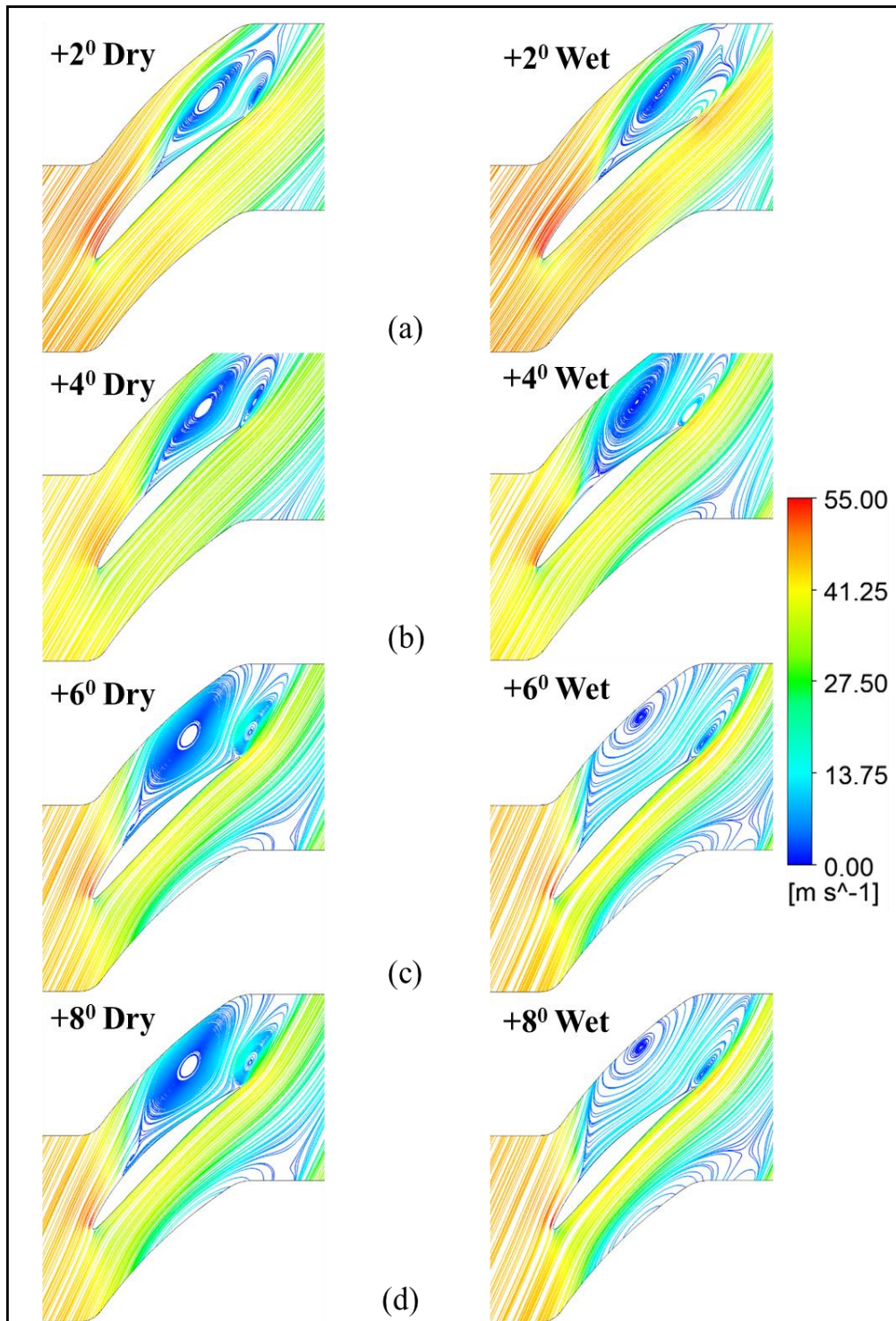


Figure 4.14 Variation of surface streamlines near end wall for different incidence angles(at 4 % of span) (a) +2° (b) +4° (c) +6° (d) 8°

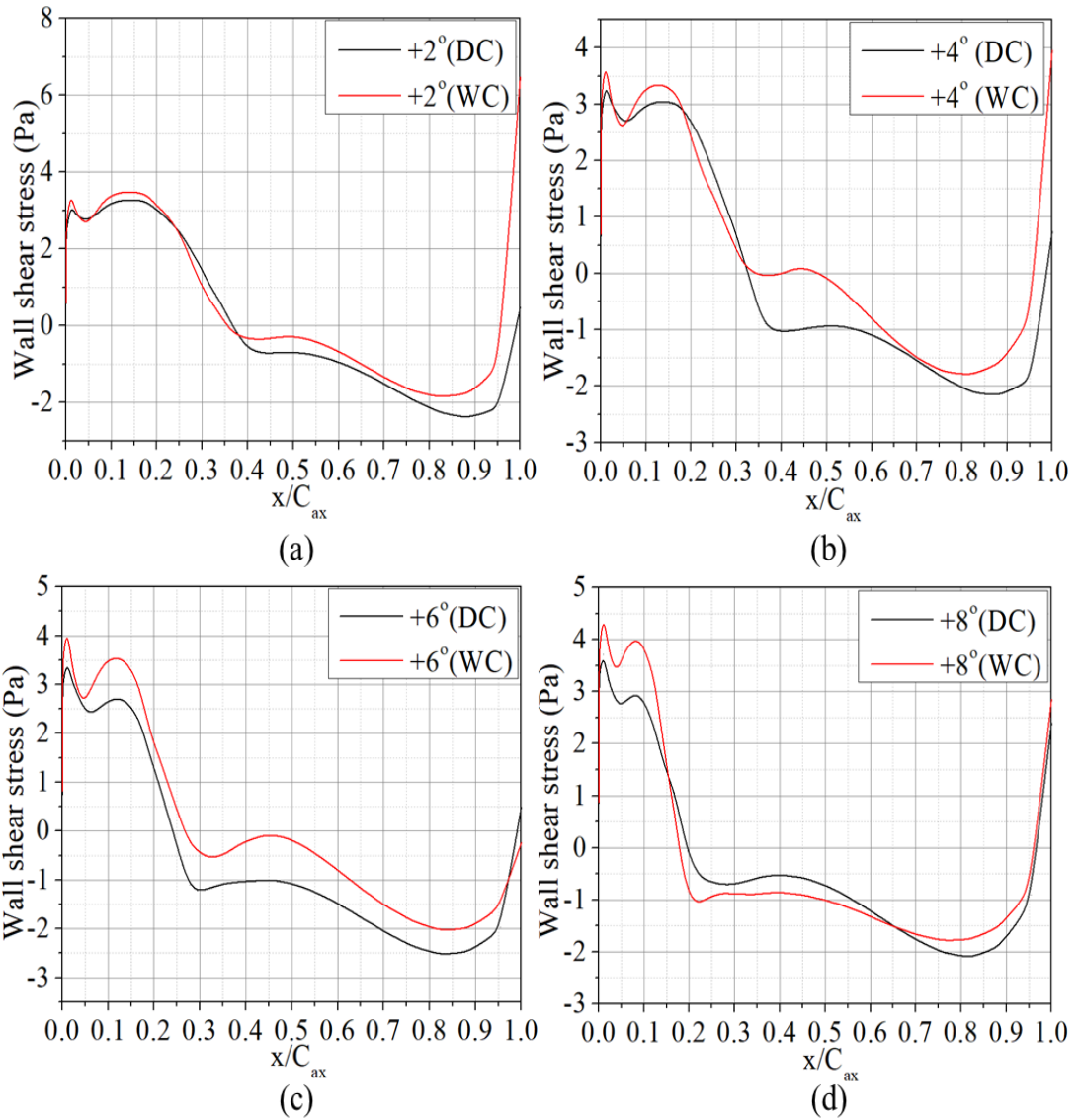


Figure 4.15 Variations of wall shear on the suction surface of the blade near end wall for different incidence angles (at 4 % of the span) (a) $+2^\circ$ (b) $+4^\circ$ (c) $+6^\circ$ (d) 8°

The effect of reattachment is quite evident from the velocity coefficient contours plotted in Figure 4.16 and Figure 4.17. These are plotted at the blade mid-chord ($x/C_{ax} = 0.50$) and near the trailing edge region ($x/C_{ax} = 0.96$). The hub corner vortex is visible in the mid chord region and its strength varies depending upon the incidence angles. The stagnation zone is visible in the blue color contour. Near the trailing edge, the stagnation zone is pushed upwards by the trailing edge vortices to establish a reattachment point in that region.

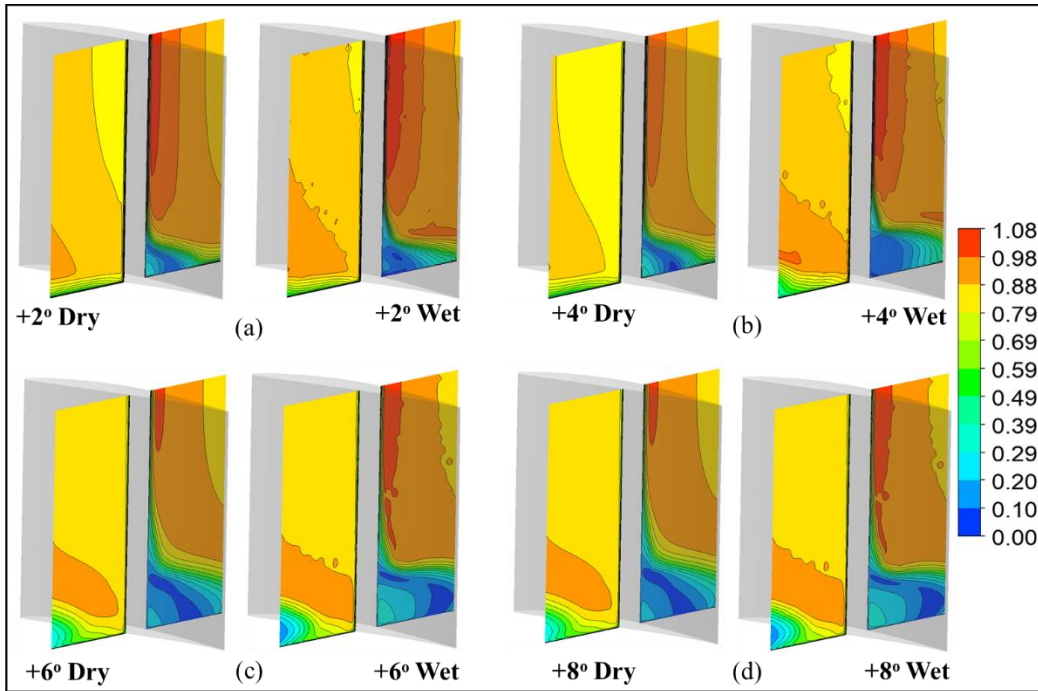


Figure 4.16 Variation of velocity coefficient contour for different incidence angle at $0.50 C_{ax}$ (a) $+2^\circ$ (b) $+4^\circ$ (c) $+6^\circ$ (d) 8°

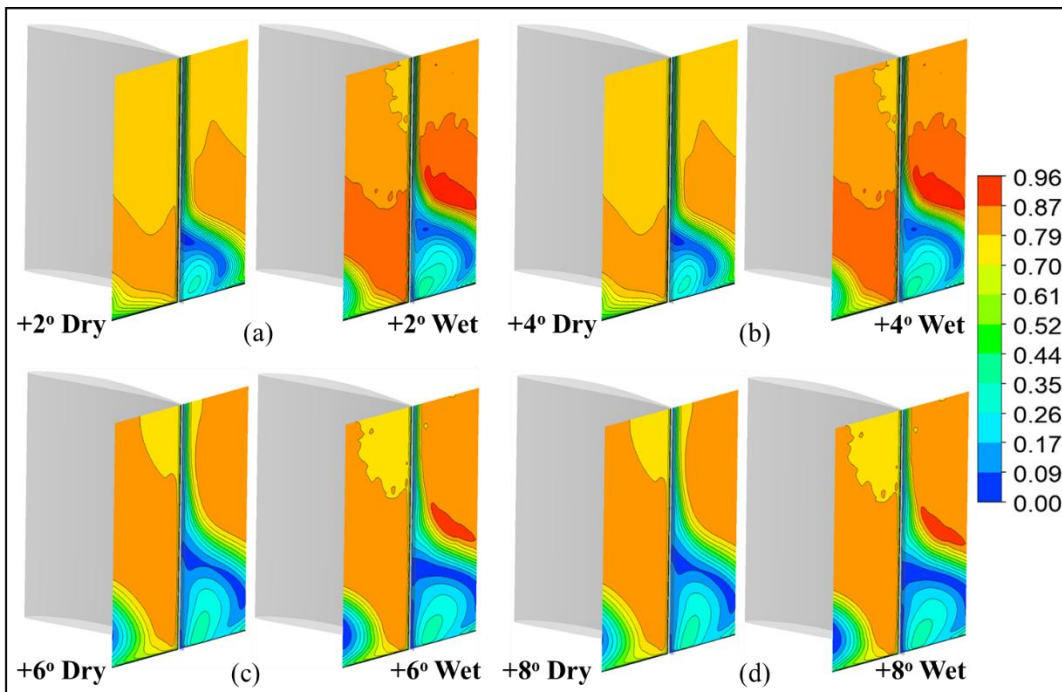


Figure 4.17 Variation of velocity coefficient contour for different incidence angle at $0.96 C_{ax}$ (a) $+2^\circ$ (b) $+4^\circ$ (c) $+6^\circ$ (d) 8°

Furthermore, the lack of smoothness of the contour may be observed in the wet case. This is exaggerated in the trailing edge as compared to the midchord region. Even though it is not significantly observed inside the separated flow region, the contour close to the blade surface on the pressure surface is slightly disturbed. The particle track disrupts the contours in the mean flow area. However, the presence of particle tracks inside the separated flow regime is considerably less, and therefore, the flow is less disturbed in this area. Particle tracks are plotted by giving velocity coefficient as a variable in Figure 4.18. The particle tracks appear to be shifting upwards from the end wall. The upward movement of the tracks can be observed from the separation point ($0.35 C_{ax}$ for 2° and 4° , $0.27 C_{ax}$ at 6° , and $0.17 C_{ax}$ at 8°). Near the trailing edge area, the separated flow regime extends up to 20-30% of the span, and water particle presence in this region is found to be minimal, while it is almost entirely devoid of any particles very close to the end wall.

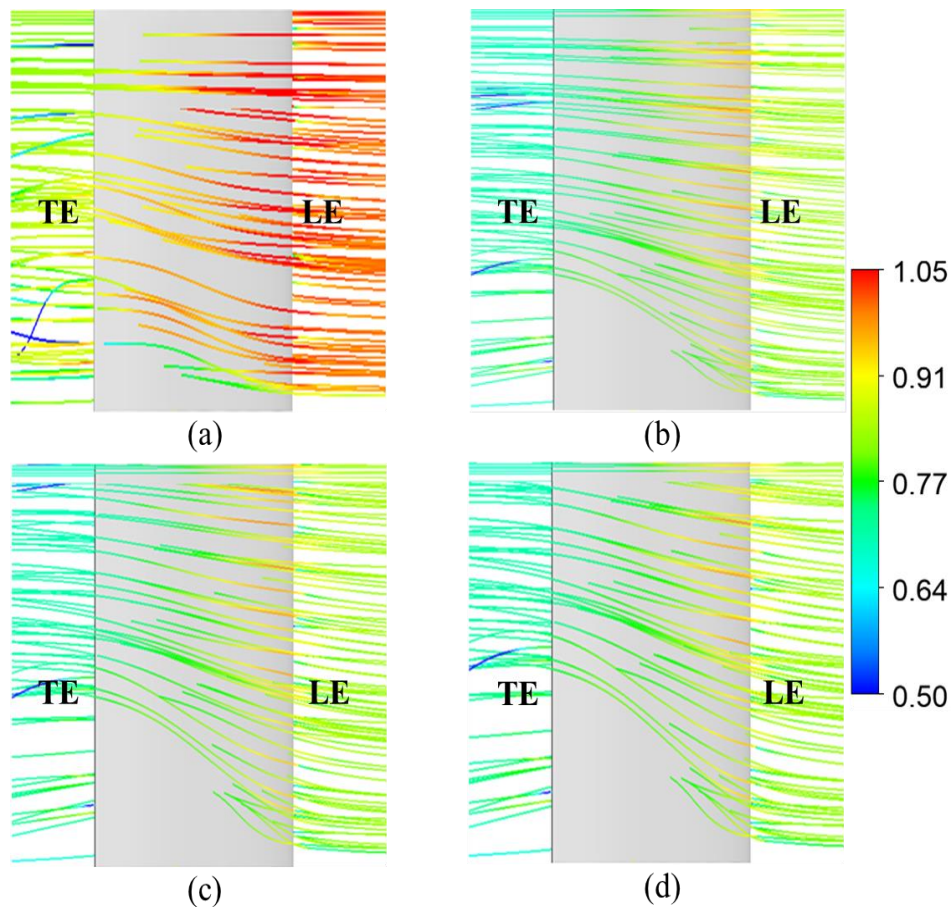


Figure 4.18 Variations of water particle track inside blade the blade passage different incidence angles (a) $+2^\circ$ (b) $+4^\circ$ (c) $+6^\circ$ (d) 8°

4.3.2 Variation of Blade Loading at Positive Incidence Angles

Blade loading is the static pressure coefficient difference between the pressure surface and suction surface). This is one of the most important aerodynamic design parameters in turbomachinery blades, it defines both the amount of work made or extracted, by the blade and the distribution of such work from hub to tip / shroud. Analyzing the blade loading of a given blade is a mandatory step for all design activities, as it gives valuable information on the localized blade performance and shows potential issues which would affect the blade efficiency. Figure 4.19 and Figure 4.20 show the variations of the blade loading at different positive incidence angles near the endwall and midspan region respectively. Figure 4.19 (a) represents the polyline along which the static pressure coefficient is calculated on the blade surface . Some of the general characteristics of the loading curves for all the cases are listed below. These are common for all the cases, observed near the endwall.

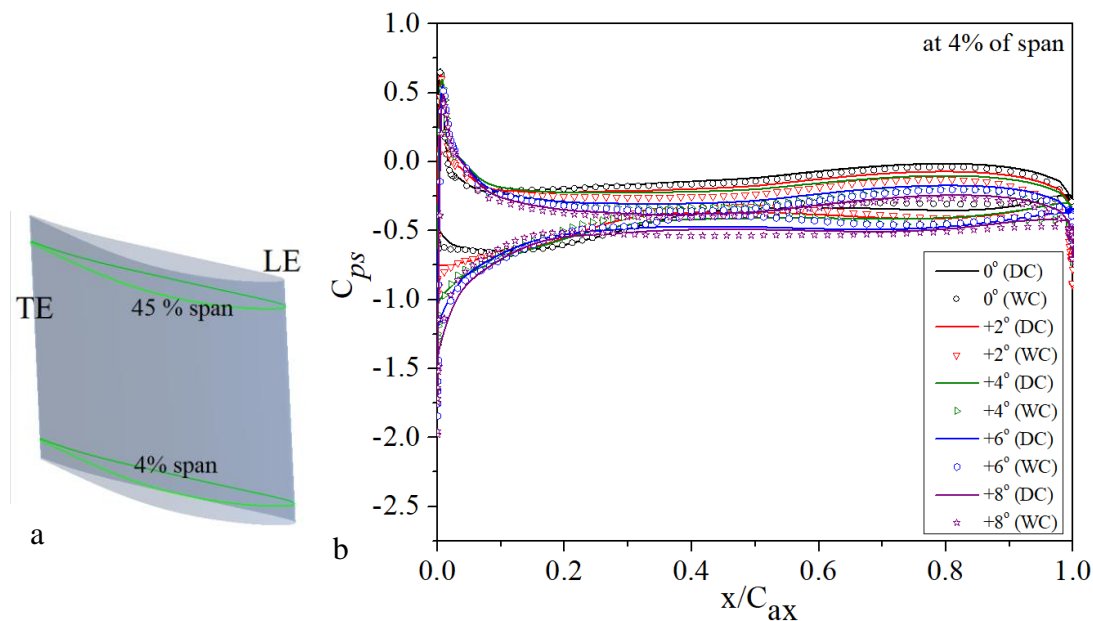


Figure 4.19 (a) Schematic diagram representing the measurements locations
 (b) Variation of static pressure coefficient on the blade surface at 4 % of the span

- Loading is high just after the leading edge, the maximum thickness area of the blade.

- At the mid-chord region, loading is minimum. It again increases at around 80 % chord.
- Close to the trailing edge ($x/C_{ax}=1$) unloading is observed.

Apart from these common characteristics, we need to look for the difference caused by the water droplets. It is observed that in wet cases the loading is marginally lower at the midchord region. Particularly for 4° and 6° cases, the differences between dry and wet cases are quite significant in the mid-chord region.

On the contrary in the midspan region, there is no significant difference between the blade loading for dry and wet cases. With the increase in the incidence angle, there is a steady increase in the blade loading as well. The unloading towards the trailing edge is gradual and smooth for all the cases at this span location.

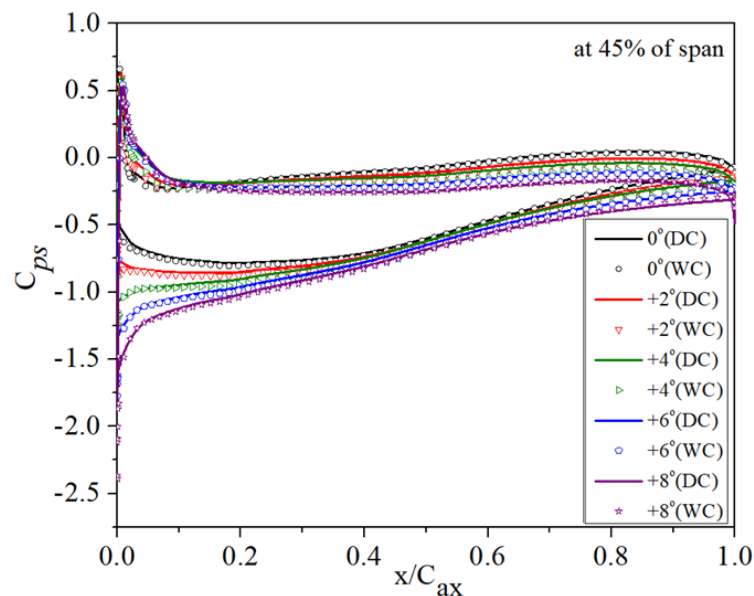


Figure 4.20 Variation of static pressure coefficient on the blade at 45 % of the span

4.4 The behavior of Flow at Negative Incidence Angles

Figure 4.21 displays the velocity vectors close to the endwall for negative incidence angles. When there are water droplets, the flow behavior close to the endwall degrades at lower incidence angles. The mean flow tilts more in favor of the top suction surface

as the incidence turns more negative. At higher negative incidence angles (-6° and -8°), the divided flow regime which has been seen at lower negative incidence angles (-2° and -4°) is absent. The wall shear stress variation (Figure 4.22) displays an early flow separation for wet cases at -2° and -4° incidence angles. The flow separation is taking place only after the flow passes the mid chord region in the case of -2° incidence. The flow separation starts at only $0.75 C_{ax}$ in the -2° dry case.

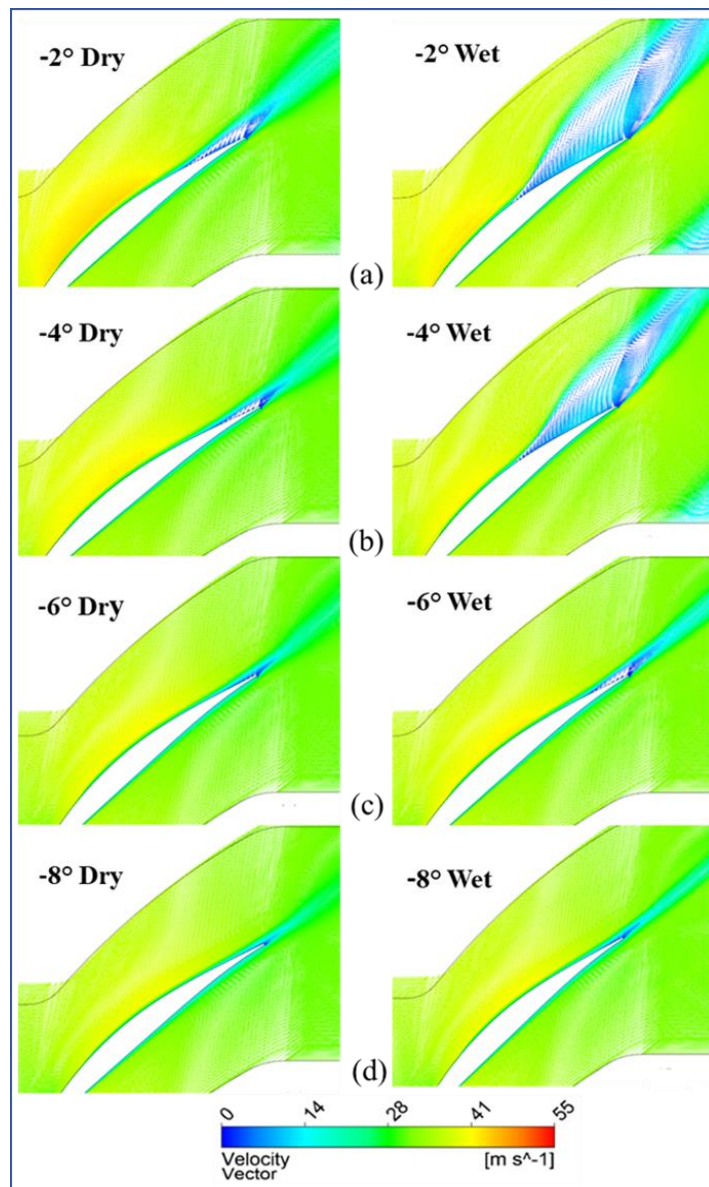


Figure 4.21 Variation of velocity vector near end wall at different negative incidence angles (a) -2° (b) -4° (c) -6° (d) -8°

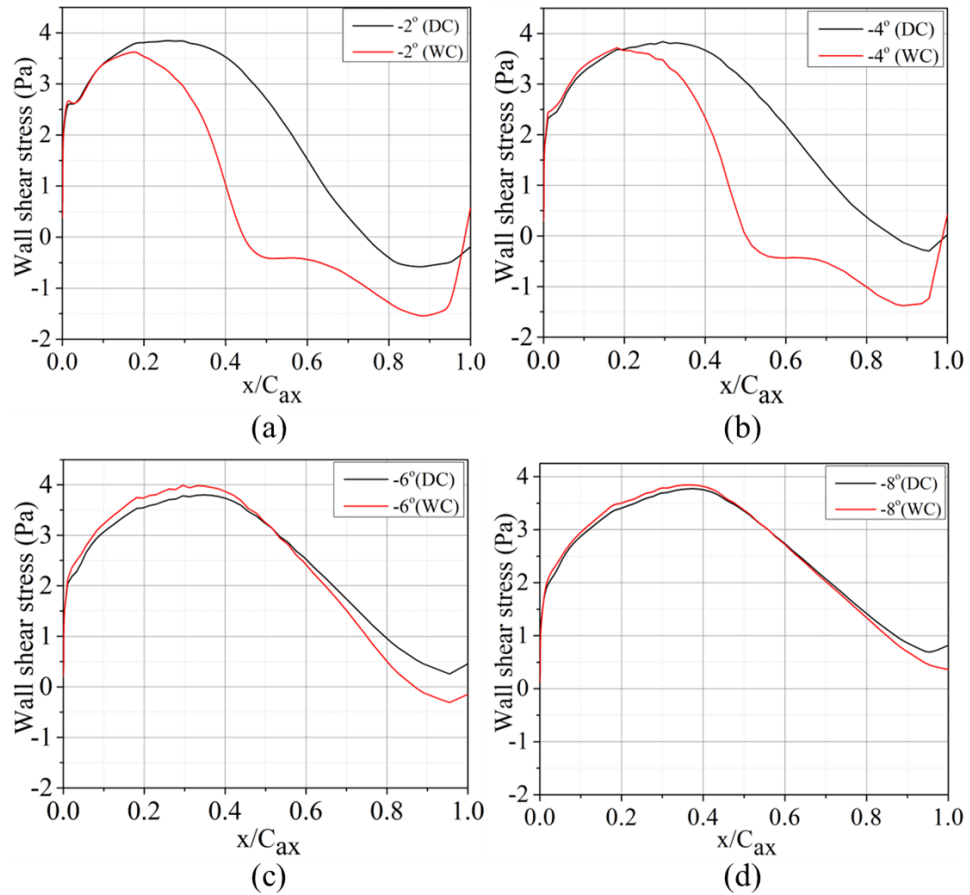


Figure 4.22 Variations of wall shear on the suction surface of the blade near end wall (at 4 % of the span) (a) at -2° (b) at -4° (c) at -6° (d) at -8°

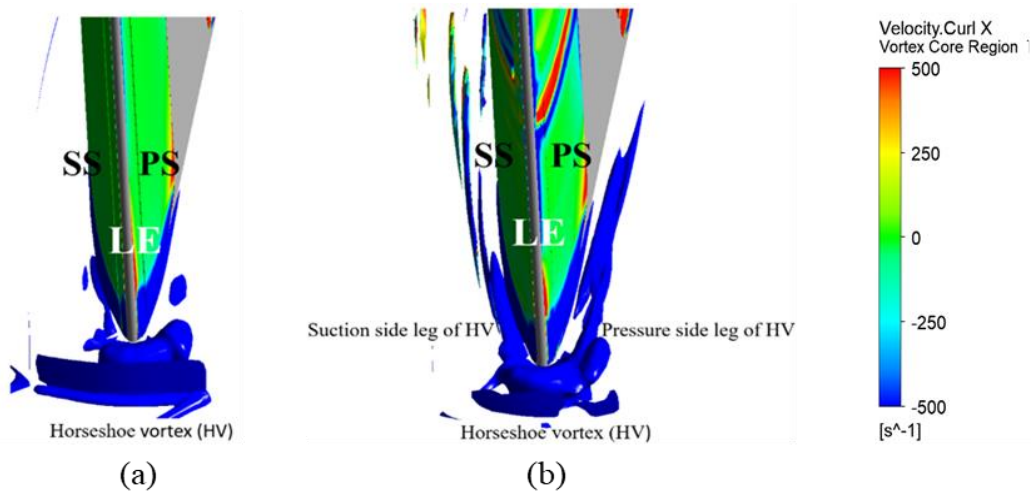


Figure 4.23 Variation of Q-criteria plotted near the leading edge region (a) Dry case (b) Wet case

The intensity of the horseshoe vortex and its propagation on the pressure side and suction side of the blade as the pressure side leg and suction leg of the horseshoe vortex

is found to be minimum in the dry case. On the other hand in the -2° wet case, the intensity of this vortex is more, the strength of the suction and pressure side leg is higher. This extension of the suction side leg of the horseshoe vortex may lead to earlier flow separation in the wet case. This is shown in the Q-criteria plot in Figure 4.23.

Limiting streamlines are plotted on the end wall and blade suction surface (Figure 4.24). The saddle point S3 is located at $0.512 C_{ax}$, $0.549 C_{ax}$, $0.630 C_{ax}$, and $0.657 C_{ax}$ for the -2° , -4° , -6° , and -8° incidence angles respectively in the dry case. In the wet case, the saddle point S3 is moved towards the leading edge direction by $0.28 C_{ax}$, $0.255 C_{ax}$, $0.179 C_{ax}$, and $0.145 C_{ax}$ at the incidence angle -2° , -4° , -6° , and -8° respectively (at -2° wet case S3 is located at $0.232 C_{ax}$, at -4° wet case, S3 is located at $0.294 C_{ax}$, at -6° wet case, S3 is located at $0.451 C_{ax}$, at -8° wet case, S3 is located at $0.512 C_{ax}$). Interesting results are observed while following the locations of the saddle point S3 in the wet case corresponding to these incidence angles. The deviation in the location of S3 in the dry case and the wet case is getting reduced when the incidence angle becomes more negative.

The dividing streamlines from the saddle point S3 on the surface are extended on the suction surface near the trailing edge region up to 7.91 %, 26.66 % of the blade height, and the streamline spirals into a vortex of focal point F3 at 5.8 %, 16.35 % in the dry case and wet case respectively at -2° incidence. When the angle of incidence increases from -2° to -8° , the dividing streamline in the flow separation regime does not spiral into a vortex F3 in the dry case, but it happens with the wet cases. The F3 is located at 7.797 %, and 4.54 % of the blade height at -4° and -6° incidence angles respectively. The separated flow region at the trailing edge is decreased by 2.1 % when the incidence angle varies from -2° to -4° in the dry case. On the other hand in the wet case, when the negative angle of incidence increases from -2° to -4° , the flow separation is reduced significantly by an amount of 13.83 % (the extent of flow separation at the -4° incidence angle is 12.83 % of the blade height). The forming of the vortex at the end wall by the springing of the dividing streamline from the saddle point S3 is not found in the dry case at all negative incidence angles. However, in the wet case, the vortex is visible on the end wall at all incidence angles except -8° .

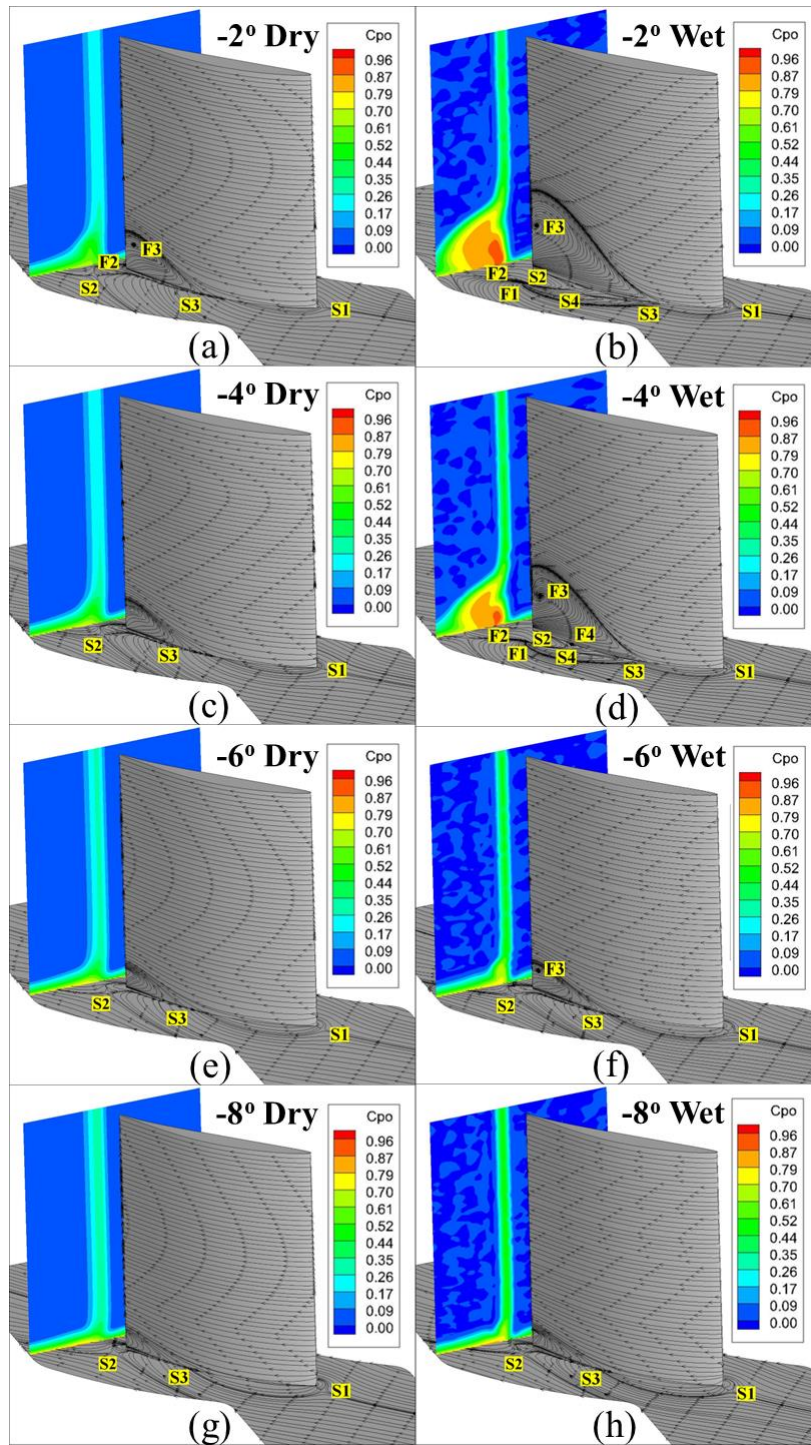


Figure 4.24 Limiting streamlines on the blade suction surface and end wall superimposed with total pressure loss coefficient at 1.1 C_{ax} at different incidence angles (a) -2° (b) -4° (c) -6° (d) -8°

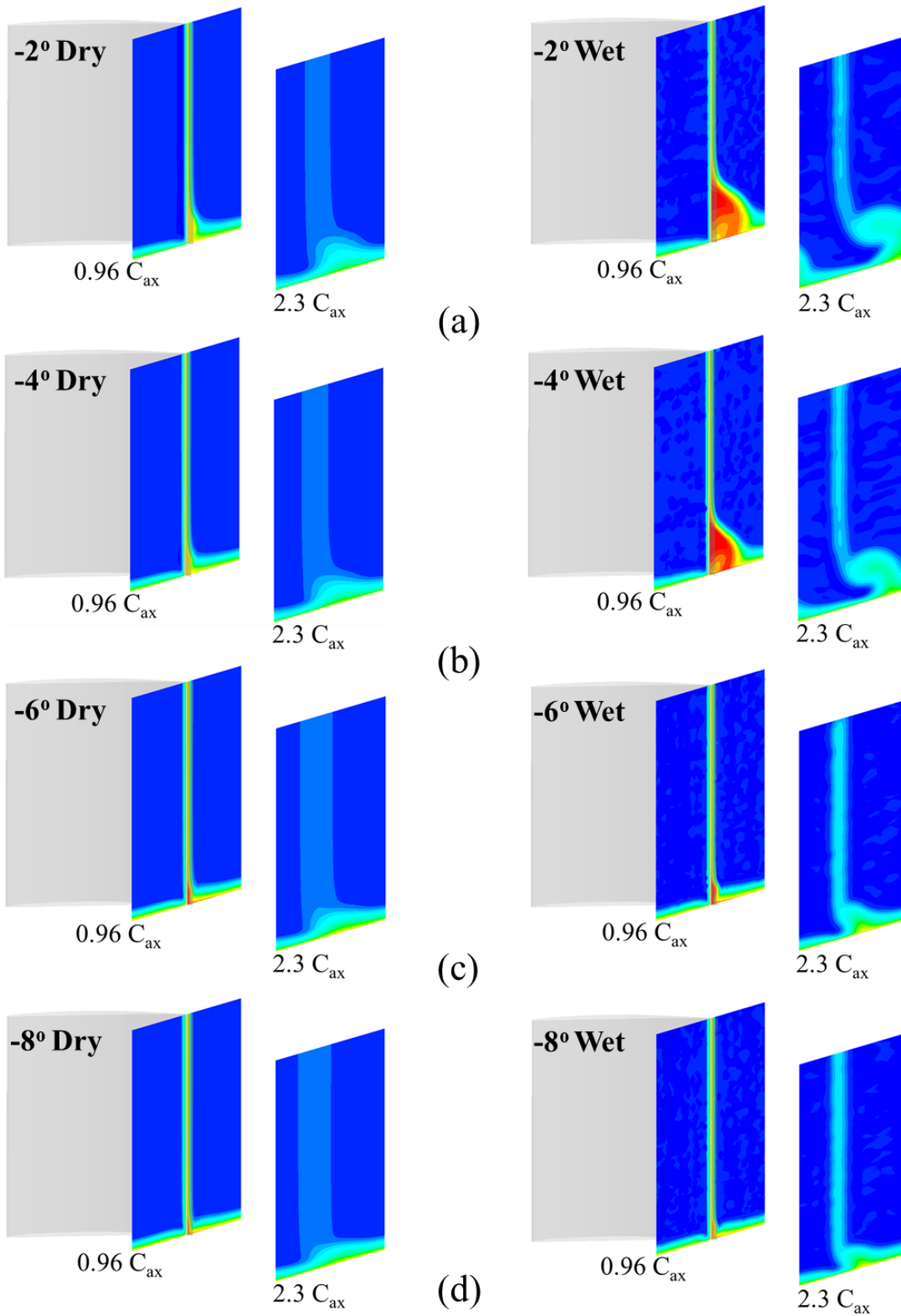


Figure 4.25 Variation of total pressure loss coefficient at $0.96 C_{ax}$ and $2.3 C_{ax}$

For dry and wet instances with negative incidence angles, Figure 4.25 illustrates the

fluctuation of the total pressure loss coefficient at $0.96 C_{ax}$ and $2.3 C_{ax}$ (The mass averaged total pressure loss coefficient at $2.3 C_{ax}$ is, 0.0477, 0.0484 for the dry case and wet case respectively). At -2° incidence, the addition of water droplets reduces the total pressure loss coefficient at the $0.96 C_{ax}$ of the blade in the dry case by 17.09 %; however, as the flow moves further downstream, this difference in the total pressure loss coefficient decreases, and instead of reducing total pressure loss in the wet case, the total pressure loss coefficient increase by 1.56 %.

The total pressure loss coefficient at the $0.96 C_{ax}$ of the blade in the dry case is decreased by 19.38 %, 31.80 %, and 33.57 % by the effect of injection of water droplets for -4° , -6° and -8° incidence angles respectively. At -4° incidence when the flow is moving towards the outlet, the difference in the total pressure loss coefficient between the dry case and wet case is further reduced. It is evident from the difference in the total pressure loss coefficient at $2.3 C_{ax}$. At $2.3 C_{ax}$, the total pressure loss coefficient in the dry case is reduced by 2.76 %. A smaller difference in the total pressure loss coefficient at $2.3 C_{ax}$ compared to the location of $0.96 C_{ax}$ implies that after the trailing edge location, the total pressure loss is getting increased for the wet case (Figure 4.25). This increment in the total pressure loss is caused by the influence of axial propagation of end wall vortex F1, present in the wet case. In the case of incidence angles -6° and -8° , the total pressure loss coefficient is decreased by 31.80 %, 33.57 % at $0.96 C_{ax}$, and reduced by 28.25 %, 30.27 % at $2.3 C_{ax}$ respectively. This means the total pressure loss of wet cases at -6° and -8° incidences is not increased as in the cases of -2° and -4° incidences.

4.4.1 Variation of Blade Loading at Negative Incidence Angles

Figure 4.26 shows the variations in blade loading at different negative incidences near the endwall at 4 % of the span. At lower negative incidence angles the loading is small and it behaves similar to the positive incidence angles. However, at higher negative incidence angles there is a reversal of loading near the leading edge and the loading starts after 10 % of the chord. There is no significant difference in the loading between the wet and dry cases. Near the midspan location also, there is no significant difference between the wet and dry cases and the pattern of loading is similar. At midspan also,

there exists a reversal of loading at the beginning and the loading starts gradually at a later stage (Figure 4.27).

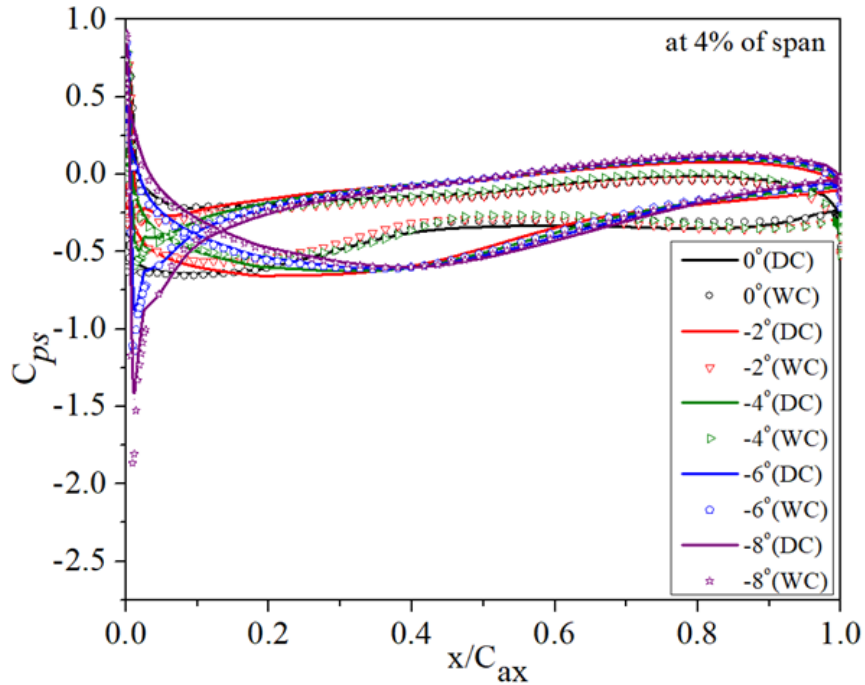


Figure 4.26 Variation of static pressure coefficient on the blade at 4 % of the span

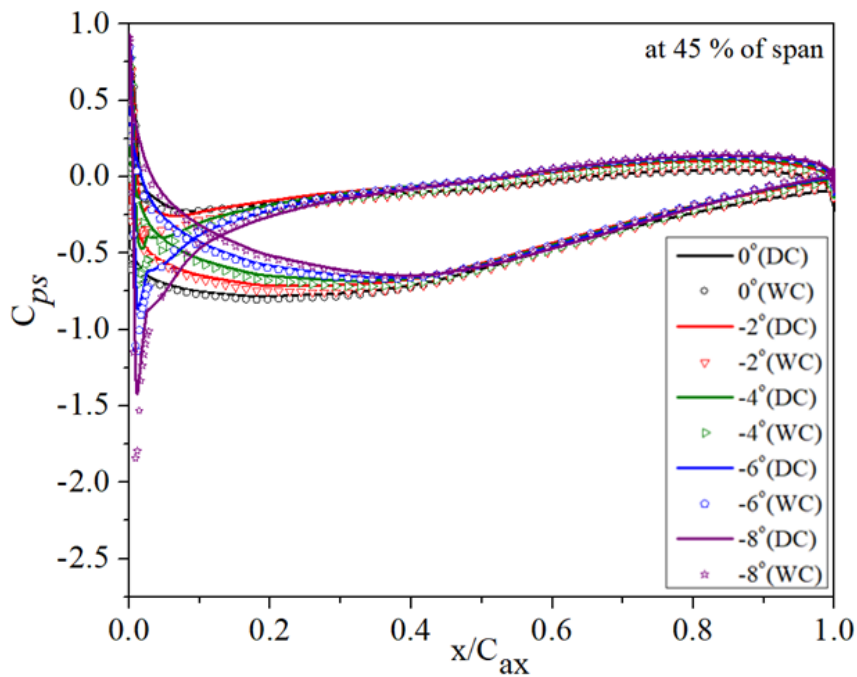


Figure 4.27 Variation of static pressure coefficient on the blade at 45 % of the span

4.5 Summary

The findings of the incidence angle are summarized in Table 4.1 and Table 4.2. The tables indicate that the water injection is highly beneficial at positive incidence angle as far as the corner separation is considered (Table 4.1). The total pressure loss coefficient comes down with the introduction of water droplets. This reduction is prominent at higher incidence angle (Table 4.2).

Table 4.1 Variation of flow separation at different incidence angles

SL No.	i	Location of S3 (x/C_{ax})		Spanwise extension of the corner of separation near the trailing edge (%)	
		DC	WC	DC	WC
1	-8°	0.657	0.512	3.64	3.5
2	-6°	0.630	0.451	4.72	5.4
3	-4°	0.549	0.294	5.81	12.83
4	-2°	0.512	0.232	7.91	26.66
5	0°	0.23	0.18	16.0	19.30
6	2°	0.16	0.11	17.43	22.83
7	4°	0.11	0.048	21.75	25.27
8	6°	0.076	0.062	24.72	29.86
9	8°	0.017	0.0061	34.45	29.32

Table 4.2 Variation in the mass flow averaged total pressure loss coefficient

Sl No	i	Mass averaged total pressure loss coefficient at $0.96 C_{ax}$			Mass averaged total pressure loss coefficient at $2.3 C_{ax}$		
		DC	WC	% Reduction	DC	WC	% Reduction
1	-8°	0.0468	0.0311	33.57	0.0535	0.0373	30.27
2	-6°	0.0429	0.0292	31.80	0.0496	0.0356	28.25
3	-4°	0.0407	0.0328	19.39	0.0476	0.0463	2.76
4	-2°	0.0401	0.0333	17.09	0.0477	0.0484	-1.56
5	0°	0.0462	0.0323	29.95	0.0611	0.0410	32.78
6	2°	0.0519	0.0373	28.04	0.0751	0.0614	18.17
7	4°	0.0577	0.0419	27.39	0.0816	0.0725	11.08
8	6°	0.0687	0.0457	33.40	0.108	0.0737	32.25
9	8°	0.0782	0.0562	28.20	0.112	0.102	9.65

CHAPTER 5

FLOW ANALYSIS IN COMPRESSOR CASCADE AT VARIOUS DROPLET SIZES AND INJECTION RATIOS

5.1 Effects of Droplet Size

Droplet size is one of the most critical factors in wet compression in a multistage compressor. The present investigation addresses the influence of droplet size on compressor aerodynamics. Simulations have been carried out at five Sauter mean droplet sizes in a range of $D_d = 12 \mu\text{m}$ - $60 \mu\text{m}$. The influence of the droplet diameters on the flow parameters and the loss coefficient is studied in detail. All the analyses are carried out at a standard incidence angle of $+6^\circ$ and a 1 % injection ratio.

5.1.1 The flow deviation at the leading edge

Since two-way coupling is employed in the present simulations, the influence of droplet particles on the continuous media is considered. It is observed that the introduction of water droplets alters the axial velocity of mainstream flow. This leads to deviations in the incidence angle at the inlet. As a result, the pressure distribution over the blade is altered. Similar observations are also made by Utamura et al. The flow deviation angle near the leading edge upstream is shown in Figure 5.1. The flow angle deviation at the inlet is calculated by subtracting the flow angle measured at the inlet from the given incidence angle ($+6^\circ$). A zero deviation angle implies that the actual incidence angle at the leading edge is 6° . It is to be noted that, for the flow angle calculation, only axial and streamwise velocities are considered.

Figure 5.1 shows that near the leading edge, the deviation angle is negative, whereas, in the mid-span region, the deviation angle is positive. The flow angle deviation is higher in the case of smaller droplet sizes ($12 \mu\text{m}$) and larger droplet sizes ($48 \mu\text{m}$ and $60 \mu\text{m}$). The deviation is found to be minimum at $20 \mu\text{m}$ and $30 \mu\text{m}$. It is observed that there exists a deviation angle for the dry case as well. This deviation is caused by the secondary flows in the blade passage. The deviation angle is obtained just before the

leading edge. Near the endwall of the leading edge, the flow is under the influence of the horseshoe vortex. The negative deviation is attributed to this phenomenon. The deviation near the midspan is due to the blockage that is created inside the blade passage.

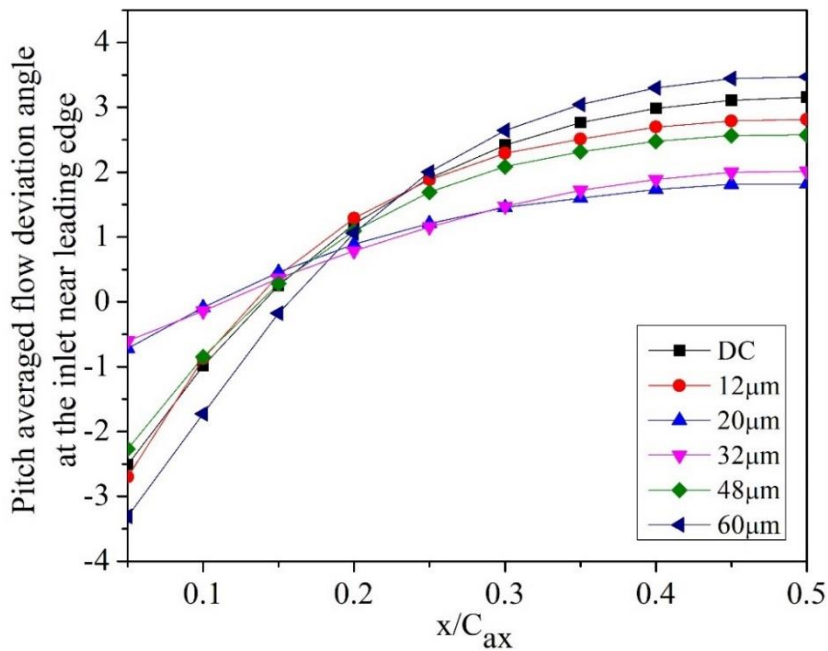


Figure 5.1 Variation in flow deviation angle at the inlet section near leading edge for different droplet sizes

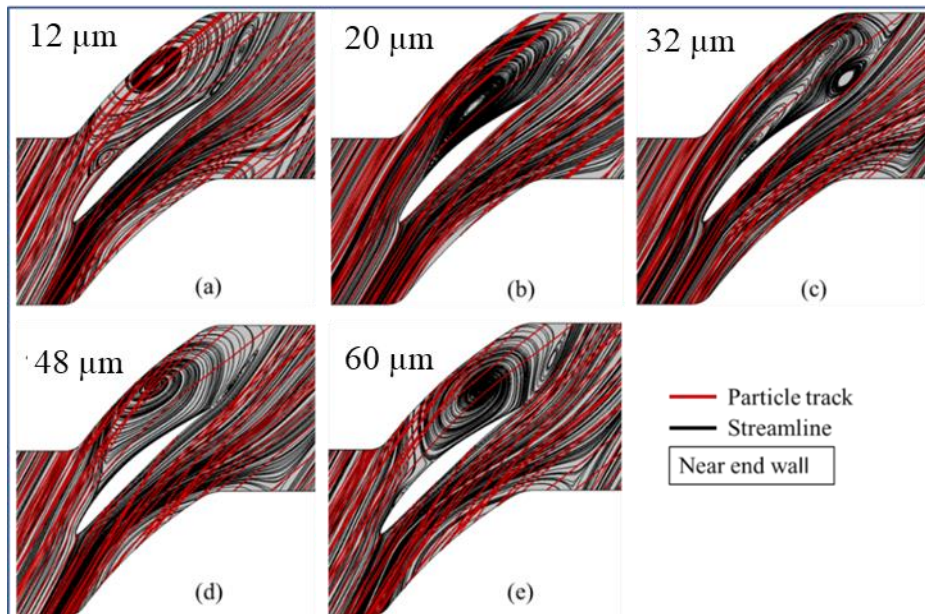


Figure 5.2 Variation of particle track superimposed with surface streamline in the case of different droplet sizes near endwall

The interaction of the droplets with the air is different for tiny and very large droplets. Depending upon the droplet size, the number of droplets may vary in each case (as the injection ratio is the same). The number of droplets for a fixed mass would be large for smaller droplets. They are scattered evenly with continuous fluid, and many droplets ensure more interaction with the fluid. On the other hand, larger droplets would be smaller in number, but they carry higher momentum. Additionally, larger droplets would encounter higher drag force also.

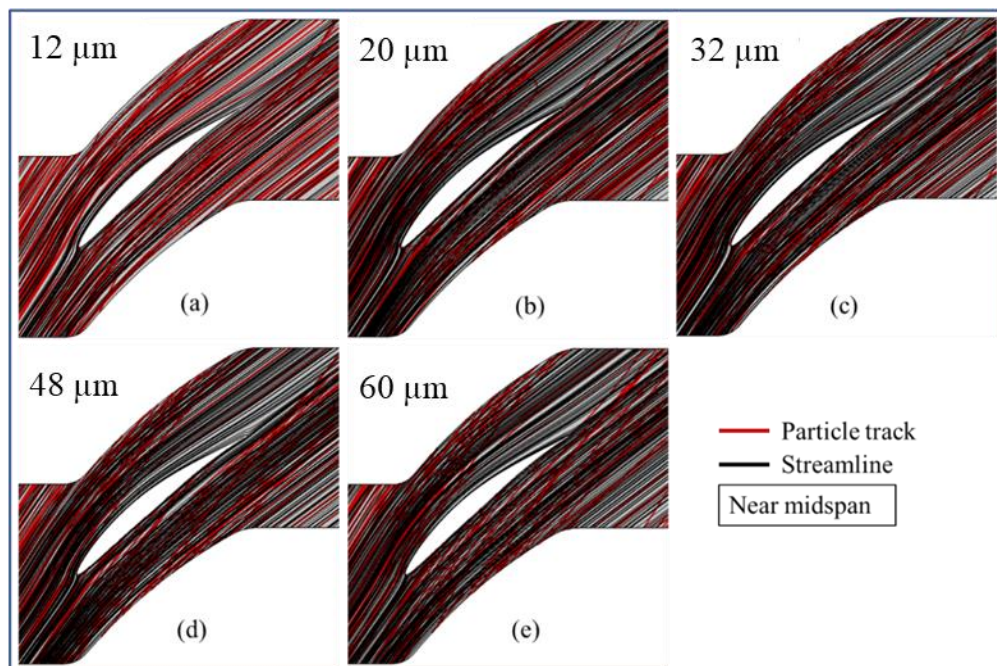


Figure 5.3 Variation of particle track superimposed with surface streamline in the case of different droplet sizes near midspan

Figure 5.2 and Figure 5.3 shows the surface streamlines (black lines) near the endwall and the midspan location respectively. Over to this, 3D particle tracks are superimposed to understand the trajectory of the droplets. At the midspan location, the particle tracks and the streamlines are aligned for smaller droplet sizes. As the droplet diameter increases the particle tracks are deviating from the streamlines. Smaller droplets follow the streamline path as they are carried away by air due to their lightweight. Due to the larger mass bigger droplet does not follow the streamlines faithfully. The higher momentum of the bigger droplets causes the deviation from the continuous phase. The

interaction of the larger droplets influences the airflow and this causes variation in the incidence angles.

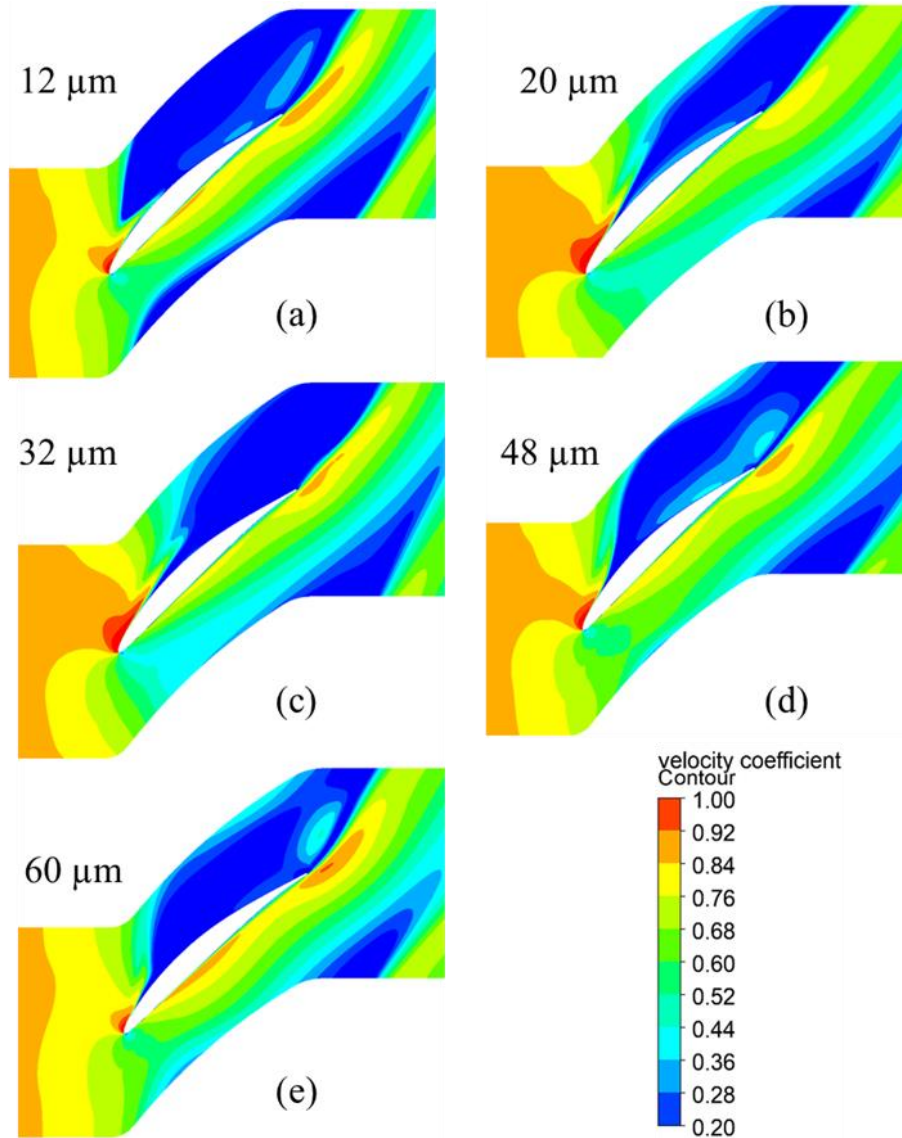


Figure 5.4 Velocity coefficient contour plotted at 1 % of span for different droplet sizes (a) 12 μm (b) 20 μm (c) 32 μm (d) 48 μm (e) 60 μm

The velocity coefficient contours near the endwall are shown in Figure 5.4. It shows that for 20 μm and 30 μm the flow separation from the suction surface is smaller compared to other cases. The flow is leaning more towards the pressure surface in these two cases. This leaning results in increased acceleration just after the leading edge on the suction surface. The increased acceleration on the suction surface delays the flow

separation near the endwall. For smaller droplet sizes (12 μm) and larger droplet sizes (48 μm and 60 μm), the deviations are high near the endwall, resulting in a lower leading edge acceleration.

5.1.2 Static pressure on the blade surface

Figure 5.5 and Figure 5.6 depicts the static pressure coefficient distribution on the pressure surface and suction surface for various water droplet sizes. On the pressure surface, the effects of droplet size are mostly discernible close to the endwall area. The static pressure distribution is homogeneous across the blade pressure surface at a droplet size of 32 μm . As the droplet size exceeds this diameter, the pressure distribution becomes uneven. A low-pressure region is observed near the endwall and grows bigger with the droplet size. The suction surface has a lower static pressure region ($C_{ps} = -0.950$) near the leading edge. This region corresponds to the acceleration region observed in the velocity coefficient contours. Near the midspan region, the pressure rise is uniform from the leading edge to the trailing edge. This can be concluded from the vertical contour lines near the midspan region. Near the endwall, the contours are in the form of islands, indicating a separated flow region.

In addition to the global view, the distributions of static pressure at two locations on the blade are plotted. This forms the blade loading and is shown in Figure 5.7 and Figure 5.8. The first location is at mid-span ($z/h = 50\%$); the second one is near the endwall ($z/h=5\%$). With the difference in the droplet diameter, variations in the blade loadings are observed near the leading and trailing edge. The trailing edge region is enlarged and shown in the inset. There is an unloading of the blade near the trailing edge. At this point, the loadings on the pressure and suction surface get reversed. The point of unloading slightly advances with the wet cases. After the unloading, the pressure on the pressure surface sharply decreases for the dry case. This causes enhanced trailing edge vortices. In the wet cases, the droplet diameter of 20 μm and 32 μm exhibits the lowest pressure difference after the unloading point; hence, these two cases exhibit the lowest pressure loss coefficient.

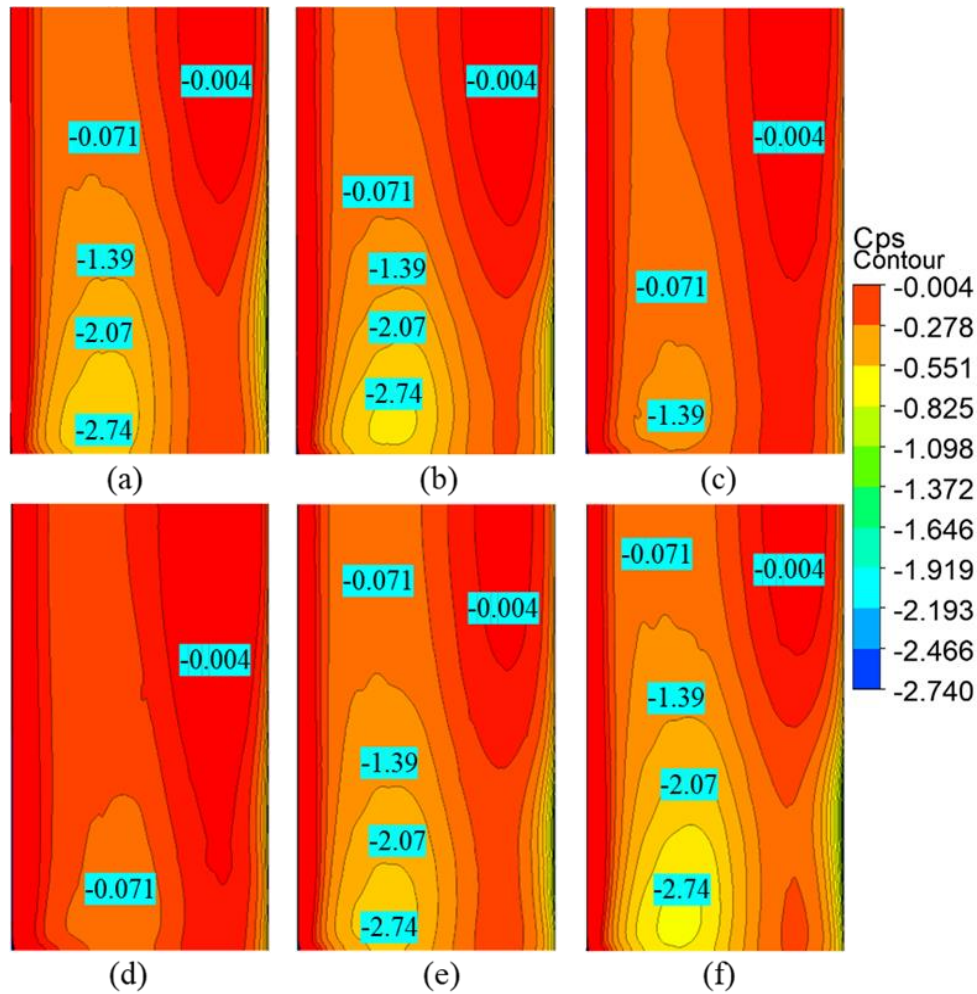


Figure 5.5 Static pressure distribution contour on the pressure surface of the blade
(a) DC (b) 12 μm (c) 20 μm (d) 32 μm (e) 48 μm (f) 60 μm

The separation point moves upstream near the endwall, which is reflected in the blade loading. Blade loading (the static pressure difference between the suction side and the pressure of the blade) is reduced near the endwall. With larger droplet sizes, loading reduces. A strong inclination of the C_{ps} isoline is observed in the dry case, and wet cases with larger droplet sizes of 48 μm and 60 μm . This is the immediate result of the blocking effect brought on by corner separation, which causes the flow to curve up to the leading edge (Barrio et al. 1982). However, in the wet cases with 12 μm to 32 μm droplet diameter, this strong inclination is getting reduced, and the inclination is minimum for the droplet size of 32 μm . It implies that corner separation is lowest with 32 μm droplet size among all these droplet sizes. Similar to the midspan area, changes can be seen near the trailing edge region's unloading point.

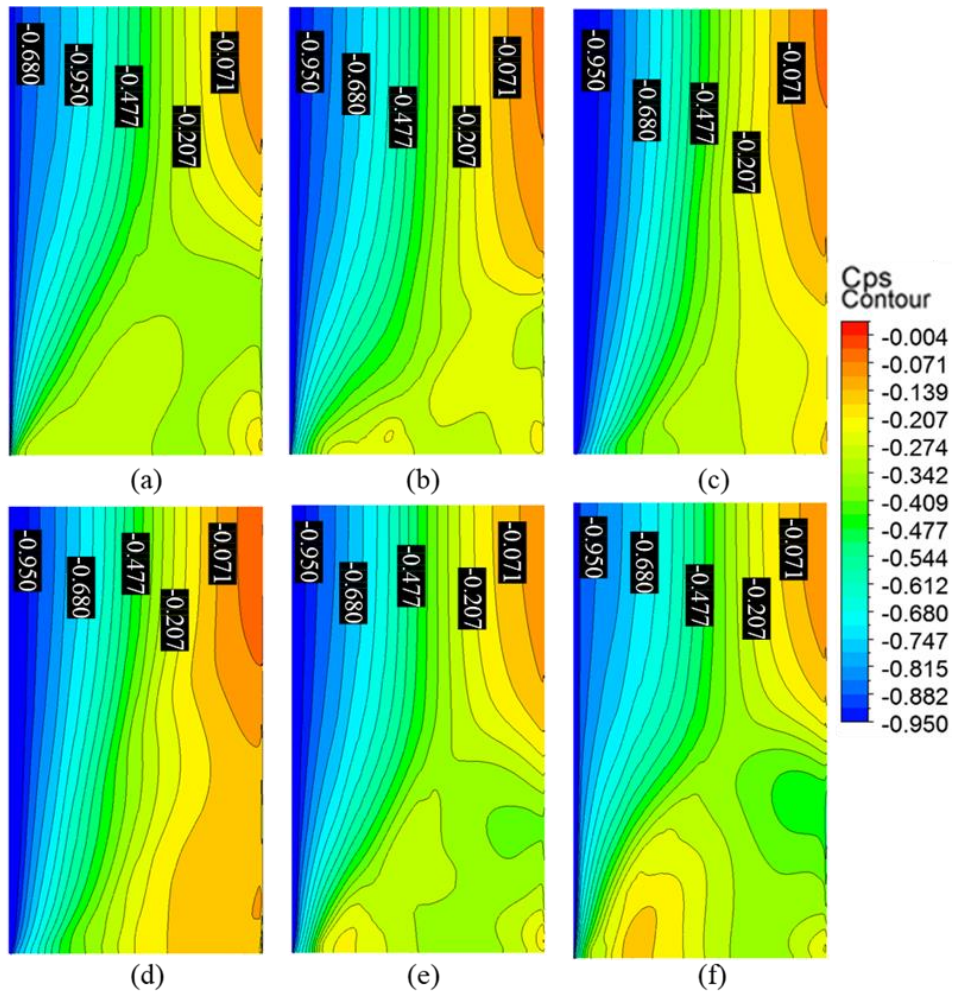


Figure 5.6 Static pressure distribution contour on the suction surface of the blade (a) DC (b) 12 μm (c) 20 μm (d) 32 μm (e) 48 μm (f) 60 μm

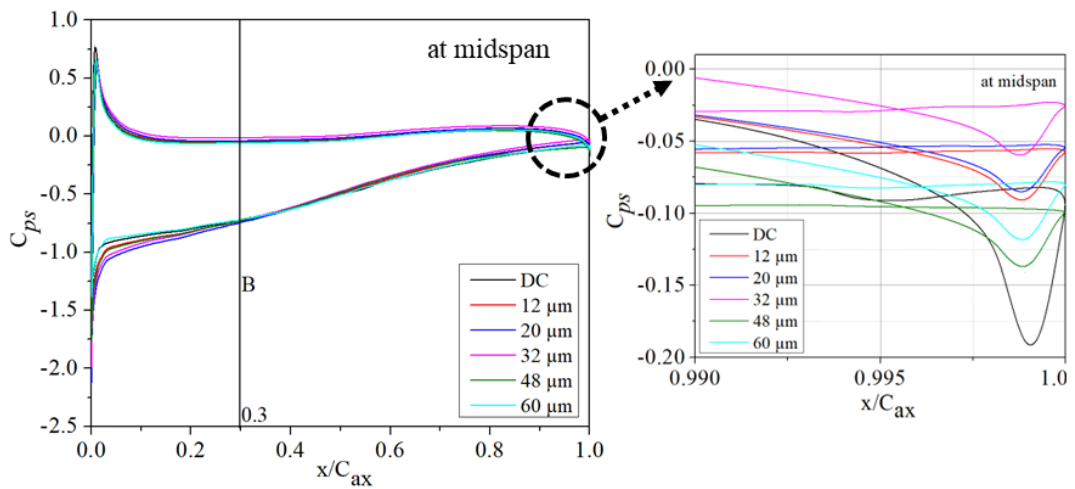


Figure 5.7 Blade loading on the blade at midspan for dry case and wet case at different droplet size

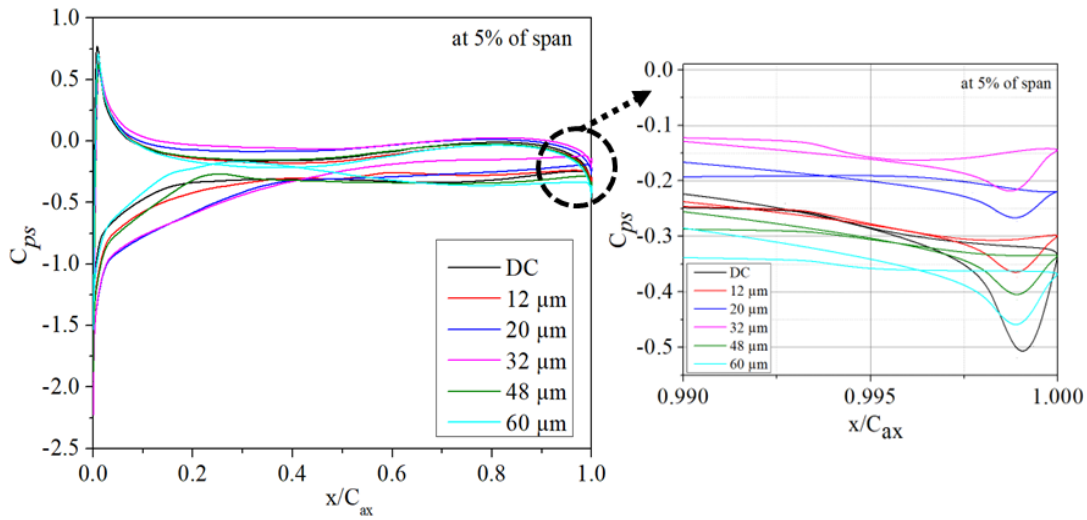


Figure 5.8 Static pressure distribution on the blade near end wall for dry case and wet case at different droplet size

5.1.3 Influence of droplet size on the loss coefficient

The mass averaged total pressure loss coefficient is plotted along the axial direction from the leading edge to downstream location $1.45 C_{ax}$ (Figure 5.9). For comparison purposes, dry case (DC) simulation is also included in the graph.

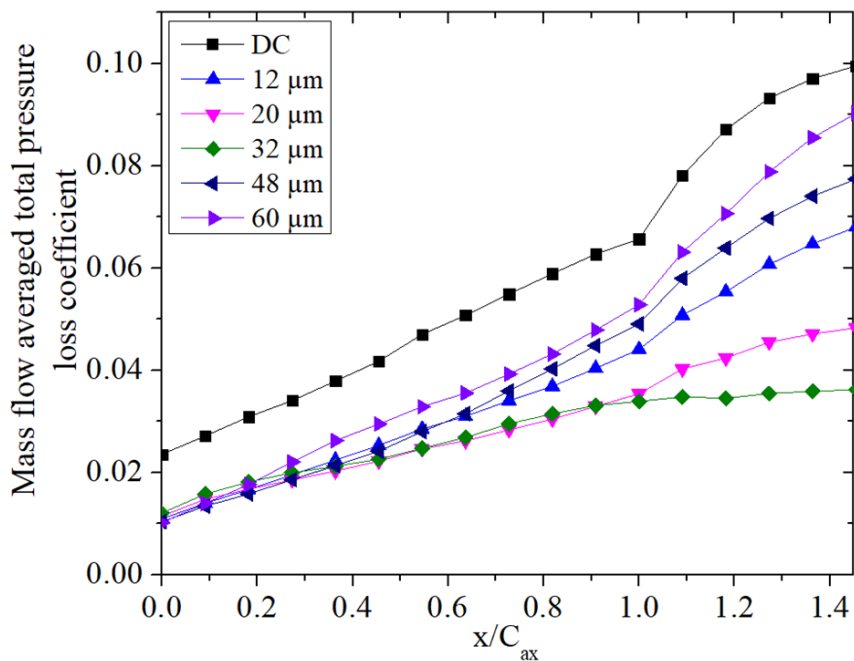


Figure 5.9 Mass flow averaged total pressure loss coefficient (a) 12 μm (b) 20 μm (c) 32 μm (d) 48 μm (e) 60 μm

As the droplet size increases the loss coefficient also increases. This does not imply that a very small droplet would give the smallest losses. The graph indicates that there is an optimum droplet size for keeping the losses minimum. The total pressure loss coefficient is observed minimum in the blade passage and downstream location for 20 μm and 32 μm and is higher for the rest of the droplet sizes. This variation is in accordance with the flow deviation and velocity variation observed in the previous Figures.

5.1.4 Total pressure losses at the downstream of trailing edge

Figure 5.10 shows the total pressure loss coefficient at the downstream side of the domain (at 1.1 C_{ax}). These are displayed immediately following the blade's passage. The flow from the trailing edge close to the endwall region is represented by the red area. The losses are high in this region due to the trailing edge and corner vortices. The losses are minimum in the droplet diameter range of 20 – 32 μm , indicating the presence of optimum droplet diameter within this range. The mass averaged total pressure loss at this plane is calculated and plotted as a bar diagram (Figure 5.11).

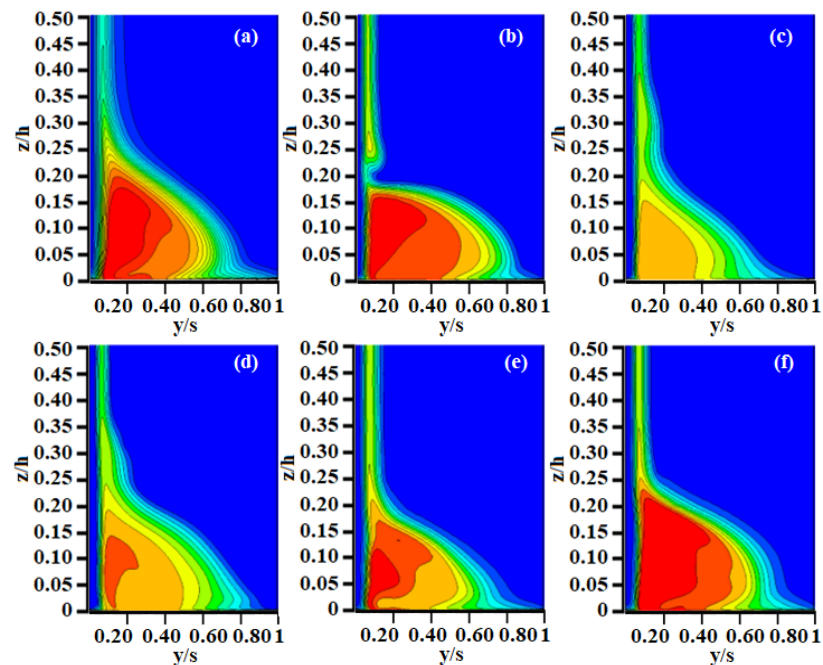


Figure 5.10 Total pressure losses coefficient distributions at downstream section 1 for dry case and all droplet sizes (a) DC (b) 12 μm (c) 20 μm (d) 32 μm (e) 48 μm (f) 60 μm

The percentage reduction in the loss coefficient for the 12 μm case from the dry case is 35 %. The mass flow averaged total pressure loss is reduced by 13 % when droplet diameter is changed from 12 to 20 μm and the loss is further reduced by 6 % at 32 μm . Compared with the dry case, the reduction in the losses with a droplet size of 32 μm is 54 %. However, injection of the water droplet at larger droplet sizes, (48 μm and 60 μm) lead to a higher loss coefficient.

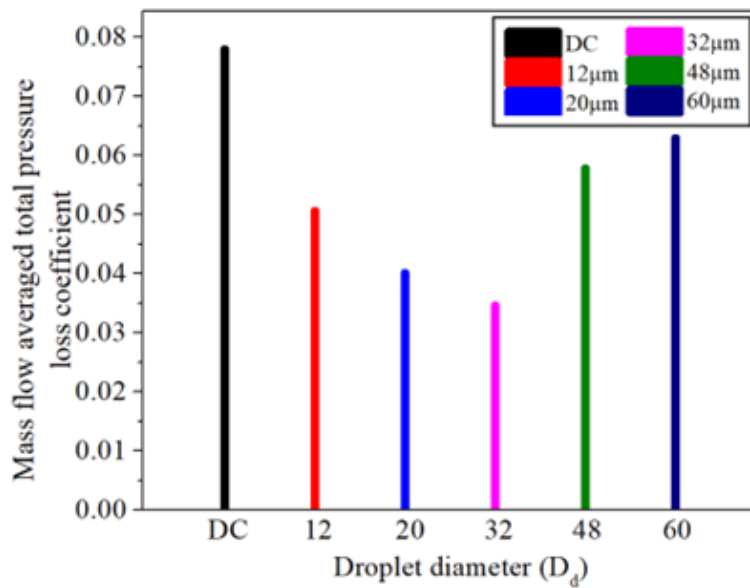


Figure 5.11 Mass flow averaged total pressure loss coefficient at $1.1 C_{ax}$ for the dry case and the wet case of different droplet diameters

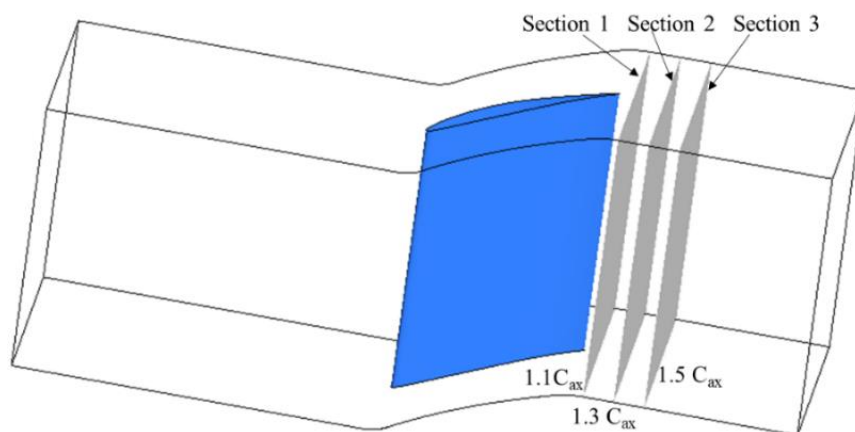


Figure 5.12 Schematic representation of measurement locations downstream of the trailing edge

The downstream flow development is discussed using the loss coefficient pattern observed in three sections 1 to 3 (section 1 at $1.1 C_{ax}$, section 2 at $1.3 C_{ax}$, and section 3 at $1.5 C_{ax}$). These measurement locations are shown in Figure 5.12. The trends are similar for all the droplet sizes. Therefore, only the results for droplet size $48 \mu\text{m}$ are presented and discussed in Figure 5.13

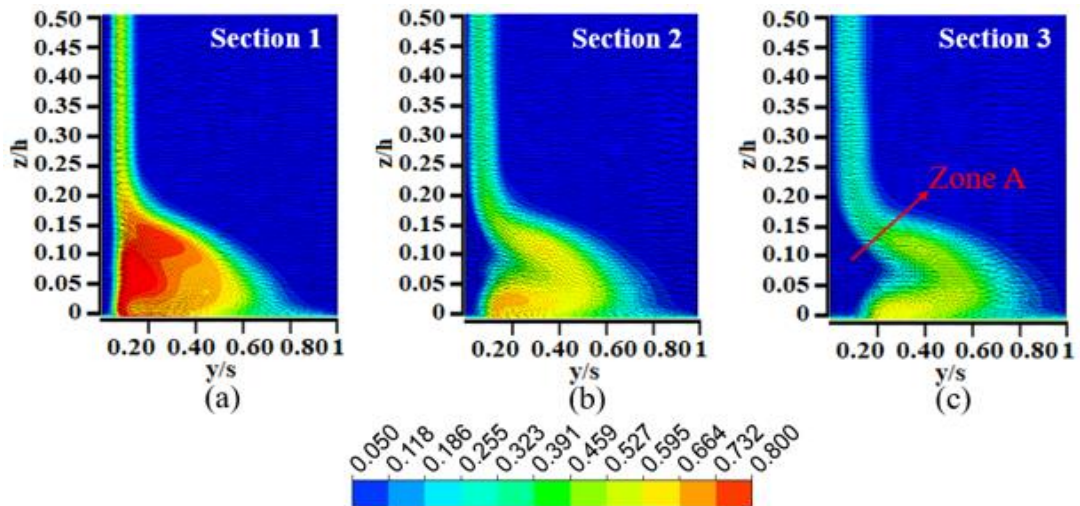


Figure 5.13 Total pressure losses coefficient distributions at three outlet sections downstream of the cascade, for droplet size of $48 \mu\text{m}$

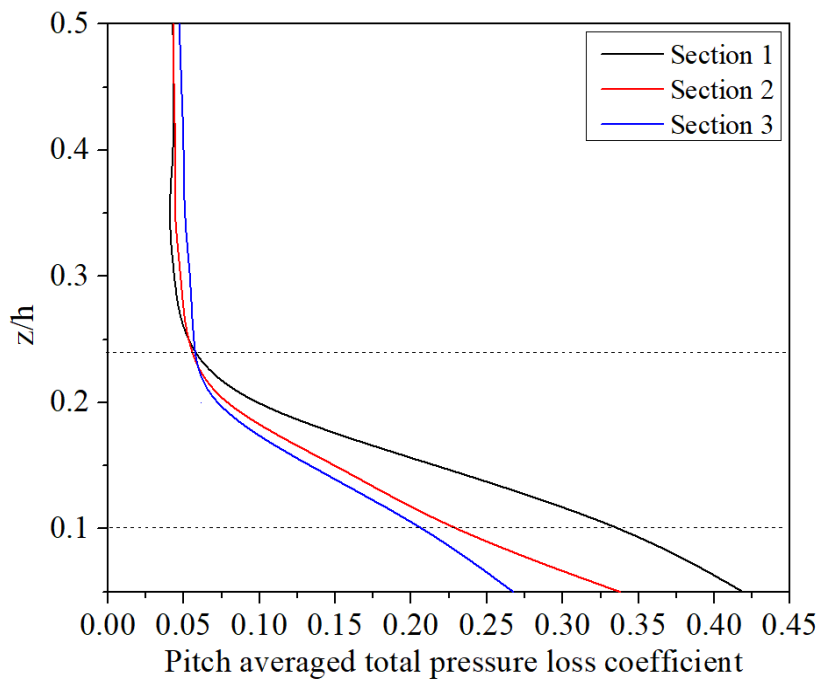


Figure 5.14 Pitch averaged total pressure loss coefficient from along spanwise direction at three downstream locations

The loss coefficient contours are spreading in the spanwise and the transverse direction. The red color denotes the peak value at the core region. As flow progresses from section 1 to 3 the peak value reduces, but loss regions spread more in the transverse-upward direction (denoted by Zone A). As a result, the pitch averaged value of the loss coefficient comes down near the endwall and increases slightly in the midspan region (Figure 5.14). Pitch averaged total pressure loss coefficient is shown in Eq.5.1 in the wet case

$$\bar{C}_{po} = \frac{\frac{m_{\infty}}{m_{\infty}+m_w} \bar{P}_{t,\infty} + \frac{m_w}{m_{\infty}+m_w} \bar{P}_{t,w} - \bar{P}_t}{0.5\rho_{\infty}U_{\infty}^2} \quad (5.1)$$

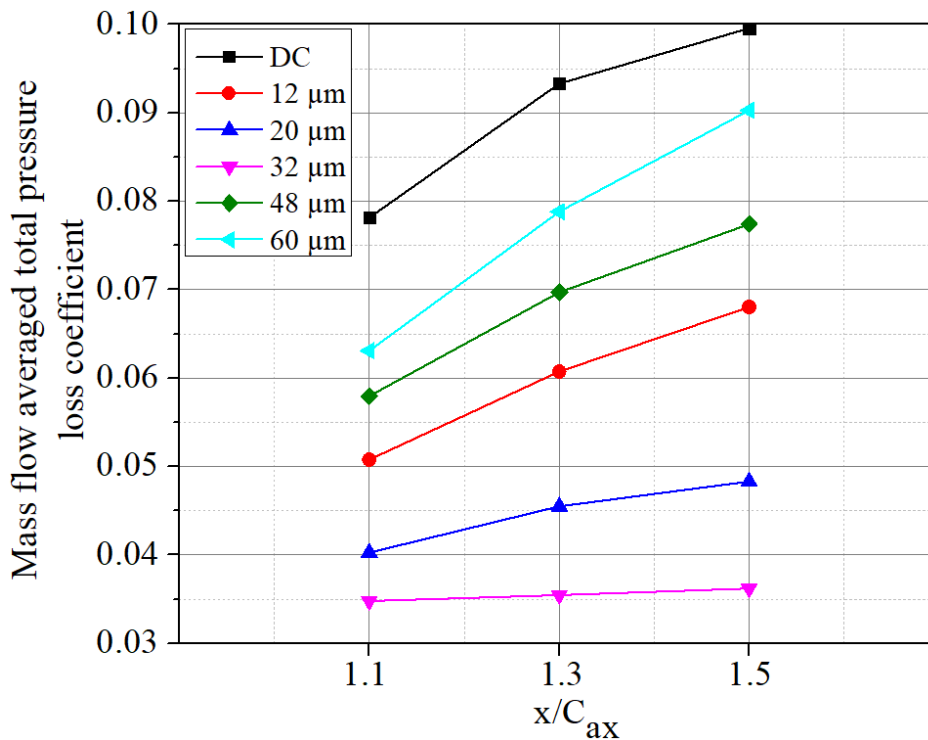


Figure 5.15 Mass flow averaged total pressure loss coefficient at three outlet sections for dry case and wet case of different droplet sizes

The mass flow averaged total pressure loss coefficient for all droplet sizes at three different sections is shown in Figure 5.15. The disturbances are pretty high for the dry case on the downstream side. As a result, the loss coefficient for the dry case increases from sections 1 to 3. The wet case simulations indicate that the loss coefficients are

minimum for droplet size of 32 μm . For this droplet size, the rate of increment in the total pressure loss coefficient from the first section to the third section is significantly lower.

5.1.5 Velocity vectors and secondary flow

The trends of total pressure loss coefficient results for the wet case and dry case are almost similar even though the rate of increase of total mass averaged total pressure loss from section 1 to section 3 is different. Therefore, only the results for droplet size 48 micron are presented in Figure 5.13. The reduction in the magnitude of velocity is the fundamental reason for total pressure losses. This is further reinforced by the observation in Figure 5.13 (a–c), where the magnitude of the velocity is less in the high losses zone ($C_{po} > 0.4$). A zone with high energy (small losses, $C_{po} < 0.05$) appears in each measurement section, which is depicted as "zone A" in Figure 5.13 (c) based on the development of total pressure losses in Figure 5.13. This zone's size grows from the first to the third measurement segment, and it lies between the corner stall and the trailing edge's wake. The main flow lifts due to the blockage of the corner stall and batters the edge of the zone with high losses

The three-dimensional velocity vector project to the plane perpendicular to the flow direction gives an idea about the secondary flows. Three-dimensional flow at three sections (section 1 at 1.1 C_{ax} , section 2 at 1.3 C_{ax} , and section 3 at 1.5 C_{ax}) at the dry case, the wet case having moderate droplet size 32 μm , and the wet case of higher droplet size 48 μm , are plotted in Figure 5.16. The positions of the high magnitude of secondary flow vectors are consistent with high total pressure losses.

The strength of secondary flow vortices decreases from the first to the third measurement section. However, as the flow proceeds downstream, these vortices stretch in the transverse direction. For the dry case, this vortex grows big and occupies a significant portion of the plane. Comparing all these three cases, it is observed that the intensity of the secondary flow vortex is lower for a droplet size of 32 μm . Unlike the other two cases, a single vortex appears at the trailing edge for 32 μm . It gets stretched, grows, and occupies a bigger space in section 3.

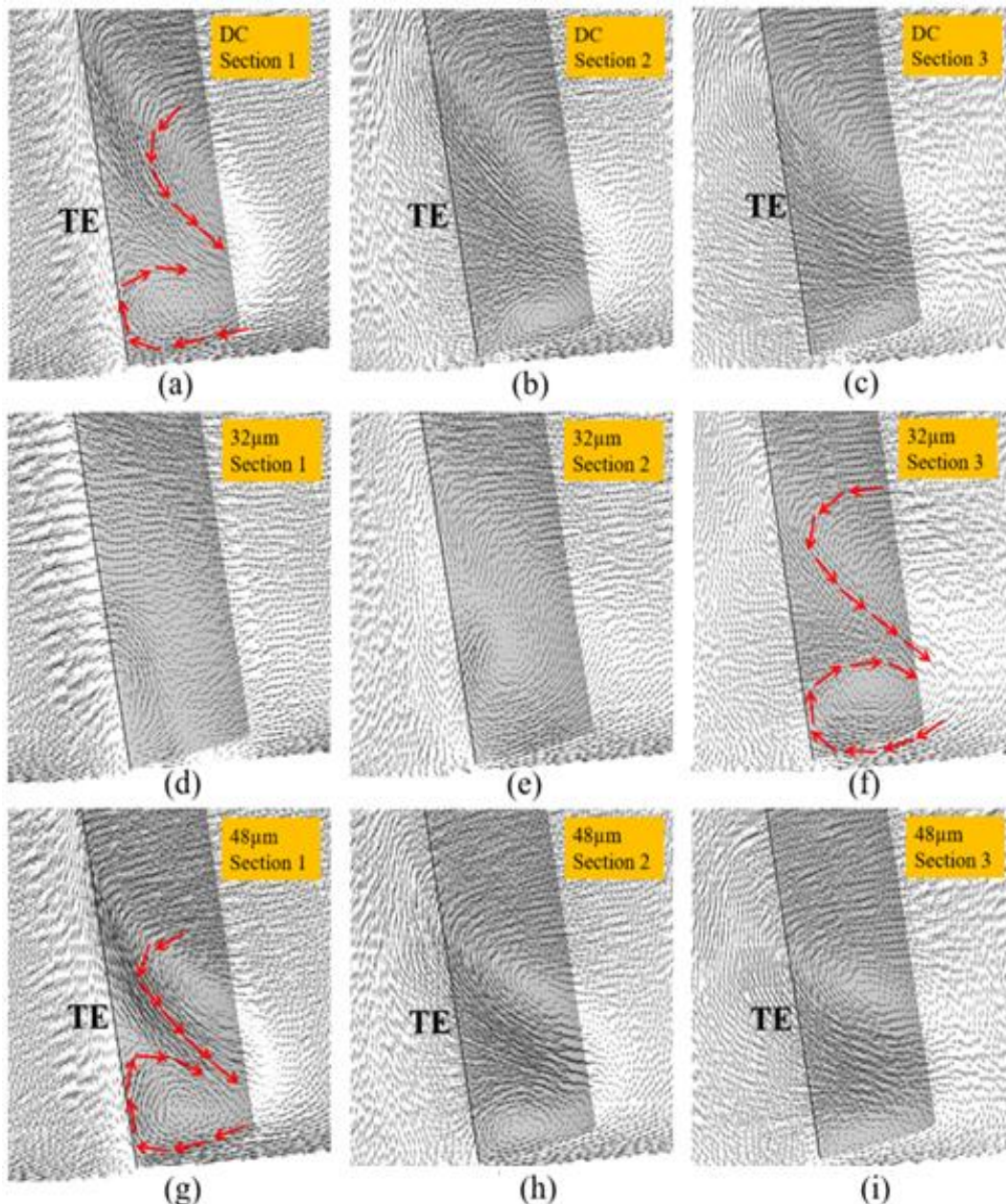


Figure 5.16 Velocity vector plotted at three downstream locations for dry case, wet case of droplet size $42\ \mu\text{m}$ and wet case of droplet size $32\ \mu\text{m}$

5.1.6 Trajectories of the wake and the Trailing Edge Vortex (TEV) center

Figure 5.17 (a) and Figure 5.17 (b) depicts the path taken by the blade wake near the midspan and the path taken by the corner vortex at the trailing edge. From $1.0 C_{ax}$ to $2.4 C_{ax}$, the trajectories are discovered. The point of greatest axial velocity loss at midspan is assumed to be the center of the blade wake. In contrast, the point of greatest

axial vorticity close to the endwall is considered to be the TEV's center. The graph's X-axis is the normalized axial distance from the blade trailing edge to $2.4 C_{ax}$, and the Y-axis represents blade pitch expressed in non-dimensional form. The wake trajectories for the dry case and wet case with $32 \mu\text{m}$ droplet size are almost identical. The TEV trajectories of these two cases show a similar trend. The trajectory of blade wake starts from the trailing edge and moves towards the suction side up to $1.4 C_{ax}$. After that, it is shifted to the pressure side up to $1.9 C_{ax}$. Further downstream, the movement of the blade wake towards the pressure side ceases, and it starts to move close to the dividing line between the pressure side and suction side. On the other hand, the trajectories of blade wake and TEV for the wet case of droplet size $48 \mu\text{m}$ are quite different. In this case, the trajectory of the blade wake moves towards the suction side up to $1.7 C_{ax}$. At this location, it changes its course and moves towards the pressure and suction sides' dividing lines.

The resemblance of the dry case with the wet case of droplet size $32 \mu\text{m}$ infers that adding water droplets with moderate droplet size does not disturb the downstream flow. On the other hand, a higher droplet diameter can alter the downstream flow significantly. This finding is quite helpful for the design of multistage compressors used in wet compression.

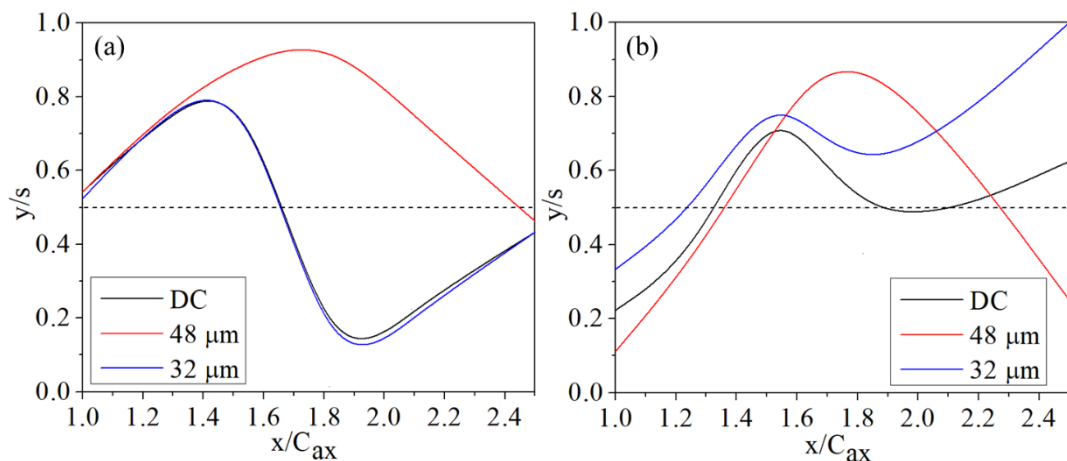


Figure 5.17 Trajectories of the blade wake and core of the TEV downstream of the cascade at dry case and wet case having droplet sizes $48 \mu\text{m}$, $32 \mu\text{m}$

5.1.7 Velocity and vorticity fields downstream of the blade

Two cross-sectional planes are used to study the flow structure downstream of the cascade, at $x/C_{ax}=1.1$ and 1.5 , respectively. The contours are plotted at these two planes with the axial velocity (u) normalized by the inflow velocity (Figure 5.18). For the dry case, and wet case with droplet sizes of $48\ \mu\text{m}$, and $32\ \mu\text{m}$, the contours are plotted. For easier understanding, normalized span (z/h) and pitch distance (y/s) are displayed along the sides of the charts. Near the endwall, the TEV is perceived as a significant velocity deficit. The TEV is smaller in the wet scenario with a moderate droplet size of $32\ \mu\text{m}$, but it is larger with a narrower wake for $48\ \mu\text{m}$.

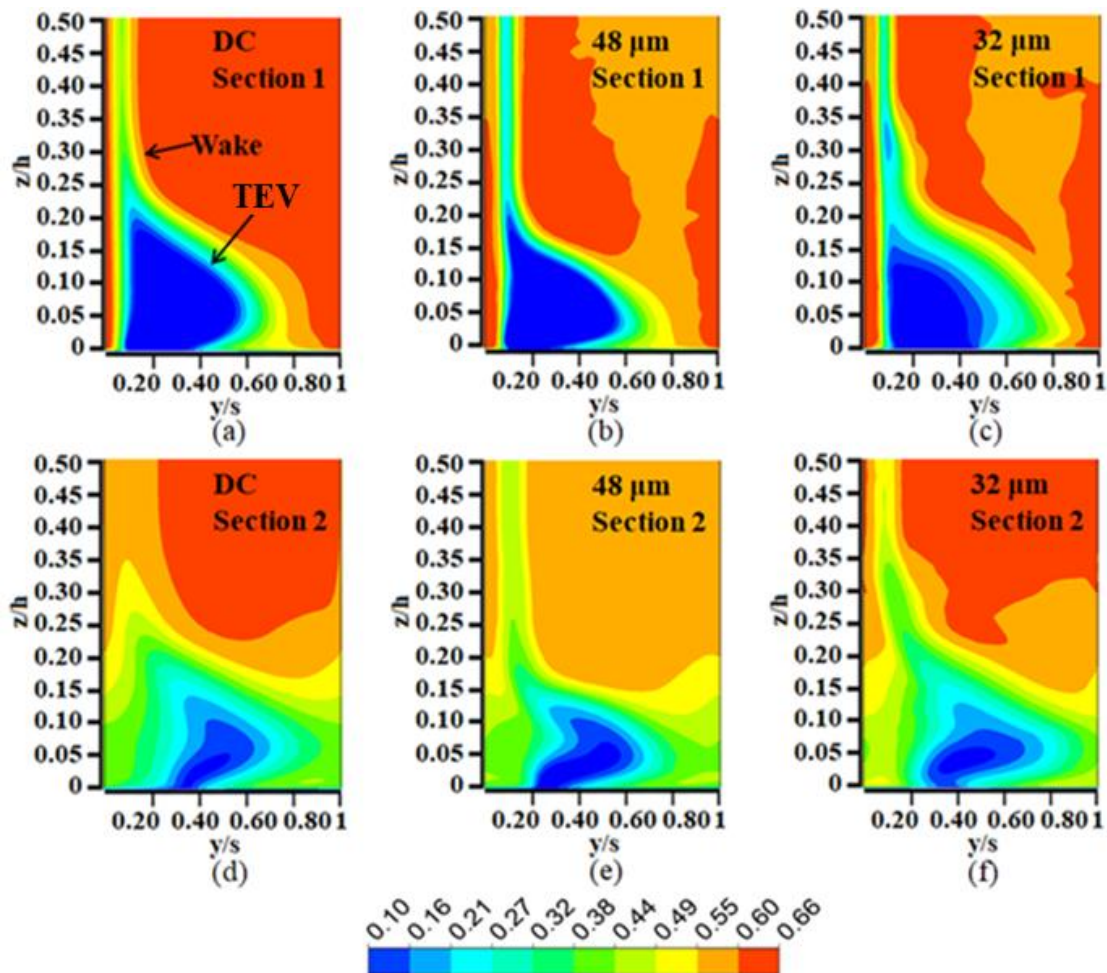


Figure 5.18 Normalized mean velocity at two downstream location (section 1 at $1.1 C_{ax}$, section 2 at $1.5 C_{ax}$) for dry case and wet case having droplet sizes $48\ \mu\text{m}$ and $32\ \mu\text{m}$

Axial vorticity ($\Omega_x = \partial w / \partial y - \partial v / \partial z$) normalized by the inflow velocity and the axial chord ($\Omega_x * C_{ax} / U_\infty$) is shown in Figure 5.19. The stretching of the vortex at the downstream side is visible in these contours. The positive vorticity (represented by the red color contours) has an anticlockwise spin. It moves downward and pushes the negative vortex in the pitch-wise (transverse) direction. These movements cause the spreading of the loss coefficient in the transverse direction.

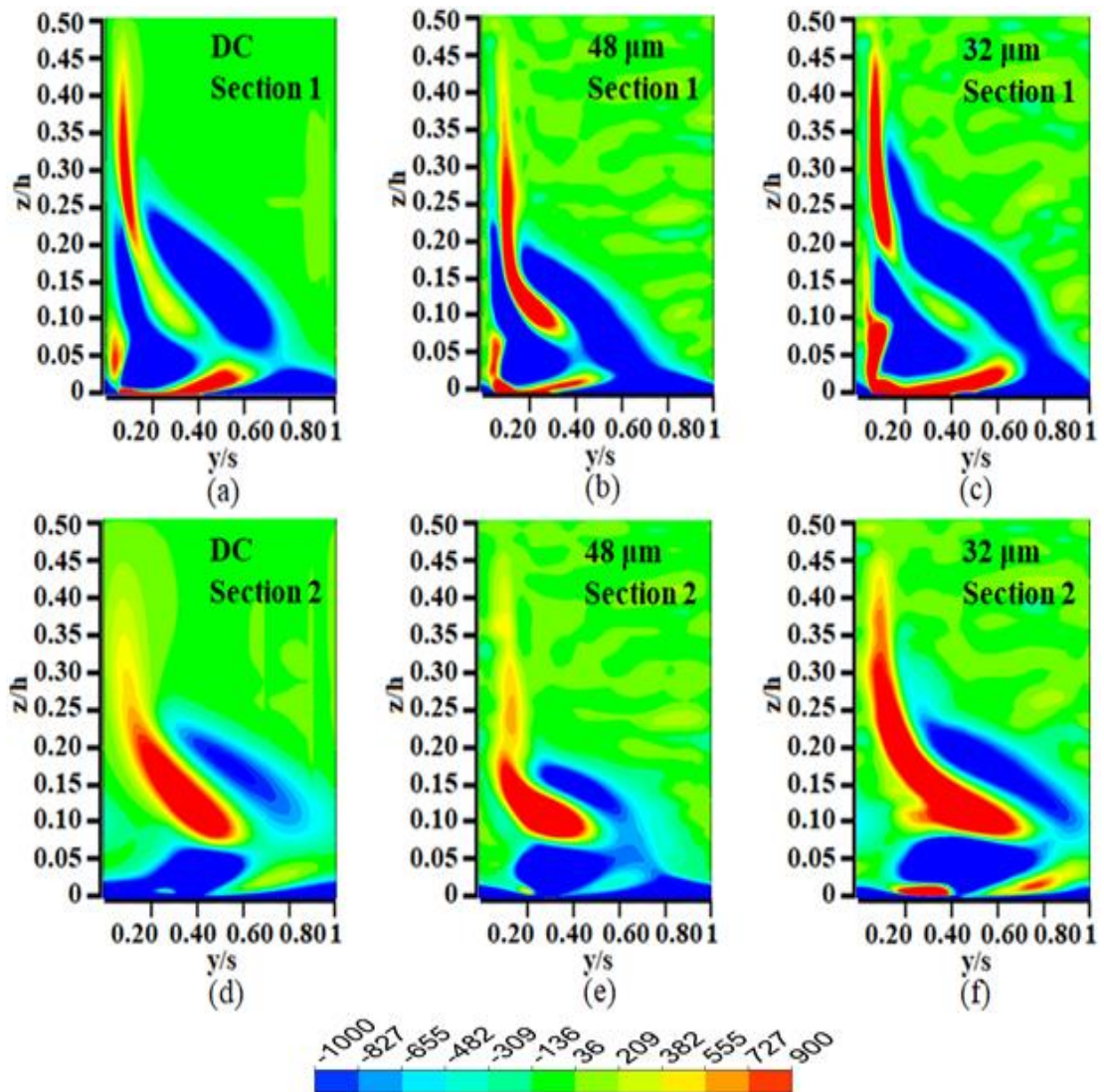


Figure 5.19 Axial vorticity at two downstream location (section 1 at $1.1 C_{ax}$, section 2 at $1.5 C_{ax}$ for dry case and wet case having droplet sizes 48 μm and 32 μm

5.2 Effect of Injection Ratio

The injection ratio (IR) is another crucial variable for wet compression in the compressors. The mass of the water injected to the mass of the airflow through the computational domain is the injection ratio. To explore the effect of injection ratio on the flow behavior and performance of the compressor cascade, simulations are run at five injection ratios (0.5 %, 1 %, 2 %, 3 %, and 4 %). The analysis is carried out as in the previous section, where we studied the effect of droplet size. However, all the simulations are carried out at a fixed droplet size and incidence angle.

5.2.1 Flow deviation at the inlet and aerodynamic blockage inside the blade passage

The flow deviation angle has been plotted just before the leading edge in Figure 5.20. The deviation is minimum at a 2 % injection ratio. The deviation increases as we move away from this injection ratio. As the injection ratio increase, the water droplets' mass flow rate increases. The variation in the deviation angle reveals that there exists an optimum injection ratio for the minimum deviation angle. The velocity coefficient near the endwall (1 % of span) is shown in Figure 5.21.

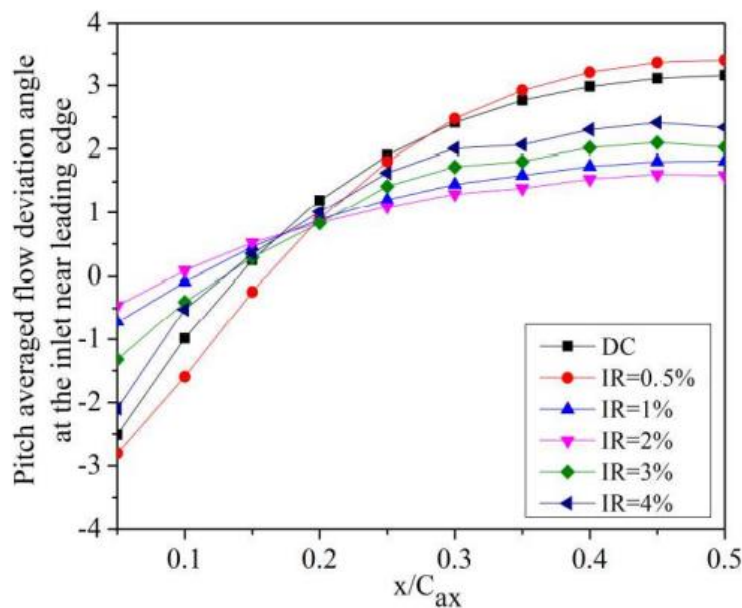


Figure 5.20 Variation in flow deviation angle at the inlet section near leading edge for different injection ratios

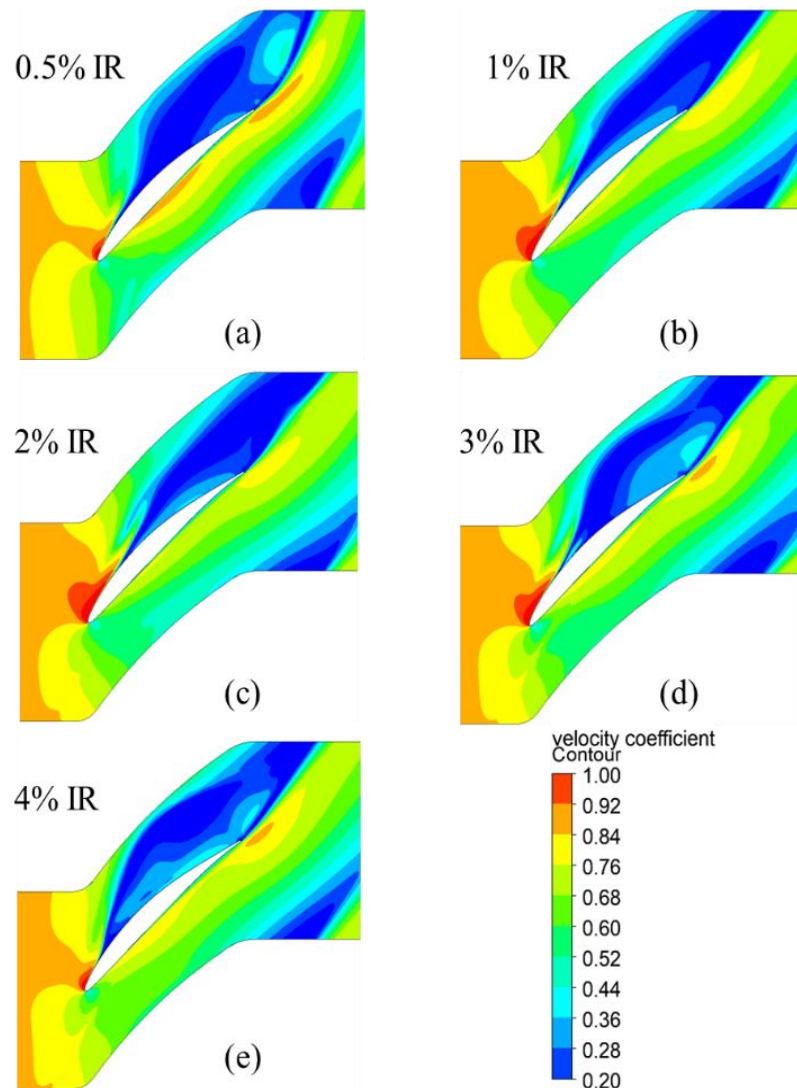


Figure 5.21 Velocity coefficient contour plotted at 1 % of span for different droplet sizes (a) IR=0.5 % (b) IR=1 % (c) IR =2 % (d) IR =3 % (e) IR=4 %

The separation of the flow from the suction side is visible in these contours. At a 2 % injection ratio, the acceleration of the flow aft the leading edge is higher for a 2 % injection ratio. Accordingly, this case exhibits a lower flow separation and blockage in the passage. On the other hand, significant flow separation occurs in the case of 0.5 % IR, 3 % IR, and 4 % IR, where the deviation of the flow is more dominant near the end wall (Figure 5.21). These initial analyses revealed that the effect of injection ratio on the compressor aerodynamics is similar to the effect of droplet diameter. A higher injection ratio implies higher momentum to the water droplets. Hence, at a large

injection ratio, the particle trajectories would be different from the streamlines of the continuous media. At the smaller injection ratio, particle trajectory and streamlines are aligned. Hence, the case with a 0.5 % injection ratio (IR) behaves similar to the dry case (DC).

5.2.2 Static pressure on the blade and the blade loading

Figure 5.22 show the distribution of static pressure on the blade at the suction surface. The blue region represents the flow past the leading edge. Owing to the acceleration of the fluid, a depression in the static pressure is observed here. For an ideal compressor cascade, the pressure in the blade passage must steadily rise from the leading edge to the trailing edge. This steady rise is observed with moderate injection ratios of 1 % and 2 % for all the different injection ratios studied. For other injection ratios, the isobars near the endwall form small islands. These island formations are associated with the severe flow separation in this region.

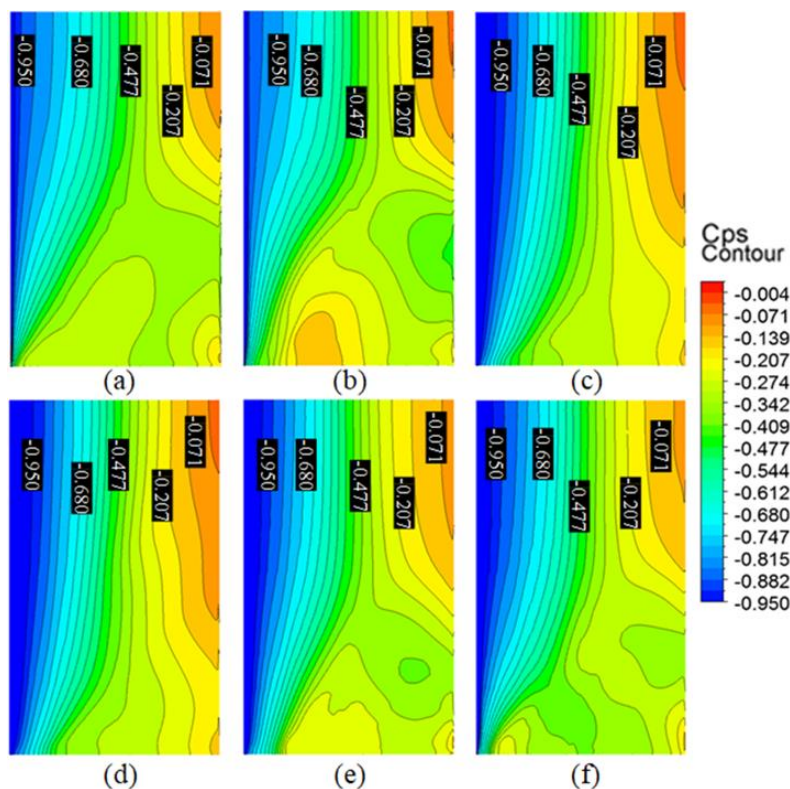


Figure 5.22 Static pressure coefficient distribution on the suction surface of the blade (a) dry case (b) IR=0.5 % (c) IR=1 % (d) IR=2 % (e) IR= 3 % (f) IR=4 %

The region on the suction surface where $C_{ps} = -0.950$ (lower static pressure region) is getting extended downstream by the addition of water droplets than the dry case, but it is limited for the size of the droplets in the range of 1 %-2 % ratio. The development of a lower static pressure region on the suction surface is favorable for improved aerodynamic performance. The region with a higher static pressure coefficient ($C_{ps} = -0.071$) is limited to only a tiny region in the midspan for the dry case. This high-pressure region grows more prominent and extends downward with the increase in injection ratio up to 2 %. Further increase in the injection ratio causes this high-pressure region to shrink again.

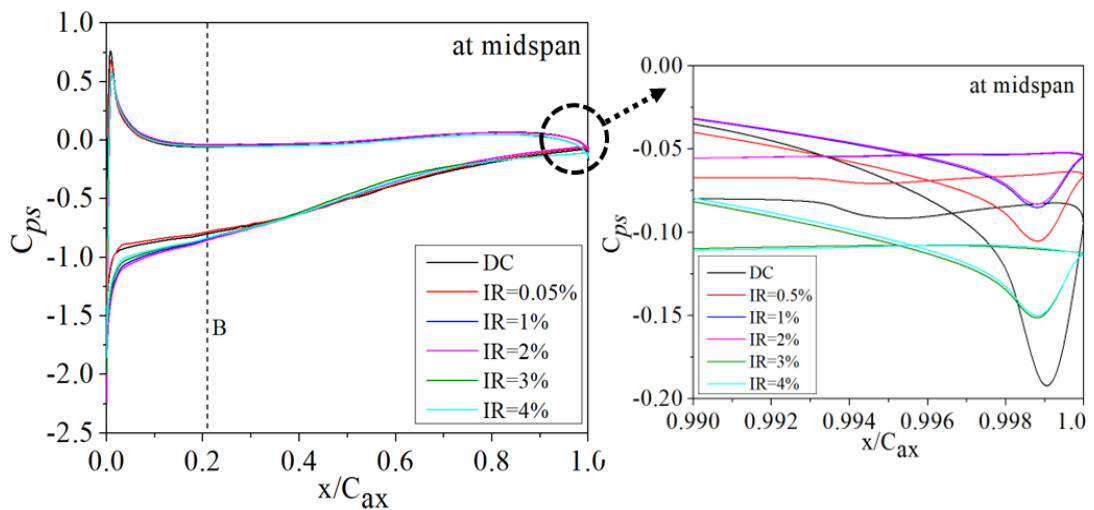


Figure 5.23 Static pressure coefficient distribution over the blade at 50 % of span

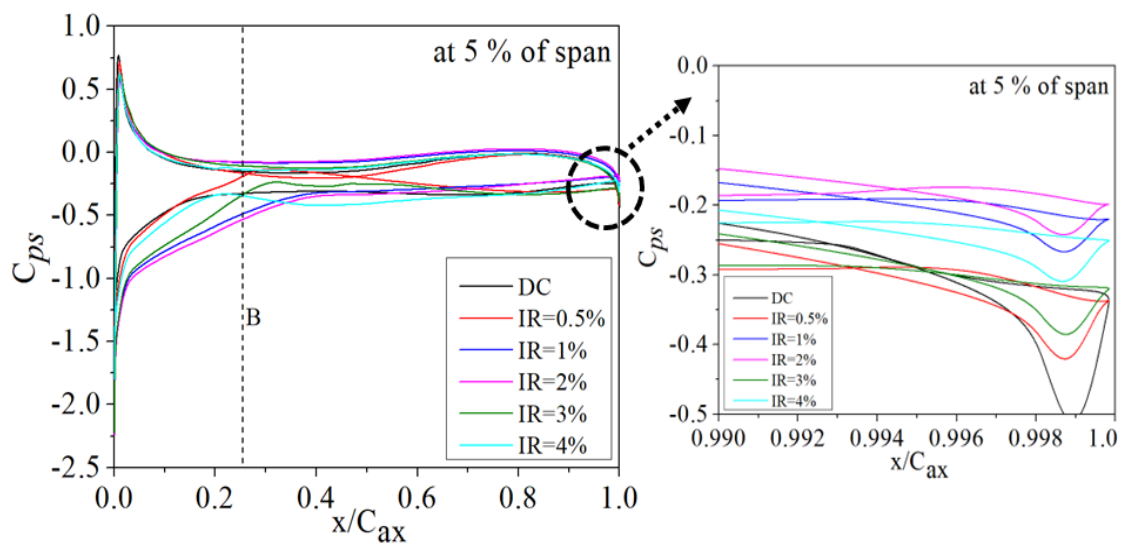


Figure 5.24 Static pressure coefficient distribution over the blade at 5 % of span

The blade loading at midspan ($z/h=50\%$) and near endwall ($z/h=5\%$) are shown in Figure 5.23 and Figure 5.24. The general characteristics of the blade loadings are similar to the standard dry and wet case simulations presented earlier. With the variations in the injection ratio, significant differences are visible near the endwall. On the other hand, at midspan, the loading is almost similar for all the cases, except for leading and trailing edge regions. Near the trailing edge, the unloading point is different for each injection ratio. The unloading point is marked by the point of inversion of the pressure coefficient on the pressure and suction surface. After this point, the loading reverses, which is highest for the dry case. Introducing water droplets brings down the inverse loading in the trailing edge region. The loading is lowest for 1% and 2% injection ratio, and it can minimize the formation of trailing edge vortices.

5.2.3 Variation in the total pressure losses coefficient

The mass averaged total pressure loss coefficient is plotted for all injection ratios along the axial direction (Figure 5.25). All scenarios show a consistent increase in the loss coefficient. The maximum loss coefficient is shown by the 0.5% injection ratio. It has been observed earlier that the compressor aerodynamics is almost similar to the dry case at this injection ratio. The water droplets at this injection ratio lack sufficient energy to influence and suppress the flow separation of the continuous media. The optimum injection ratio turned out to be 2% among the tested cases. This is evident from the mass averaged loss coefficient calculated at $1.1 C_{ax}$ (Figure 5.26). The mass flow averaged total pressure loss in the dry case reduces by 58% with an injection ratio of 2%. The loss coefficient increases as we move away from this injection ratio. Further increases in injection ratios (3% and 4%) bring down the percentage reduction of total pressure loss from 58% to 16% and 27%, respectively.

The loss regions at the exit ($1.1 C_{ax}$) of the compressor blade is shown in Figure 5.27. The peak loss coefficient region (marked in red) is caused by the corner vortex from the hub-suction side and the trailing edge vortices. The normalized spanwise distance (z/h) and the normalized pitch-wise distance are shown in the contour. The injection of the water droplet with a very lower injection ratio ($IR = 0.5\%$) reduces the extent of the total pressure loss region at the wake region ($0.25 < z/h < 1.0$) and broadens the loss

region near the end wall. With a further increase in droplet size from 0.5 % to 2 % IR, the total pressure loss is notably reduced.

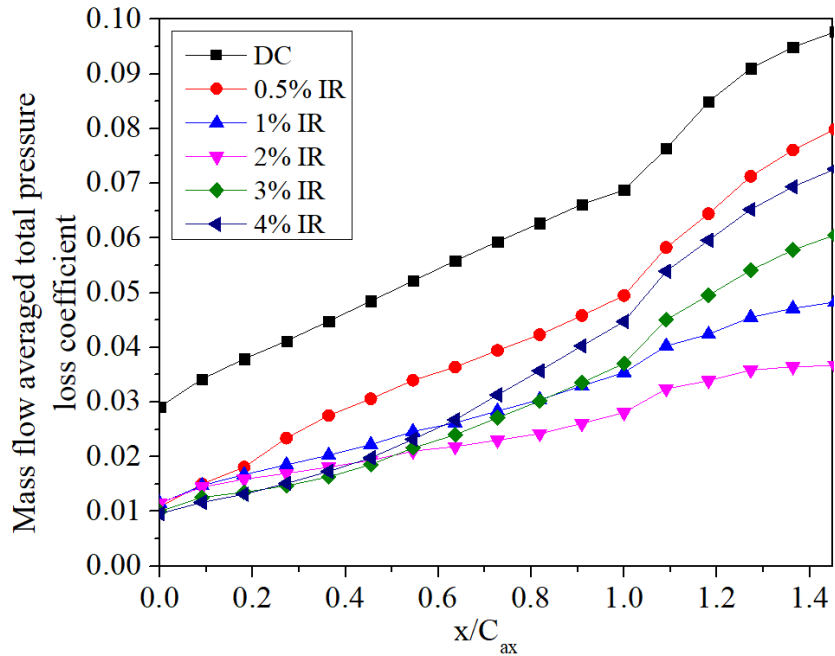


Figure 5.25 Mass flow averaged total pressure loss coefficient along the axial direction

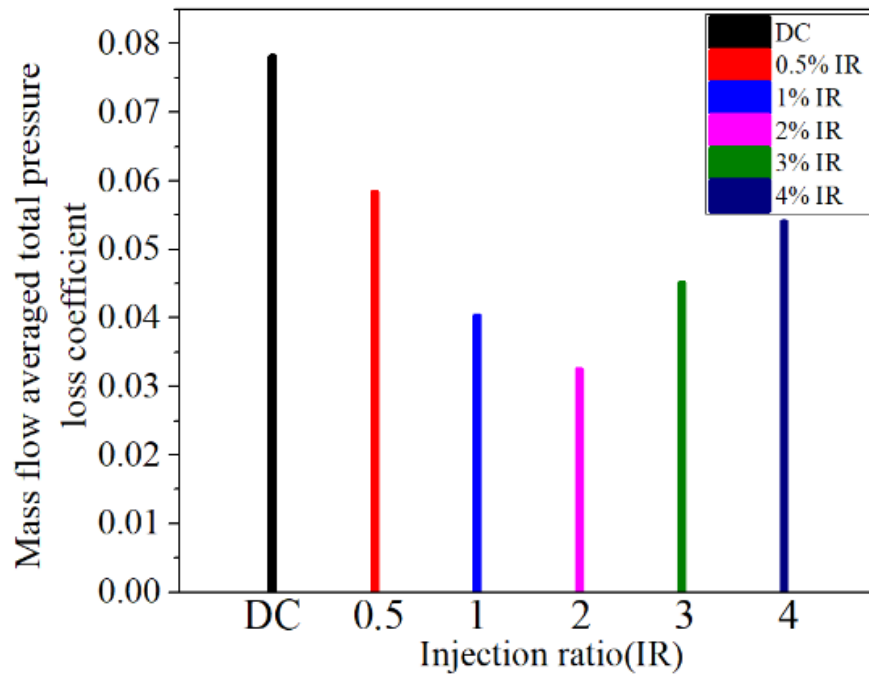


Figure 5.26 Mass flow averaged total pressure loss coefficient at $1.1C_{ax}$

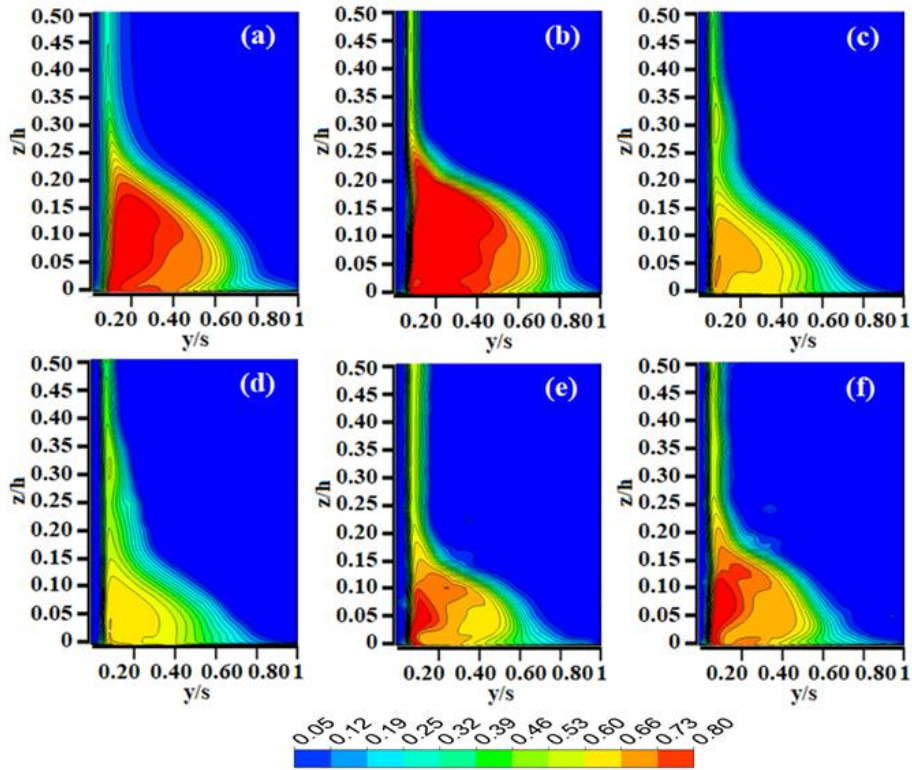


Figure 5.27 Total pressure loss coefficient of dry case and wet case with different injection ratio at $1.1 C_{ax}$

5.2.4 Velocity and vorticity fields downstream of the cascade

The wake near the midspan and the secondary vortex at the downstream location is shown in the normalized velocity and the vorticity contours in Figure 5.28 and Figure 5.29, respectively. For brevity, the comparative analysis is shown for the dry case, the wet case with a higher injection ratio (IR = 4 %), and the wet case with a moderate injection ratio (IR = 2 %). The contours are plotted at two cross-sectional planes at $1.1C_{ax}$ and $1.5C_{ax}$. The trailing edge vortex (TEV) and the corner vortices are merged at the blade exit and are seen as a large velocity deficit close to the endwall. The wet case with a moderate injection ratio of 2 % shows a smaller TEV with a broad wake, and the wet case with a higher injection ratio of 4 % shows a larger TEV with a thinner wake. The dry case also exhibits larger TEV; however, the wake region is comparatively smaller than that of the wet case.

Mean axial vorticity defined by $\Omega_x = \partial w / \partial y - \partial v / \partial z$ normalized by the inflow velocity and the axial chord ($\Omega_x * C_{ax} / U_\infty$) are shown in Figure 5.29. The vorticity contours

predominantly appear near the trailing edge and endwall for the dry case. The rest of the plane is free of any vorticity. However, for the wet case, the contours are different. With the introduction of water droplets, several minor vortices are visible in the domain. At a higher injection ratio (IR =4 %), apart from the strong vortices near the endwall, the entire passage is filled with several smaller vortices with a positive and negative spin. As the flow proceeds to section 2, these smaller vortices interact and merge. In all these cases, the positive vortex near the trailing edge gets stronger and moves downward to the endwall. It moves toward the endwall in the anticlockwise direction and splits the vortex with the negative spin. This causes the stretching of the vorticity contours in the pitch-wise direction. Due to this, an enhancement of the losses occurs on the downstream side.

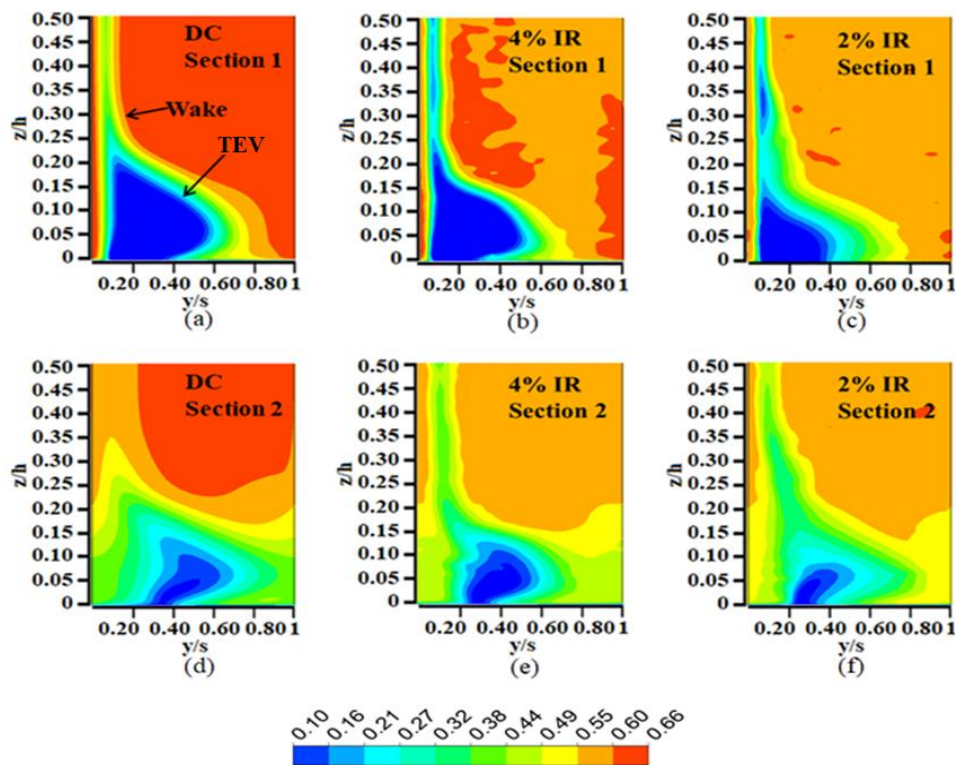


Figure 5.28 Normalized mean velocity at two downstream location (section 1 at $1.1 C_{ax}$, section 2 at $1.5 C_{ax}$ for dry case and wet case with injection ratios 4 % and 2 %

The trajectories of the blade wake and the core of the TEV downstream of the cascade are shown in Figure 5.30. The construction of the trajectories is explained in a previous section (section 5.1.6), hence not repeated here. It is observed that the wake trajectories

for the dry case and the wet cases are similar. However, the trajectory of the trailing edge vortex is different for IR= 4 %, which indicates that excess amount of injection ratio can alter the blade exit flow. In practical application, this may create additional losses in the subsequent stage of a multistage compressor.

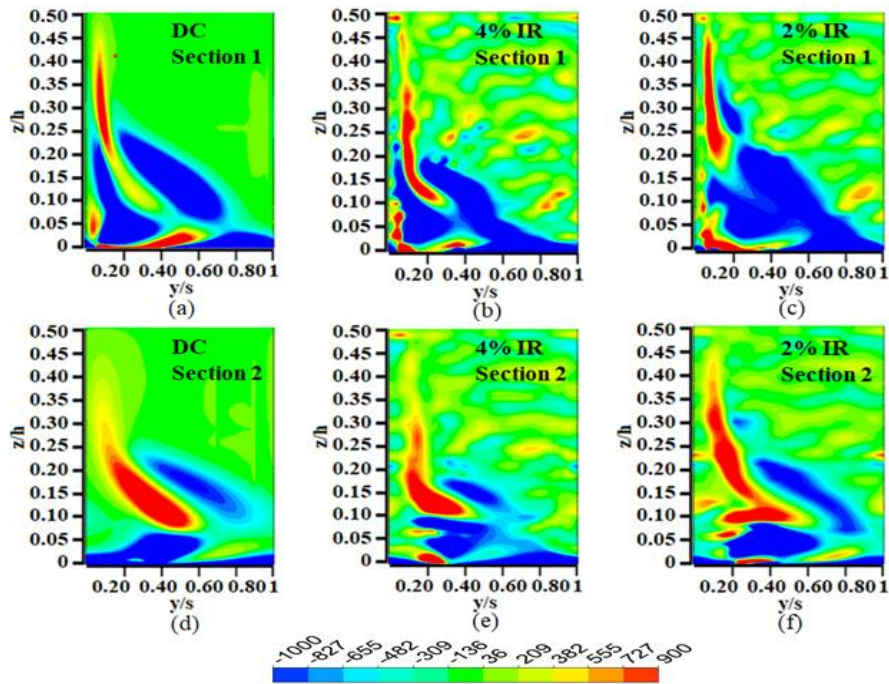


Figure 5.29 Normalized mean axial vorticity at two downstream location (section 1 at $1.1 C_{ax}$, section 2 at $1.5 C_{ax}$ for dry case and wet case with injection ratios 4 % and 2 %

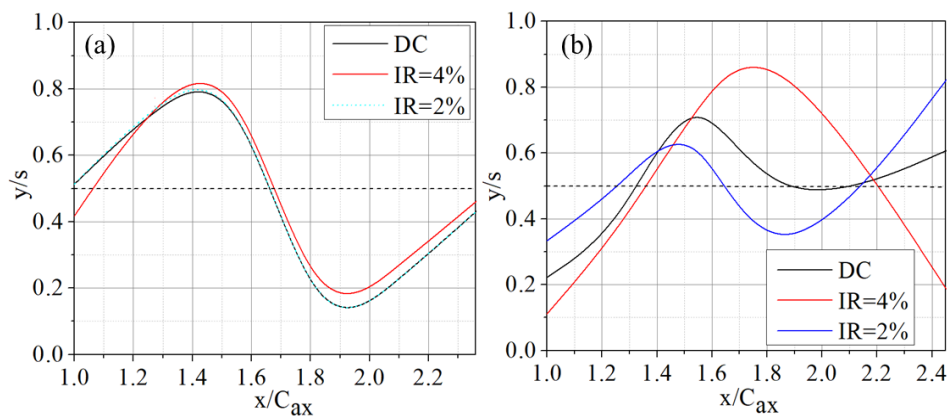


Figure 5.30 Trajectories of the (a) blade wake and (b) core of the TEV downstream of the cascade at dry case (DC) and wet case having injection ratios 4 % and 2 %

5.3 Summary

- Flow deviation at the inlet is more in the case of higher droplets and the lowest droplet size (48 μm , 60 μm , and 12 μm , however moderate droplet sizes 20 μm and 32 μm give minimum flow deviation near endwall.
- Flow deviation at the inlet is more in the case of higher injection ratios and lowest injection ratios (3 %, 4 %, and 0.05 %, however moderate injection ratios of 1% and 2% give minimum flow deviation near the endwall.
- Water injection with moderate droplet diameter size and injection ratio reduces the flow separation, however, the injection with smaller droplet size and injection ratio as well as higher droplet diameter and injection ratio increases the flow separation.
- Blade loading is increased in the case of moderate droplet size 32 micron and injection ratio of 2 %.
- Total pressure loss is reduced by 54 % and 58 % with water injection having a droplet size of 32 μm and Injection of 2 % respectively.
- The formation of secondary flow due to the corner separation is found to be minimum in the case of moderate droplet size 32 μm and injection ratio of 2 %.
- The resemblance in the trajectory of the dry case with the wet case of droplet size 32 μm infers that adding water droplets with moderate droplet size does not disturb the downstream flow

CHAPTER 6

WATER INJECTION IN AN ACTIVE FLOW CONTROL ENVIRONMENT

One accepted method to minimize or delay the flow separation from the blade surface is to provide suction slots at the appropriate locations on the blade surface. Bleeding a small amount of fluid through these slots can effectively minimize the loss coefficient on the compressor blade passage. This chapter provides a detailed investigation of the use of suction slots in dry and wet environments.

6.1 Identifying the Axial Location for the Slot

From the previous analysis, it is understood that a significant portion of the flow separation occurs from the blade suction surface. Naturally, the slot needs to be provided on the suction surface of the blade, but at what location? To answer this question, simulations are carried out by keeping the slot at different axial locations. Six different models are generated based on the slot locations. In *Model-1*, the slot is kept at a distance of 20 % of the axial chord from the leading edge ($0.2 C_{ax}$). In the subsequent models, the slot is moved towards the trailing edge in steps of 10 % C_{ax} , and in *Model-6* the slot is positioned at $0.7 C_{ax}$. A representative model is shown in Figure 6.1. In Figure 6.1, the 'x' denotes the percentage of axial distance. The loss coefficient of each of these models is compared with the base case (without slot).

Table 6.1 shows the percentage deviation of mass averaged total pressure loss coefficient for each of these models compared to the base case. The loss coefficients are calculated at the outlet of the respective models. The table indicates that keeping the slot at 60 % of the axial chord significantly decreases the loss coefficient. The percentage deviation of the loss coefficient that occurs in the case of model-5 from the base case is 52.20 %. Even if Model-5 gives a maximum reduction in loss coefficient, it can not be assured that Model 5 is an ideal slot location. For further assurance, the

flow field has to be analyzed. Hence the flow field analysis has been carried out to select an ideal slot location.

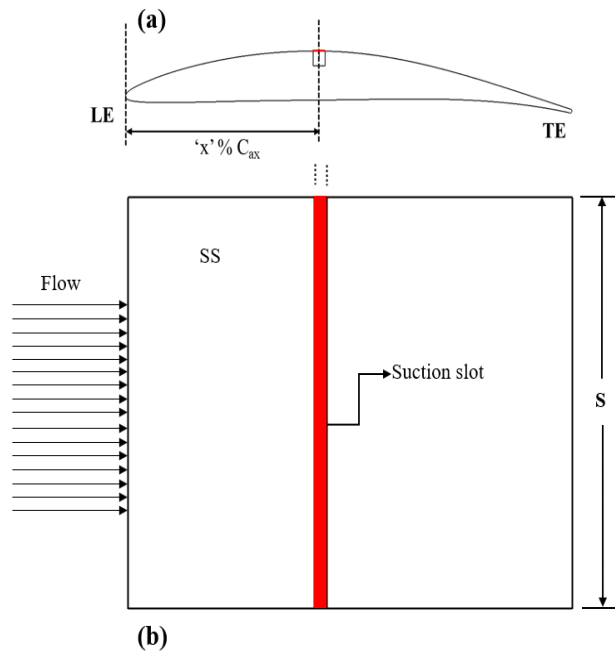


Figure 6.1 Geometric details of Model

Table 6.1 Percentage reduction of mass averaged total pressure loss coefficient at the outlet

SI No.	Name	Slot location	% Reduction in $\overline{C_{po}}$
1	Model-1	20 % C_{ax}	21.82
2	Model-2	30 % C_{ax}	12.98
3	Model-3	40 % C_{ax}	5.71
4	Model-4	50 % C_{ax}	8.13
5	Model-5	60 % C_{ax}	52.20
6	Model-6	70 % C_{ax}	5.34

Figure 6.2 depicts the limiting streamlines on the suction side of the blade. The singularities on the wall caused by the flow losses are seen in the limiting streamlines. In cases of high losses, the singularities or critical places are typically encased in the dividing streamline on the walls. The spanwise distribution of the flow slightly improves when the suction slot is positioned at $0.2 C_{ax}$. At the tip of the blade, the separation's spanwise extent is diminished, which weakens the separation's suction side focal point. While comparing the flow topology of $60\% C_{ax}$ with $70\% C_{ax}$, it is revealed that the extent of the separated flow regime is smaller for $60\% C_{ax}$. When the slot is placed at $60\% C_{ax}$, the saddle point shifts downstream of the flow, thus minimizing the extent of blockage in the blade passage. Considering these parameters, $60\% C_{ax}$ is found to be an ideal location for the slot. Hence this location is chosen for further analysis.

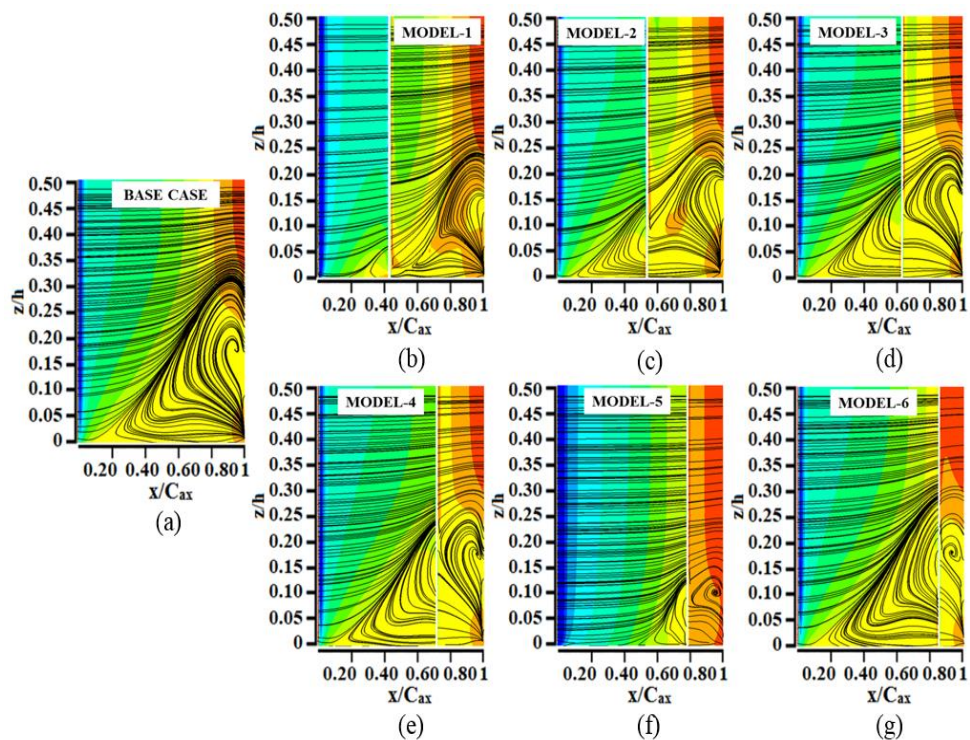


Figure 6.2 Static pressure coefficient superimposed with limiting streamlines on the blade suction surface for all models

6.2 Effect of Wet Compression and Suction Slot on the Performance

At the chosen location of 60 % C_{ax} , further analysis is carried out with water injection. In this analysis, two additional configurations of the slot are tested. These configurations are selected based on the studies carried out by Tian Liang et al and are made based on the slot's percentage coverage of the span. In the first configuration, the slot is kept on the lower end of the blade and covered 25 % of the blade height on the suction side. This configuration is named as near-end wall slot (NES). In the second configuration, the slot is positioned at the center of the blade and occupied 50 % of the blade span. This configuration is named as “near midspan slot” (NMS). The third configuration is the “full span slot” (FSS), where the slot runs through the entire span. Figure 6.3 shows all three configurations.

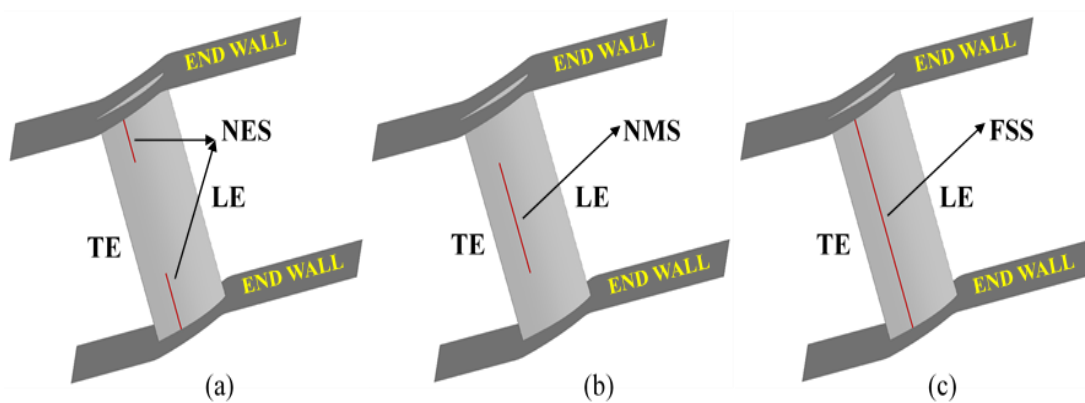


Figure 6.3 Different slot configurations on the suction surface (a) NES (b) NMS (c) FSS.

6.3 Effect of Water Injection on NES Configuration

The effect of water injection on the near edge slot (referred to as NES-wet) configuration is discussed in this section. Initial comparisons are made with dry operating conditions of NES (referred to as NES-dry) and the without slot (base case) configurations. Figure 6.4 shows static pressure coefficient contours superimposed with surface streamline on the suction surface of the blade. For the base case (Figure 6.4 (a)), flow separation appears aft the leading edge and grows in the spanwise and streamwise directions. The separated flow region has a saddle point at S3 and the focal point at F2.

It can be observed from Figure 6.4 (b) that the separated region has greatly reduced with the NES-dry configuration. The extent of the corner separations is restricted to 10 percentage of the blade span. The point of separation (saddle point S3) moves to the mid-chord region. On the other hand, an additional separation line SL2 is visible just above the slot. A recirculation region is formed at the top end of the slot with a focus F3.

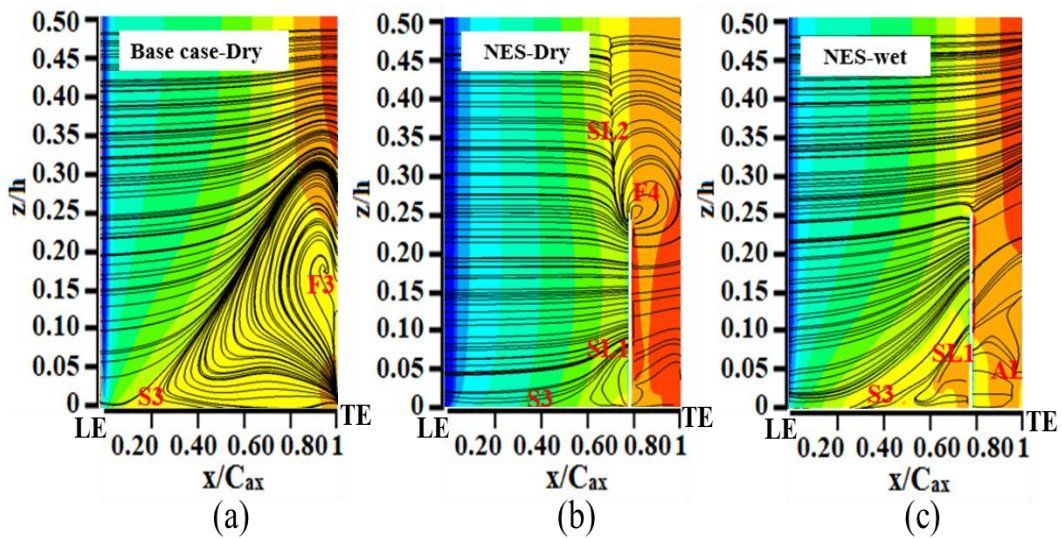


Figure 6.4 Static pressure coefficient superimposed with surface streamline on the suction surface of the blade (a) Base case-Dry (b) NES-Dry (c) NES-Wet

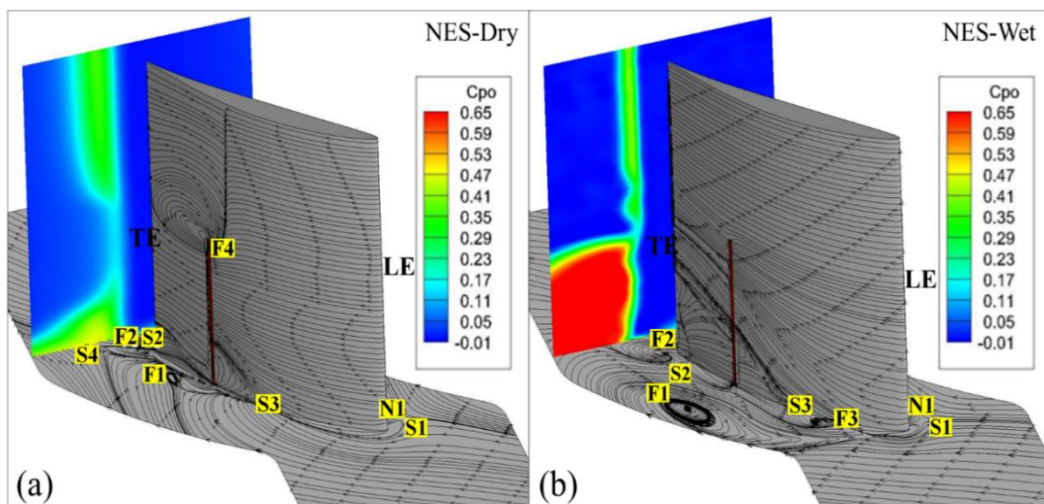


Figure 6.5 Limiting streamlines on the suction surface and end wall (a) NES-Dry (b) NES-Wet

With the introduction of water injection, the separation region SL2 disappears (Figure 6.4 (c)). The vortex region at the top end of the slot is also removed. The flow field in the mid-span of the blade has been improved. On the contrary, the flow separation in the corner region of the blade is significantly higher than NES-Dry. The corner separation extends to a 15 % span for NES -wet and one separation and re-attachment line (AL) is seen to form near the trailing edge due to the entrainment of flow into the slot.

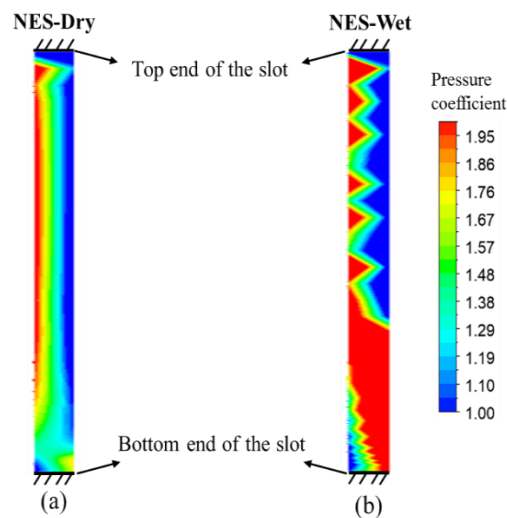


Figure 6.6 Static pressure coefficient contour on the slot (a) NES-Dry (b)NES-Wet

Figure 6.5 indicates the limiting streamlines drawn on the blade's suction surface and end wall. The total pressure loss coefficient at the wake region near the trailing edge is also shown in this Figure. The loss coefficient indicates a heavy loss region near the endwall for the NES-wet case due to the vortex formation. The vortex (with focus F1) is formed by the interaction of dividing streamline from saddle point S1 and the recirculated flow of the slot. Its strength is quite different in both dry and wet cases. The strength of the vortex (with focus F1) is higher for the NSE-wet case compared to the NSE-dry case, and it is located away from the blade surface. The aspiration through the slot is not uniform for the NSE wet case. Figure 6.6 shows the pressure coefficient plotted over the slot for both cases. For the NSE-dry case, the slot provides a more uniform pressure gradient along the slot length, whereas with the wet case, it is highly distorted. A lower value for the pressure coefficient indicates a higher suction. In that sense, near the endwall NSE-dry case provides a higher suction through the slot, pulling

the F1 closer to the blade suction surface. The suction generated for the NSE-wet case is weaker near the endwall, and the F1 remains far away from the blade surface. Thus, for the wet case, most of the aspirated flow entering the slot is from the reversed flow. The arrows in the streamlines indicate that streamlines from the trailing edge side enter the slot (Figure 6.5 (b)). The wall shear stress plotted (Figure 6.7) around the slot shows that the shear stress is dominant on the trailing edge side of the slot for the NSE-wet case. This is due to the acceleration of the reversed flow before entering the slot. However, for the NSE dry case, the onward flow is dragged into the slot.

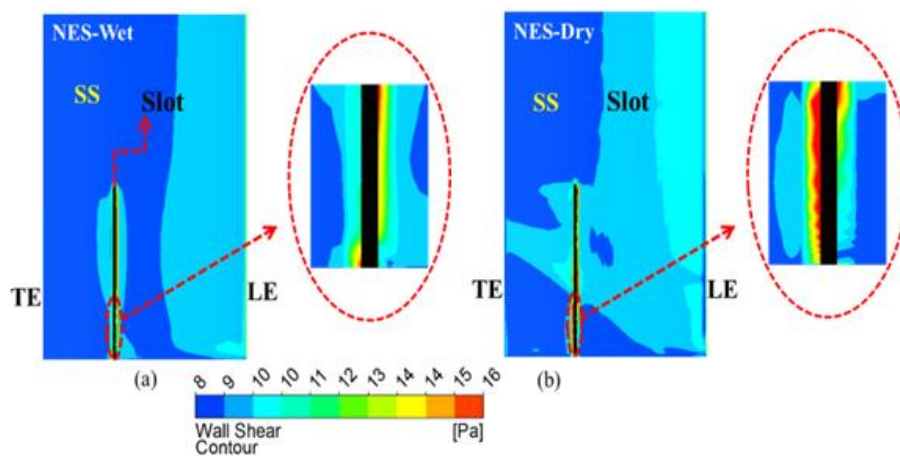


Figure 6.7 Variations in the wall shear distribution in the axial direction around the slot and the enhanced view near end wall (a) NES-Dry (b) NES-Wet

These results show that the presence of water droplets enhances the endwall losses. However, towards the midspan, the flow conditions are different. In the midspan region, the top end of the slot generates a vortex with focus F4. This creates additional losses in the midspan region for the NSE-dry case. The flow that enters the slot is recirculated in the form of a vortex. The curl of the velocity vector normal to the slot is shown in Figure 6.8. Near the top end of the slot negative value of the curl supports the formation of a vortex normal to the suction surface. For the NSE-dry case, the negative curl is quite stronger compared to the wet case. This recirculation within the slot leads to an additional vortex from the top end of the slot, identified with a focus as F4. The negative curl is present in the NSE-wet case also, but it is limited to a small portion at the top end of the slot. Hence, it does not develop into a full vortex as observed with the NSE-dry case.

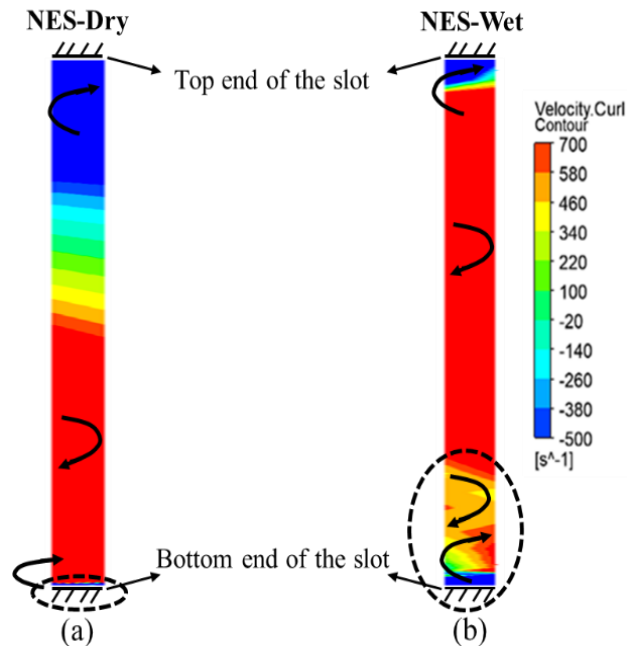


Figure 6.8 Velocity curl on the plane normal to the slot (close to the slot, 0.05 mm from the slot) (a) NES-Dry (b) NES-Wet

6.4 Effect of Water Injection on NMS Configuration

Figure 6.9 shows contours of static pressure coefficient superimposed with surface streamline over the suction surface of the blade for NMS dry and wet cases. No significant variations are observed for the corner separation for the NMS configuration in comparison with the base case. However, the flow field gets modified at the slot end. The presence of the slot pushes down the recirculation region towards the endwall. The crowding of streamlines near the separation line is smaller with NMS dry and wet cases in comparison with the base case. Additionally, the curvature of the limiting streamline at a 30 % span gets decreased with NMS configurations. The saddle point S3 is shifted a little bit downstream location in the case of NMS-Wet and the focal point F3 is moved further upward along the blade height in the separated region.

Figure 6.10 shows the limiting streamlines which are drawn on the end wall and suction surface of the blade superimposed with the total pressure loss coefficient contour at the wake region. The contours of the loss coefficient indicate a slight decrease for the loss core region (red area) for the NMS wet case. At the midspan region, there is only a

marginal difference between the two cases, However, few changes are observed near the endwall.

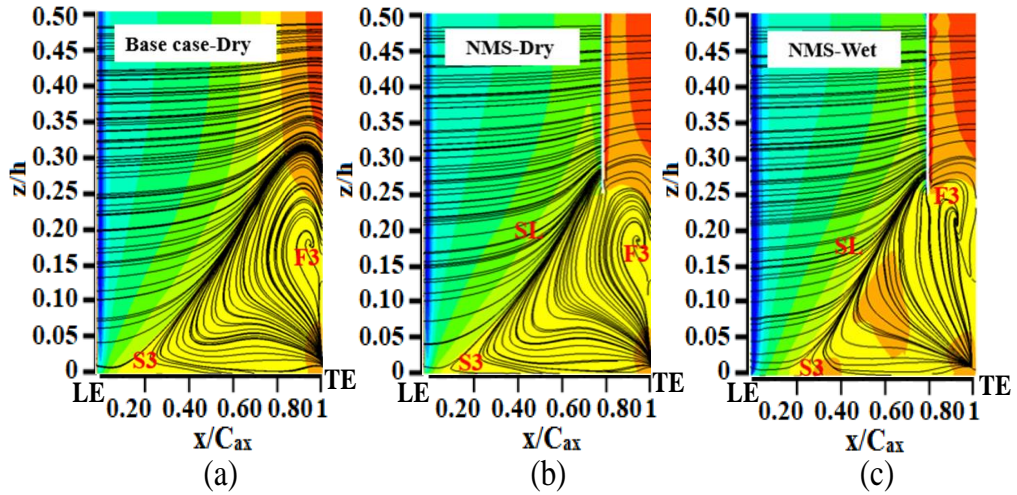


Figure 6.9 Static pressure coefficient superimposed with surface streamline on the suction surface of the blade (a) Base-Dry (b) NMS-Dry (c) NMS-Wet

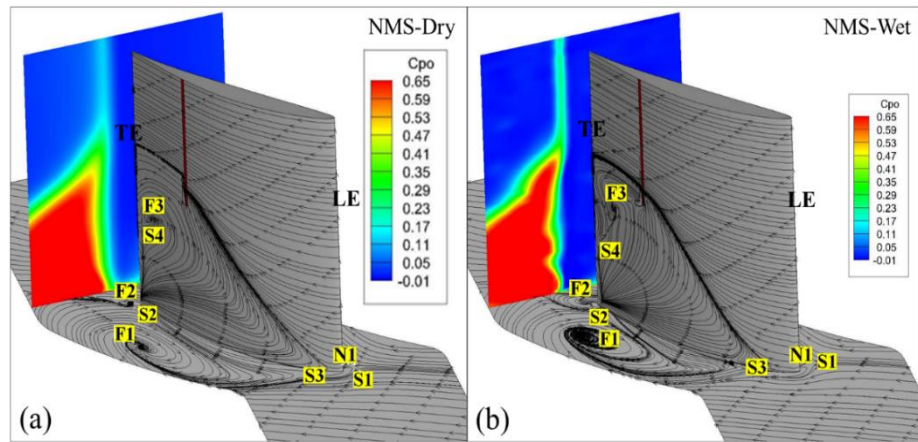


Figure 6.10 Limiting streamlines on suction surface and end wall (a) NMS-Dry (b) NMS-Wet

When analyzing the total pressure contour at the downstream location in the vicinity of the trailing edge (Figure 6.10). Total pressure loss at the region in the plane corresponding to the suction side is maximum for the wet case. However, the wake region forming aft of the trailing edge is minimized due to the injection of water in the NMS-Wet. The tendency of the pressure side leg of dividing limiting streams to be turned towards the suction side near trailing more in the case NMS-Wet. Hence the intensity of wake formation near the aft of the trailing edge gets reduced in the NMS-

Wet. Hence even if the total pressure loss contour for both these cases resembles the same, the magnitude of mass averaged total pressure loss at this plane is less in the case of NMS-Wet. It is calculated and plotted in a later section.

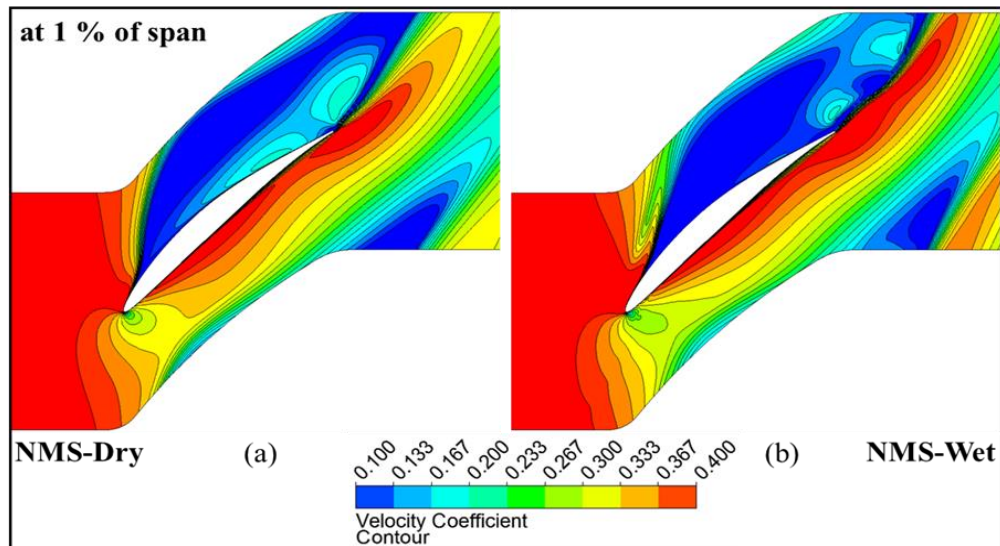


Figure 6.11 Velocity coefficient contour on the plane at 1 % of span (a) NMS-Dry (b) NMS-Wet

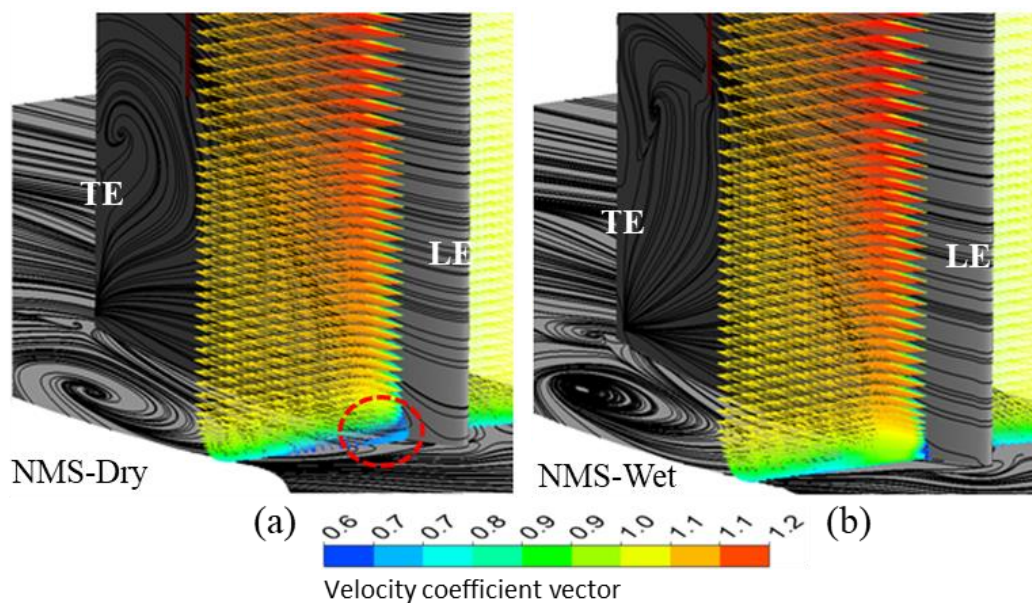


Figure 6.12 Velocity coefficient vector plotted at the initial point of separation of the dry case, $0.0095 C_{ax}$ for (a) NMS-Dry (b) NMS-Wet

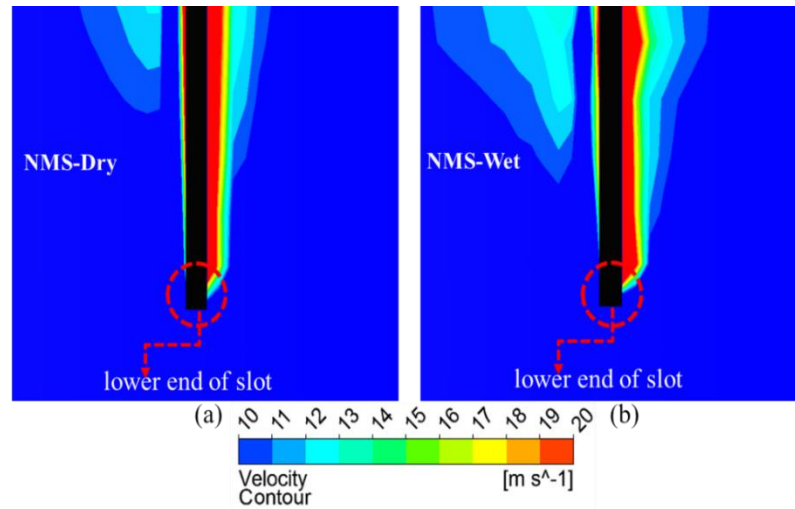


Figure 6.13 Axial velocity contour plotted on the plane normal to the blade suction surface (0.05 mm distance from the blade surface towards flow direction) (a)NMS-Dry (b) NMS-Wet

The velocity contours are plotted near endwall at 1 % of span (Figure 6.11). It shows a delayed suction surface-endwall corner separation with the NMS-wet case. The viscous effect at the corner region is reduced with the presence of water. Hence in the wet case, the fluid layer just above the wall surface attains higher velocity than in the dry case (Figure 6.12). Thus, the accumulation of low-energy fluid in this region is minimized due to the water interaction of water-air particles. The fluid near the corner in the wet case could be able to negotiate the pressure rise in the blade passage for a bit longer, resulting in the delay of hub corner separation occurring in the wet case. Thus, the focal point F1 in the wet case is shifted a little downstream than in the dry case.

The presence of lower energy fluid at a streamwise location close to the slot is slightly higher in the wet case compared to the dry case. This pulls the pressure side leg of the dividing limiting streamline to the suction side of the blade near the trailing edge region. It is evident from the plot that the pressure side leg of limiting is more turned towards the suction side. Hence the cross-flow reaching near this region becomes more spiral than in the dry case due to stronger interaction with the pressure side leg of the limiting streamline. Thus, the strength of focal point F1 is stronger compared to the dry case. The energy of the fluid at the lower end corner of the slot region is minimum for both NMS-Dry and NMS-Wet cases. This can be observed from the velocity contour plotted at the plane near the suction surface of the blade (Figure 6.13). The velocity around the

corner of the slot for both these cases is found to be minimum. However, at the lower end corner of the slot, the flow seemed to be entrained more in the NMS-Wet than NMS-Dry due to the presence of higher wall shear around the corner of the slot (Figure 6.14).

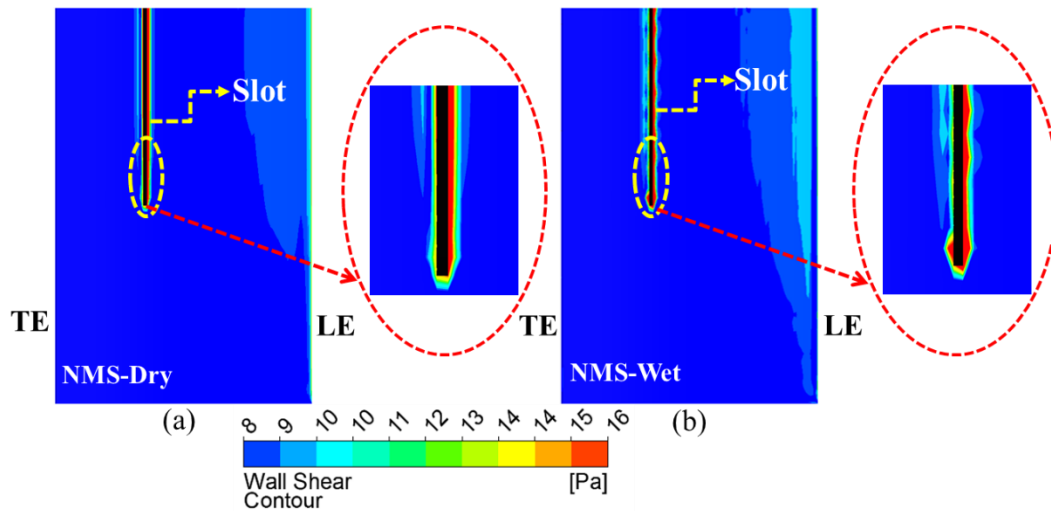


Figure 6.14 Variations in the wall shear distribution in the axial direction around the slot and the enhanced view near end wall (a) NMS-Dry (b) NMS-Wet

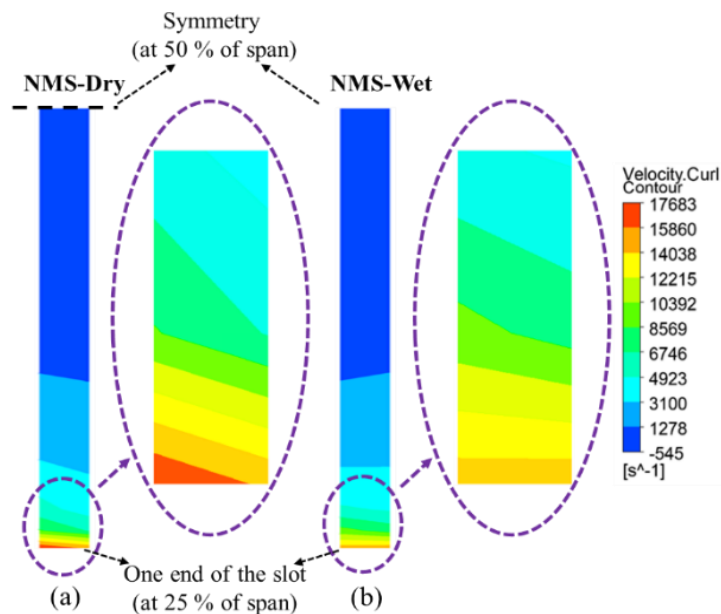


Figure 6.15 Velocity curl on the plane normal to the slot (close to the slot, 0.05 mm from the slot) (a) NMS-Dry (b) NMS-Wet

Figure 6.15 shows the contour of velocity curl normal to the slot. The distribution of velocity curl is almost similar for these cases except a slight difference is notable near the lower end of the slot. At the lower end corner of the slot, a red region is found in the contour for the dry case than the wet case. The red region indicates the positive value for the velocity curl. The presence of comparatively higher wall shear around the corner of the slot in the wet case than in the dry case is due to the injection of the water droplet (Figure 6.14). The interaction of water-air droplets reduces the viscous effect. As a result of the higher entrainment of fluid through the lower end corner of the slot in the wet case. The dividing streamlines on the separated region near the lower end of the slot are pulled to it. This is the reason for the more turning of the streamline near this region and shifting of focal point F3 a little upward along the blade height.

6.5 Effect of Water Injection on FSS Configuration

Figure 6.16 shows static pressure coefficient contours superimposed with surface streamline on the suction surface of the blade for the original cascade and the cases with boundary layer suction provided on the suction surface blade which covers the full span. The cascade without suction is shown in Figure 6.16 (a). Figure 6.16 (b and c) shows the limiting streamline for FSS-Dry suction and FSS-Wet suction respectively.

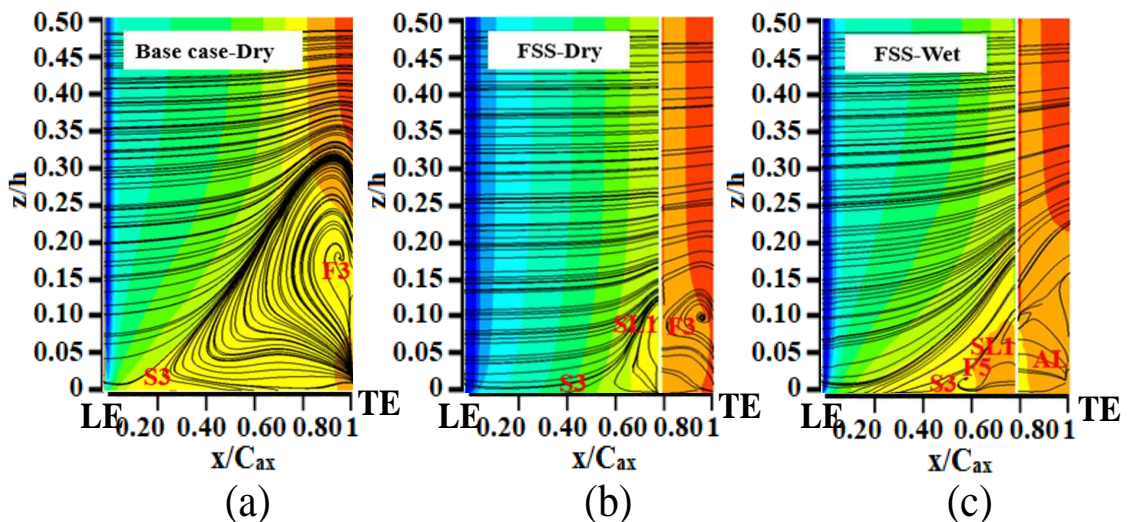


Figure 6.16 Static pressure coefficient superimposed with surface streamline on the suction surface of the blade (a) Base case-Dry (b) FSS-Dry (c) FSS-Wet

The extent of the corner separation on the suction surface of the blade near the end wall is significantly reduced in the FSS-Dry and FSS-Wet configurations. The introduction of the slot reduces the thickness and length of the separation line, indicating a less severe flow separation. The aspiration of flow through the slot causes further separation of the separated flow field along the slot axis and formed two separation lines in the FSS-Dry case, which are SL1 and S2-F3 respectively. In the FSS-Wet case, the initial separated flow field gets again separated near the slot and reattached near the trailing edge on the suction surface, the separation line and reattachment lines are named SL1 and AL respectively. Among the two FSS cases, the separation region is much more contained in the FSS dry case. With the presence of water droplets, the loss regions at the trailing edge are showing an increasing trend.

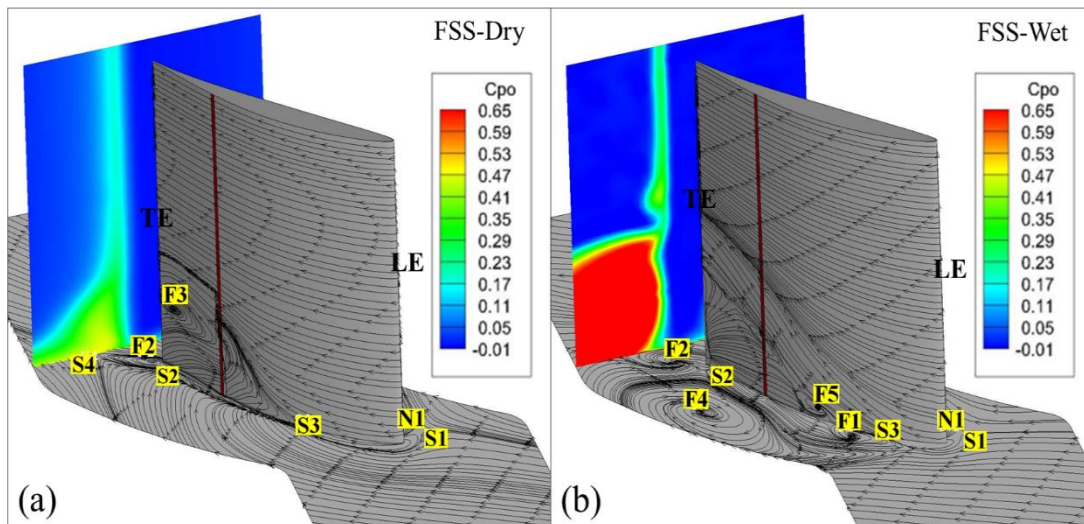


Figure 6.17 Limiting streamlines on the suction surface and end wall (a) FSS-Dry (b) FSS-Wet

Figure 6.17 shows the limiting streamlines which are drawn on the end wall and suction surface of the blade superimposed with the total pressure loss contour at the wake region. When comparing Figure 6.17 (a) and Figure 6.17 (b), it is observed that the intensity of the hub corner vortex is more in the wet case. An additional vortex is formed near the endwall- blade corner in the vicinity of the leading edge due to the interaction of the dividing streamline from saddle point S1 and the streamline of recirculated flow from the slot. When the suction flow rate is inadequate, the flow that enters the aspiration is not confined to it. It re-circulates in the form of a vortex normal to the wall

of the suction side. The focus of this vortex is named as F1. In addition to this one more vortex is formed on the end wall away from the corner of endwall-suction surface of the blade due to the interaction of the suction side leg of dividing streamline from the semi saddle point S3 and cross passage, named F4. It is already discussed that the skin friction lines from the saddle point S3 form two separate local dividing streamlines, one part of the streamline spirals to the suction surface by the action of cross passage flow. This streamline gets interacted with recirculated flow from the slot in FSS-Wet and on the suction surface of the blade near the endwall and spirals into a focal point F5. In the dry case, recirculation is not observed at the lower end corner of the slot compared to wet case and proper suction takes place in this region because the fluid near this region has lesser energy where the viscous effect is dominant. Thus, the suction rate provided is enough to suck this lower energy fluid from this region. It is evident from the velocity curl contour plot drawn on the plane near to suction slot (Figure 6.18).

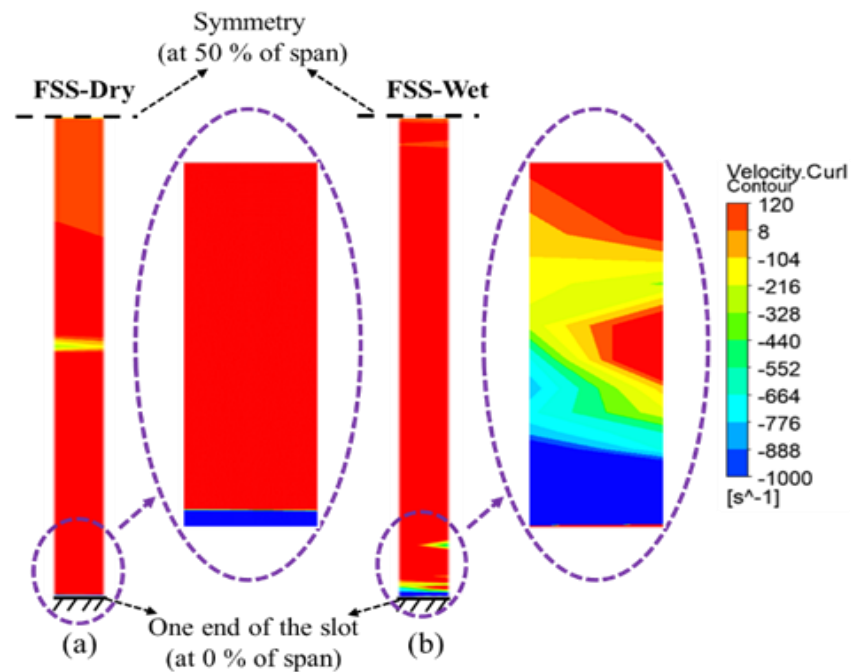


Figure 6.18 Velocity curl on the plane normal to the slot (close to the slot, 0.05 mm from the slot) (a) FSS-Dry (b) FSS-Wet

However, in the wet case, the interaction of water droplet-air reduces the viscous effect of fluid, hence fluid near this region has a little higher energy than in the dry case. As a result, proper suction is not taking place by the suction rate provided in the FSS-Wet.

The absence of recirculated flow from the slot in the FSS-Dry makes the flow more uniform near the end wall and prevents the formation of additional vortex found by the interaction of water droplets and air.

As discussed in the previous section, the pressure side leg of the dividing limiting streamlines to the suction side of the blade near the trailing edge region is due to the comparatively higher rate of suction in the wet case than in the dry case. It is evident from the plot that the pressure side leg of limiting is more turned towards the suction side. Hence the cross-flow reaching near this region becomes more spiral than in the dry case due to stronger interaction with the pressure side leg of the limiting streamline. Thus, the strength of focal point F2 in the wet case is stronger compared to the dry case.

When analyzing the total pressure contour at the downstream location in the vicinity of the trailing edge (Figure 6.17). The stronger hub-corner vortex formation led to the increased aerodynamic blockage in the wet case. Hence the total pressure loss at the downstream location of the blade the total pressure loss is more compared to the dry case. It is clearly evident from the notable difference in the total pressure loss distribution in the contour plot. Thus, the magnitude of the mass average value calculated at this plane is higher in the FSS-Dry case compared to FSS-Wet.

6.6 Comparison of Blade Loading

The blade loadings are compared for all the slot cases at the Near endwall (5 % span) and near midspan (50 % span). The loading is represented by means of static pressure coefficient C_{ps} . Near the endwall and midspan, the loading characteristics are different. For the wet cases, the loading is meagre aft the leading edge at a 5 % span. It is observed that providing slots does not improve the loading at this location, on the contrary, it reduces loading slightly. However, the slots are helpful to increase the loading for the dry cases (Figure 6.19 (a)). The FSS-dry and NES-dry cases display significant loading at a 5 % span, whereas the NMS configuration failed to provide a good loading. For the NMS configuration, the slot is located in the midspan region and it is understood from the Figure that the aspiration at the midspan region does not help to improve the loading near the end wall.

Comparing the blade loading at 50 % span reveals a similar static pressure coefficient for all the configurations at the pressure surface. Over the suction surface also the static pressure coefficient is almost similar, except near the slot region. The suction is more felt for the NMS configuration which helps to improve the blade loading.

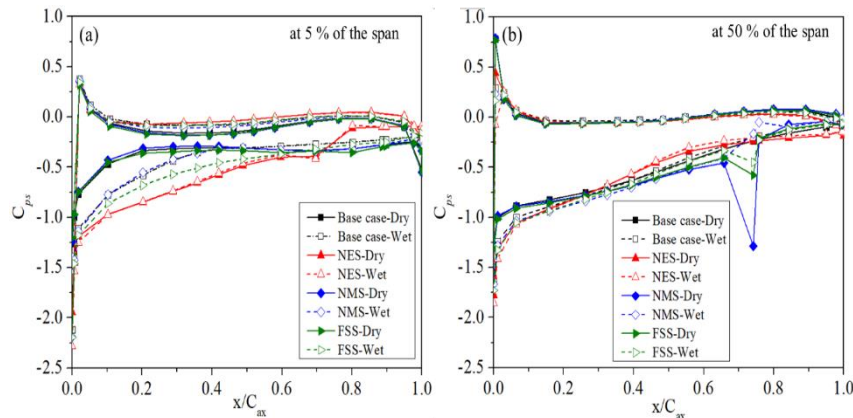


Figure 6.19 Static pressure coefficient distribution over the blade at 5 % of the span and midspan

It is found that in both NMS and FSS the suction led to an increase in blade loading between the suction slot position and the trailing edge near the mid-span, and the static pressure coefficient at the trailing edge also increased near the mid-span. Even though the flow is improved at the midspan, the blade loading was comparatively reduced in the NMS than in the FSS near the hub end wall which attributed to a higher corner separation and greater loss in the case of NMS. Suction scheme 1 (NES) can only influence the blade loading in the region of the span at which the suction slot exists. On the other hand, the other two schemes NMS and FSS not only improved the blade loading and diffusion ability at the mid-span but also near the end wall, However, comparing the flow field of NMS and FSS, FSS is more adventurous than NMS as per the analysis.

6.7 Need and Creation of Additional Configuration

6.7.1 Total pressure loss in the streamwise direction

The mass averaged total pressure loss coefficient is plotted along the axial direction from the leading edge ($0 C_{ax}$) to a downstream location of $1.45 C_{ax}$ (Figure 6.20). The

mass averaged values are calculated on several streamwise planes which are created along the blade passage. Due to the generation of recirculation of flow from the slot, additional losses have occurred in slotted configurations apart from the expected advantage of the aspiration. The total pressure loss is found to be less for all wet cases. In the NES as well as FSS the mass averaged total pressure loss of wet cases are getting increased after the slot position along the downstream direction. The rate of increase of total pressure loss is higher in the case of FSS and the magnitude of total pressure loss for the wet case is attained similar total pressure loss magnitude at 1.2 % C_{ax} . Further moving in the downstream direction, the total pressure loss is continued to increase. The total pressure loss value for the wet case and the dry case meets at a 1.4 % axial location. However, for NMS the difference in the values of total pressure loss between the wet case and dry case is found to be similar. While analyzing the magnitude of the total reduction of loss coefficient from the base case, the minimum total pressure loss is observed in the case of the FSS slot scheme (Suction scheme 3), moreover, the flow field is distributed more uniformly in this scheme. The total pressure loss is reduced by 44.68 %, and 30.03 %, with the introduction of FSS and NMS respectively with respect to the cascade of no suction.

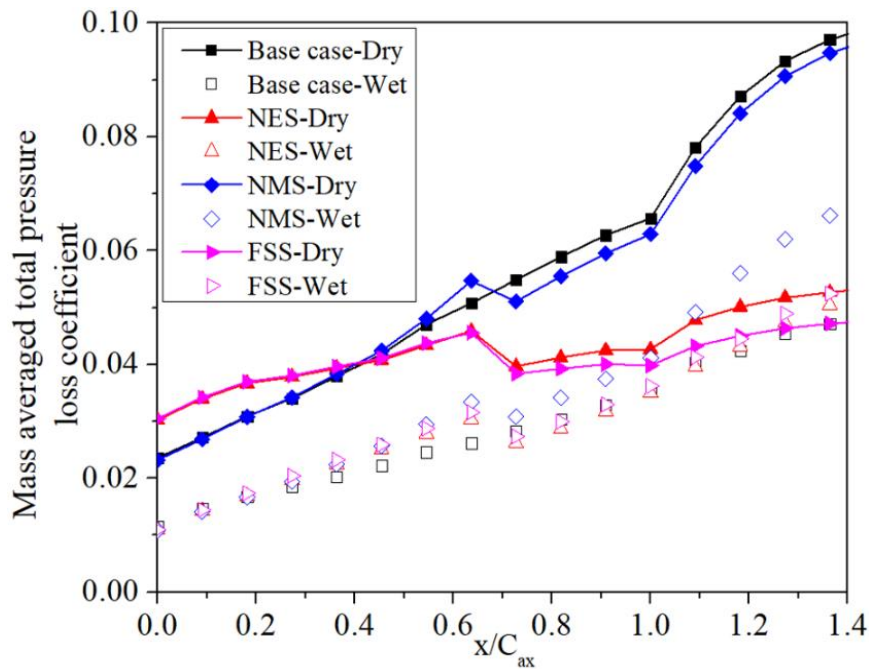


Figure 6.20 Mass averaged total pressure loss coefficient along the axial direction from leading edge to 1.45 C_{ax}

From Figure 6.20, it is observed that the combination of water injection and the suction slot has no significant advantage over wet compression. With water injection alone the losses can be brought down significantly in the blade passage. In fact, at $1.45C_{ax}$ the reduction in the loss coefficient is 52.01 % for ‘no slot wet case’. The three tested slot configurations are unable to create any more reduction in the loss coefficient. This leads to the need and creation of an additional configuration where the suction slots are provided on the blade suction surface and at the end wall also.

6.7.2 Static pressure coefficient distribution across the blade span near the suction surface of the trailing edge

The static pressure coefficient distribution across the blade span near the suction surface of the trailing edge for the cascade with no suction and each suction configuration is presented in Figure 6.21. The simulation is carried out on the half span of the blade. However, in this section, the static pressure coefficient is plotted along the full span by translating the fluid domain for discussing flow physics more conveniently.

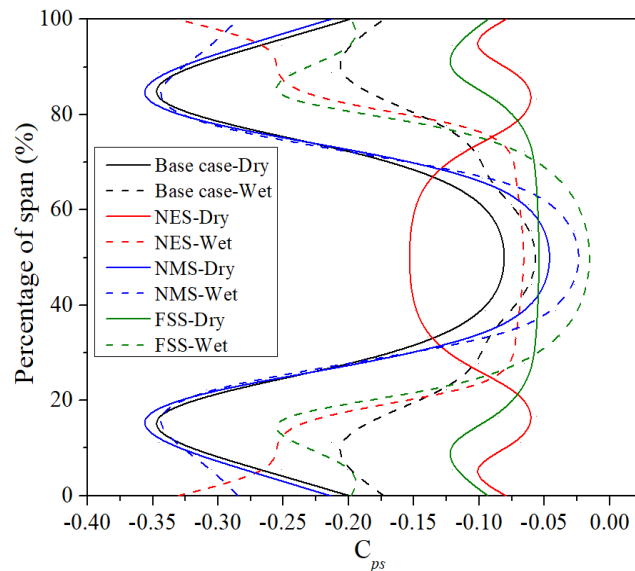


Figure 6.21 Static pressure coefficient distribution along the blade span near suction surface at trailing edge

It is observed that for the FSS aspiration the static pressure coefficient at mid-span as well as near the end-wall was improved significantly, which exhibits that the flow separation phenomenon in the blade channel is weakened and the pressure rise across the cascade was improved. However, comparing the region near the end wall and the

region away from the end wall, it is found that the static pressure coefficient is comparatively more near the midspan region than the near endwall region. It causes the movement of flow from the higher pressure gradient region (near midspan) to the lower pressure gradient (near end wall) in the FSS scheme. It may lead the additional losses near the endwall. However, the distribution of static pressure coefficient for the FSS scheme forms an “anti-C” Shape, which means static pressure is higher at mid-span than near the end-wall. Hence this kind of static pressure distribution causes the migration of low-energy fluid from mid-span to the suction surface corner which attributes to the deterioration of the flow field near the corner of the blade. Thus, other schemes of boundary layer suction are indeed for the further control of the 3D corner separation.

6.8 Combined Suction Scheme

It is observed from the previous analyses that the extent of the hub-corner vortex is minimized by the FSS configuration. The flow field becomes more uniform, reduced the aerodynamic blockage compared, and leads to minimum total pressure loss. However, the corner separation from the suction surface-endwall corner is not fully eliminated by this configuration. It emphasized that additional aspiration is required on the end wall near the corner of the suction surface of the blade for further control of corner separation in these regions. Hence an end wall suction slot is positioned from 1 to 98 % of the axial chord and 2 mm away from the suction surface with a width of 1 mm. The combined suction scheme is indicated in the discussion as FEWS. The combined slot scheme is shown in Figure 6.22.

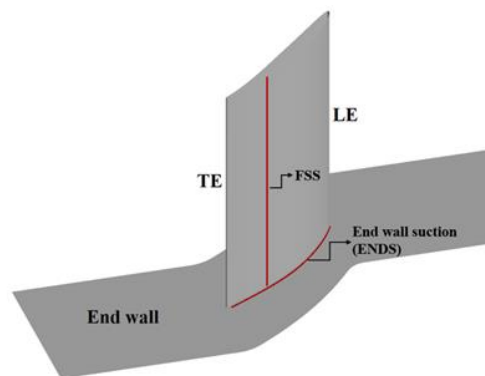


Figure 6.22 Schematic representation of combined slot scheme (FEWS)

6.8.1 The flow field analysis of the combined suction slot scheme

Figure 6.23 shows total pressure loss coefficient contours superimposed with surface streamline on the suction surface of the combined suction slot scheme for the dry case as well as the wet case. The distribution of limiting streamline on the suction surface is improved by the incorporation of end wall suction into the FSS configuration. There are no separation and reattachment lines on the blade suction surface. The static pressure coefficient at the trailing edge of the blade is raised and the flow field becomes more uniform (Figure 6.23). The boundary layer separation from the suction surface and the corner separation is reduced significantly.

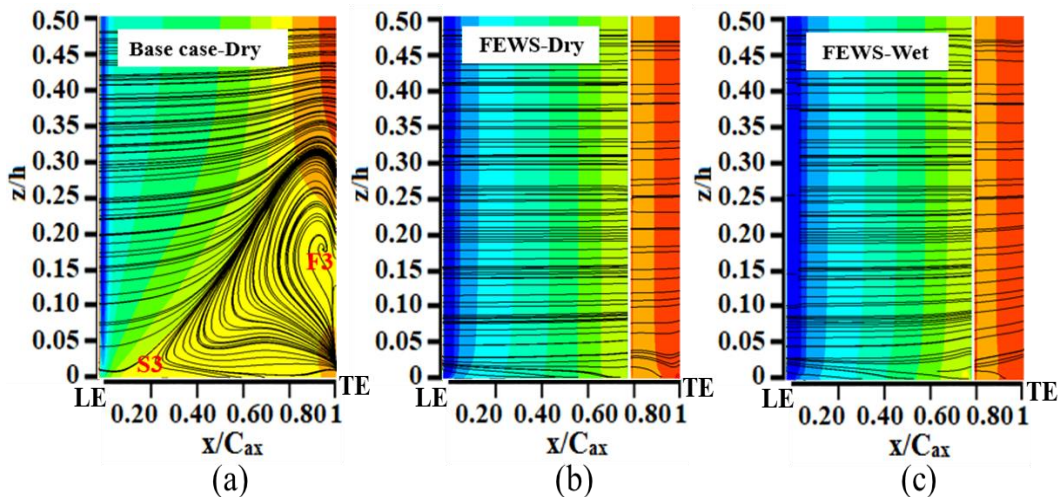


Figure 6.23 Static pressure coefficient superimposed with surface streamline on the suction surface of the blade (a) Base-Dry (b) FEWS-Dry (c) FEWS-Wet

The detailed limiting streamline is plotted in Figure 6.24. When it compares Figure 6.24 with Figure 6.17, it can be observed that termination of the suction side leg of the leading-edge horseshoe vortex (SH) has happened at a faster rate after it bypasses the leading-edge point compared to the FSS scheme.

In the wet case, the deposition of water droplets is more near the corner of the slot compared to other regions where the velocity gets decelerated due to the impingement (Figure 6.25). Thus, the water droplet particle concentration is found to be more near the corner region of the endwall slot at 98 % C_{ax} , close to the trailing edge region. The chance of deposition is comparatively less/minimum at the corner of the slot near the leading edge where the energy of the fluid is more. The accumulation of water droplets

near the corner of the slot obstructs the flow being sucked through the slot in these regions. Hence the flow is more recirculated in the wet case as a result of improper suction taking place close to the corner region of the slot in between 88.6 % and 98 % of the axial chord.

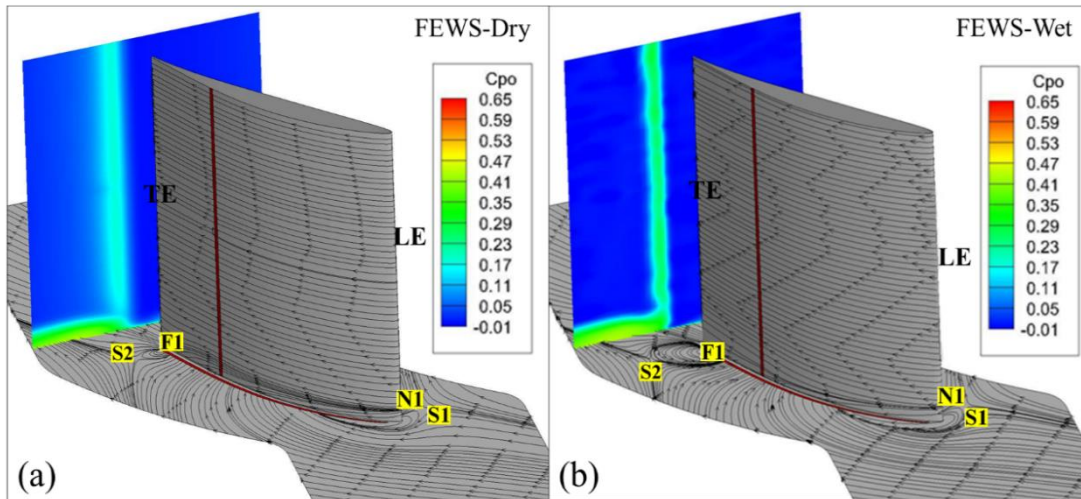


Figure 6.24 Limiting streamlines on the suction surface and end wall (a) FEWS-Dry (b) FEWS-Wet

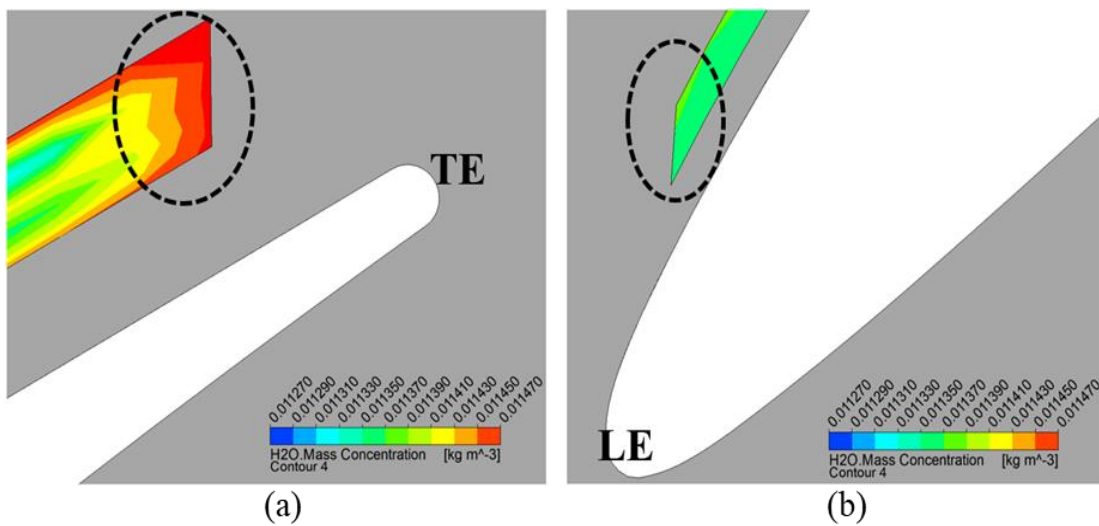


Figure 6.25 Variations in water droplet mass concentration at the corners of the end wall slot (a) at the corner near the trailing edge (b) at the corner near the leading edge

It is already noticed that the FSS configuration improves the blade loading and diffusion ability at the mid-span, but not near the end wall. With the introduction of endwall aspiration, the loading is improved considerably at a 5 % span (Figure 6.26)

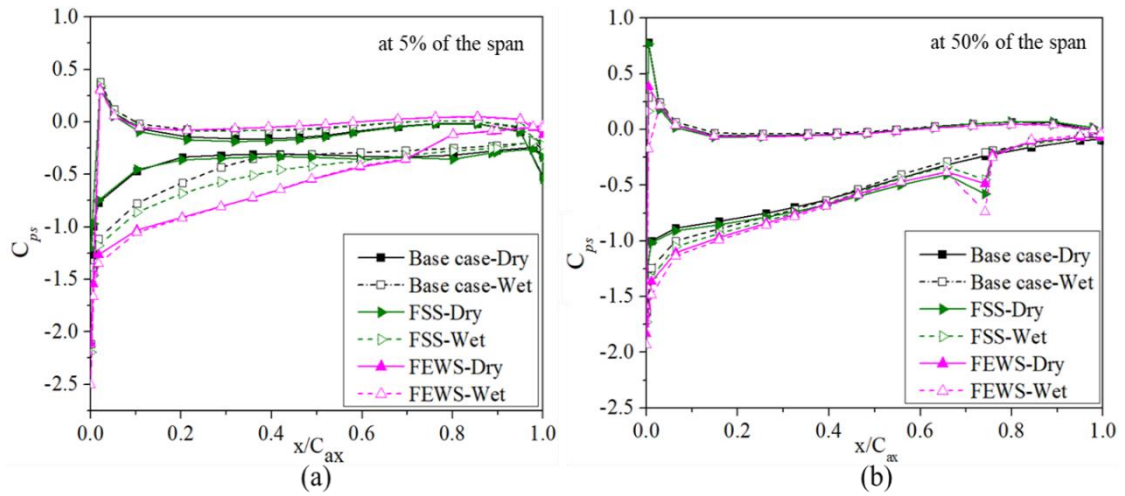


Figure 6.26 Static pressure coefficient distribution over the blade at 5 % of the span and midspan

6.8.2 Total pressure loss in the streamwise direction

It has been observed and discussed in the previous section that the implementation of the suction slot scheme FSS reduces the total pressure losses at the outlet by 52.01 %. However, the extent of hub corner separation on the blade surface is not fully eliminated. The introduction of the new scheme, “the combined scheme” further sucked the lower energy fluid and led to the reduced accumulation of lower energy near the corner of the endwall-blade corner. As a result, the intensity of hub corner separation was minimized near the end wall. It helps the further reduction of aerodynamic blockage in the blade passage. Hence the total pressure loss at the outlet gets decreased by 17.09 %. The addition of water droplets at a lower injection rate enhances the overall performance of the compressor by reducing the boundary layer effect of the wall boundary. The air-water interaction reduces the viscous effect leading to the reduction of accumulation of lower energy fluid near the endwall-blade suction surface corner and leads to the delay/reduce flow separation in the wet case. In order to depict this phenomenon by the effect of water injection, the velocity coefficient contour is plotted without considering the suction (Figure 6.27).

The velocity coefficient is observed to a minimum near blade suction surface and blade suction surface-endwall corner regions for the dry case, however the velocity coefficient is comparatively higher for wet case in these regions; which emphasizes

differences in the viscous effect in these cases (Figure 6.27). As a result, the reduction of total pressure is overcome by the effect of water injection. Hence in the FEWS, the decrement in total pressure inside the blade passage as well as the downstream location is minimized. Thus, compared to FEWS-Dry, the total pressure loss is reduced further by 57.8 % in the FEWS-Wet.

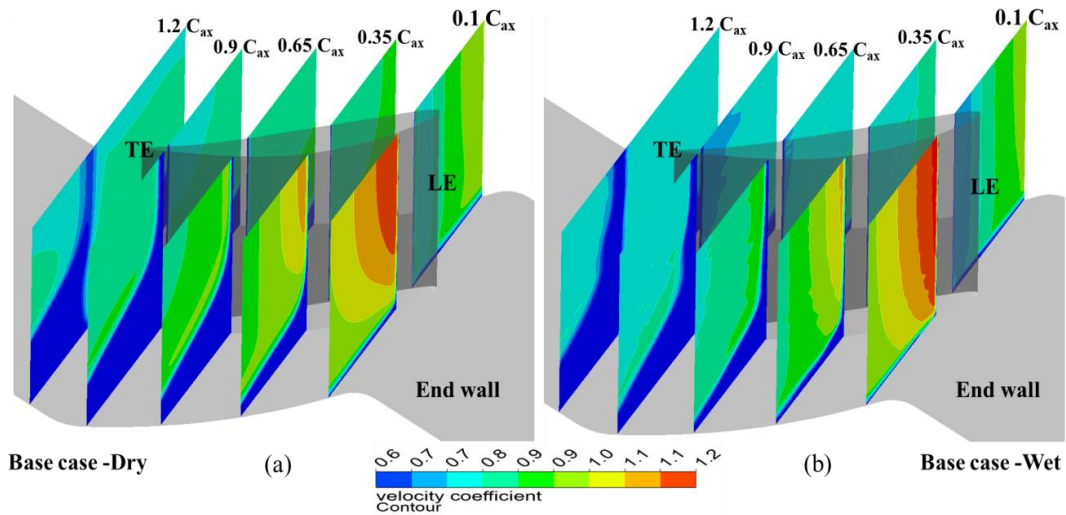


Figure 6.27 Variations of the velocity contour coefficient along the streamwise direction (a) dry case (b) wet case

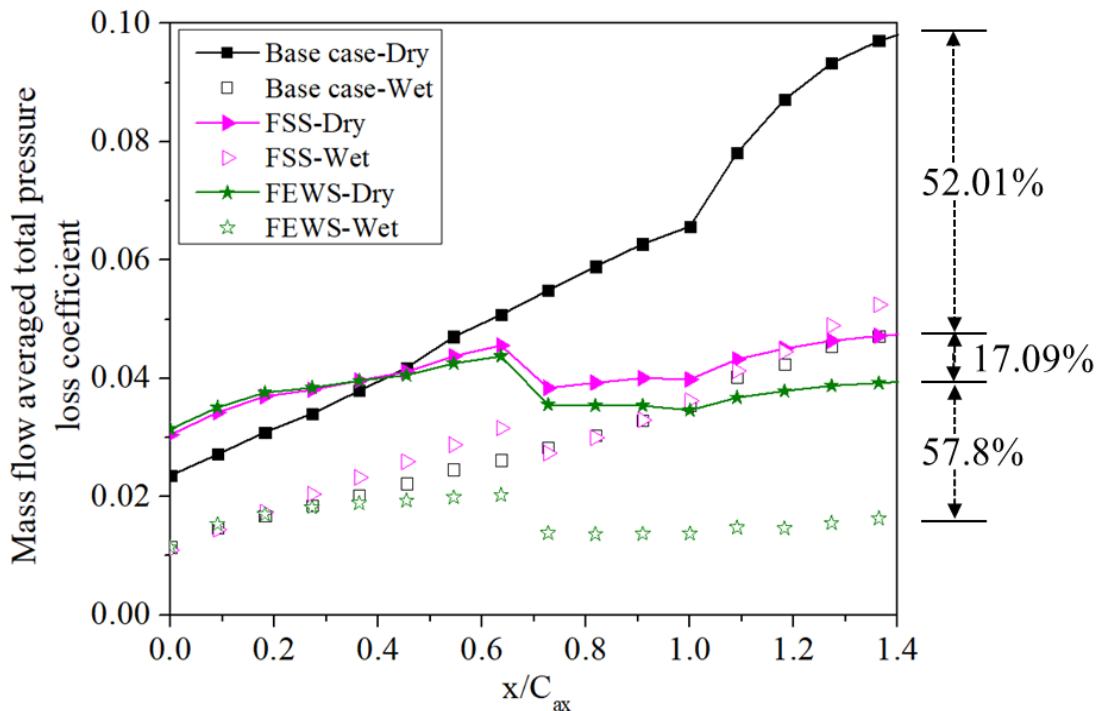


Figure 6.28 Variation of total pressure along the streamwise direction

6.8.3 Variations in the Turbulent kinetic energy

Figure 6.30 shows the variations in the turbulent kinetic energy which is plotted for dry case and wet case without slot and different slot configuration in the wet case along the flow domain from leading edge to to $1.5 C_{ax}$. It is observed that the turbulent kinetic energy gets increased while moving fom leading to trailing edge location ($1.0 C_{ax}$). After trailing edge positive slop of the graph ceases, the magnitude of turbulent kinetic energy starts decreased. While comparing the wet cases (with slot and without slot) with dry case (without slot), it is noted that the turbulent kinetic energy of dry case is having less magnitude , except from the case of FEWS-Wet which is having minimum value. It emphazies that the injection of water droplets disturbances the mainstream flow more inside the blade passage and this interaction and mixing cause the increase of turbulence inside the blade passage. The optimum slot configuration FEWS which gives better flow filed inside the blade passage could reduce the turbulence inside the flow passage as well as downstream location even in the case of water injection. The curve corresponds to the FEWS-Wet seems almost linear from leading to $1.5 C_{ax}$ of the blade.

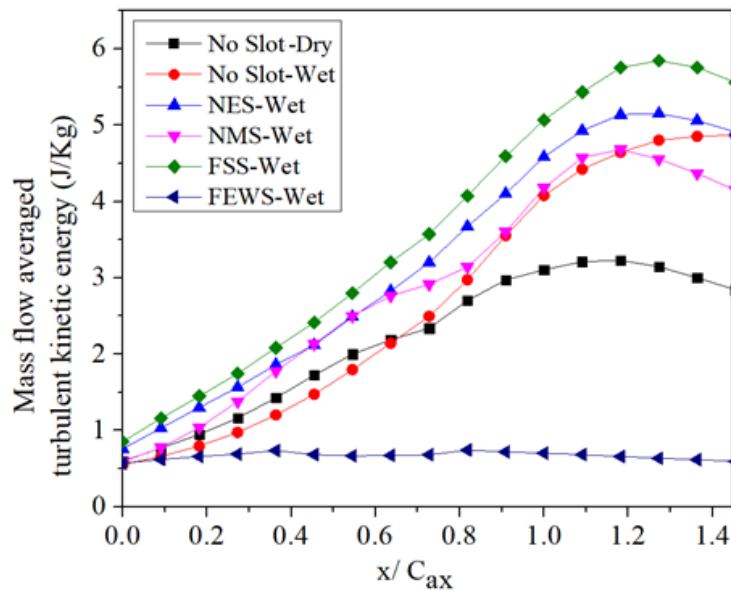


Figure 6.29 Variation of total pressure along the streamwise direction

6.8.4 Distribution of static pressure coefficient along the blade span near the suction surface of the trailing edge

The static pressure coefficient distribution across the blade span near the suction surface of the trailing edge for the cascade with no suction and combined slot scheme for both dry case as well as wet case are presented in Figure 6.30. As mentioned in the previous section, the static pressure coefficient is plotted along the full span by translating the fluid domain for discussing flow physics more conveniently. It is observed that in the FSS scheme even if the static pressure rises at mid-span as well as near the end-wall was improved significantly, the distribution of static pressure coefficient for the FSS scheme forms an “anti-C” Shape and is not able to transfer the lower energy from end wall to midspan, which causes the deterioration of the flow field near the corner of the blade. Hence it emphasizes that C-shaped static pressure distribution is good for the transfer of low-energy fluid from the end wall to the midspan. The anti-C-shaped distribution of static pressure is changed to C-shaped distribution in the combined slot scheme by the incorporation of the endwall suction slot with FSS, which is shown in Figure 6.30.

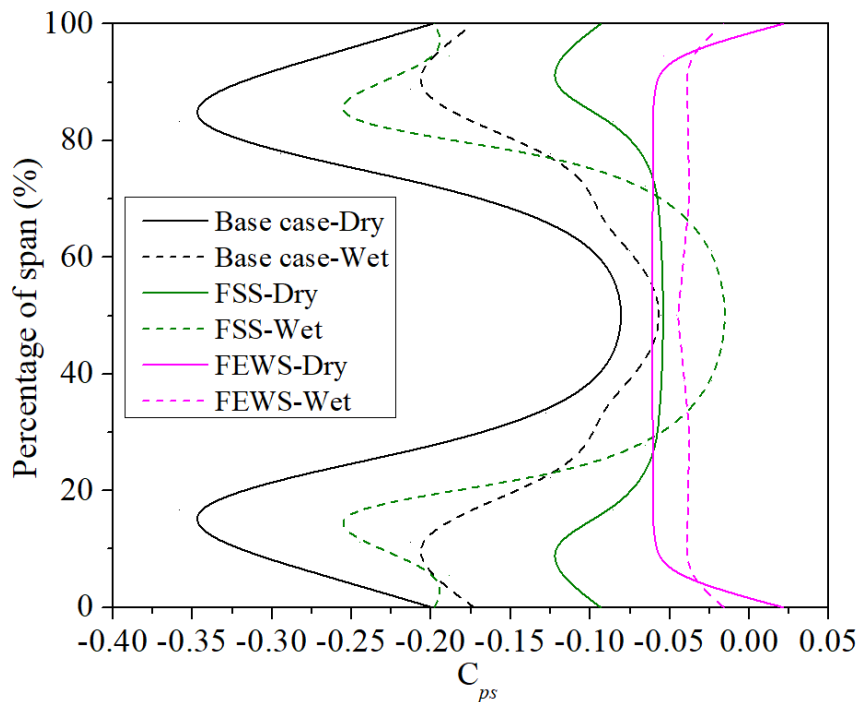


Figure 6.30 Static pressure coefficient distribution along the blade span near suction surface at trailing edge

6.9 Summary

The capability of different slotted suction configurations was examined in controlling both boundary layer separation and 3D corner separation in a highly loaded compressor cascade. The following conclusions can be formed based on the reported findings:

- The suction scheme on the suction surface along part of the blade span efficiently decreased separation in the region of the span covered by the suction slot but deteriorated the flow field at other portions of the span. The suction surface's full-span suction strategy (FSS) not only reduced boundary layer separation in the middle of the blade but also considerably enhanced flow field homogeneity near the end wall.
- Combined suction applied to the suction surface and the end-wall of the blade (FEWS) significantly improved the blade loading and diffusion ability across the whole blade span and chord. Total pressure loss is reduced by 83 % compared to the base case (cascade with no suction).
- The incorporation of injection of a water droplet with aspiration led to additional flow separation and non-uniformity in the flow field near wall boundaries in the case of non-optimum slot configurations. However, the combined slotted scheme 'FEWS' give a better aerodynamic performance. The injection of a water droplet in this case further enhanced the overall aerodynamics performance of the cascade. The total press loss at the outlet in the FEWS scheme is reduced by 57.8 % with the addition of a water droplet.

CHAPTER 7

EXPERIMENTAL ANALYSIS: FLOW VISUALIZATION

A flow visualization study has been carried out on a linear compressor cascade in the Turbomachinery Laboratory at NITK. This study aims to understand the behavior of water droplets upon impinging on the blade surface, the water film formation, and its propagation on the blade surface. The study has been carried out at different incidence angles and mainstream velocities.

7.1 Experimental Setup

For this investigation, a linear compressor cascade at the NITK Turbomachinery Laboratory has been used (Figure 7.1). It is a low-speed linear cascade, and instead of geometrical resemblance, the blades are made to be aerodynamically similar to actual machines. The wind tunnel is of a blown-down type with an axial flow fan. The circular entrance part has a conical inlet with a safety screen. A 5KW AC motor (440V, 3-Phase) with a variable frequency drive powers the fan. The settling chamber downstream of the fan consists of screens and a straw honeycomb. A water injection system is fitted downstream of the honeycomb with mist-type nozzles having a 0.1mm diameter to provide fine droplets. The water injection is sufficient upstream of the test section to ensure homogeneous water distribution for the blades in the middle of the cascade. A 0.5 HP pump with a 200-liter tank is provided for the water supply. A digital flow controller is provided to vary the injection mass flow rate. The nozzle is dismantlable (Figure 7.1 (c)). Inside the settling chamber, three nozzles are positioned with equal spacing between them. It is fitted to the root of the stem by making an internal thread. The test section is bolted to the exit of a contraction section. The cascade pack is supported by a table and is positioned on a horizontal circular base that can be moved along a vertical axis to adjust the entrance angle. The possible range of incidence angles is ± 20 degrees from the center position of the variation mechanism. The test section's maximum speed is 30 m/s. The test section (450 mm \times 120 mm) is equipped

with seven aluminum compressor blades, in a linear cascade configuration mounted between two side walls.

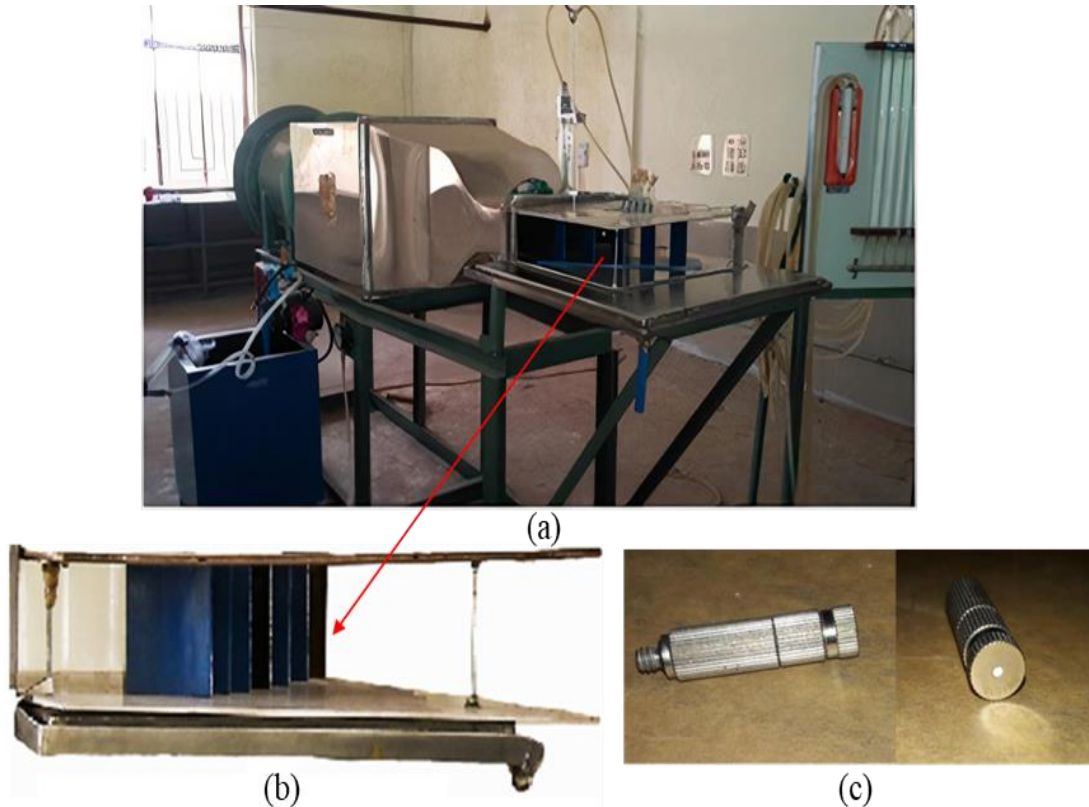


Figure 7.1 (a) Wind tunnel of low-speed compressor cascade (b) Enhanced view of cascade (c) Nozzle

7.2 Water Film Measurement and Image Processing

For the investigation of the water film pattern, a DSLR camera (Canon EOS-77D 24.3Mega pixel cropped sensor (6000x 4000 at a 22.5mm x 15 mm sensor)) with a lens (canon EF 18-135 mm f/3.5-5.6 is with 1:1.2 magnification factor) has been chosen. An external flashlight was used to capture the images (Figure 7.2). Image processing software ‘Image J’ was used to evaluate the water structures on the blade. Image J is a commercial software used for the processing of multidimensional scientific images. Error associated with the method ImageJ is normally in between 3-5 % (Bonyi et al. 2020; Hiner et al. 2017; Igathinathane et al. 2008; Rueden et al. 2017)The incoming light from the flash source is reflected from the surface of the blade. If water is present, the light is refracted at the gas-liquid interface. Hence image would be more bright

where water droplet is present, and the rest of the region seems to be dark comparatively. The image processing stages could be briefly illustrated with the images which have been taken for the case $+15^\circ$ (Figure 7.3 (a)) incidence angle at an averaged mainstream velocity of 19.19m/s. There are four major steps involved in image processing. The initial step is the pre-processing of the image (Figure 7.3 (b)) followed by various filtering techniques that result in a grayscale image along having enhanced contrast and reduced background noise with 0-225 brightness value in order to distinguish the dark region from the image.

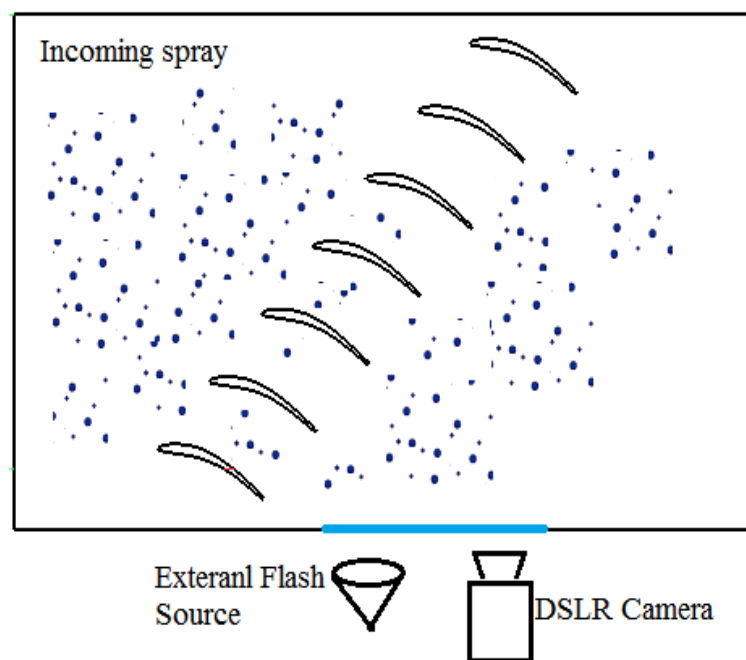


Figure 7.2 Schematic representation of water film measurement set up

In the present investigation, the bandpass filter has been used. Even though the image is undergoing this process, the resulted image will have the regions where the scattering of light occurred and regions where the amount of incidence of light is low. Hence, the chances of the unwanted bright and dark regions are there in the resulting image. The background has been blurred out. It becomes difficult to match the measuring image and background image when the brightness distribution of the background is highly non-uniform, significantly if the medium between the lens and surface of reflection alters because of the existence of water. Water alters the actual location and the background's size, leading to an illogical noise reduction. Additionally, minute

structures having a low quantity of dispersed light becomes blurred. As a result, a different method is used to process the background image. The background image's filtering for blurred dark regions is done using a Gaussian filter (Figure 7.3 (c)) so that a momentous increase in the detectability of water droplets is achieved. A CLAHE method was adopted to further improve the detection range of minute structures and ensure the global threshold, to which the contrast was accustomed (Figure 7.3 (d)). The resulting image has been passed through a sharpening stage in the second step for highlighting the edges (due to dips, projection, crack, other irregularity on the blade surface, and the presence of tracking particles), which were not visible in the unprocessed image (Figure 7.3 (e)). After this, edge finding options are enabled to the image (considered the third stage). This option made the edges more visible, which are described above. The grayscale image has been corrected with a reference image captured from the same configuration where water droplets are not present to extract the image of the object of interest from the background noise (The reference image also went through all the steps mentioned above). A subtraction of the images has been carried out so that the resulting image (processed image) is free from undesirable objects (Figure 7.3 (f)).

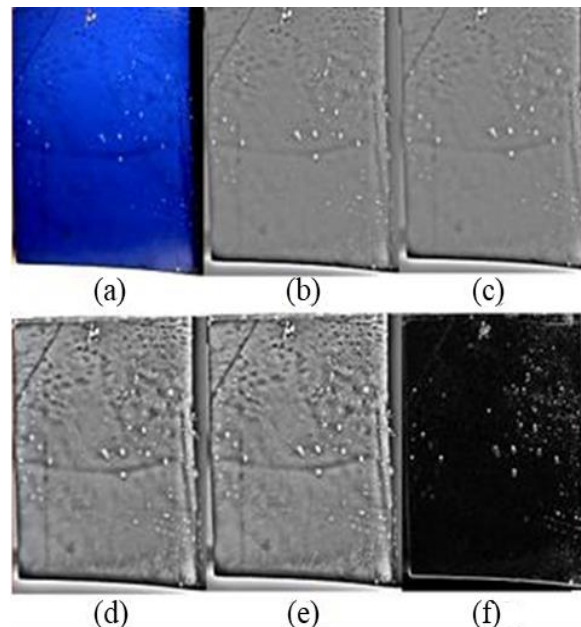


Figure 7.3 Various stages of processing of wanted image (a) Unprocessed image (b) Image after bandpass filtration (c) Image after gaussian filtration (d) Image after CLAHE (e) Sharpened image (f) Detected image.

7.3 Particle Tracking

Required samples are extracted (videos having a total time of 10s after the flow got uniform in nature) from the captured videos. These samples are used for the particle tracking process. Particle tracking is carried out using the track mate algorithm provided in the Image J software. Track mate has a modular design; it means that it is made of different modules, each having a specific role. The module types are spot detectors, spot analyzers, views, spot trackers, track analyzers, and actions. The spot detectors will take image data (In this present study DoG detector is used). The difference of Gaussian (DoG) is an algorithm with enhanced features.

In this algorithm blurred vision of an original image is subtracted from another less blurred vision. In the case of grayscale images convolving of original grayscale images with Gaussian kernel with different standard deviations is done to obtain the blurred images. Only high-frequency spatial information is suppressed during blurring an image using a Gaussian kernel. The spatial information that is present in between the range of frequencies is preserved when subtracting. Thus, it acts as a bandpass filter that passes a handful of spatial frequencies present in the original grayscale image, stops the rest of the frequencies, and detects the spots. Each spot can get a broad scope of highlights, determined from their area, span, and image information. Spot analyzers are then used to filter out deceptive spots and hold just good ones for the subsequent tracking step. The module “view” shows the segmentation and tracking results overlaid on the image data. The spot trackers module takes filtered spots and links them together to form tracks. Track analyzers act like spot trackers but operate on the entire track. It can be used to report ‘ track mean velocity,’ ‘displacement,’ etc. They are also used to filter ‘deceptive’ tracks. Finally, the ‘action’ module can extract entire tracking results.

7.4 Flow Visualization at Different Incidence Angles and Free Stream Velocities

7.4.1 Water rivulets at different incidences angles

When analyzing the deposition of water rivulets on the blade at different incidences angles, some differences are found in the region where water rivulets are being

concentrated and the total number of rivulets formed. Figure 7.4 shows the processed image of detected water rivulets for different incidences angles ($+5^\circ$, $+15^\circ$, -5° , and -15°) at time instances of the 20s, 25s, and 30s, respectively.

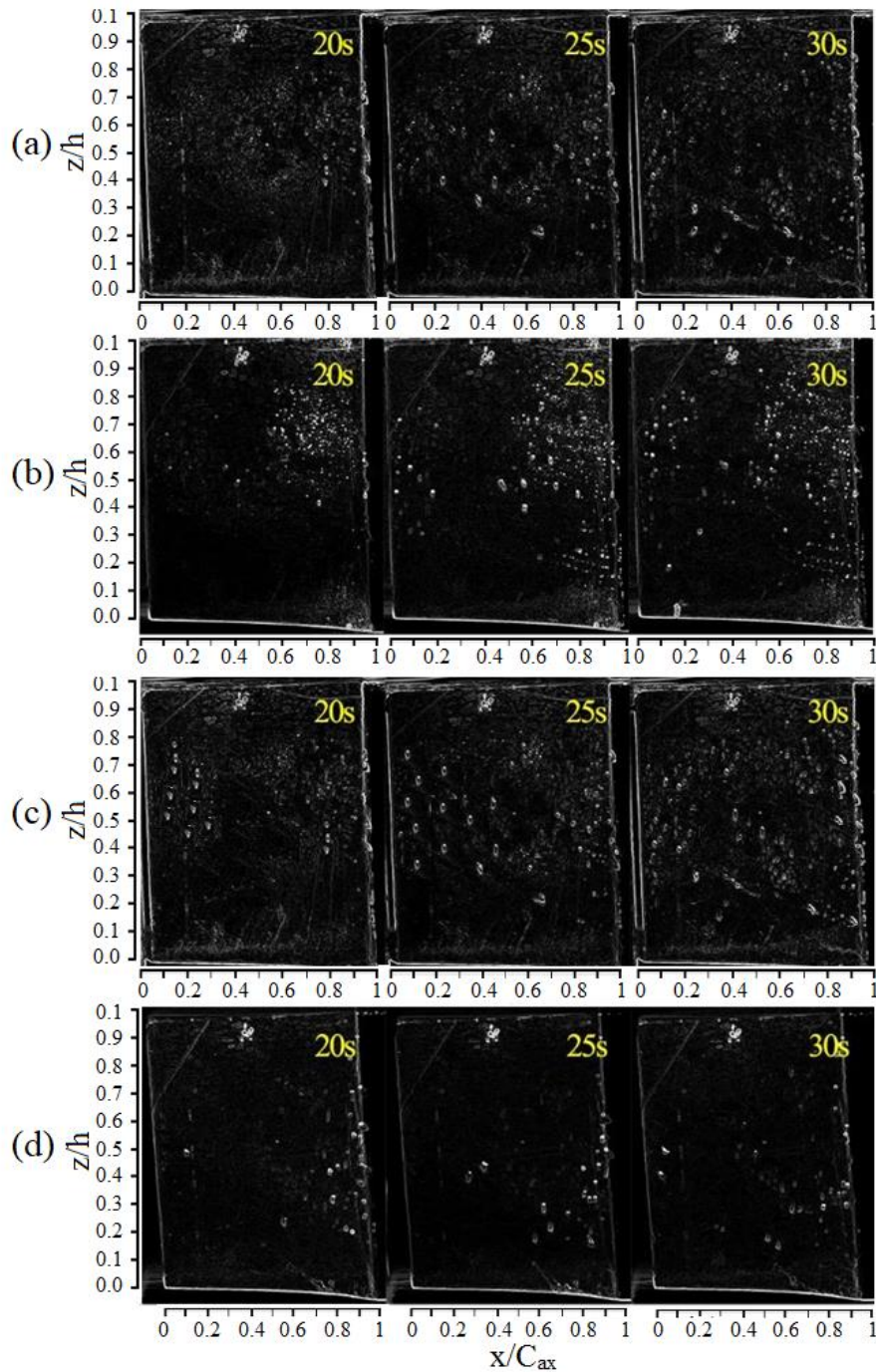


Figure 7.4 Variation of water rivulets concentration at different incidence angles at different time periods the 20s, 25s, and 30s from the experimental investigation (a) $+5^\circ$ (b) $+15^\circ$ (c) -5° (d) -15°

At lower incidence angles either positive incidence or negative incidence ($+5^\circ, -5^\circ$), water rivulets are concentrated somewhat uniformly on the entire blade region, and rivulets formed is more compared to higher incidence angles ($+15^\circ, -15^\circ$). However, at higher incidence angles, water rivulets seem to be more concentrated on the blade's top portion and trailing edge and less on the center region.

For a -15° incidence angle, small patches of water film are observed near the leading and trailing edge alone. Most of the blade suction surface is devoid of any droplet accumulation at this angle. Less concentration of water rivulets means more water is flowing as a thin layer (wall film) which is difficult to show in an image that is obtained by the processing of the captured video. Refraction happens when water is flowing as film and rivulets (rivulets mean a small stream or streamlet) are different. The film is a thin layer over the blade, hence if the light is refracted, it will be more uniform, and the threshold value of the processed image is uniform in that area. The threshold value will be much closer to the condition where water is not present. Instead of film, water is flowing as rivulets, the light will be refracted more, and such region can be distinguished easily with the help of the image processing tools.

The variations in the impact angle of the droplets on the surface of the blade cause changes in the accumulation of droplets. However, it is difficult to measure droplet size experimentally. Hence with the aid of particle tracks obtained by the numerical simulations (Figure 7.5), the changes in the accumulation of droplets at different incidence angles could be analyzed.

Moving along the axial location from the leading edge to the trailing edge region the intensity of particle impingement is found to be different in these cases and it is represented in the Figure as high-low impingement regions (HI=High impingement region, LI= Low impingement region). It is visible that at $+5^\circ$ and -5° incidence angles, particle track is denser in the region from leading to $0.8 C_{ax}$ ($0 < x/C_{ax} < 0.8$). At lesser incidence angles of $+5^\circ$ and -5° , the droplet trajectories cover almost the whole pressure surface. Hence wall film is formed over the entire pressure surface even though found a difference in the concentration of formation moving along different axial locations. For a $+5^\circ$ incidence angle, the impact angle becomes lower in the mid chord area due to the curvature of the blade. Hence in this region, wall film becomes thicker. For higher

incidence angles, the wall film formation seemed to be more near the leading edge and trailing edge regions, while the minimum occurs between these regions (Figure 7.4). When analyzing the corresponding axial locations in the Figure 7.5, it is seen that the particle track is denser near leading and trailing edge region and lesser between $0.2 < x/C_{ax} < 0.7$, $0 < x/C_{ax} < 0.7$ for 15° , -15° respectively. At a $+15^\circ$ incidence angle, the trajectory of the droplet that impinges on the pressure surface of the blade is almost parallel to the leading region, resulting in a thicker film. Moving away from the leading edge the angle of impact becomes higher. Hence, the film formed near the mid-chord region, and the trailing edge region is thin. Similar findings are observed at an incidence angle of -5° . On the other hand, the droplet trajectories hardly touch the pressure surface at a -15° angle of incidence and led to minimal wall film formation in this case.

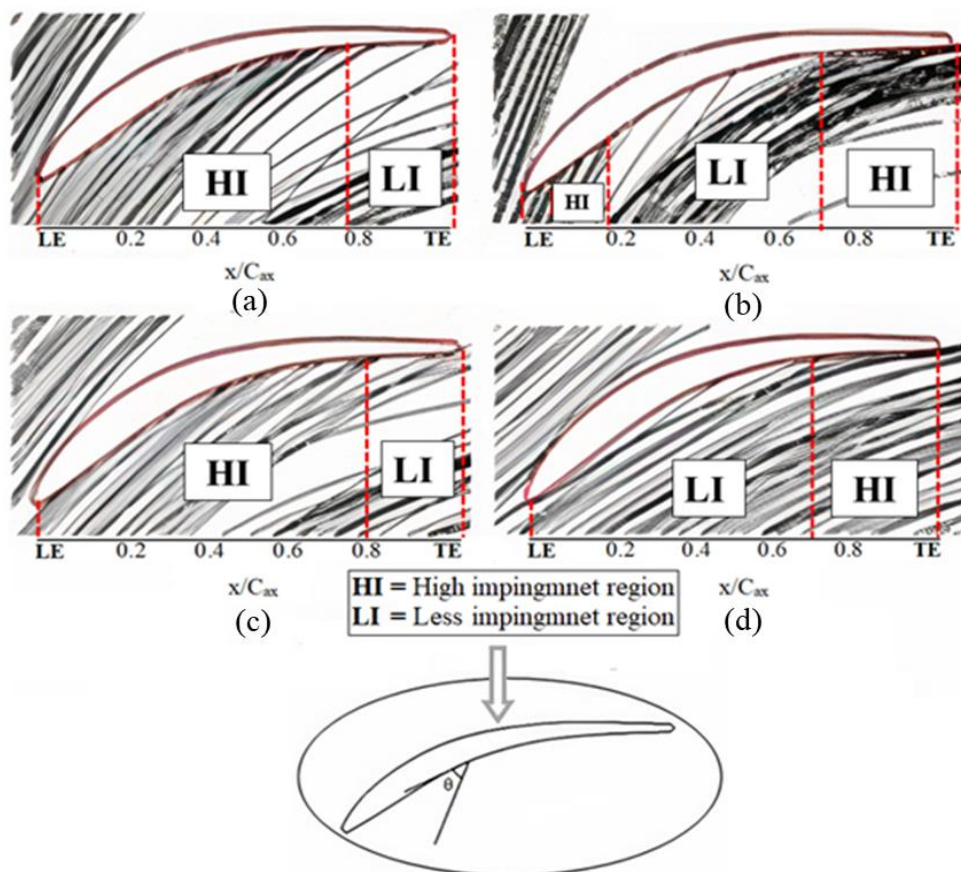


Figure 7.5 Droplets trajectories on the blade at the various angle of incidence (a) $+5^\circ$, (b) $+15^\circ$, (c) -5° , (d) -15° and (e) schematic representation of impact angle (θ)

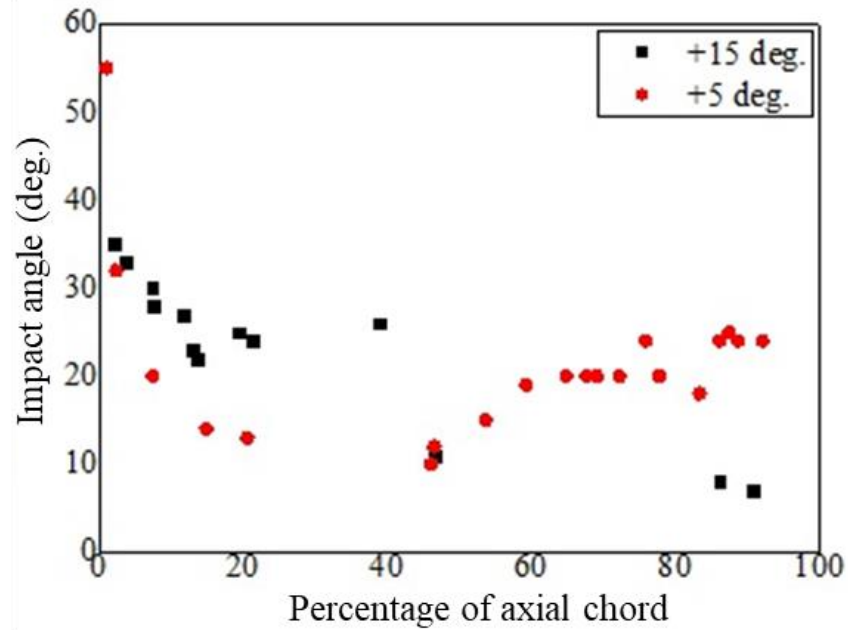


Figure 7.6 The change in the angle of impact with respect to axial location for +15° and +5° incidence angle.

For analyzing the difference in the behavior of accumulation of water droplets at lower incidence angle and higher incidence angle, the impact angle is calculated for a higher incidence angle of +15° and lower incidence angle +5° from the particle track, which is obtained from the numerical simulations (Figure 7.6). For both these cases, the angle of impact seems to be maximum adjacent to the leading edge, while the impact angle reduces towards the trailing edge at an angle of incidence +15°.

7.4.2 The water rivulets formation at different air stream velocities

When air stream velocity changes, the shear force exerted on the blade by the air stream also varies. Due to variation in shear force, the velocity of rivulet flow on the blade will be changed. Hence it affects the formation of water film and water rivulets. The aerodynamic skin coefficient ($C_{f,c}$) can be expressed in terms of surface tension, contact angle, and mainstream velocity as in Eq.7.1

$$C_{f,c} = \frac{2\sigma}{\rho_{air}U_{\infty}^2} (1 - \cos\theta) \quad 7.1$$

Variation in the skin friction coefficient leads the uniform liquid film to transition to an unstable water stream and form rivulets. From the above relation, it is seen that the skin friction coefficient will be less if the mainstream velocity is higher. Surface tension at the solid-liquid interface depends upon the contact angle, which in turn depends on the incidence angle. Due to this the water rivulets formation is different at various incidence angles and mainstream velocities. Figure 7.7 shows the behavior of water droplets at different air stream velocities (19.19m/s, 21.74 m/s,24.31 m/s, and 26.86 m/s) for zero incidence angle. It is understood from Figure 7.7 that if the air stream velocity is higher, the chances of rivulets formation are small. In compressors, flow passes through different stages via consecutive stator-rotor arrangements.

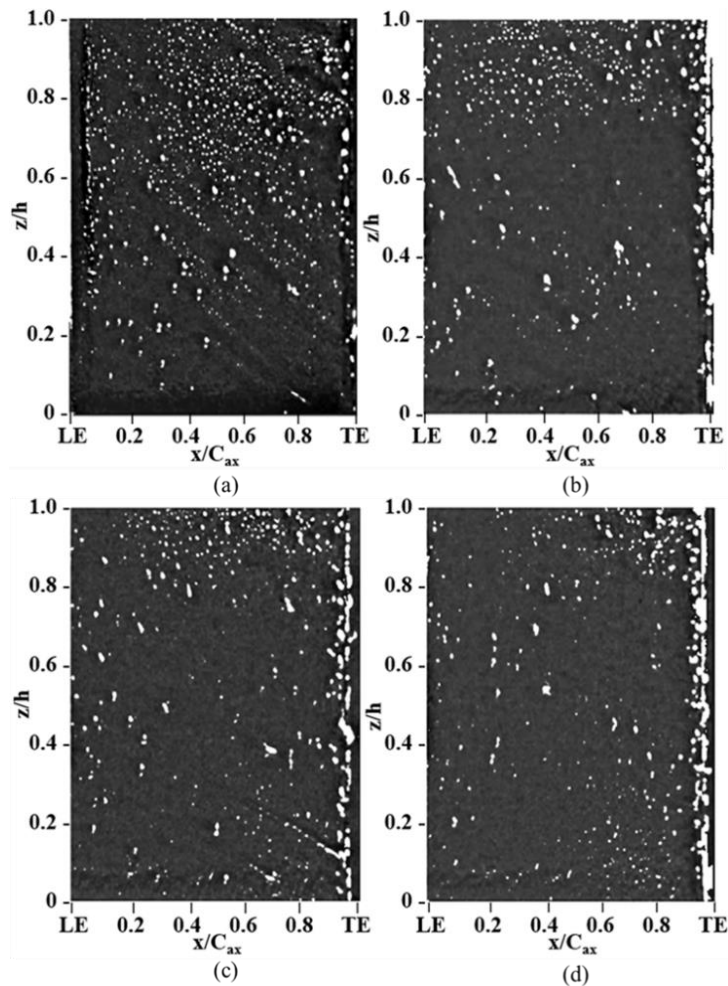


Figure 7.7 Variation in concentration of water rivulets on the pressure side of the blade for 0° incidence angle at different air stream velocity (a) 19.19 m/s (b) 21.74 m/s (c) 24.31 (d) 26.82 m/s

Hence the study of changes in water stream motion near the trailing edge is important. From the flow visualization, we observed that the water stream velocity gets reduced when it reaches the trailing edge. Small rivulets could be seen near the trailing edge's top and middle portions. All these smaller rivulets and the rivulets from the rest of the region are flowing towards the bottom side of the leading edge. Most of the rivulets collide with other rivulets and form larger rivulets and it finally seems like a secondary jet for the later stage wet compression process.

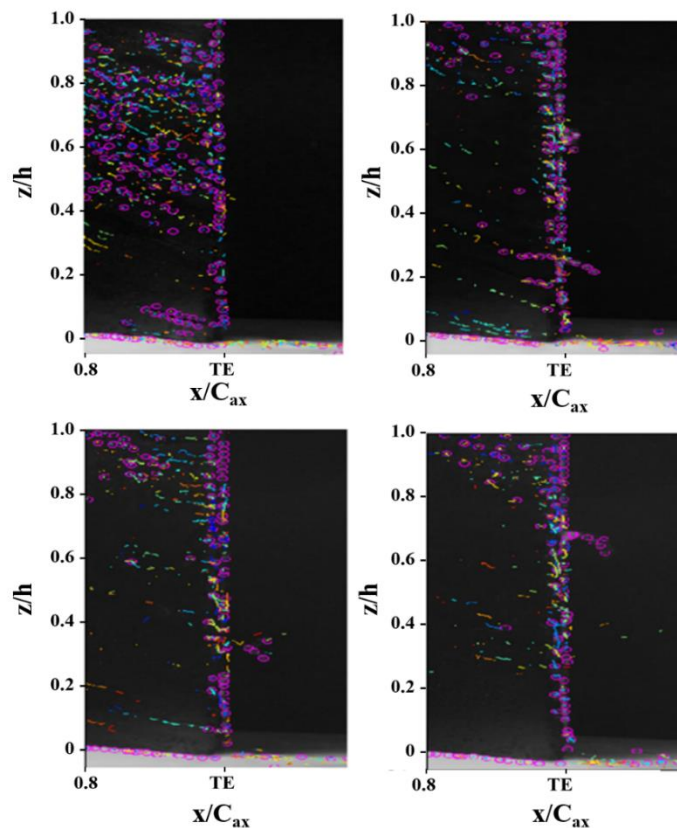


Figure 7.8 Flow modification near trailing edge for 0° incidence angle at different air stream velocity (a) 19.19 m/s (b) 21.74 m/s (c) 24.31 (d) 26.82 m/s

Figure 7.8-Figure 7.12 show the trailing edge portion of the blade after 80 % of the chord for the incidence angles and at different air stream velocities. It is evident from the Figure that most of the rivulets flow towards the trailing edge, and some of them are again disintegrated and become much smaller rivulets. The rest of the rivulets combine with adjacent rivulets and become larger rivulets and have been thrown out

from the tip of the trailing edge. It may act as a nozzle for the following stages of the compression process.

The concentration of rivulets is getting reduced for all incidence angles when the freestream velocity increases. At low velocity (19.19 m/s), water rivulets lie over the entire span near the trailing edge region (more concentrated near the top wall, in between $z/h=0.8$ and $z/h=1$). At higher velocities, the water rivulets are concentrated near the top wall region instead of spreading over the entire span of the trailing edge. The slope of the water rivulets trajectories is higher at a lower velocity, which means the rivulets are more leaned towards the bottom side of the trailing edge at lower velocities. The concentration of rivulets near the trailing edge significantly differs if incidence angles vary. Even at higher velocities, the water rivulets are present at zero incidence angles over the entire span. In the case of higher incidence angles ($+10^\circ$ and -10°), water rivulets deposition at the trailing edge is more than the lower incidence angles.

At negative incidence angles (-5° , -10°), water rivulets concentration is less than other incidence angles between $z/h=0.4$ and $z/h=0.8$. The location of splashing out of water rivulets from the trailing edge is shifting when the freestream velocities vary. At low velocities, primarily for all incidence angles, the water rivulets are sheared away from the bottom side of the trailing edge. But at higher velocities, it is shifted to the top wall region. In Figure 7.8 (a), it can be seen that the water rivulet is getting detached near the bottom side of the trailing edge at a lower velocity. When the velocity increases from 19.19 m/s to 21.74 m/s, the water rivulets are sheared away from the trailing edge at about $z/h=0.3$ (Figure 7.8 (b)). At 24.31 m/s, it is shifted more toward the top wall (water rivulets are sheared nearly at $z/h=0.4$ (Figure 7.8 (c)). Finally, at a higher velocity (26.82 m/s), the location is shifted more closely to the top wall (water is sheared away from $z/h=0.7$ (Figure 7.8 (d)). This trend is found to be the same for all the incidence angles.

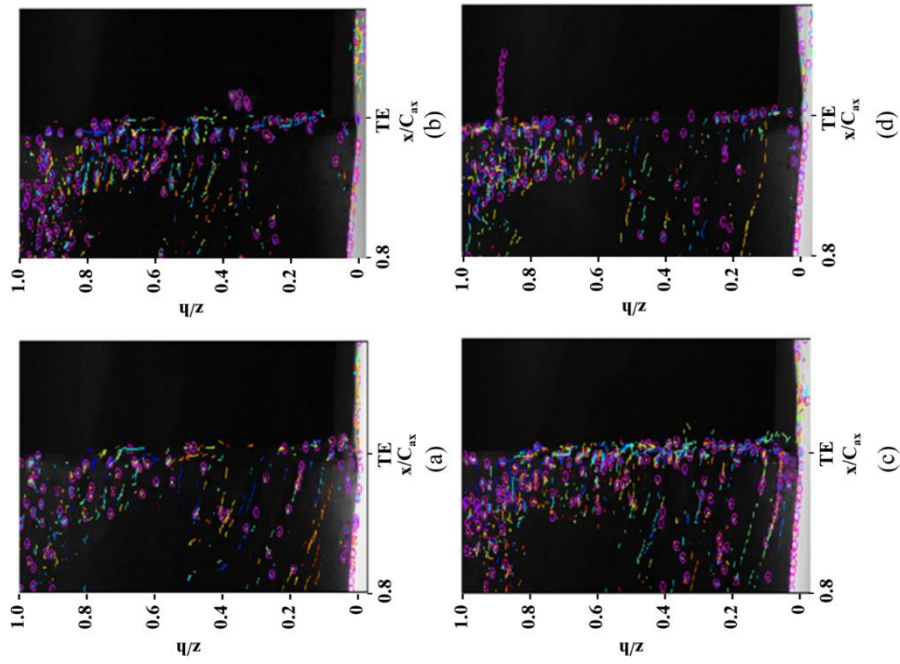


Figure 7.9 Flow modification near trailing edge for $+5^\circ$ incidence angle at different air stream velocity (a) 19.19 m/s (b) 21.74 m/s (c) 24.31 (d) 26.82 m/s

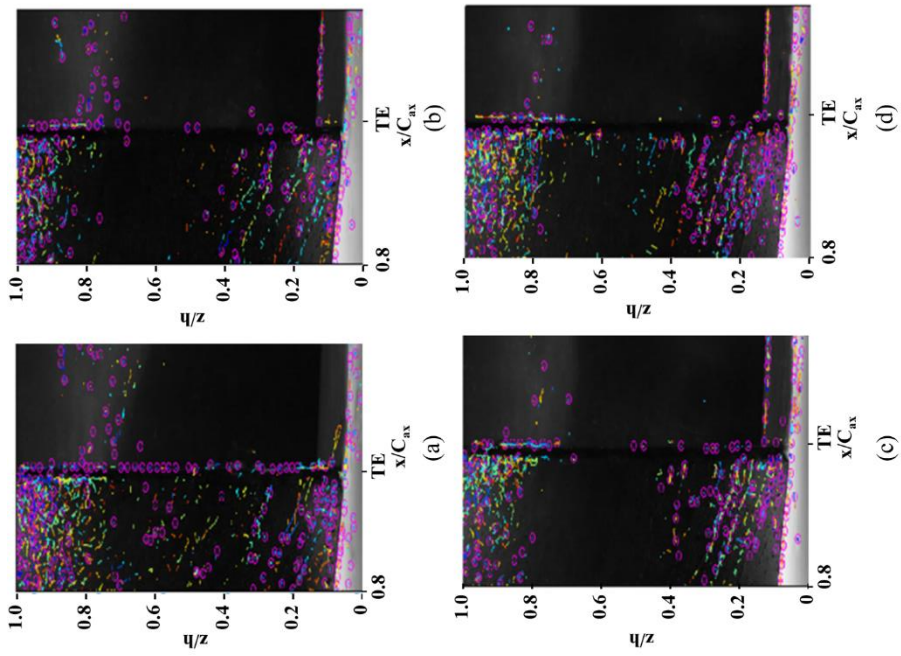


Figure 7.10 Flow modification near trailing edge for -5° incidence angle at different air stream velocity (a) 19.19 m/s (b) 21.74 m/s (c) 24.31 (d) 26.82 m/s

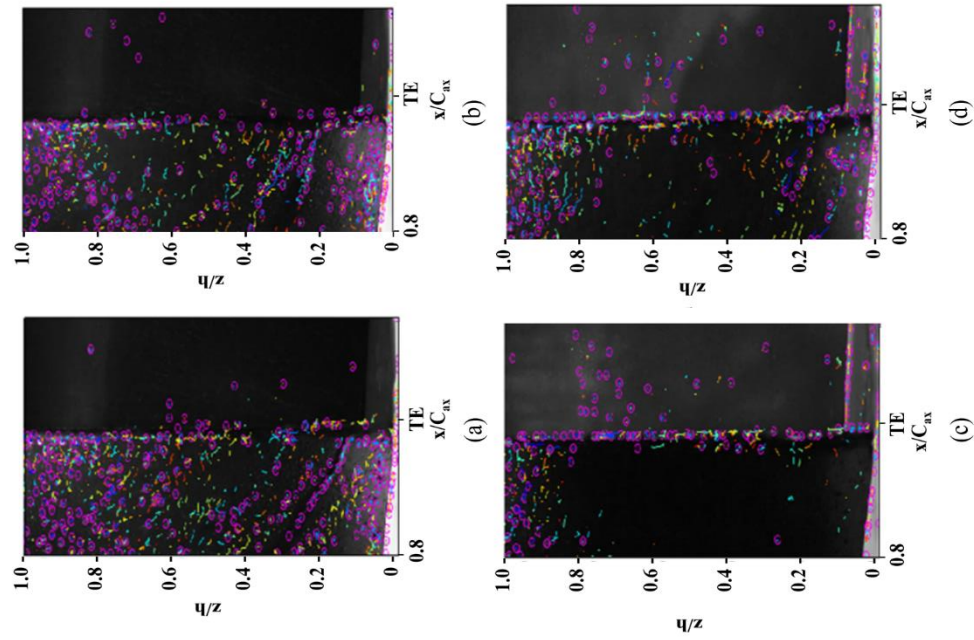


Figure 7.11 Flow modification near trailing edge for -
 10° incidence angle at different air stream velocity (a)
 19.19 m/s (b) 21.74 m/s (c) 24.31 (d) 26.82 m/s

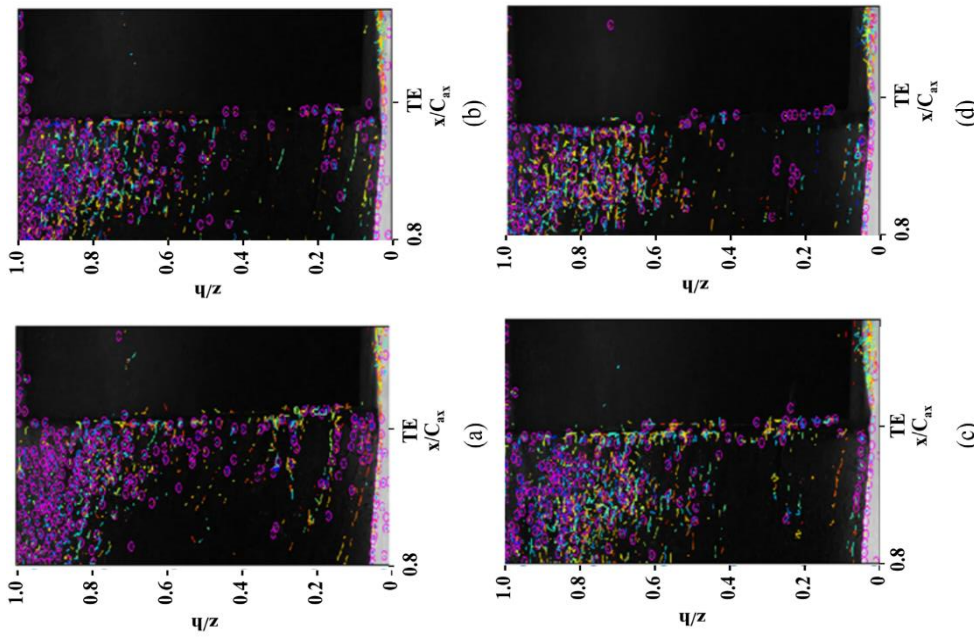


Figure 7.12 Flow modification near trailing edge for + 10° incidence
 angle at different air stream velocity (a) 19.19 m/s (b) 21.74 m/s (c)
 24.31 (d) 26.82 m/s

7.5 Summary

- The water film formation is found to be more dominant at pressure surface compare to suction surface.
- A higher impact angle can be seen near the leading edge region, whereas downstream, a smaller impact angle is obtained due to the camber of the blade.
- The amount of water deposited on the blade is determined by the impact angle, which in turn influences the film thickness on the blade.
- The amount of deposited water decreases with the increase of water velocity and increases with the low velocity at a low impact angle. At negative incidence angles, the film thickness is smaller than the positive incidence angles.
- The skin friction coefficient causes the transition of uniform liquid flow film to an unstable water stream and to form rivulets. Hence it can be stated that if water rivulets are more the water film flow is less, in vice versa the water film flow is more when the water rivulets presence is less
- Surface tension force causes the disintegration of these rivulets into small rivulets that convect individually toward the trailing edge where they coalesce into a larger stream of water. Then this stream is sheared away from the trailing edge by the external flow and is transported into the downstream wake (act as a secondary nozzle for the next stage of compression).
- The location of transportation of water rivulets from the trailing edge is getting shifted when the free stream velocities vary. At low velocities mostly for all incidence angles, the water rivulets are sheared away from the bottom side of the trailing edge but at higher velocities, it is shifted to the top wall region.

CHAPTER 8

CONCLUSIONS AND SUGGESTIONS FOR FUTURE WORK

8.1 Conclusions

In this work, water injection's effect on the compressor cascade's aerodynamic characteristics is investigated numerically and experimentally. Three-dimensional Reynolds-averaged Navies-Stokes equations coupled with the SST turbulence model are used for the numerical simulations. Experimental studies are carried out with flow visualization techniques.

The present investigation has five-parts. The first four parts are carried out by steady-state numerical simulations only. Simulations are carried out for both dry and wet cases. An experimental study is conducted in the last part for analyzing the water film formation and its propagation on the pressure surface of the blade. The first part involves the study of flow in compressor cascade with water injection at various incidences angles ranging from -8° to 8° . It can be seen that at higher incidence angles, the effect of water injection plays a key role in delaying flow separation and increasing the overall performance of the cascade. Hence higher incidence angle $+6^{\circ}$ is chosen apart from selecting incidence angles $-6^{\circ}, -8^{\circ}, 8^{\circ}$ for the further study by considering the design aspect also. The second part of study is the analysis of flow in the cascade by varying droplet size from $12\ \mu\text{m}$ to $60\ \mu\text{m}$ at fixed incidence angle $+6^{\circ}$. Among the five droplet, sizes, it is found that $20\ \mu\text{m}$ and $32\ \mu\text{m}$ gives minimum loss coefficient and flow separation. In the third part of study), flow is analysed at various injection ratios (0.5 to 4 %) by keeping incidence angle ($+6^{\circ}$) and droplet size constant ($20\ \mu\text{m}$). The analysis has reached in a finding that 1-2 % injection ratios gives better aerodynamic performance. Even if the water plays a vital role in the control of the flow separation occurs in the cascade, it is observed that an additional flow control method is necessary for the further elimination of the flow separation and enhance the overall aerodynamic performance of the cascade, which leads to increased efficiency of the system. The

suction slot helps to minimize boundary layer growth and helps to delay the flow separation. However boundary layer suction on the blades is already a well-established technique in the field of turbo machines. But the concept of incorporating of boundary layer suction with wet compression technology would be a new method. The fourth part of study is thus water injection in the active flow control environment. For these cases incidence angle (6^0), droplet size ($20\ \mu\text{m}$) and injection ratio (1 %) are kept constant. The values are taken from the previous parts of the study. Literature says that in the water injection case, water droplets will accumulate on the surface of the blade, where water films may develop on the pressure surface. Water film has aerodynamic, thermodynamic, and mechanical impacts on gas turbine engines. Droplet impacts may increase the effective roughness of the surface that the airflow experiences, which leads to the earlier transition of the boundary layer and deteriorated aerodynamic performance. Hence, the formation of water film and its propagation on the blade surface is studied in the last part of this research work

Simulations are carried out for dry and wet cases. It is observed that the mass flow averaged total pressure loss coefficient is reduced inside the blade passage by the introduction of water droplets. The loss coefficient at the exit is reduced by 32.7 % for the zero-incidence angle with the introduction of water droplets. Water injection is more beneficial in the positive incidence angles than the negative. However, the presence of water droplets enhances the flow separation near the endwall and causes an increase in the loss coefficient near the endwall region. Studies with different droplet sizes indicate that the flow angle deviation is higher in the case of smaller droplet sizes ($12\ \mu\text{m}$) and larger droplet sizes ($48\ \mu\text{m}$ and $60\ \mu\text{m}$). The deviation is found to be minimum at $20\ \mu\text{m}$ and $32\ \mu\text{m}$. Water injection with a moderate droplet diameter size enhances the aerodynamic performance of the size, however, the injection with a smaller droplet size and higher droplet diameter adversely affects the performance of the compressor cascade. The formation of secondary flow due to the corner separation is found to be minimum in the case of moderate droplet size $32\ \mu\text{m}$. The impact of droplet size on blade loading and loss coefficient in the blade passage is being studied. Total pressure loss is reduced by 54 % with water injection having a droplet size of $32\ \mu\text{m}$. The studies indicate the possibility of optimum droplet size in the range of $20\ \mu\text{m}$ and $30\ \mu\text{m}$.

Similar studies are carried out with injection ratio and it is revealed that total pressure loss is reduced by 54 % injection ratio of 2 %

In the second part of the thesis influence of an active flow control method is studied in the presence of water injection. The capability of different suction slot configurations is examined in controlling boundary layer separation and 3D corner separation in a highly loaded compressor cascade. The suction scheme on the suction surface along part of the blade span efficiently decreased separation in the region of the span covered by the suction slot. Still, it deteriorated the flow field at other portions of the span. The suction surface's full-span suction strategy (FSS) not only reduced boundary layer separation in the middle of the blade but also considerably enhanced flow field homogeneity near the endwall. Due to the large cross-passage pressure gradient commonly observed in highly loaded blade rows, this suction strategy could not entirely remove the 3D separation near the end-wall. Combined suction applied to the suction surface and the end-wall of the blade (FEWS) significantly improved the blade loading and diffusion ability across the whole blade span and chord. The total pressure loss coefficient is reduced by 83 % compared to the base case (no suction).

Experimental study through flow visualization is carried out. The water rivulet formation on the blade surface is analyzed. The amount of water rivulet formed is more in the case of smaller incidence angle ($+5^\circ$, -5°), and in the case of higher incidence angle, deposition of water is comparatively less. The successive water rivulets move towards the trailing edge; from there, it detaches from the blade surface at specific locations in the blade span. These locations act as secondary ejection points of the water to the succeeding row in a multistage compressor. The secondary ejection points are found to be varying at different incidence angles.

8.2 Suggestions For Future Work

The present study is undertaken on a linear turbine cascade. As a future prospect, the study may be extended to an annular cascade wherein the rotational effects are also present. Experimental analysis of the active flow control method can be done in the water injection environment. The flow visualization of water rivulets formation and its propagation can be undertaken by varying droplet diameter sizes and nozzles.

REFERENCES

Afshari, A., Azarpeyvand, M., Dehghan, A. A., and Szoke, M. (2016). “Trailing edge noise reduction using novel surface treatments.” *22nd AIAA/CEAS aeroacoustics Conf.*, 2834.

Afshari, A., Azarpeyvand, M., Dehghan, A. A., and Szoke, M. (2017). “Effects of streamwise surface treatments on trailing edge noise reduction.” *23rd AIAA/CEAS Aeroacoustics Conf.*, 3499.

Alam, H., Sasso, J., and Djunaedi, I. (2015). “Performance Enhancement of Gas Turbine Power Plant via Wet Compression Technique and Its Effects on Economic Aspects.” *Br. J. Appl. Sci. Technol.*, 11(1), 1–12.

Alstrom, R. B. (2013). “Aerodynamic flow control of a high lift system with dual synthetic jet arrays.” Doctoral dissertation, Clarkson University.

Arivoli, D., and Singh, I. (2016). “Self-adaptive flaps on low aspect ratio wings at low Reynolds numbers.” *Aerosp. Sci. Technol.*, 59, 78–93.

Atlantic, N., Organisation, T., and Organisation, T. (2002). “Performance prediction and simulation of gas turbine engine operation. ” RTO Technical Report 44, 1, 3-39, 40, 47

Bagnoli, M., Bianchi, M., Melino, F., Peretto, A., Spina, P. R., Bhargava, R., and Ingistov, S. (2004). “A parametric study of interstage injection on GE frame 7EA gas turbine.” *Proc. ASME Turbo Expo 2004*, 4, 489–499.

Bario, F., Leboeuf, F., and Papailiou, K. D. (1982). “Study of secondary flows in blade cascades of turbomachines.” , 497-509.

Bhargava, A., Colket, M., Sowa, W., Casleton, K., and Maloney, D. (2000). “An experimental and modeling study of humid air premixed flames.” *J. Eng. Gas Turbines Power*, 122(3), 405–411.

Bhargava, R. K., Meher-Homji, C. B., Chaker, M. A., Bianchi, M., Melino, F., Peretto,

A., and Ingistov, S. (2007). “Gas turbine fogging technology: A state-of-the-art review - Part II: Overspray fogging - Analytical and experimental aspects.” *J. Eng. Gas Turbines Power*, 129(2), 454–460.

Bhargava, R., and Meher-Homji, C. B. (2005). “Parametric analysis of existing gas turbines with inlet evaporative and overspray fogging.” *J. Eng. Gas Turbines Power*, 127(1), 145–158.

Bonyi, E., Kioko, B., Meyer, C. S., Adesina, O., Obafemi-Babatunde, T., Guy, J., O’Brien, D. J., Haque, B. Z., Gillespie Jr, J. W., and Aslan, K. (2020). “Toward automated identification and quantification of meso-scale damage modes in plain weave glass/epoxy composite laminates.” *Int. J. Damage Mech.*, 29(5), 831–848.

Brun, K., Kurz, R., and Simmons, H. R. (2006). “Aerodynamic instability and life-limiting effects of inlet and interstage water injection into gas turbines.” *J. Eng. Gas Turbines Power*, 128(3), 617–625.

Cao, Z., Gao, X., Zhang, T., and Liu, B. (2020). “Flow mechanism and aspiration strategies in an ultra-highly loaded supersonic compressor cascade.” *Aerosp. Sci. Technol.*, 104, 105989.

Cao, Z., Zhang, X., Zhang, F., Song, C., Gao, X., and Liu, B. (2021). “Tip leakage vortex and its breakdown mechanism in aspirated compressor cascades designed with conventional method and curvature induced pressure recovery concept.” *Aerosp. Sci. Technol.*, 113, 106692.

Cater, J. E., and Soria, J. (2002). “The evolution of round zero-net-mass-flux jets.” *J. Fluid Mech.*, 472, 167–200.

Chaker, M., Meher-Homji, C. B., and Mee, T. (2004a). “Inlet fogging of gas turbine engines-part I: Fog droplet thermodynamics, heat transfer, and practical considerations.” *J. Eng. Gas Turbines Power*, 126(3), 545–558.

Chaker, M., Meher-Homji, C. B., and Mee, T. (2004b). “Inlet fogging of gas turbine engines - Part II: Fog droplet sizing analysis, nozzle types, measurement, and testing.” *J. Eng. Gas Turbines Power*, 126(3), 559–570.

- Chen, P. P., Qiao, W. Y., Liesner, K., and Meyer, R. (2014). “Location effect of boundary layer suction on compressor hub-corner separation.” In *Turbo Expo: Power for Land, Sea, and Air*, vol. 45608, p. V02AT37A003. American Society of Mechanical Engineers.
- Dam, C. P. Van. (2002). “The aerodynamic design of multi-element high-lift systems for transport airplanes.” *Prog. Aerosp. Sci.*, 38(2), 101–144.
- Dayyabu Gambo Kofar-bai, Qun Zheng, Hai Zhang, and Adil Malik. (2018). “The Influence of Water Droplets on the Heat and Mass Transfer of the Wet Compression of Single Stage Compressor.” *Int. Energy J.*, 17, 257–270.
- Donovan, J., Kral, L., and Cary, A. (1998). “Active flow control applied to an airfoil.” *36th AIAA Aerosp. Sci. Meet. Exhib.*, p 210.
- Eisfeld, T., and Joos, F. (2009). “Experimental investigation of two-phase flow phenomena in transonic compressor cascades.” *Proc. ASME Turbo Expo*, 7(PART A), 103–112.
- Feng, J., Lin, Y., Zhu, G., and Luo, X. (2019). “Effect of synthetic jet parameters on flow control of an aerofoil at high Reynolds number.” *Sādhanā* 44: 1-10.
- Fischer, A. C., Frutschi, H. U., and Haselbacher, H. (2001). “Augmentation of gas turbine power output by steam injection.” *Proc. ASME Turbo Expo*, 3, 1–8.
- Fish, Fe., and Lauder, G. V. (2006). “Passive and active flow control by swimming fishes and mammals.” *Annu. Rev. Fluid Mech.*, 38, 193–224.
- Fu, C., Yanping, S., Huanlong, C., and Zhongqi, W. (2006). “Effects of boundary layer suction on the performance of compressor cascades.” *Proc. ASME Turbo Expo*, 6 PART A, 91–100.
- Gajjar, H., Chaker, M., Dighe, A., and Meher-Homji, C. B. (2003). “Inlet Fogging for a 655 MW Combined Cycle Power Plant: Design, Implementation and Operating Experience.” *Turbo Expo Power Land, Sea, Air*, 853–861.
- Genç, M. S., Koca, K., Açıkel, H. H., Özkan, G., Kırıkcs, M. S., and Yıldız, R. (2016). “Flow characteristics over NACA4412 airfoil at low Reynolds number.” *EPJ*

web Conf., 2029.

Giorgi, M. G. De, Luca, C. G. De, Ficarella, A., and Marra, F. (2015). “Comparison between synthetic jets and continuous jets for active flow control: application on a NACA 0015 and a compressor stator cascade.” *Aerosp. Sci. Technol.*, 43, 256–280.

Guo, S., Chen, S. W., Lu, H. W., Song, Y. P., and Chen, F. (2010). “Enhancing aerodynamic performances of a high-turning compressor cascade via boundary layer suction.” *Sci. China Technol. Sci.*, 53(10), 2748–2755.

Guo, S., Lu, H., Chen, F., and Wu, C. (2013). “Vortex control and aerodynamic performance improvement of a highly loaded compressor cascade via inlet boundary layer suction.” *Exp. Fluids*, 54(7), 1–11.

Guo, S., Lu, H., Gao, N., Liu, J., and Wu, C. (2016). “Simplified compound suction schemes of an aspirated highly loaded compressor cascade.” *Proc. Inst. Mech. Eng. Part G J. Aerosp. Eng.*, 230(4), 628–638.

Hale, A., Klepper, J., and Hurwitz, W. (2005). “A numerical capability to analyze the effects of water ingestion on compression system performance and operability.” *Proc. ASME Turbo Expo*, 1, 113–125.

Handley, P. F. (1922). “Wing and similar member of aircraft.” Google Patents. U.S. Patent No. 1,427,012.

Härtel, C., and Pfeiffer, P. (2003). “Model analysis of high-fogging effects on the work of compression.” *Am. Soc. Mech. Eng. Int. Gas Turbine Institute, Turbo Expo IGTI*, 2, 689–698.

Hill, P. G. (1963). “Aerodynamic and Thermodynamic Effects of Coolant Injection on Axial Compressors.” *Aeronaut. Q.*, 14(4), 331–348.

Hiner, M. C., Rueden, C. T., and Eliceiri, K. W. (2017). “ImageJ-MATLAB: a bidirectional framework for scientific image analysis interoperability.” *Bioinformatics*, 33(4), 629–630.

Horlock, J. H. (2001). “Compressor performance with water injection.” *Proc. ASME Turbo Expo*, 1, 1–9.

- Hu, J., Wang, R., Li, R., and Wu, P. (2017). "Effects of slot jet and its improved approach in a high-load compressor cascade." *Exp. Fluids*, 58(11), 1–13.
- Huebsch, W. W. (2000). "Numerical investigation on the interaction between surface roughness and viscous flows." Iowa State University.
- Ibrahim, I. H., and New, T. H. (2015). "Tubercle modifications in marine propeller blades." *10th Pacific Symp. Flow Vis. Image Process.*, 1–11.
- Ingathinathane, C., Pordesimo, L. O., Columbus, E. P., Batchelor, W. D., and Methuku, S. R. (2008). "Shape identification and particles size distribution from basic shape parameters using ImageJ." *Comput. Electron. Agric.*, 63(2), 168–182.
- Ingistov, S. (2000). "FOG system performance in power augmentation of heavy duty power generating gas turbines model 7EA." *Proc. ASME Turbo Expo*, 3(C), 1–11.
- Ingistov, S. (2001). "Interstage Injection System for heavy duty industrial gas turbine model 7EA." *Proc. ASME Turbo Expo*, 3, 1–10.
- Jain, V., Nagpurwala, Q. H., and Nassar, A. (2015). "Effect of Partial Span Aspiration on the Performance of a Transonic Axial Compressor Rotor: A Numerical Study." *Int. J. Rotating Mach.*, 2015.
- Jolly, S. (2002). "Wet compression - a powerful means of enhancing combustion turbine capacity." *Power-Gen Int.* pp.1-12.
- Jolly, S., Cloyd, S., Company, C. E., and Boost, I. F. (2003). "Performance enhancement of GT 24 with wet compression. Power-Gen International", p.3.
- Joos, F. (2006). "Experimental Investigations of the Influence of Waterdroplets in compressor cascades." In *Turbo Expo: Power for Land, Sea, and Air*, vol. 4241, pp. 221-230.
- Kerrebrock, J. L., Reijnen, D. P., Ziminsky, W. S., and Smilg, L. M. (1997). "Aspirated compressors." *Proc. ASME Turbo Expo*, 1.
- Khan, J. R., and Wang, T. (2008). "Simulation of inlet fogging and wet-compression in a single stage compressor including erosion analysis." *Proc. ASME Turbo Expo*, 7, 193–206.

- Khan, J. R., and Wang, T. (2009). "Overspray fog cooling in compressor using stage-stacking scheme with non-equilibrium heat transfer model for droplet evaporation." *Proc. ASME Turbo Expo*, 4, 609–622.
- Kleinschmidt, R. V. (1947). "Value of wet compression in gas-turbine cycles." *Mech. Eng.*, 69(2), 115–116.
- Koca, K., Genç, M. S., Açıkel, H. H., Çağdaş, M., and Bodur, T. M. (2018). "Identification of flow phenomena over NACA 4412 wind turbine airfoil at low Reynolds numbers and role of laminar separation bubble on flow evolution." *Energy*, 144, 750–764.
- Kofar-Bai, D. G., Sun, L., Ibrahim, M., and Zheng, Q. (2018). "The wet compression technology for complete gas turbine engine." *6th Int. Conf. Comput. Power, Energy, Inf. Commun. ICCPEIC 2017*, 2018-Janua, 462–470.
- Lam, G. C. Y., and Leung, R. C. K. (2018). "Aeroacoustics of NACA 0018 airfoil with a cavity." *AIAA J.*, 56(12), 4775–4786.
- Lighthill, M. J. (1963). "Attachment and Separation in Three-Dimensional Flows." *Laminar Boundary layers*. pp.72-83
- Lin, A., Sun, Y., Zhang, H., Lin, X., Yang, L., and Zheng, Q. (2018). "Fluctuating characteristics of air-mist mixture flow with conjugate wall-film motion in a compressor of gas turbine." *Appl. Therm. Eng.*, 142(February), 779–792.
- Lin, A., Zheng, Q., Jiang, Y., Lin, X., and Zhang, H. (2019). "Sensitivity of air/mist non-equilibrium phase transition cooling to transient characteristics in a compressor of gas turbine." *Int. J. Heat Mass Transf.*, 137, 882–894.
- Lu, F. K., Li, Q., and Liu, C. (2012). "Microvortex generators in high-speed flow." *Prog. Aerosp. Sci.*, 53, 30–45.
- Luo, D., Huang, D., and Sun, X. (2017). "Passive flow control of a stalled airfoil using a microcylinder." *J. Wind Eng. Ind. Aerodyn.*, 170, 256–273.
- Ma, W., Ottavy, X., Lu, L., Leboeuf, F., and Gao, F. (2011). "Experimental investigations of corner stall in a linear compressor cascade." *Proc. ASME Turbo Expo*,

7(PARTS A, B, AND C), 39–51.

Mao, X., Liu, B., and Tang, T. (2018). “Effect of casing aspiration on the tip leakage flow in the axial flow compressor cascade.” *Proc. Inst. Mech. Eng. Part A J. Power Energy*, 232(3), 225–239.

Mathioudakis, K. (2002). “Analysis of the effects of water injection on the performance of a gas turbine.” *J. Eng. Gas Turbines Power*, 124(3), 489–495.

Meher-homji, C. B. (2000). “Inlet Fogging of Gas Turbine Engines: Part A—Theory, Psychrometrics and Fog Generation.” In *Turbo Expo: Power for Land, Sea, and Air*, vol. 78569, p. V003T03A008.

Meher-Homji, C. B., and Mee III, T. R. (2000). “Inlet Fogging of Gas Turbine Engines: Part B—Practical Considerations, Control, and O&M Aspects.” *Turbo Expo Power Land, Sea, Air*, V003T03A009.

Merchant, A. A., Drela, M., Kerrebrock, J. L., Adamczyk, J. J., and Celestina, M. (2000). “Aerodynamic design and analysis of a high pressure ratio aspirated compressor stage.” *Proc. ASME Turbo Expo*, 1(C), 1–10.

Merchant, A., Kerrebrock, J. L., Adamczyk, J. J., and Braunscheidel, E. (2005). “Experimental investigation of a high pressure ratio aspirated fan stage.” *J. Turbomach.*, 127(1), 43–51.

Mohan, A., Chidambaram, P. K., Suryan, A., and Kim, H. D. (2016). “Thermo-fluid dynamic analysis of wet compression process.” *J. Mech. Sci. Technol.*, 30(12), 5473–5483.

Mueller, T. J., and DeLaurier, J. D. (2003). “Aerodynamics of small vehicles.” *Annu. Rev. Fluid Mech.*, 35(1), 89–111.

Murugan, T., Deyashi, M., Dey, S., Rana, S. C., and Chatterjee, P. K. (2016). “Recent Developments on Synthetic Jets.” *Def. Sci. J.*, 66(5).

Newell, R., Raimi, D., Villanueva, S., Prest, B., and others. (2021). “Global energy outlook 2021: Pathways from Paris.” *Resour. Futur.*, 8.

Nishida, K., Takagi, T., and Kinoshita, S. (2005). “Regenerative steam-injection gas-

turbine systems.” *Appl. Energy*, 81(3), 231–246.

Ondryas, I. S., Wilson, D. A., Kawamoto, M., and Haub, G. L. (1990). “Options in gas turbine power augmentation using inlet air chilling.” *Proc. ASME Turbo Expo*, 4(April 1991).

Payne, R. C., and White, A. J. (2008). “Three-dimensional calculations of evaporative flow in compressor blade rows.” *J. Eng. Gas Turbines Power*, 130(3), 1–6.

Pechlivanoglou, G. (2013). “Passive and active flow control solutions for wind turbine blades.”

Rosti, M. E., Omidyeganeh, M., and Pinelli, A. (2018). “Passive control of the flow around unsteady aerofoils using a self-activated deployable flap.” *J. Turbul.*, 19(3), 204–228.

Roumeliotis, I., and Mathioudakis, K. (2006). “Evaluation of interstage water injection effect on compressor and engine performance.” *J. Eng. Gas Turbines Power*, 128(4), 849–856.

Roumeliotis, I., and Mathioudakis, K. (2007). “Water injection effects on compressor stage operation.” *J. Eng. Gas Turbines Power*, 129(3), 778–784.

Rueden, C. T., Schindelin, J., Hiner, M. C., DeZonia, B. E., Walter, A. E., Arena, E. T., and Eliceiri, K. W. (2017). “ImageJ2: ImageJ for the next generation of scientific image data.” *BMC Bioinformatics*, 18, 1–26.

Rumsey, C. L., and Ying, S. X. (2002). “Prediction of high lift: review of present CFD capability.” *Prog. Aerosp. Sci.*, 38(2), 145–180.

Savic, S. M., Rostek, K. E., and Klaesson, D. K. (2005). “Techno-economic evaluation of commercially available high fogging systems.” *Proc. ASME Turbo Expo*, 4, 99–107.

Schluter, J. U. (2010). “Lift enhancement at low Reynolds numbers using self-activated movable flaps.” *J. Aircr.*, 47(1), 348–351.

Sexton, W. R., and Sexton, M. R. (2003). “The effects of wet compression on gas turbine engine operating performance.” In *Turbo Expo: Power for Land, Sea, and Air*, vol. 36851, pp. 673-679.

- Shao, Y., and Zheng, Q. (2005). “The entropy and exergy analyses of wet compression gas turbine.” *Proc. ASME Turbo Expo*, 4, 161–168.
- Shuang, G., Shaowen, C., Yanping, S., Yufei, S., and Fu, C. (2010). “Effects of Boundary Layer Suction on Aerodynamic Performance in a High-load Compressor Cascade.” *Chinese J. Aeronaut.*, 23(2), 179–186.
- Shukla, V., and Kaviti, A. K. (2017). “Performance evaluation of profile modifications on straight-bladed vertical axis wind turbine by energy and Spalart Allmaras models.” *Energy*, 126, 766–795.
- Shyy, W., Berg, M., and Ljungqvist, D. (1999). “Flapping and flexible wings for biological and micro air vehicles.” *Prog. Aerosp. Sci.*, 35(5), 455–505.
- Siemann, J., Krenz, I., and Seume, S. R. (2016). “Experimental investigation of aspiration in a multi-stage high-speed axial-compressor.” *Proc. ASME Turbo Expo*, 2A-2016, 1–12.
- Singh, D. K., Jain, A., and Paul, A. R. (2021). “Active flow control over a NACA23012 airfoil using hybrid jet.” *Def. Sci J*, 71(1), 721–729.
- Smith, M. J. C. (1996). “Simulating moth wing aerodynamics-towards the development of flapping-wing technology.” *AIAA J.*, 34(7), 1348–1355.
- Sun, J., Hou, H., Zuo, Z., Tang, H., and Chen, H. (2019). “Numerical study on wet compression in a supercritical air centrifugal compressor.” *Proc. Inst. Mech. Eng. Part A J. Power Energy*, 0(0), 1–14.
- Sun, L., Zheng, Q., Li, Y., Luo, M., and Bhargava, R. K. (2013). “Numerical simulation of a complete gas turbine engine with wet compression.” *J. Eng. Gas Turbines Power*, 135(1), 1–9.
- Svorcan, J., Stupar, S., Trivković, S., Petrašinović, N., and Ivanov, T. (2014). “Active boundary layer control in linear cascades using CFD and artificial neural networks.” *Aerosp. Sci. Technol.*, 39, 243–249.
- Szoke, M. (2019). “Trailing edge noise control using active flow control methods.” University of Bristol.

- Talay, T. A. (1975). "Introduction to the Aerodynamics of Flight." No. NASA-SP-367
- Timpe, A., Zhang, Z., Hubner, J., and Ukeiley, L. (2013). "Passive flow control by membrane wings for aerodynamic benefit." *Exp. Fluids*, 54, 1–23.
- Tobak, M., and Peake, D. J. (1981). "Topology of three-dimensional separated flows." In 14th Fluid and Plasma Dynamics Conference, p. 1260.
- Tuck, A., and Soria, J. (2008). "Separation control on a NACA 0015 airfoil using a 2D micro ZNMF jet." *Aircr. Eng. Aerosp. Technol.*
- Utamura, M., Kuwahara, T., Murata, H., and Horii, N. (1999). *Effects of intensive evaporative cooling on performance characteristics of land-based gas turbine.*
- Utamura, M., Takehara, I., Horii, N., and Kuwahara, T. (1997). "A new gas turbine cycle for economical power boosting." *Turbo Expo Power Land, Sea, Air*, V001T06A002.
- Wang, T., and Khan, J. R. (2008). "Overspray and interstage fog cooling in compressor using stage-stacking scheme - Part 2: Case study." *Proc. ASME Turbo Expo*, 7, 111–121.
- Wang, T., Khan, J. R., and Orleans, N. (2008). "GT2008-50322." 1–11.
- Wang, Y., Shen, S., Li, G., Huang, D., and Zheng, Z. (2018). "Investigation on aerodynamic performance of vertical axis wind turbine with different series airfoil shapes." *Renew. energy*, 126, 801–818.
- Wang, Z., and Zhuang, M. (2017). "Leading-edge serrations for performance improvement on a vertical-axis wind turbine at low tip-speed-ratios." *Appl. Energy*, 208, 1184–1197.
- White, A. J., and Meacock, A. J. (2004). "An evaluation of the effects of water injection on compressor performance." *J. Eng. Gas Turbines Power*, 126(4), 748–754.
- White, E., and Saric, W. (2000). "Application of variable leading-edge roughness for transition control on swept wings." *38th Aerosp. Sci. Meet. Exhib.*, 283.
- Willems, D. E., and Ritland, P. D. (2003). "A pragmatic approach to evaluation of inlet

fogging system effectiveness.” *Int. Jt. Power Gener. Conf.*, 71–76.

Williams, J., and Young, J. B. (2007). “Movement of deposited water on turbomachinery rotor blade surfaces.” *J. Turbomach.*, 129(2), 394–403.

Yadav, K. R., Paul, A. R., Hegde, N., and Jain, A. (2020). “A Comparison of Circular and Slotted Synthetic Jets for Flow Control in a Twin Air-Intake.” *Def. Sci. J.*, 70(2).

You, D., and Moin, P. (2008). “Active control of flow separation over an airfoil using synthetic jets.” *J. Fluids Struct.*, 24(8), 1349–1357.

Zhang, H., Chen, S., Gong, Y., and Wang, S. (2019). “A comparison of different unsteady flow control techniques in a highly loaded compressor cascade.” *Proc. Inst. Mech. Eng. Part G J. Aerosp. Eng.*, 233(6), 2051–2065.

Zhang, L., Chen, S., Xu, H., Ding, J., and Wang, S. (2013). “Effect of boundary layer suction on aerodynamic performance of high-turning compressor cascade.” *Turbo Expo Power Land, Sea, Air*, V06AT35A017.


Zheng, Q., Sun, Y., Li, S., and Wang, Y. (2003). “Thermodynamic analyses of wet compression process in the compressor of gas turbine.” *J. Turbomach.*, 125(3), 489–496.

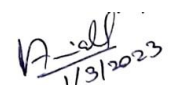
List of Publications based on Ph.D. Research Work

Sl. No.	Title of the paper	Authors (in the same order as in the paper. Underline the Research Scholar's name)	Name of the Journal/ Conference, Vol., No., Pages	Month, Year of Publication	Category*
1	Investigation of water rivulets formation on the pressure side of a linear cascade under wet compression	<u>Deepak Narayanan</u> , S Anand, S Anish	Journal of Institution of Engineers (India): Series C	May 2022	SCIE
2	Numerical Investigation on the Effect of Dry and Wet compression on a Linear compressor cascade	<u>Deepak Narayanan</u> , S Anand, S Anish	Journal of Applied Fluid Mechanics	Jan 2020	SCIE
3	Aerodynamic behavior of a linear subsonic compressor cascade in a droplet laden flow	<u>Deepak Narayanan</u> , S Anand, S Anish	International conference on Computational Methods for Thermal problems, 2018, (223309), pp.246-250 2018	2018	Book Chapter
4	Experimental Investigation of Water Film Formation and Its Propagation on the Linear Subsonic Compressor Cascade	Deepak Narayanan, S Anand, S Anish	The 7 th Asian Joint Workshop on Thermophysics and Fluid Science, November 21-24, 2018	2018	Book Chapter

5	Unsteady analysis of Water Film Formation and Its Propagation on the Linear Subsonic Compressor Cascade	Deepak Narayanan, S Anand, S Anish	7 th international and 45 th National Fluid Mechanics and Fluid Power Conference (FMFP) 2018, December 10-12, 2018	2018	Book Chpater
6	Effect of droplet size on the aerodynamic performance and operability of the axial compressor cascade	Deepak Narayanan, S Anish	Under review		
	Effect of injection ratio on the corner separation of a compressor cascade	Deepak Narayanan, S Anish			
7	Active Flow Control Method in a droplet-laden flow inside a compressor cascade	Deepak Narayanan, S Anish			

*Category: 1: Journal paper, full paper reviewed 2: Journal paper, Abstract reviews 3: Conference/Symposium paper, full paper reviewed 4: Conference/Symposium paper, abstract reviewed 5: Others (including papers in Workshops, NITK Research Bulletins, Short notes etc.)


Deepak Narayanan
 Research Scholar
 Name & Signature, with Date


Dr. Anish S
 Research Guide
 Name & Signature, with Date

CURRICULUM VITAE

Deepak Narayanan
Sreyas (Near:Muchilottu Kavu)
Karivellur P O
Onakkunnu, Kannur, Kerala,India
Pin - 670521
Email: narayanandeepak10@gmail.com
Contact Details: +919746760017,



PROFESSIONAL SUMMARY

To work in a healthy, innovative, and challenging environment extracting the best out of me, which is conducive to learning and growing at a professional as well as personal level thereby directing my future endeavors as an asset to the organization.

ACADEMIC RECORDS

- Doctoral Program: Turbomachinery, National Institute of Technology Karnataka, India, July 2022 (CGPA 7.75).
- M.Tech: Thermal and Fluid Engineering, LBS College of Engineering Kasaragod, Kerala, India, 2014 (CGPA 7.91).
- Gate examination qualified (2012)
- B.Tech: Vimal Jyothi Engineering College Kannur, Kerala, India, 2012 (65%).
- Plus Two: A V S G H S S Karivellur, Kannur, Kerala, India, 2008 (84%).
- SSLC: A V S G H S S Karivellur, Kerala, India, 2006 (86%).

SKILLS

- AUTO CADD, ICEM CFD, Pro. E, Design Modeler
 - ANSYS, Image J
 - LATEX, ORIGIN Pro
 - Proficient in Numerical Simulations (FVM)
-